The Dissertation Committee for Jongsoo Hwang Certifies that this is the approved version of the following dissertation:

Factors Affecting Injection Well Performance and Fracture Growth in Waterflooded Reservoirs

Committee:

Mukul M. Sharma, Supervisor

Kishore Mohanty

Maša Prodanović

Chun Huh

Martin Chenevert

Desmond Lawler

Factors Affecting Injection Well Performance and Fracture Growth in Waterflooded Reservoirs

by

Jongsoo Hwang, B.S.; M.S.E.

Dissertation

Presented to the Faculty of the Graduate School of

The University of Texas at Austin

in Partial Fulfillment

of the Requirements

for the Degree of

Doctor of Philosophy

The University of Texas at Austin

December 2014

Dedication

I dedicate this dissertation for the moment that my sons grow to realize that the world can be truly changed by the power of engineers.

Acknowledgements

I am very grateful for being given the opportunity to study at the University of Texas at Austin and indebted to all those who have contributed to my development during my graduate study here. First of all, I would like to express sincere gratitude to my supervising professor, Dr. Mukul Sharma for his thoughtful guidance and valuable assistance during my program of study. His effort, advice and time with enthusiasm were great inspirations to me and deepened my understanding on various aspects of petroleum engineering. I acknowledge my deep appreciations to Dr. Kishore Mohanty, Dr. Chun Huh, Dr. Martin Chenevert, Dr. Desmond Lawler, and Dr. Maša Prodanović for valuable advices, guidance, and serving as my committee members.

Administrative support from Jin Lee was essential to make all the work happen, and engineering knowledge of Rod Russell, the technical support from Glen Baum, Gary Miscoe, Mark Smith and Daryl Nygaard, the experimental support from Sam Lehardi and Ben Fox were crucial for design, constructing and conducting experiments. Dr. Ajay Suri and Dr. Zongyu Zhai are acknowledged for their valuable advices related to my research. I also thank companies sponsoring the Joint Industry Project on Hydraulic Fracturing and Sand Control at UT Austin.

I also would like to thank all of my friends for their friendship, support and sharing their valuable insights regarding my research throughout my graduate study in Austin. It has been a great honor for me to be a friend with Hisanao, Heesong, Prateek, Andrew, Dongkeun, Dohoon, Amos, Himanshu, Changmin, Doohyun, Mac, Sahil, Haotian, Evan, Hoonyoung, Lionel, Eric, Amit, Hyungjoo, Somnath, Ripu, Sap, Samarth, Hunjoo, Chris,

Michael, Karn, Hojung, Deepen, Shawn, Kyunghaeng, Kwangjin, Junhao, Jeff, Emmanouil, Sanghyon, Do, Anand, Bo, Shiting, Sunghyun, Roman, Weiwei, Ashish, Steve, Bongjun, Pratik, Kaustubh, Shashvat, Peng, Ahra, Hyuntae, Yongdo, Ijung, Beomhee, Nico including all who I have not mentioned here explicitly.

All of my work were impossible without my wife, Jisun's sacrifice and encouragement. My parents and parents-in-law were a real support, and my sons were the pillar of hope for me. I really appreciate what I have received and enjoyed during my study here in Austin.

Factors Affecting Injection Well Performance and Fracture Growth in Waterflooded Reservoirs

Jongsoo Hwang, Ph.D.

The University of Texas at Austin, 2014

Supervisor: Mukul M. Sharma

Waterflooding involves the injection of water to displace oil from oil and gas reservoirs. Well over 80% of oil reservoirs will undergo waterflooding at some point in their life. It is, therefore, important to understand some key aspects of this process that have hitherto not been well studied. This dissertation investigates the following aspects of waterflooding: (i) the filtration of solids and oil-in-water emulsions in fractured and unfractured injection wells, (ii) the generation and filtration of oil-in-water (O/W) emulsion droplets in the near-well region or in the fracture, (iii) the height-growth and containment of injection-induced fractures, and (iv) the stress reorientation induced by water injection when waterflooding reservoirs. These aspects are investigated as separate physical phenomena, but their impacts are integrated using the platform of a comprehensive waterflooding injection well model.

The first phenomenon investigated is filtration in frac-packed injectors. During long-term water injection, solid particles in the injection water may deposit in the proppant pack of frac-packed injectors. Researchers have not fully understood whether particles will travel without plugging the frac-packs or deposit in the near-well area under the high-

velocity flow conditions in the proppants. Filtration behavior under frac-pack flow conditions is the most important factor that determines overall injector performance. In this dissertation the filtration of injected solids under these conditions was experimentally studied, and the effect of frac-pack filtration on the injector performance was predicted.

The flow of dilute oil droplets in a porous medium under near-well conditions was experimentally investigated. When the porous medium has a residual oil saturation, oil droplets can be generated by viscous forces overcoming entrapping capillary forces. The generated oil droplets will subsequently participate in filtration processes along with injected oil droplets. If this occurs in the near-injector area, the injectivity can severely decline and this may require expensive remediation processes. In this study, prediction of O/W emulsion flow was improved by experimental observations of the rates of generation and filtration of oil droplets.

In a larger scale problem, a 3-dimensional model of water-injection-induced fracture was developed to predict the fracture height growth. If a fracture breaches the bounding layers, the sweep efficiency can be significantly impaired and it could have severe environmental consequences (such as contamination of shallower aquifers or the seabed). During long-term water injection, fracture growth can only be simulated properly when the filtration near fractures, thermo-elastic stress changes and reservoir fluid flow behavior are all concurrently calculated. Based on this new model, the impact of reservoir stress conditions, mechanical properties, and injection-water quality on fracture growth was studied.

On a reservoir-scale, the stress reorientation caused by injection-production activities during waterflooding was investigated. A new finite-volume multi-phase reservoir simulation with poro- and thermo-elasticity was developed. This model was applied to various waterflooding well patterns, such as five-, nine-spot, line-drive and

horizontal well pairs, and the critical geomechanical responses by injection-production activities during waterflooding operations were analyzed. The model can be used to predict the direction of induced fractures, design infill well locations and configurations and optimize the reservoir sweep.

Through the use of both experimental observations and numerical models this work has elucidated various physical phenomena affecting fracture growth and injection-well performance. The findings in this dissertation provide critical data and models that help us to more confidently specify injection water quality, the design of pumping and water treatment facilities, and the optimization of well planning. The models developed in this work can be used to substantially improve the predictions of injection well performance and improve reservoir oil recovery by waterflooding.

Table of Contents

List of Tables

List of Figures

Chapter 1 : Introduction

1.1 INTRODUCTION

1.1.1 Water Injection in the Petroleum Industry

In the oil and gas industry, waterflooding is the most common and economical technique to displace oil not recoverable from primary recovery. Waterflooding supports the reservoir pressure and displaces the oil phase. Many oil reservoirs currently in production apply this technique to improve oil recovery. According to Thomas (2013), waterflooding has been used since the initiation of the oil and gas industry. Waterflooding became a standard operational method in the 1950's. Waterflooding oil recoveries are typically 35% to 100% of the oil recovered during primary recovery.

Waterflooding requires careful design and implementation. This dissertation addresses some of these aspects specific to well completions recently used in large scale waterflooding projects, i.e., frac-packed injectors. Various scales of problems encountered in waterflooding projects are investigated in this dissertation. It includes micro-scale subjects and classical fluid flow problems, e.g., oil-in-water (O/W) emulsion flow in porous media, which can be encountered in waterflooding reservoirs. Larger scale problems are investigated as well, e.g., fracture growth in water injection wells and the field-wide stress reorientation problems induced by poro- and thermo-elastic effects during waterflooding.

1.1.2 Produced Water in the Petroleum Industry

Because waterflooding requires a significant amount of water over a long period of time, it is important to have a secure and continuous source of water. Water injection

operations during waterflooding use different types of water sources, mainly produced water and seawater. Produced water is water from subsurface formations that is brought to the surface during oil and gas production activities. It should be noted that flowback water, which is injected water returned to the surface, is also included in the category of produced water. However, in this study, we focus on the produced-water that is produced from the hydrocarbon bearing reservoir.

Produced water from the subsurface is the largest volume stream in the oil and gas industry. Water production is inextricably linked to hydrocarbon production. Although it is challenging to gather statistical data for international water production, there is some information available, such as Bailey et al. (2000), Veil (2009), Clark & Veil (2009), and SPE (2011). Ali (2013) stated that more than 20 billion barrels (bbl) of water produced each year in the United States is associated with oil and gas industrial activities, and more than 90 billion bbl of water is produced annually worldwide by the oil and gas industry. BP (2014) reported that in 2013, the crude oil production in the U.S. was 3.7 billion bbl, and the worldwide oil production was 31.7 billion bbl. Water production is more than five times oil production in the U.S. and three times as high oil production worldwide (Figure 1.1). This fact that more water is typically produced than oil in the petroleum industry suggests how the treatment and usage of produced water is a critical concern. These studies of water statistics also predict a gradual increase in water production between 2025 and 2040 (Figure 1.2).

There have been increasing efforts to manage this large volume of water technically, economically, and environmentally. This tremendous amount of water requires additional treatment and handling to meet environmental regulations. In some cases, produced water is disposed on the surface, particularly offshore, after treatment. However, most treated water is re-injected to the subsurface for either disposal or improved oil recovery including

waterflooding (PWRI; Produced Water Re-Injection) (Veil et al., 2004). Produced water also can be used for other purposes, such as hydraulic fracture stimulation, industrial processes, crop irrigation, livestock consumption, farming, and electricity generation (Myers, 2014). The ultimate use of produced water is determined based on the location and its needs. Subsurface injection is the most common method of disposal of produced water. Clark & Veil (2009) showed that of the 20 billion bbl of produced water in the U.S. in 2007, 10 billion bbl was re-injected for improved oil recovery and 7 billion bbl was re-injected for subsurface disposal.

Ali (2013) stated that the associated cost to handle produced water comprises a substantial portion in the industry. It was understood that, in the U.S., each barrel of produced water had a treatment and handling cost of approximately $0.9 USD. Globally, the treatment cost varies with location and associated logistics. Bailey et al. (2000) shows this cost varies between $0.05 to 1.5 USD per barrel of produced water worldwide. Considering that, on average, three barrels of water is produced per oil barrel (75% water cut), and approximately three dollars is spent per oil barrel produced purely for water treatment. This represents a significant financial cost to the industry. If the cost could be reduced by 1%, it would be equivalent to $50 to 100 million USD per year in the U.S. It can be argued that the effectiveness of the water treatment, especially the optimization of the water re-injection, can dramatically reduce the cost to the industry and improve oil recovery. Khatib & Verbeek (2002) showed a breakdown of water handling costs, as shown in Figure 1.3. This figure includes capital and operating expenses, but excludes drilling, possible workover, and remediation costs. Because these well construction and management expenses can be substantial, a critical risk management issue also lies in the produced water treatment economics, especially those related to re-injection well management.

1.1.3 Produced Water Chemistry and Treatment

As produced water comes from varying sources of water and from many stages of waterflooding, each source of water has its own chemistry. Geographical locations and geologic formations also change the water chemistry and physical properties considerably. Produced water requires chemical analysis prior to reuse, recycling or disposal to optimize the treatment method. The main components in produced water are oil, grease, solids, metals, and other organic and inorganic elements. Tibbetts et al. (1992) explained that these components exist in different forms as emulsion, suspension, solution, adsorbed particles, and solid particles. Among them, dispersed oil and grease, i.e., oil-in-water (O/W) emulsions, and suspended solid particles are the main components known to cause formation damage near the injection wells. The treatment facilities for produced water focus on removing these components. Salt content is an important characteristic of produced water. It varies widely from different sources. Sometimes formation water has a higher salt content than seawater. Produced water can be classified into the following categories based on its salt contents (Mantell, 2011): 'brackish' water containing 5,000 to 35,000 mg/L TDS (Total Dissolved Solid content), 'saline' water containing 35,000 to 50,000 mg/L TDS, and 'brine' containing 50,000 to 150,000 mg/L TDS.

Seawater used as injection water can contain microbes. Even after the filtration process, microbes are the primary particles that can plug the formation around injection wells. Chang (1985) reported significant formation plugging by biomass, e.g., microbes contained in injection water. The microbes are typically plankton, including zooplankton and phytoplankton, which are single cell microbes filled with gelatinous matter. Gelatinous matter can cause a higher degree of formation damage as compared to inorganic particulates.

Due to the variability of injection water sources, treating produced water or

seawater can be a challenging task. As the quantity or quality of the water is variable due to the production stages and source of injected water, researchers need to carefully select the right water treatment facilities. In the early stages of waterflooding, the water production rate is low compared to oil production, but it can increase substantially as the production stage changes. The associated water chemistry can be significantly different. These complicated changes are dependent on the reservoir properties, initial reservoir fluids, and rock-fluid interaction properties as well as additive chemicals used during operations. There are various technologies available for water treatment. Most commonly used methods are coagulation, sedimentation, filtration, coalescers and hydrocyclones. Some potential technologies are membrane filtration, thermal evaporation, membrane bioreactor process, and advanced oxidation process (Hussain et al., 2014).

1.1.4 Importance of Injection Well Performance

The performance of an injection well can be represented as an index of injectivity. The injectivity index, I is defined as the ratio of the injection rate and the pressure drop between the bottom-hole pressure and the average reservoir pressure.

$$I = \frac{q_{inj}}{P_{iwf} - P_{r,avg}} \tag{1.1}$$

Here, I is the injectivity index, q_{inj} is the total injection rate, P_{iwf} is the flowing injection wellbore pressure, and $P_{r,avg}$ is the average reservoir pressure. The injectivity decline typically observed in water injection wells significantly impacts the economics of the waterflooding operation. There are case studies that show the injectivity declines very quickly. Much of the literature, including Sharma et al. (2000), Bedrikovetsky et al. (2005), and Suri et al. (2010), has shown the injectivity decline in actual waterflooding field cases. Many injection wells experience injectivity decline ratios of 5 to 10 as compared to the initial values. This decline sometimes continues gradually over a timescale of years;

however, some other wells were observed to have a rapid decline within months, as in Figure 1.4. Remedial operations, including acidization, are required every few months to maintain the injectivity above the economic well operation objectives. The remedial cost and the operation's down-time can be significant. The best way to avoid this situation is to properly predict the injectivity during the waterflooding design stage.

This injectivity decline issue has been regarded as a critical subject since the inception of waterflooding. It is not only from the field cases that the injectivity decline can be observed. There have been a substantial number of experimental observations related to this issue to extend their observations to better predict the injectivity decline in the field. The importance of water quality on predicting injectivity has been acknowledged widely since Barkman & Davidson (1972)'s work. They focused on the filtration of suspended solids in injection water on the wellbore face and perforations. They suggested injectivity impairment mechanisms and derived corresponding predictive equations for injector half-life. Eylander (1988), Todd et al. (1990), van Oort et al. (1993) and Zhang et al. (1993) estimated the degree of injectivity impairment by using experimental methods in which solid particles or oil droplets were injected into cores. These methods suggested basic formation damage mechanisms, and they extended these observations to well impairment models. These models have been used as prediction methods for many waterflooding designs. They have limitations, however, in being applied to different well configurations and completions, and in being implemented with the other physical phenomena involved in injection wells, for example, fracture growth and thermal effects.

The importance of injection well performance is not limited to waterflooding. Along with waterflooding, waste disposal has been another important reason for water injection in the petroleum industry. Subsurface waste disposal has been an environmentally sound method approved by legislatures worldwide, and this has been a critical drilling-

waste management method. Water disposal wells have the same injectivity decline issue, so similar prediction techniques are required. Tenizbaeva et al. (2012) showed that waste water injectivity can control the operability of a whole field. Bentley et al. (1986) reported permeability damage in core-flood experiments with a waste slurry. Saripalli et al. (2000) applied an injectivity decline model to a waste slurry injection case. In addition, in other types of improved oil recovery methods, such as polymer flooding, the injectivity issue is of critical concern. Some types of improved oil recovery methods and the corresponding mechanisms are the following:

- Mobility improvement by polymer and steam
- Reduction in residual saturation by surfactants and low-salinity waterflooding
- A combination of the above two methods by alkali-surfactant-polymer (ASP) flooding

All of these methods require injectivity predictions. Fletcher et al. (1992) and Seright et al. (2009) show examples of the injectivity issue and observations of polymer injectivity decline. Zechner et al. (2014) studied the injectivity issue when polyacrylamides are used for polymer-flooding in a field pilot test. These polymers exhibit a significant increase in apparent viscosity due to the viscoelastic properties of polymer solutions. They also reported severe degradations of polymer solutions at high velocity conditions. In many polymer injections, injection under fracturing conditions are preferred to avoid these issues. These characteristics unique in polymer injections need to be taken into account along with factors controlling water injectivity declines.

1.2 MOTIVATION OF RESEARCH

1.2.1 Factors Controlling Performance of Water Injectors

The injectivity decline models introduced in the previous sections have served as

good estimation methods for injectivity decline prediction. They mainly focused on injectivity impairment by particle deposition mechanisms. They were also found useful in specifying the injection water quality to eventually design surface treatment facilities. However, there are other critical factors along with particulate filtration that control the injectivity of long-term injection wells. They can be listed as follows:

- Internal (deep-bed) filtration of solids/emulsions
- External (filter-cake) filtration
- Poro- and thermo-elastic effect of injection and production
- Fracture growth
- Transient effect of shut-in and injection rate change
- Sand control issues
- Formation heterogeneity (layering)

These are actually critical issues, as they affect the reservoir sweep, not only the individual injector performance. The issues here can be classified as either design or operational issues. They need a careful investigation from the design stage and require verification during the operational stages. Upon any change of operational conditions, the above issues will need to be reviewed during the waterflooding operations to prevent rapid injectivity declines. The scale of these problems range from microscopic physics to field-wide phenomena.

Importantly, the above factors are related to each other, and a change in one of these factors can lead to changes in the other. For example, if the injection temperature decreases by operational requirements, the thermal effect further reduces the *in situ* stress and fracture growth will be promoted. Then, the lengthening of the fracture provides additional area for particle filtration, which changes the pressure drops near the fractures. Suarez-Rivera et al. (2002) conducted experiments on fracture propagation by injecting water with particles to

show the combined effect of fracture growth and filtration (Figure 1.5).

Hence, it can be emphasized that the water injectivity prediction requires a comprehensive model to address the combined effect of the factors mentioned above. By applying this comprehensive well model to actual field cases, the specifically critical factors can be identified, and an operational strategy can be established to avoid any rapid injectivity decline. Until the 1990's, research efforts were focused more on the individual physics of the above factors. Afterwards, the industry started to pay closer attention to comprehensive injection well models. In the following sections, research on individual factors, comprehensive well models, and applications to field cases are introduced.

1.2.2 Particle Plugging near Water Injection Wells

Dilute suspended particles of various types, in solid and oil droplet form, can deposit on the wellbore, fracture faces, proppants, gravels, or any porous space in well completions. The mode of filtration can be mainly internal (deep-bed) or external (filter cake). The internal filtration of suspensions typically occurs within a few centimeters from the surface of the porous medium near the well completions. However, in this narrow zone of internal damage, the flow resistance caused by internal filtration can increase significantly. Once the internal deposition exceeds its critical value, typically when the near-surface pores are completely plugged by particles, the external filtration begins on the surface of the porous medium. External filtration results in a filter cake, typically a compressible soft filter cake on wellbores, or fracture faces. The transition time from internal to external filtration in water injection wells can be in the order of days to months depending on water quality and well configurations. The flow resistance of an external filter cake can be much higher than internal plugging, even though the thickness of the filter-cake deposition is thin (the order of millimeters). These two modes of filtration essentially lead to a severe decline in permeability near the wellbore and substantially

increase the bottom-hole pressure with injection time. This phenomena has been investigated specifically for waterflooding applications.

Barkman & Davidson (1972) showed that the half-life of injectors, which is the time required for initial injectivity to decrease by 50%, is a direct function of water quality during filter cake build-up in wellbores and perforations. Sharma & Yortsos (1987) developed a population-based material balance of the capture and release of suspended-particles. The associated permeability-reduction was modeled using a network model that allowed for a more accurate description than permeability-porosity type correlations to describe permeability damage by particle deposition. Eylander (1988) presented a method to predict injectivity decline based on the coreflood data and filter cake properties. This method is valuable in that it provides data about the nature of impairment (external and internal), impairment reversibility, and the depth of impairments. Todd et al. (1990) suggested that care must be taken while laboratory-based models are used to history match the well performance. The preparation of the core affected the formation behavior of an external filter cake. The importance of layer-by-layer analysis was also evaluated. van Oort et al. (1993) also conducted coreflood experiments focusing more on internal filtration. They improved the injectivity impairment models by suggesting that, at higher injection rate (in linear velocities exceeding 10cm/min), the particle deposition is smaller.

Wennberg & Sharma (1997) adopted the concept of filtration coefficient, which indicates the degree of filtration in a unit length of filter, to properly account for various injection conditions, e.g., injection rate, particle size, concentration and the amount of deposition. This implementation improved the predictions of the rate of internal filtration, transition time to external filtration, and hence allowed a proper material balance, eventually improving injectivity prediction. Pang & Sharma (1997) suggested type curves for injectivity declines observed in coreflood experiments. Their models combine internal

and external filtration and show the primary importance of the mode of filtration, particle-invasion depth, and cake properties. Injectivity impairment from internal and external filtration were individually established into numerical models, and they were validated with previous experimental results. Bedrikovetsky et al. (2003) conducted internal filtration experiments to measure the initial filtration coefficient and damage factor, and showed the dependency of filtration coefficient on particle deposition. Different types of particles, solid and oleic suspensions, were used to show that the solid filtration coefficient was higher than for oil droplets due to penetration through pore throats in oil droplet cases.

1.2.3 Fracture Propagation during Water Injection

When the bottom-hole pressure increases because of particle plugging with water injection, it can exceed the pressure above which the rock can crack by different modes of failure. This phenomenon can also be affected by the thermal effects of cold injection water on the *in situ* stress. The magnitude of the stress can decrease with cold-water injection, which results in fractures being created at smaller bottom-hole pressures. Hence, the fracture propagation prediction requires an understanding of thermal stresses. Once the fracture starts to grow or changes its dimensions in length or width, the injectivity can change dramatically, because the new fluid-flow pattern will change the pressure distribution. In addition, newly created fracture faces have less fluid resistance, and suspended particles will preferentially plug the new fracture faces. These factors again interact with each other during long-term injection. These effects were shown by field cases reported by Paige et al. (1995).

Hagoort et al. (1980) included a fracture growth model in a waterflooding reservoir simulation. They built a conventional single-phase reservoir simulation coupled with an analytic fracture model. Pang & Sharma (1995) developed single well injector models for open-hole, perforated and fractured injectors. They applied internal and external filtration

calculations to the different geometries of well completions. van den Hoek et al. (1996) built a fractured injection well model under fracturing conditions, including analytic calculations of poro- and thermo-elastic effects on fluid injection. This model was used for a Middle East field example which showed that fractured-well injectivity is partially reversible.

In recent years, the fractured injector has been preferred when choosing a well completion for water injectors. Even in cases of unfractured wells, injection pressure can be maintained intentionally above the fracturing gradient to induce fracture and take advantage of high injectivity. Injection into the formation matrix without fracture growth may not be a good option due to the rapid injectivity decline. Instead, growing a fracture can slow the injectivity decline. Abou-Sayed & Zaki (2005) showed that when particle plugging is active, injectivity can be sustained to a certain level only with the aid of fracture growth (Figure 1.6). However, injection-induced fractures can not only grow, but can also be shortened by changing the injection rate. When transient effects associated with the injection history are accounted for, the injection well performance can be predicted more accurately. Suri et al. (2011) estimated a fracture length in horizontal wells by performing a history match, and they were able to better understand the effect of fracture length changes and their effect on injectivity by taking pressure transient effects into account.

1.2.4 Thermal Effect during Water Injection

The temperature of the injection water is typically lower than that of reservoirs. For example, the typical surface temperature of injection water is approximately 30˚C, but reservoir temperatures can be more than 100˚C depending on the depth and the local geothermal gradient. This temperature difference can cause the *in situ* stresses around the injection well to decrease significantly. The direction of principal stresses will reorient as well. The poro-elastic effect of fluid injection can also cause the stress to reorient in

magnitude and directions. However, the degree of thermo-elastic effect in typical field conditions is more dominant than the poro-elastic effect. The stress reduction by cold water injection can change the fracture gradient, typically inducing favorable conditions for fracture growth. The reorientation of local stress directions can change the direction of fracture propagation to deviate from far-field principal stress directions. This effect will significantly affect the fracture orientation, and hence the sweep efficiency and ultimate oil recovery. These thermo-poro-elastic effects will also change the difference between maximum and minimum horizontal stresses. Depending on this pattern, natural fractures can be stimulated locally, which will also significantly impact the sweep patterns.

The impact of thermo-elastic stress changes have been understood to be important for a long time, but a systematic approach still has not been taken to clearly understand this effect. Perkins & Gonzalez (1985) built a fractured-well model with elliptical thermal and waterflood fronts. The reservoir flow and temperature was semi-analytically described, and the thermal stress change was calculated. In their study, a reduction of *in situ* stress of more than 1000 psi can be achieved by injecting 80˚F water into 200˚F reservoirs. This calculation has been used in numerous models to apply fracture growth predictions. Martins et al. (1995) showed an important impact of the thermal effect on Prudhoe Bay waterflooding injection wells. Thermally induced fracturing was one of essential reasons that high injectivity was maintained. It was also shown that the thermally induced stress change can sometimes promote fracture growth into bounding layers (although it usually prevents it). This can impact the waterflooding efficiency. Detienne et al. (1998) also developed a simple analytic model to predict the injection well performance. They applied a semi-analytic method for fracture growth description to account for the thermal stress change. The model was validated with offshore West Africa field cases. Minner et al. (2002) introduced the importance of well patterns and configurations on a field scale,

where the poro-thermo-elastic effect of fluid injection and production on stress change has been investigated (Figure 1.8).

1.2.5 Water Injection Well Completions and Relevant Well Models

Fracture orientation and injectivity models are all dependent on which well type is used for water injection. Open-hole, gravel-packed, cased and perforated, and frac-packed wells are typically used for vertical water injection wells. Recently, the application of horizontal wells is increasing. All of these wells are subject to both formation damage by plugging and the ability of fractures to grow from the wellbore. For high permeability waterflooding reservoirs, typically found in the Gulf of Mexico (GoM) and West Africa offshore projects, large numbers of frac-pack completions are applied. Filtration and fracturing occurs differently for different well completions, so specific well models incorporating these different physics are required.

Sharma et al. (2000) built a comprehensive model for open-hole, cased-perforated, and fractured wells and applied it to an offshore GoM case study. They suggested guidelines for water quality, i.e., particle size, concentration, and injection rate by "what if" analysis to evaluate the economics of waterflooding projects. In unfractured wells, it was critical to find the optimum point to balance the higher water-quality treatment cost and remediation (acidization) cost. Bachman et al. (2003) built a coupled fluid flow, stress, dynamic fracture, and permeability damage model. They applied this coupled simulation to match the injectivity changes in GoM wells. Detailed stress direction and fracture dimensions, however, were not shown. Detienne et al. (2005) also developed a comprehensive well model for the fractured injector which accounts for particle plugging and thermal effect on stresses. Fracture length was calculated based on constant height fracture models, such as the PKN model.

Abou-Sayed et al. (2007) suggested strategies and best practice examples for

different types of water injectors. Matrix injection required high-quality separation and treatment for injection water; the treatment cost increased the CAPEX. A fractured injector can provide benefits to reduce the water treatment specification by the fracture growth and thermal effect. However, it was recommended that injection rate should be determined not to induce out-of-zone propagation.

Horizontal injectors have been preferred recently as they allow more access to the reservoirs with higher injectivity. Suri & Sharma (2009) suggested an injection well model for horizontal wells with longitudinal and transverse fractures. This model also allows operators to simulate the injection of a power-law fluid into horizontal injectors. The authors screened out the importance of injection parameters to show that injectivity was primarily dependent on *in situ* stresses, thermal effect, injection rate, and water quality.

Gadiyar et al. (2004) and Goodman (2008) reviewed the construction and applications of frac-pack completions. While constructing wells, a fracture is created and packed by proppants, as shown in Figure 1.7. The wellbore space is gravel-packed as well to minimize the hollow space in well completions, which prevents sand production. By plugging the tip of the growing fracture by proppants, fracturing fluid forces are delivered more to the main body of fractures, and the created fracture becomes thick and short. This is ideal to stimulate unconsolidated reservoirs that require sand-control. This technique, tip screen-out method is now commonly used in frac-packing unconsolidated sand reservoirs. Suri & Sharma (2010) developed a frac-packed injection well model. In this model, the particle filtration in the proppant section of frac-packs is described. If particles plug the proppant section near the wellbore, the advantage of a frac-pack may be diminished and the injector performance will be aggravated. It was shown by the comprehensive frac-pack injector model that the degree of particle filtration in proppants can significantly impact the well injectivity. Suri et al. (2010) also conducted a case study on frac-packed wells. In

their field observations, the injectivity of wells in the same field were different by a factor of 50. This was caused primarily by differences in the filtration in the proppant pack.

de Souza et al. (2005) conducted a study on how the sweep efficiency changes with injectivity and fracture growth. They coupled a commercial reservoir simulator and a semi-analytic fracture propagation model to estimate the fracture length in different well patterns, i.e. five-spot, line-drive, combination of horizontal injector-producers. For each well pattern, the recovery factor and NPV's were predicted and compared to show that injection-induced fractures have a larger impact than well types like vertical and horizontal wells. Ochi et al. (2013) applied a Monte-Carlo analysis using a comprehensive well model to screen out the degree of impact of each injection parameter. Using this approach, they suggested a method to statistically assess the uncertainty of parameters related to injection-well design. By showing a statistical prediction of simulation results, the injectivity predicted was more reliable.

1.2.6 Limitations of Previous Research

The waterflooding process has various physical aspects in various size scales, from microscopic to the field-scale. As explained previously, these physical phenomena strongly interact with each others' results. To predict waterflooding performance as well as how to design a water injection well, researchers need to understand the individual physics previously explained. Limitations of our current understanding are identified here, and individual physical phenomena were analyzed by experimental and simulation approaches in this work.

Frac-packed injectors are used extensively for offshore injection wells in unconsolidated reservoirs. Their main purpose is to provide sand control and maintain high injectivity over a long period of time. This can help in reducing the water treatment requirement. However, the water treatment may not be reduced when the suspended

particles plug the near-well portion of the proppant pack. It is not very well understood if the solid particles will travel through the frac-pack section without plugging or depositing in the near-well section. This is because there is no systematic information on the filtration in the high velocity flows encountered in a frac-pack propped fracture. The flow of water with suspended dilute particles in proppant needs to be measured with the actual fluid flow conditions encountered in frac-packs.

Another micro-scale aspect that can strongly change the fluid flow behavior near injection and production wells is O/W emulsion flow. Most produced water contains some concentration of O/W emulsions. These oil droplets behave differently from solid particles when injected into reservoirs, especially those with residual or higher oil saturation. O/W emulsions can be generated by a high shear rate induced by high velocity fluid flow along the interface of water-oil phases. This phenomenon has not been quantified, and relevant theories are not available. However, the formation damage can be severe when large amounts of emulsions are generated in a near-well area where fluid velocities are high. In addition, how emulsions can deposit in a porous medium, the filtration behavior, is not well understood, especially when emulsion generation and filtration occur simultaneously. There are no adequate models available for these phenomena, and experimental measurements are also required to better understand the near-well formation damage.

A larger scale phenomenon which is critical to a water injection operation is the fracture containment issue. In some geologic formations, the *in situ* stress conditions of the target and bounding layers may not be favorable to contain the induced fractures during long-term water injections. Once a fracture starts to grow into bounding layers, the sweep efficiency of waterflooding will be seriously compromised. This breaching of a shale barrier by fracture growth into bounding layers must be predicted during the design stage. Only a 3-dimensional fracture simulation model can predict the proper fracture geometry

in such cases. The water-injection-induced fracture simulation also requires concurrent calculations of thermal stress change, filtration on fracture faces, and reservoir flow calculations. The proper fracture growth prediction can only be made when the fluid leak-off on the fracture faces is calculated. However, researchers have not attempted to develop the leak-off calculation accounting for proper filtration behavior during long-term water injection.

In a field-scale problem pertaining to waterflooding, improvements to stress management issues are required to better estimate sweep efficiency. For example, when an infill water injection well is drilled and fractured, the effect of the historical injection and production can change the *in situ* stresses for infill locations. These reoriented stress directions and changes in stress magnitudes can be significantly different from the initial conditions. Without accurate predictions of stress reorientation, the infill well stimulation and associated sweep efficiency can be difficult to control. There has been research to address the thermal effects on stress, but critical information on principal stress directions, which actually determine fracture orientation and eventually sweep efficiency, has not been developed. The magnitude of stresses needs to be studied so the local chances of natural fracture stimulation in waterflooding reservoirs can be properly predicted. To predict these behaviors, a coupled simulation of multi-phase fluid flow with thermal- and poro-elastic calculation is necessary.

1.3 RESEARCH OBJECTIVES

The objective of this study is to provide a deeper understanding of the phenomena related to the four major limitations described in the previous section by conducting experiments and simulations. Each of the major subjects is organized into separate chapters in this dissertation. The main objectives for each of the four subjects are:

- Identify the filtration behavior of solid particles at high flow rates such as those

encountered in a frac-pack

- Measure the generation and filtration of O/W emulsions in simulated near-well or near-fracture conditions and utilize them in an emulsion flow model in porous media
- Understand fracture confinement and leak-off behavior by building an injection well model with 3-dimensional fracture propagation
- Investigate the stress reorientation in waterflooding reservoirs caused by injection and production activities and then analyze its impact on stimulation effectiveness and reservoir sweep and recovery

Each subject includes subdivided objectives detailed in each chapter.

Even though the individual objectives are limited to the specific phenomena, the eventual goal for this dissertation is to combine these individual investigations and suggest improved methods to:

- Predict the injectivity decline of injection wells
- Mitigate the adverse effects of near-well formation damage on well performance
- Understand and improve reservoir sweep efficiency during waterflooding operations
- Understand the ultimate recovery by understanding individual physical phenomena studied in this dissertation.

The fundamental physical phenomena pertaining to these aspects range from microscopic pore-scale effects to macroscopic field-scale effects. These aspects are observed by experiments, and the related observations are included into models applicable in a comprehensive well simulation. All of the improvements in the form of empirical or numerical models are to be included in a comprehensive well model or a waterflooding field model to see the combined effect of various aspects in the waterflooding process.

1.4 ORGANIZATION OF THE DISSERTATION

This dissertation is organized into four main topics:

In **Chapter 2**, the theories of solid particle filtration in a porous media were reviewed first. Experimental results are presented for the filtration of solid particles in high velocity flow. Relevant models are suggested to capture the essential physics of this process. These results are used to show how solid particles are deposited in propped fractures in frac-packed injection wells.

Chapter 3 presents the experimental results of O/W emulsion flow in porous media. The theoretical background is explained first. Then, the emulsion generation and filtration processes are individually treated as separate processes. Also, the measured rate of generation and filtration are measured and suitable models developed. The effects of fluid velocity and grain sizes as well as other important parameters are evaluated.

In **Chapter 4**, a 3-dimensional fracture propagation model in water injection wells is developed. Fundamental equations and discretization methods are introduced, and the algorithm to combine filtration physics and fracture propagation calculation is introduced. The adaptive leak-off calculation method based on filtration models, which is essential to simulate injection-induced fractures, is introduced as well. The application of the model is shown in various cases.

Chapter 5 details the development process of reservoir simulator that includes poroelastic effects, two-phase flow, an energy balance as well as poro- and thermo-elasticity. The model development algorithms are presented, and validation to known solutions for individual physics are shown. Then, the model is applied to describe the stress reorientation that may be expected in basic waterflooding well patterns when waterflooding reservoirs with multiple wells under typical reservoir conditions.

Chapter 6 reviews each chapter's improvements and sums up the impact of the

studies presented in this dissertation. It also discusses ideas for potential future studies to continue the research started in this dissertation.

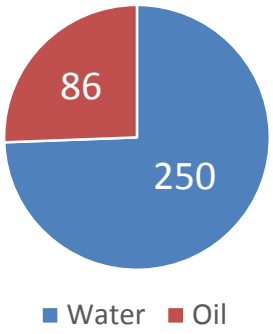

Figure 1.1: Comparison of global daily production rate of water and oil in million barrels per day.

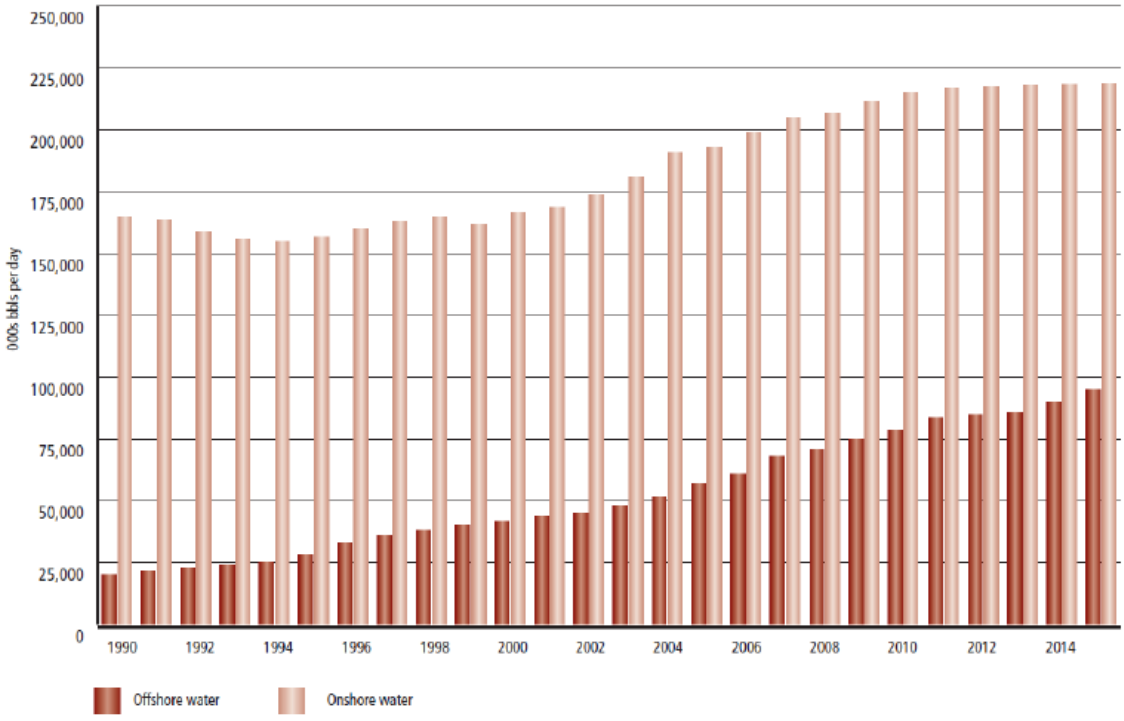

Figure 1.2: Daily rate of produced water globally from onshore and offshore oil and gas production (from SPE, 2011).

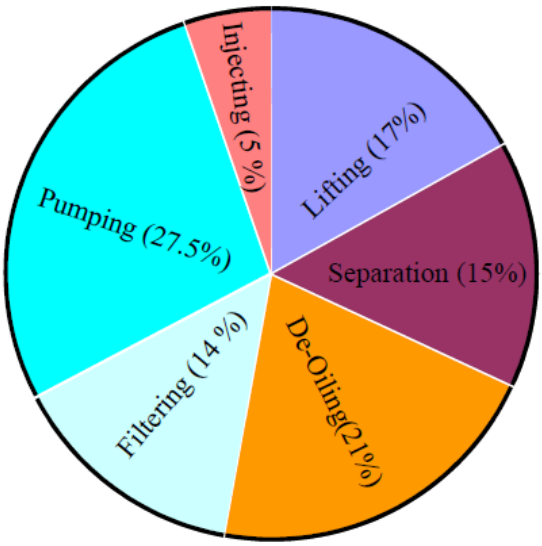

Figure 1.3: The breakdown of the handling and treatment costs for produced water (from Khatib and Verbeek, 2002).

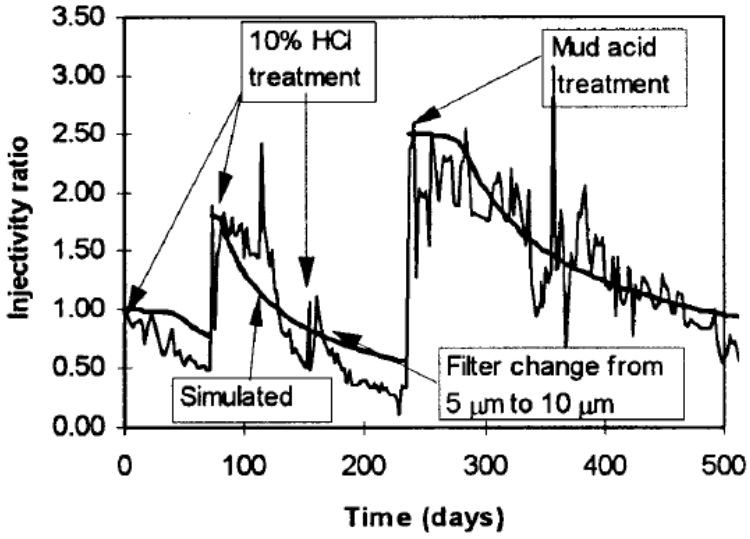

Figure 1.4: Field case of rapid injectivity decline and associated remediation processes (from Sharma et al., 2000).

Figure 1.5: Experimental observations on particle plugging near growing fracture faces visualized by fluorescent acrylic particles (from Suarez-Rivera, 2002).

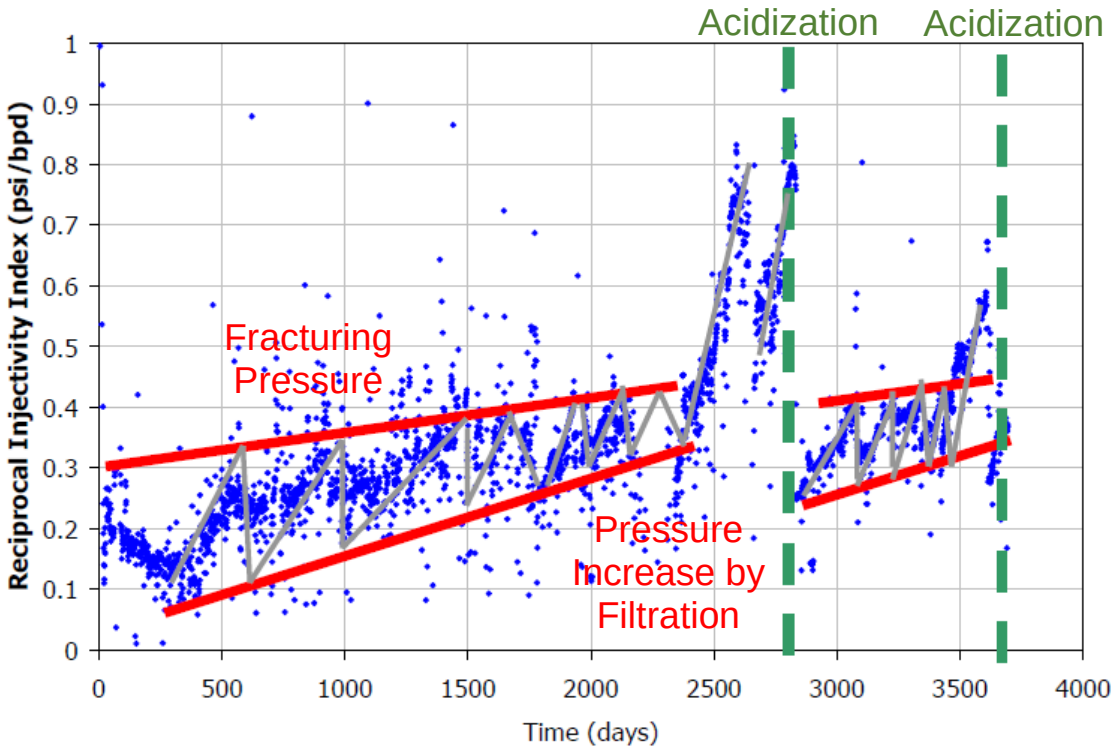

Figure 1.6: Reciprocal Injectivity changes showing simultaneous fracturing and filtration (from Abou-Sayed & Zaki, 2005).

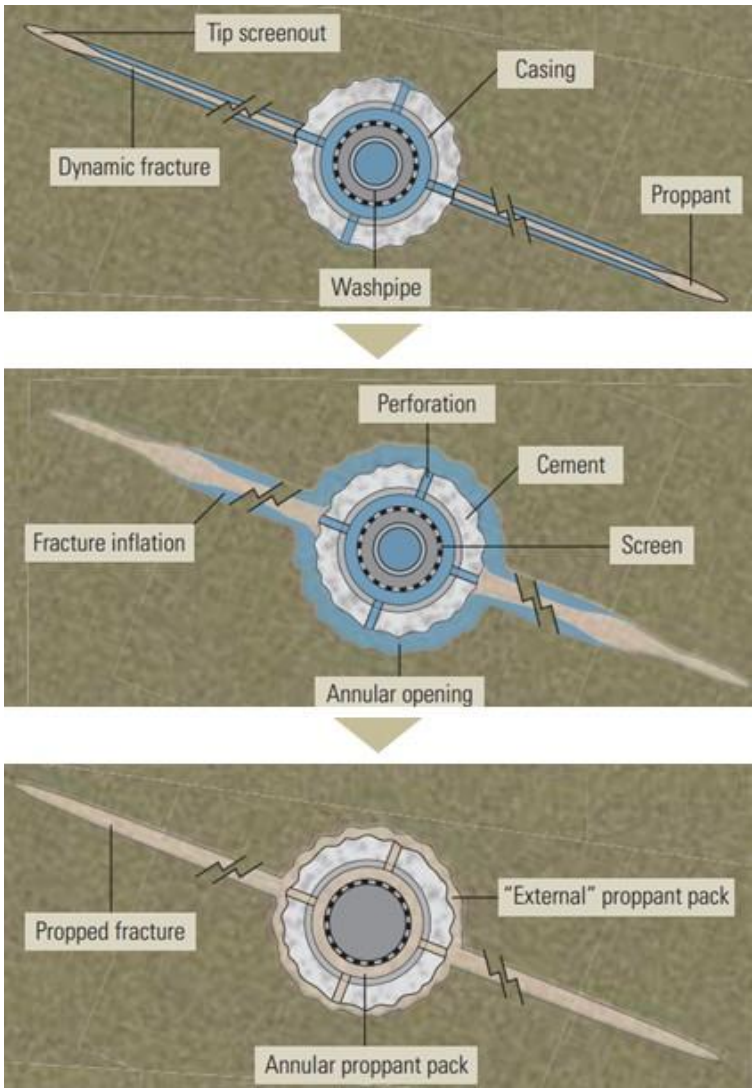

Figure 1.7: Construction of frac-packed well (from Gadiyar, 2004)

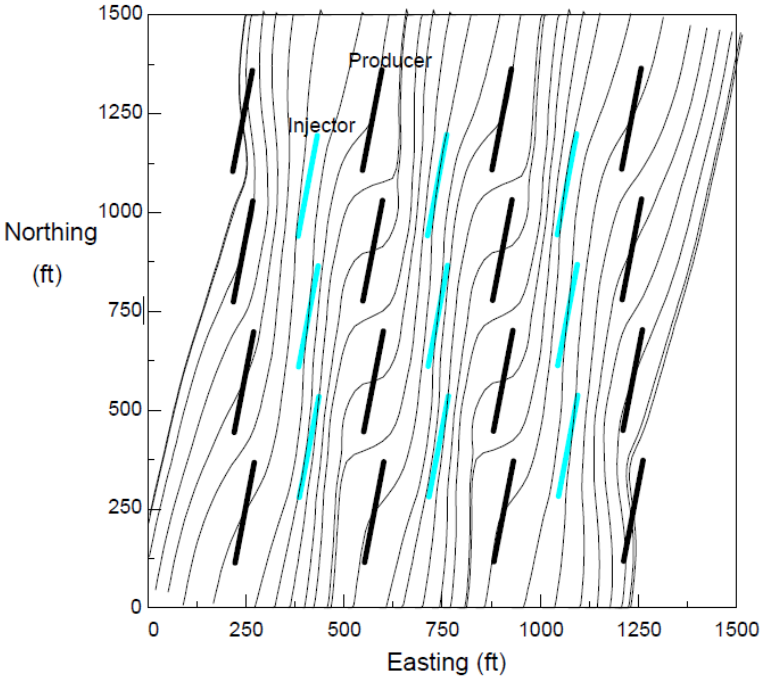

Figure 1.8: Conceptual diagram of the change in maximum horizontal stress direction caused by fluid injection and production. Thick lines indicate fracture directions, and thin lines indicate the maximum horizontal stress directions (from Minner et al., 2002).

References

Abou-Sayed, A., & Zaki, K. 2005. A Mechanistic Model for Formation Damage and Fracture Propagation During Water Injection. Paper SPE 94606 presented at the SPE European Formation Damage Conference, 25-27 May 2005, Sheveningen, The Netherlands. http://dx.doi.org/10.2118/94606-MS

Abou-Sayed, A., Zaki, K., Wang, G., Sarfare, M., et al. 2007. Produced Water Management Strategy and Water Injection Best Practices: Design, Performance, and Monitoring. *SPE Production & Operations*, **22** (1). http://dx.doi.org/10.2118/108238-PA

Ali, S. A. 2013. Water Management. *Journal of Petroleum Technology*, **65** (12): 124–134.

Bachman, R. C., Harding, T. G., Settari, A. T., & Walters, D. A. 2003. Coupled Simulation of Reservoir Flow, Geomechanics, and Formation Plugging With Application to High-Rate Produced Water Reinjection. Paper SPE 79695 presented at the SPE Reservoir Simulation Symposium, 3-5 February, Houston, Texas. http://dx.doi.org/10.2118/79695-MS

Bailey, B., Elphick, J., Kuchuk, F., Romano, C., et al. 2000. Water Control. *Oilfield Review*, **12** (1): 30–51.

Barkman, J. H., & Davidson, D. H. 1972. Measuring Water Quality and Predicting Well Impairment. *Journal of Petroleum Technology*, **24** (7): 865–873. http://dx.doi.org/10.2118/3543-PA

Bedrikovetsky, P., Da Silva, M. J., Rocha Fonseca, D., Da Silva, M. F., et al. 2005. Well-History-Based Prediction of Injectivity Decline during Seawater Flooding. Paper SPE 93886 presented at the SPE European Formation Damage Conference, 25-27 May, Sheveningen, The Netherlands. http://dx.doi.org/10.2118/93886-MS

Bedrikovetsky, P., Tran, T. K., Van den Broek, W. M. G. T., Marchesin, D., et al. 2003. Damage Characterization of Deep Bed Filtration From Pressure Measurements. *SPE Production & Facilities*, **18** (2): 119–128. http://dx.doi.org/10.2118/83673-PA

Bentley, W. E., Kent, R. T., & Myers, G. R. 1986. Site availability for waste injection, Vickery, OH pp. 330–354. Presented at the International Symposium on the Subsurface Injection of Liquid Wastes, New Orleans.

BP. 2014. *BP Statistical Review of World Energy*. BP. Retrieved from http://www.bp.com/statisticalreview

Chang, C. K. 1985. Water Quality Considerations in Malaysia's First Waterflood. *Journal of Petroleum Technology*, **37** (09): 1689–1698. http://dx.doi.org/10.2118/12387-PA

Clark, C. E., & Veil, J. A. 2009. *Produced Water Volumes and Management Practices in the United States* (No. ANL/EVS/R-09/1). Argonne National Laboratory. Retrieved from http://www.netl.doe.gov/File%20Library/Research/Coal/ewr/water/anl-produced-water-volumes-sep09.pdf

De Souza, A. L. S., Fernandes, P. D., Mendes, R., Rosa, A. J., et al. 2005. The Impact of Fracture Propagation on Sweep Efficiency During a Waterflooding Process. Paper SPE 94704 presented at the SPE Latin American and Caribbean Petroleum Engineering Conference, 20-23 June, Rio de Janeiro, Brazil. http://dx.doi.org/10.2118/94704-MS

Detienne, J. L., Creusot, M., Kessler, N., Sahuquet, B., et al. 1998. Thermally Induced Fractures: A Field-Proven Analytical Model. *SPE Reservoir Evaluation & Engineering*, **1** (01): 30–35. http://dx.doi.org/10.2118/30777-PA

Detienne, J. L., Ochi, J., & Rivet, P. 2005. A Simulator For Produced Water Re-injection in Thermally Fractured Wells. Paper SPE 95021 presented at the SPE European Formation Damage Conference, 25-27 May, Sheveningen, The Netherlands. http://dx.doi.org/10.2118/95021-MS

Eylander, J. G. R. 1988. Suspended Solids Specifications for Water Injection From Coreflood Tests. *SPE Reservoir Engineering*, **3** (4): 1287–1294. http://dx.doi.org/10.2118/16256-PA

Fletcher, A. J. P., Lamb, S. P., & Clifford, P. J. 1992. Formation Damage From Polymer Solutions: Factors Governing Injectivity. *SPE Reservoir Engineering*, **7** (02): 237–246. http://dx.doi.org/10.2118/20243-PA

Gadiyar, B., Meese, C., Stimatz, G., Morales, H., et al. 2004. Optimizing Frac Packs. *Oilfield Review*, **16** (3): 18–29.

Goodman, H. E. 2008. Wellbore Integrity, Sand Management, and Frac Pack. *Journal of Petroleum Technology*, **60** (9): 100–114.

Hagoort, J., Weatherill, B. D., & Settari, A. 1980. Modeling the Propagation of Waterflood-Induced Hydraulic Fractures. *Society of Petroleum Engineers Journal*, **20** (04): 293–303. http://dx.doi.org/10.2118/7412-PA

Hussain, A., Minier-Matar, J., Gharfeh, S., Janson, A., et al. 2014. Advanced Technologies for Produced Water Treatment. *OTC-24749-MS*. Paper OTC 24749 OTC presented at the Offshore Technology Conference-Asia, 25-28 March, Kuala Lumpur, Malaysia. http://dx.doi.org/10.2118/24749-MS

Khatib, Z., & Verbeek, P. 2002. Water to Value - Produced Water Management for Sustainable Field Development of Mature and Green Fields. Paper SPE 73853 presented at the SPE International Conference on Health, Safety and Environment in Oil and Gas Exploration and Production, 20-22 March, Kuala Lumpur, Malaysia. http://dx.doi.org/10.2118/73853-MS

Mantell, M. E. 2011. *Produced Water Reuse and Recycling Challenges and Opportunities Across Major Shale Plays*. presented at the EPA Hydraulic Fracturing Study Technical Workshop #4. Retrieved from http://www2.epa.gov/sites/production /files/documents/09_Mantell_-_Reuse_508.pdf

Martins, J. P., Murray, L. R., Clifford, P. J., McLelland, W. G., et al. 1995. Produced-Water Reinjection and Fracturing in Prudhoe Bay. *SPE Reservoir Engineering*, **10** (03): 176–182. http://dx.doi.org/10.2118/28936-PA

Minner, W. A., Wright, C. A., Stanley, G. R., Pater, C. J., et al. 2002. Waterflood and Production-Induced Stress Changes Dramatically Affect Hydraulic Fracture Behavior in Lost Hills Infill Wells. Paper SPE 77536 presented at the SPE Annual Technical Conference and Exhibition, 29 September-2 October 2002, San Antonio, Texas. http://dx.doi.org/10.2118/77536-MS

Myers, J. E. 2014. Chevron San Ardo Facility Unit (SAFU) Beneficial Produced Water Reuse for Irrigation. Paper SPE 168401 presented at the SPE International Conference on Health, Safety, and Environment, 17-19 March, Long Beach, California, USA. http://dx.doi.org/10.2118/168401-MS

Ochi, J., Dexheimer, D., & Corpel, V. 2013. Produced Water Re-Injection Design and Uncertainties Assessment. Paper SPE 165138 presented at the SPE European Formation Damage Conference & Exhibition, 5-7 June, Noordwijk, The Netherlands. http://dx.doi.org/10.2118/165138-MS

Paige, R. W., Murray, L. R., Martins, J. P., & Marsh, S. M. 1995. Optimising Water Injection Performance. Paper SPE 29774 presented at the Middle East Oil Show, 11-14 March, Bahrain. http://dx.doi.org/10.2118/29774-MS

Pang, S., & Sharma, M. M. 1995. Evaluating the Performance of Open-Hole, Perforated and Fractured Water Injection Wells. Paper SPE 30127 presented at the SPE European Formation Damage Conference, 15-16 May, The Hague, Netherlands. http://dx.doi.org/10.2118/30127-MS

Pang, S., & Sharma, M. M. 1997. A Model for Predicting Injectivity Decline in Water-Injection Wells. *SPE Formation Evaluation*, **12** (3): 194–201. http://dx.doi.org /10.2118/28489-PA

Perkins, T. K., & Gonzalez, J. A. 1985. The Effect of Thermoelastic Stresses on Injection Well Fracturing. *Society of Petroleum Engineers Journal*, **25** (1): 78–88. http://dx.doi.org/10.2118/11332-PA

Saripalli, K. ., Sharma, M. ., & Bryant, S. . 2000. Modeling Injection Well Performance During Deep-Well Injection of Liquid Wastes. *Journal of Hydrology*, **227** (1–4): 41–55. http://dx.doi.org/10.1016/S0022-1694(99)00164-X

Seright, R. S., Seheult, J. M., & Talashek, T. 2009. Injectivity Characteristics of EOR Polymers. *SPE Reservoir Evaluation & Engineering*, **12** (05): 783–792. http://dx.doi.org/10.2118/115142-PA

Sharma, M. M., Pang, S., Wennberg, K. E., & Morgenthaler, L. N. 2000. Injectivity Decline in Water-Injection Wells: An Offshore Gulf of Mexico Case Study. *SPE Production & Facilities*, **15** (1): 6–13. http://dx.doi.org/10.2118/60901-PA

Sharma, M. M., & Yortsos, Y. C. 1987. Transport of Particulate Suspensions in Porous Media: Model Formulation. *AIChE Journal*, **33** (10): 1636–1643. http://dx.doi.org /10.1002/aic.690331007

SPE. 2011. *Challenges in Reusing Produced Water*. Society of Petroleum Engineers. Retrieved from http://www.spe.org/tech/2011/10/challenges-in-reusing-produced-water/

Suarez-Rivera, R., Stenebråten, J., Gadde, P., & Sharma, M. 2002. An Experimental Investigation of Fracture Propagation During Water Injection. Paper SPE 73740 presented at the International Symposium and Exhibition on Formation Damage

Control, 20-21 February 2002, Lafayette, Louisiana. http://dx.doi.org/10.2118/73740-MS

Suri, A., & Sharma, M. 2009. Fracture Growth in Horizontal Injectors. Paper SPE 119379 presented at the SPE Hydraulic Fracturing Technology Conference, 19-21 January 2009, The Woodlands, Texas. http://dx.doi.org/10.2118/119379-MS

Suri, A., & Sharma, M. 2010. A Model for Water Injection Into Frac-Packed Wells. *SPE Reservoir Evaluation & Engineering*, **13** (3): 449–464. http://dx.doi.org /10.2118/110084-PA

Suri, A., Sharma, M., & Moreno, J. M. M. 2010. Injectivity of Frac-Packed Wells: A Case Study of the Guando Field. Paper SPE 125897 presented at the SPE International Symposium and Exhibiton on Formation Damage Control, 10-12 February 2010, Lafayette, Louisiana, USA. http://dx.doi.org/10.2118/125897-MS

Suri, A., Sharma, M., & Peters, E. 2011. Estimates of Fracture Lengths in an Injection Well by History Matching Bottomhole Pressures and Injection Profile. *SPE Reservoir Evaluation & Engineering*, **14** (4): 385–397. http://dx.doi.org/10.2118/132524-PA

Tenizbaeva, B. M., Macary, S. M., Seitim, M., & Yessaliyeva, A. 2012. Waste Water Disposal Has Become Critical Strategic Focus Area. Paper SPE 160769 presented at the SPE Russian Oil and Gas Exploration and Production Technical Conference and Exhibition, 16-18 October, Moscow, Russia. http://dx.doi.org /10.2118/160769-MS

Thomas, M. 2013. Enhanced Production. *BP Magazine*, (4): 31–35.

Tibbetts, P. J. C., Buchanan, I. T., Gawel, L. J., & Large, R. 1992. A Comprehensive Determination of Produced Water Composition. In J. P. Ray & F. R. Engelhardt (Eds.), *Produced Water*, Environmental Science Research (pp. 97–112). Springer US. Retrieved from http://link.springer.com/chapter/10.1007/978-1-4615-2902-6_9

Todd, A. C., Kumar, T., & Mohammadi, S. 1990. The Value and Analysis of Core-Based Water-Quality Experiments as Related to Water Injection Schemes. *SPE Formation Evaluation*, **5** (02): 185–191. http://dx.doi.org/10.2118/17148-PA

Van den Hoek, P. J., Matsuura, T., de Kroon, M., & Gheissary, G. 1996. Simulation of Produced Water Re-Injection Under Fracturing Conditions. Paper SPE 36846

presented at the European Petroleum Conference , 22-24 October 1996, Milan, Italy. http://dx.doi.org/10.2118/36846-MS

Van Oort, E., van Velzen, J. F. G., & Leerlooijer, K. 1993. Impairment by Suspended Solids Invasion: Testing and Prediction. *SPE Production & Facilities*, **8** (3): 178–184. http://dx.doi.org/10.2118/23822-PA

Veil, J. A. 2009. *Produced Water Management Options - One Size Does Not Fit All*. presented at the SPE Distinguished Lecturer Program. Retrieved from https://www.onepetro.org/other/27233

Veil, J. A., Puder, M. G., Elcock, D., & Redweik, R. 2004. *A White Paper Describing Produced Water from Production of Crude Oil, Natural Gas, and Coal Bed Methane* (Submitted to U.S. Department of Energy No. W-31-109-Eng-38). Argonne National Laboratory. Retrieved from http://netl.doe.gov/research/energy-analysis/publications/details?pub=2061f020-2f50-4c65-b464-779f0e23a628

Wennberg, K. E., & Sharma, M. M. 1997. Determination of the Filtration Coefficient and the Transition Time for Water Injection Wells. Paper SPE 38181 presented at the SPE European Formation Damage Conference, 2-3 June 1997, The Hague, Netherlands. http://dx.doi.org/10.2118/38181-MS

Zechner, M., Clemens, T., Suri, A., & Sharma, M. M. 2014. Simulation of Polymer Injection under Fracturing Conditions - A Field Pilot in the Matzen Field, Austria. Paper SPE 169043 presented at the SPE Improved Oil Recovery Symposium, 12-16 April, Tulsa, Oklahoma, USA. http://dx.doi.org/10.2118/169043-MS

Zhang, N. S., Somerville, J. M., & Todd, A. C. 1993. An Experimental Investigation of the Formation Damage Caused by Produced Oily Water Injection. Paper SPE 26702 presented at the Offshore Europe, 7-10 September, Aberdeen, United Kingdom. http://dx.doi.org/10.2118/26702-MS

Chapter 2 : Deep-Bed Filtration of Solid Particles in Frac-Pack

2.1 INTRODUCTION

Filtration of solids in the injection water of a frac-pack is the primary factor that controls the injectivity decline in frac-packed water injection well completions. The injectivity may decline rapidly or much more slowly depending on the degree of frac-pack filtration. The widening and lengthening of frac-packs and the associated loss of sand control are also affected by the frac-pack filtration degree. However, there is no experimental data available for the filtration coefficient at high velocities that is typical in frac-packs. In this research, the filtration coefficients were experimentally measured in high velocity flows encountered in frac-packs. The solid concentrations and pressure drops across proppant pack sections were measured and correlated with earlier filtration theory and permeability decline models. The filtration coefficients were measured at various flow rates and for different proppant sizes. The experiments show that at high fluid velocities, the filtration coefficient is significantly lower than that estimated from prior correlations that were based on low velocity filtration.

Empirical correlations for the filtration coefficient at high-velocity flow in frac-packs were developed in this work. The improved filtration coefficients were used as the primary input into a well injectivity model. The proper estimation of the filtration enabled us to more accurately analyze the impact of injection rates and proppant selection on injector performance, i.e., to predict the long-term injection well behavior. The effect of particle filtration in the frac-pack and its effect on injector performance was captured accurately for the first time. The newly presented empirical correlations coupled with a model for frac-pack growth in the injection well allowed us to accurately estimate fracture

dimensions and the long-term water injectivity of frac-packed injectors. These results can be used for frac-pack design, proppant selection and specification of injection water quality.

2.2 PERFORMANCE OF FRAC-PACKED INJECTORS

2.2.1 Factors Controlling Injector Performance

The change in injectivity over time is the most common measure of injector performance. It is essential to have a comprehensive well injectivity model to describe and predict long-term injector performance. There are various factors that control well injectivity, and their combined effect needs to be accounted for to properly predict injectivity. Some of the critical factors are: (i) plugging by solid particles or oil-in-water emulsions, (ii) *in situ* stress change caused by thermo- and poro-elastic effects, (iii) fracture widening, lengthening and/or height containment along with associated proppant redistribution in the frac-pack, and (iv) well configurations and flow distributions between layers. Within the practical range of injection parameters, one or more of these can be the most influential parameter depending on the condition of the injection well. A comprehensive model for the injection well is very useful to screen out critical factors and to properly predict well performance.

There have been several approaches to investigating these factors. Classic papers include Barkman & Davidson (1972) in which a method of predicting the injectivity impairment from water quality data was presented. Perkins & Gonzalez (1985) focused on thermo-elastic stress changes caused by the injection of cold water and its impact on fracture growth. Suarez-Rivera et al. (2002) experimentally investigated fracture propagation caused by injecting various types of particle suspensions into large blocks of rocks. The concentration, shape, size, and compressibility of particles greatly affect the

fracture growth rate and leak-off behavior in their study. The filtration and particle concentration along the injection induced fractures were visually inspected, and pressure information was used to analyze the impact of filtration and fracture growth on the injectivity. None of these studies investigated injectivity decline in frac-packed wells. Such completions are now quite common in injection wells, and there are some unique issues that arise when injecting into wells that have an existing propped fracture, including the plugging and fracture growth of the original frac-pack.

2.2.2 Frac-Packed Injector Model

Frac-packing has been a common completion strategy for sand control in injection wells. Other options include sand screens or cased-hole gravel packs. The early advantage of frac-packing (high injectivity), however, can be significantly impacted if particles from the injected water are deposited near the fracture entrance instead of traveling through the frac-pack to the tip. It is therefore essential to properly quantify the filtration of these suspended particles in the frac-pack in order to predict the injectivity in the frac-packed injection well.

Suri & Sharma (2010) developed a semi-analytic model for frac-packed injection wells. The model accounts for all the factors described in the previous section for frac-packed injection wells. The bottom-hole pressure and the injectivity for long-term water injection are calculated based on the combined effect of these physical processes. They showed that the filtration of solids in the injection water by the frac-pack is the main factor that controls the injectivity decline of frac-packed injectors. The model describes the filtration in both the frac-pack and in the formation near the fracture in terms of internal and external filtration. Their model calculates fracture widening with continued injection and injectivity. However, due to the fixed volume of proppant in the frac-pack, the lengthening of the frac-pack was estimated approximately. Note their model assumed an

initial width profile with a fixed frac-pack height equal to the sand thickness.

2.2.3 Field Case Examples of Frac-Packed Injectors

Shumbera et al. (2003) reported a prolonged period of good injector performance without any injectivity decline by applying a frac-pack completion in a Gulf of Mexico (GoM) water injection project. In other GoM field cases without frac-packs reported by Sharma et al. (2000), the injectivity declined quickly and was affected by changes in reservoir conditions or water quality. In Suri et al. (2010)'s case study, the injectivity in wells in the same field were different by a factor of 50. This was caused primarily by differences in the *in situ* stresses. The deeper wells had higher *in situ* stresses; hence higher pump pressures were needed to propagate the injection induced fractures. In some cases, the available pump pressures were sufficient to propagate the fractures (sustained high injectivity) while in other cases they were not (declining injectivities that were much lower). The other important parameters that determined injectivity over time was water quality and the initial frac-pack lengths.

2.2.4 Effect of Frac-Pack Filtration on Injectivity

Suspended particles in the injection water can be deposited by various modes of filtration while traveling through the frac-packed completion. Figure 2.1 conceptually shows these different mechanisms along with changes in fracture dimensions during long term water injection. Particles can first deposit within the frac-pack by internal (deep bed) filtration. At the fracture face, particles start to deposit within adjacent zones in the formation. This is described as an internal filtration in the rock matrix. After the deposited particle concentration exceeds a critical value, an external filter cake will build up at the interface. The pressure change in the frac-pack caused by solids deposition results in fracture widening and lengthening. It is difficult to predict how the proppant will

redistribute as the fracture dimensions grow over time. The subsequent filtration in the redistributed proppant pack is even more complicated. However, it is clear that deep bed filtration in the frac-pack is the first phase of filtration, and that this will play the most important role in controlling fracture dimensions and the injectivity decline over time.

Suri & Sharma (2010) showed that the filtration coefficient in the frac-pack is an important factor when predicting the pressure distribution in the frac-pack and the dimensions of the fracture. Once the pressure in the frac-pack exceeds a fracture-widening pressure, the fracture width can increase which will change the subsequent filtration in the frac-pack. The same applies when the frac-pack lengthens to satisfy the fracture propagation criteria at the tip. The subsequent filtration after fracture dimension changes will again impact the pressures and fracture dimensions. The combined effect of filtration and fracture growth will control the long term injectivity response of the well.

Example calculations based on this model show how filtration in the frac-pack can affect the long-term injectivity. In Figure 2.2, two simulation cases, one with a high and one with a low filtration coefficient in the frac-pack, are compared. When the filtration coefficients λ in the frac-pack were high, the injectivity declined very rapidly. When it was low, however, the injectivity decline rate was low and injectivity was maintained over a prolonged duration. From these results, it is evident that the magnitude of the filtration coefficient can change the prediction for the fracture dimensions and injectivity significantly. The filtration coefficient in the frac-pack determined the degree of particle retention, and a proper estimation of λ was necessary to estimate a reliable injectivity. This study aims to provide reliable estimates for λ for high velocity flows that are typical of flow conditions in frac-packs.

2.3 BACKGROUND ON FILTRATION IN FRAC-PACKS

2.3.1 Flow Characteristics in Frac-Packs

One of the main fluid flow characteristics in the frac-pack is the very high flow velocities that happen there. A typical rate of water injection in a well is in the order of 10,000 bbl/day. This large volume of flow goes into the small diameter of the well and the narrow fracture width. The flow leads to a very high linear velocity of fluid in the propped section of the fracture. This hydrodynamic characteristic also affects the particle filtration behavior. It is important to understand the filtration behavior experimentally in this velocity regime. If the injection rate is assumed to be within the range of 10,000 to 30,000 bbl/day, the fracture height to be 50 to 200 ft, and the average fracture width near the wellbore to be 0.5 to 1.5 inch, a simple calculation shows that the Darcy (superficial) linear velocity, u_s ranges from 0.008 to 0.12 m/s in the frac-pack section. This range of linear velocity is much higher than the flow in the far-field region of the reservoir.

It was experimentally verified that the flow in the frac-pack with the above range of linear velocity is in the non-Darcy region. The same experimental setup and materials with filtration experiments as detailed in this research were used for this verification. Pressure drops at a steady state were measured with different linear velocities of water flowing through a proppant pack. The pressure drops and linear velocities were converted to characteristic dimensionless numbers, the modified friction factor and the modified Reynolds number, respectively. These values were compared with Forchheimer's equation. The Forchheimer's equation is equivalently the same as Ergun (1952)'s equation:

$$\frac{-\Delta P}{\Delta x} = \frac{\mu u_s}{k} + \beta_F \rho u_s^2 \qquad (2.1)$$

Where u_s is the superficial velocity and β_F is the Forchheimer inertial flow parameter. The above equation describes the flow rate-pressure drop relationship encompassing Darcy and

non-Darcy flow regimes. The second term on the right hand side of equation describes the additional pressure drop caused by non-Darcy flow. Figure 2.3 shows that the experimental conditions of this study indicating the fluid flow in the actual frac-pack falls under the non-Darcy regime, which is not included in the usual Darcy equation. This is important, because the previous filtration theory has been established based on low fluid velocity (creeping flow) or in Darcy's flow regime. The systematic experimental filtration data for this high velocity flow (order of 1 to 10 cm/s) is not available.

2.3.2 Predictive Models for Filtration Coefficient

The filtration of suspended solid particles through a porous medium has been an important subject applied to multiple disciplines. The filtration process occurs as an internal filtration inside a porous medium and later as an external filtration on the face of the porous medium. In water injection projects, we focused on internal filtration of solid particles or oil-in-water emulsion droplets suspended in sea water or produced water injected into the frac-pack. The average particle diameter suspended in the injection water is in the order of 1 to 30 μm, and the grain size of the porous medium (proppant) is about 10 to 300 times the injected particle size. The solid particles in concentrations varying between about 1 to 50 mg/L are injected into the formation with the injection water.

The rate of particles being captured per unit distance while a particle flows through a filter is represented by a filtration coefficient, λ. Many numerical models are available to predict the initial filtration coefficient, λ_0, for clean filter beds. O'Melia and coworkers developed mechanistic models, as can be found from Yao et al. (1971). Their work explains the particle deposition process as a combined physical process of interception, sedimentation, and Brownian diffusion. The force balance of a particle traveling along a collector cell is solved while considering the above adhesion mechanisms. Fitzpatrick & Spielman (1973) and Rajagopalan & Tien (1976) improved the particle capture mechanism

with combined London, gravity and hydrodynamic forces in addition to some experimental validations. Sharma & Yortsos (1987) developed a general population model to predict λ and then explicitly relate it to macroscopic parameters such as pressure drop and permeability. Cushing & Lawler (1998) extended the capture mechanism in a single collector to that of packed filter grains. Tufenkji & Elimelech (2004) suggested another predictive model for λ_0 with the aid of numerical solutions. Models by these researchers and others have addressed different specific features of the filtration process, and their models can be used to fit different specific experimental conditions better than the others. However, they present the equivalent data within the framework of a numerical model to predict the initial filtration coefficient. In this work, Rajagopalan and Tien's (RT) model was primarily used.

2.3.3 Deep-Bed Filtration in High Velocity Flow

There are a large number of experimental studies that have presented experimental data and models at low fluid flow velocities (u_s<0.01m/s, flow condition in the far-field or near-fracture area); However, these models were not experimentally validated for high velocity ranges (u_s>0.01m/s, flow condition in frac-pack proppants). Only a single experimental data set is available for this relevant fluid velocity range. Maroudas & Eisenklam (1965) conducted experiments at high flow velocities and showed that, above a certain interstitial velocity, there was virtually no particle retention, which indicated very low values of λ. They conducted filtration experiments using dilute suspensions of spherical and angular particles of 20 to 1100 μm diameter. Their results showed cases with both complete blocking leading to filter cake formation and no retention of particles. The latter was observed to occur when the interstitial velocity exceeded a critical value, v_{cr}, above which no particle deposition was observed. This information was interpreted by Suri & Sharma (2010) to suggest a correlation for v_{cr} as a function of d_g/d_p where filtration

coefficient was set to a zero value when flow velocities exceeded v_{cr}. This correlation was established based on a limited number of experiments where some experimental conditions were not comparable with typical water injection conditions. Measurements presented in this work provide a much more detailed set of data that help researchers understand the filtration behavior at these high flow rates typical to frac-packed injection wells.

2.4 EXPERIMENTAL

2.4.1 Materials and Setup

A filtration experiment, shown in Figure 2.4, was designed in which a frac-pack is closely approximated. Proppants were packed in a filtration cell, and water with solid particles were pumped into the cell. The cell has pressure ports to measure pressures at different locations along the length of the cell, and these tabs were sometimes used to collect samples to measure solid concentrations in different parts of the pack. For most experiments, the pressure drop through the cell and the inlet and outlet concentrations were measured over time. The pressure and concentration information together with injection time were used as the primary information for the filtration coefficient calculations.

The proppants used in this experiment were US mesh size 40/60, 20/40 Ottawa sand and 16/30 CarboHSP proppant. Their diameters, $d_{g,50}$ were 336.5, 538.7 and 899.5 μm respectively. For brevity, d_g will be used instead of $d_{g,50}$ hereafter. They were flushed with distilled water at a linear velocity range of 5 to 15 cm/s to remove any debris or particles existing on the surface. The distilled water with a pH of 6.0 and an ionic strength of 0.016 M at 20°C was used as a fluid to carry particles. The solid particles used were 3M Ceramic Microspheres W-610. These are spherical alumino-silicate ceramic particles with a true density of 2.4 g/mL. They have a log-normal size distribution in volume. The 50 percentile diameter in volume distribution is 10.0 μm. However, the 50 percentile diameter, based on

the diameter distribution, is 3.0 μm, and 3.0 μm was used as d_p in this research. Most particles are distributed across this value, and 3.0 μm size particle represents the particle-grain interaction during the filtration process. By using different sizes of proppants, the grain-to-particle size ratio, d_p/d_g was varied in the experiments.

The filtration cell used was in a cylindrical tube that measures 87 cm in length and 0.95 cm in inner diameter. Proppants were vibration-packed to ensure a consistent porosity in the cell. The confining pressure to the cell was not applied. The filtration of solid particles is not significantly dependent on the confining pressure as it is controlled by physical and chemical properties rather than mechanical conditions.

For linear velocity ranging between 0.03 and 0.13 m/s, a Moyno progressive cavity pump A4015 was used. For lower velocities of 0.006 to 0.03 m/s, a DCI VPA syringe pump series 16 was used. Rosemount pressure transducers were used for monitoring differential pressures throughout the filtration cell. The particle concentration and size distributions were measured using a Coulter counter, Multisizer 3 manufactured by Beckman Coulter.

The particle suspension in the tank was continuously stirred to ensure suspension and consistent inlet concentration to the cell. The water with suspended particles was pumped directly through the Moyno pump or indirectly by the syringe pump to the cell. Pump fluid was a mineral oil, and the mineral oil displaced the particle suspension in the accumulator. Both metering pumps maintained the flow rates constantly throughout the experiments. The particle concentration at the inlet of the filtration cell was maintained around 20 ppmv. The pressure drops throughout the cell and the flow rate at the outlet of the cell with time were monitored by a data acquisition system.

2.4.2 Procedures

A series of experiments were conducted by changing d_g/d_p ratio and flow velocities. The d_g/d_p ratio was varied by changing the size of proppant between 0.34 and 0.90 mm.

Fluid superficial (Darcy) velocities were varied between 0.006 and 0.13 m/s. Once the proppant was vibration-packed, clean distilled water was pumped at a high rate to remove any debris or particles initially existing on the surface of the proppants. As the objective of the experiments is to investigate the filtration of the clean bed initially without any plugging, this procedure was repeated for every experimental run. Water with particles was then pumped into the filtration cell, and the initial set of samples from the inlet and outlet were collected. With filtration time (or pumped pore volume), additional sets of inlet and outlet samples were taken. These were analyzed by the Coulter counter to determine the particle size distribution and the concentration in the known volume of the sample. Coulter counter measurements were repeated to obtain a consistent concentration from the sample by measuring a statistically sufficient number of particles. This was achieved by measuring 6,000 μL of each sample.

This procedure for the individual experiment was repeated for all the runs with some modifications. The pressure measurement ports on the cell were also used as sample collection ports to measure the particle concentrations from the middle of the cell. This data were used to examine the concentration as a function of the filter depth (distance of the measurement from the inlet of the cell). The usual injection time was kept between 100 to 1,500 pore volumes (PV) of the proppant pack. There were some longer experiments conducted in which around 10,000 PV of particle solution was pumped to investigate the effect of deposited particles on the filtration coefficient.

2.5 DISCUSSIONS

2.5.1 Initial Filtration Coefficient

The main objective of the experiment was to obtain the initial filtration coefficient, λ_0, at high linear velocities as a function of fluid velocity and the grain-to-particle size ratio.

The filtration coefficient, λ was determined at a certain time by the following equation.

$$\lambda = -\frac{1}{L}\ln\frac{C_{out}}{C_{in}} \tag{2.2}$$

Where L is the filter medium (proppant pack) length, and C_{out} and C_{in} are concentrations of the suspended solids in the injected water at the filter outlet and inlet. It is practically difficult to measure and correlate the outlet concentration of suspended particles at the initial times since both the injection water front is also moving towards the outlet, and at the same time, some deposition is also happening inside the pack. For practical applications, the limiting value of the concentration ratio is used to determine the initial filtration coefficient.

$$\lambda_0 = \lim_{t\to 0}\left(-\frac{1}{L}\ln\frac{C_{out}}{C_{in}}\right) \tag{2.3}$$

The initial filtration coefficient is extrapolated towards $t\rightarrow 0$ from the filtration coefficient values with time as shown in Figure 2.5. The initial data were acquired as early as possible and a larger number of samples (with time) increased the accuracy of the initial filtration coefficient estimation. In Figure 2.6, filtration coefficient as a function of filter depth is also calculated by measuring effluent concentration at various filter depths and also with increasing time. A clear exponential decay with depth is observed, where the exponent is defined as the filtration coefficient at specific times. This is a typical first order filtration rate behavior with respect to the particle concentration. For this specific filtration materials and setup, we observed a decrease in filtration coefficient over time.

The initial filtration coefficients measured at various conditions were compared with the model prediction. Rajagopalan & Tien (1976)'s model was used for this comparison. Figure 2.7 shows the measured values at different superficial fluid velocities, u_s and grain-to-particle size ratio, d_g/d_p. Some experimental measurements from literature

were included here for comparison. Data from Ison (1967), Fitzpatrick & Spielman (1973), Gruesbeck & Collins (1982) and Ives (1962) were used and some of them were taken from Wennberg (1998). The experiments in this chapter were conducted mainly within the range of high fluid velocities encountered in frac-packs. In addition, we extended the range of the experiments down to the lower velocity range to validate the results in a more conventional area of filtration in which extensive data are available. As other filtration conditions, e.g., particle/grain types, fluid viscosity and porosity, were different, a direct comparison between previous work and this work is not possible. However, there is a trend in which the measured and model filtration coefficients were comparable, validating the experimental results with earlier experiments and models.

2.5.2 Effect of Deposition on Filtration Coefficient

The change in the filtration coefficient with injection pore volume shown in Figure 2.5 suggests that the filtration coefficient is strongly dependent on prior particle deposition. The filtration coefficient decreases by ten times for the small proppant. The deposited particles change the degree of the filtration in the proppant pack to be different from that of the clean bed. This effect needs to be represented by a function of the amount of deposition instead of filtration time because the solid concentration in injection water can change with time. Considering the very long time scales for typical water injection projects, the change in filtration coefficient with time can play an important role.

To generalize the trend shown in the experimental data and to expand the range of application of the data set, we propose an empirical correlation applicable to high velocity filtration. To derive this correlation, we start by assuming an exponential decay of the filtration coefficient shown in Figure 2.5 by the following equation.

$$\lambda = \lambda_0 e^{-N \cdot PV} \tag{2.4}$$

Where N is a function of d_p/d_g as defined in Eq. (2.8) and PV is the pore volume injected. Based on this time (or PV)-dependent filtration coefficient, the average specific deposition, σ_{avg}, in the proppant pack can be calculated numerically and they can be fitted to a logistic function in the following form:

$$\sigma_{avg} = -K + \frac{2K}{1+e^{-B \cdot PV}} \tag{2.5}$$

Where K and B are defined as a function of d_g/d_p in Eq. (2.8). This equation can be rearranged to solve for PV as below.

$$PV = \frac{1}{B} \ln \frac{K + \sigma_{avg}}{K - \sigma_{avg}} \tag{2.6}$$

When this equation is put into Eq. (2.4), the following relation for deposition-dependent filtration coefficient can be derived (Appendix C).

$$\lambda = \lambda_0 \left(\frac{K+\sigma}{K-\sigma} \right)^{-\frac{N}{B}} \quad \text{for } 1 < u_s < 10 \text{ cm/s} \tag{2.7}$$

$$\begin{cases} K = -4.672 \times 10^{-6} \left(d_g / d_p \right) + 0.001611 \\ N = 5.168 \times 10^{-6} \left(d_g / d_p \right) + 0.001775 \\ B = 7.765 \times 10^{-6} \left(d_g / d_p \right) + 0.002448 \end{cases} \tag{2.8}$$

Where σ is a specific deposit (volume of deposited particles per unit bulk volume). In summary, this correlation was derived by calculating a relation between the injected pore volume and the simulated σ_{avg} in the proppant pack. By this relation, the filtration coefficient in a function of the pore volume can be converted to a function of specific deposit. The filtration coefficient decreases with an increasing specific deposit in high fluid velocity condition. The exponential decline in filtration coefficient shown in Eq. (2.4) indicates that the filtration coefficient can decrease to a very low value after several

thousand PV of fluid injection into the proppant pack. This effect leads to a very low degree of deposition at a later stage of injection and a finite amount of specific deposit. This phenomena occurred in high fluid velocity and dilute concentrations of solid particles in this experimental condition. However, in low fluid velocity and with higher solid concentrations, specific deposit will continue to increase and external filtration will occur eventually.

This correlation may be also a function of u_s; however, within the high velocity ranges, no noticeable dependency on u_s was found from experimental data. This relation can be applied to injection well models as well as a model simulating filtration in a core. The above equation was tested with core flow tests later in this chapter. It should be noted that this equation needs to be verified when being used for other types of particles and filter media.

2.5.3 Effect of Velocity and Grain-to-Particle Size Ratio

The measured initial filtration coefficients at various flow velocities (both from literature and this work) are compared along with the RT model in Figure 2.7. All indicate decreasing initial filtration coefficient as the fluid velocity is increased. The model-predicted λ_0 was between 0.1 and 10 m^{-1} for u_s ranging from 0.001 to 0.1 m/s with a grain-to-particle size ratio of 100 to 300. λ_0 was found to decrease with increasing u_s and increasing d_g/d_p. This trend is consistent with experimental results as well as the model prediction. Specifically for a d_g/d_p of 180 and 300 when larger proppants in sizes of 16/30 and 20/40 were used, the experimental initial filtration coefficient was in a good agreement with the model predictions even for the high velocity ranges of interest. However, when d_g/d_p is 112 with smaller 40/60 proppant, experimental λ_0 started deviating from model predictions when u_s increased above around 0.004 m/s. This indicates that the RT model would predict a higher initial filtration coefficient for smaller proppants in the frac-packs.

In other words, particle deposition may not be as high as the model's deposition mechanisms predict.

These predictive models, including Rajagopalan and Tien's, explain the adhesion of particles by modeling the trajectory of the particles. They don't take into account the adhesion probability for the particles which were predicted to deposit. The adhesion probability may be smaller for the experimental conditions in this study resulting in deviations from model estimations. However, in-depth investigations for these deviations have not been conducted. This is partly due to the limited data available at these high fluid velocity ranges. It is important that these experiments suggest this deviation can be encountered in high velocity filtration with small d_g/d_p ratio. Data from Ison (1967) and Fitzpatrick & Spielman (1973) in the same figure also suggest deviations from the model when the fluid velocity becomes higher.

2.5.4 Filter Collection Efficiencies in High Velocity Filtration

The filtration coefficient is a lumped parameter which shows the particle retention behavior of the entire filter. It is helpful to use the filtration coefficient when characterizing differences between filters and to develop additional models for flow properties based on filtration. Understanding the filtration coefficient is required to investigate the effect of the deposited particles and the permeability decline, as these can be formulated based on the filtration coefficient. In contrast, the collection efficiency, η can be used to understand the particle retention ability of individual collectors. The collection efficiency, η is defined based on the change in concentrations through either the entire filter or the individual filter element or collector.

$$\eta_{\text{filter}} = 1 - \frac{C_{out}}{C_{in}} = 1 - \prod_{i=1}^{n} \left(1 - \eta_{\text{single},i}\right) \tag{2.9}$$

Where η_{filter} is the collection efficiency of the entire filter, $\eta_{\text{single},i}$ is the individual collector

efficiency of each grain, and n is the number of individual element or collectors which comprise the filter. Most of the predictive models mentioned previously were established based on Happel (1958)'s sphere-in-cell model in which a grain is surrounded by a flowing fluid. The single collector efficiency for Happel's cell can be related to the filtration coefficient by the following equation.

$$\lambda = \frac{3(1-\phi)}{2d_g}\eta_{\text{single},i} \tag{2.10}$$

The filtration coefficient can be converted to the single collection efficiency by Eq. (2.10).

As particle size distributions can be measured by the Coulter counter, we investigated what portion of different particle sizes are deposited through the proppant pack. A typical example of particle size distributions from this experiment is shown in Figure 2.8. Along with the overall filter collection efficiency, the collection efficiency of each particle size bin, $\eta_{\text{filter},\Delta d\text{p}}$ (η_{filter} will be used as notation for brevity) can also be calculated from the inlet and outlet particle size distributions. These results are shown in Figure 2.9. Larger particles are more subject to deposition in every experiment. The noise in data of large d_p/d_g ranges are caused from the small number of large particles in the fluid sample. The small number of particles reduces the statistical accuracy in the removal efficiency calculation. In (c), at very high velocity (u_s=0.131m/s) in the large proppant (16/30 size proppant), small particles ($d_\text{p}/d_\text{g}\simeq$0.002) have not been removed at all for this specific filter length. In (b) and (c), with large size proppants, the removal efficiency clearly decreased with increasing fluid velocity. However, in (a), with a smaller filter medium (40/60 size proppant), the removal efficiency does not decrease when u_s is increased above 0.02 m/s.

When the filter collection efficiency, η_{filter} is plotted for flows in different proppants with the same fluid velocity, the difference in filtration for the small proppant (40/60) is more pronounced. This is shown in Figure 2.10. The η_{filter} lines for proppants with d_g=539

and 900 μm (20/40 and 16/30) are almost the same, and their slopes are very close to each other. This indicates the same deposition mechanisms control filtration in these proppants. The small proppant (40/60) has a different slope from the others, and the dependency on u_s is weaker. This also explains why small proppant (40/60) had a deviation in λ_0 measurements from known model predictions.

2.5.5 Normalized Filtration Analysis 1: Effective Collector Number Ratio

The above information indicates how many particles of different sizes are collected through a certain length of filter. This is specific to the length of the filter used in the experiment, and it should be normalized to explain more generalized filtration behavior based on d_p/d_g and u_s. To accomplish this, our first approach was to calculate what portion of grains in the filter cell are effectively acting as collectors. It was assumed that the collector efficiency for each collector *i* is the same to get the effective number of collectors from Eq. (2.9). If $\eta_{single,i}$ for all collectors are the same, *n* in the Eq. (2.9) can be solved to give:

$$n_{eff} = \frac{\ln\left(1-\eta_{filter}\right)}{\ln\left(1-\eta_{single}\right)} \tag{2.11}$$

Where n_{eff} is the effective collector number. If it is assumed that collectors are lined up along the fluid path in the length, *L*, of the filter, n_{eff} can be normalized to give the effective collector number ratio, Λ:

$$\Lambda = \frac{n_{eff}}{L/d_g} \tag{2.12}$$

This effective collector number ratio shows what fraction of collectors in the filter are effectively functioning as collectors. This ratio is plotted in Figure 2.11 for different proppant sizes. In general, Λ decreases with increasing d_p/d_g suggesting two phenomena

during the filtration process. One is that the large size particles experience less collectors due to their limited number. The other is that, when the smaller size particles (existing in statistically sufficient numbers) flow through the series of collectors, particles have a better chance of being deposited by mechanisms described in the predictive models using Happel's cell. In other words, the large particles are likely to be captured near the entrance of the filter, and the small particles can travel further and be more evenly captured through the filter (Figure 2.12). In large proppant size experiments (16/30 proppant), Λ becomes close to unity, indicating that almost all the grains are acting as effective collectors when small particles flow through a series of collectors. This is mainly a function of d_p/d_g, and it is less dependent on fluid velocity, as shown in Figure 2.13. The data in the three plots in this figure can be superposed to give the same trend with a unique dependence of Λ on d_p/d_g which is independent of u_s in high velocity flows.

The only exception here is that, for small proppant sizes, Λ does not increase with decreasing particle size, but decreases. This is shown for filtration in proppant with d_g=337μm in Figure 2.13. This indicates that in particular cases when the proppant size is small, there is an additional filtration mechanism that starts to take effect which has not been accounted for in the predictive model for λ_0. The smaller the particle is, the less effective collectors are in capturing the particle. This is observed for all cases in experiments with small proppant size. This deviation is directly related to the deviation shown for small proppants in Figure 2.7.

2.5.6 Normalized Filtration Analysis 2: Single Collector Efficiency

Along with the analysis in the previous section, the second approach to investigate the normalized filtration behavior is introduced here. In this approach, we calculate the individual collector's efficiency from experimental data and compare it with a model prediction. The individual collector's collection efficiency can be estimated by assuming

that the collectors are lined up along the flow path in the filter, and all the grains are acting as effective collectors. If the collectors are identical and the number of the hypothetical series of collectors is assumed to be L/d_g, by rearranging Eq. (2.9) for $\eta_{\text{single},i}$, the single-collector efficiency in this system can be derived:

$$\eta_{\text{single,Exp}} = 1 - \left(1 - \eta_{\text{filter,Exp}}\right)^{\frac{d_g}{L}} \tag{2.13}$$

Where $\eta_{\text{filter,Exp}}$ is the experimental collection efficiency of the entire filter of length L, and $\eta_{\text{single,Exp}}$ is the estimated individual collector efficiency from experimental data. This $\eta_{\text{single,Exp}}$ is shown for different conditions in Figure 2.14 and compared with $\eta_{\text{single,RT}}$ which is calculated from Rajagopalan & Tien's model. For a certain u_s and d_p/d_g, the collection efficiency from the model is a single value independent of d_g. However, experimental values show a dependency on d_g, which suggests different deposition mechanisms related to the collector size. The asymptotic approaches at small d_p/d_g can be shown for large proppants (d_g=337 and 539 μm), but small proppant (d_g=337μm) does not show this trend suggesting more deviation from the model.

As the experimental single collector efficiency approaches the RT model prediction value in cases with d_g=900μm and small d_p/d_g ranges in Figure 2.14, the effective collector number ratio, Λ explained in the previous section approaches unity. With increasing d_p/d_g or particle size, the discrepancy between the model and the experimental value increases. This indicates that Λ decreases to zero, and these larger particles plug the entrance of the proppant pack quickly. For all the different fluid velocities in the figure, the particles with d_p/d_g larger than 0.02 lead to a rapid plugging at the proppant entrance. This information shows which size range of large particles needs to be avoided. Operators can conduct this analysis with specific proppants and particles to establish the operational guideline for injection water quality.

2.6 APPLICATIONS TO A FRAC-PACKED INJECTOR MODEL

2.6.1 Velocity Correction Method for High Velocity Filtration Coefficient

Based on the measurements shown in previous sections, an empirical modification method is suggested to predict the initial filtration coefficient at a high fluid velocity. The initial filtration coefficient predicted from Rajagopalan & Tien's model can be modified by introducing a correction factor for certain filtration conditions as below:

$$\text{If } \frac{d_g}{d_p} \le 150, \quad u_{s,cr}\left[\text{m/s}\right] = 10^{0.0368\frac{d_g}{d_p}-6.518} \tag{2.14}$$

$$\begin{cases} \lambda_0 = \lambda_{0,RT}\left[1-0.6416\left(1-\dfrac{u_{s,cr}}{u_s}\right)^{2.2375}\right] & \text{for } u_s \ge u_{s,cr} \\ \lambda_0 = \lambda_{0,RT} & \text{for } u_s < u_{s,cr} \end{cases} \tag{2.15}$$

$$\text{If } \frac{d_g}{d_p} > 150, \quad \lambda_0 = \lambda_{0,RT} \tag{2.16}$$

Where $u_{s,cr}$ is the critical superficial velocity above which the correction is required, and $\lambda_{0,RT}$ is the initial filtration coefficient predicted by Rajagopalan & Tien's model. The correction is conditionally applied when the proppant particles are small and the fluid velocity is over its critical value. A comparison of the predicted filtration coefficients with the experimental data is shown in Figure 2.15.

Compared to the correction method suggested by Suri & Sharma (2010) based on Maroudas & Eisenklam (1965)'s experimental data, the above method predicts reduced filtration coefficient values for certain filtration conditions, but the values are not zero. This indicates that the frac-pack filtration may be reduced under certain conditions, but a limiting condition of no particle retention or plugging in frac-pack is not realistic. However, particle filtration at a high fluid velocity in a frac-pack is generally reduced by the

correction factor, and low values of filtration coefficient are expected in frac-packs based on these experiments. The application of a time dependent λ suggested in Eq. (2.7) along with this method will further reduce the filtration coefficient at later stages of injection. This suggests that early plugging of the frac-pack is generally very unlikely. The plugging of particles will continuously occur even in the frac-pack region, however, and the injectivity will gradually decrease because of the effect of frac-pack plugging. The rate of injectivity decline in frac-packed wells is only predictable from the comprehensive injection well model in conjunction with the filtration correlation presented in this research.

2.6.2 Permeability Reduction Model in High Velocity Flow

Sharma et al. (2000) suggested a permeability reduction model to describe the permeability change caused by particle filtration in a porous medium. They explained the permeability reduction as a combination of reduced porosity, increased specific surface area and increased tortuosity from particle deposition. The permeability reduction model starts from the Carman-Kozeny equation and accounts for changes in the factors noted above. In this research, we apply a similar approach to the non-Darcy equation to predict the pressure change caused by particle deposition. This was referred to be a permeability reduction model for convenience, but it uses the same permeability reduction factors as Sharma et al. (2000) and predicts the change in Forchheimer's beta factor, β_F to eventually calculate the pressure drop in Eq. (1). β_F can be written as:

$$\beta_F = 1.75\frac{1-\phi}{\phi^3}A_s \tag{2.17}$$

Where A_s is the specific surface area per unit solid volume. Applying the change to porosity and specific surface area caused by particle trapping to the above equation leads to the following equation:

$$\frac{\beta_F}{\beta_{F_0}} = \frac{\phi_0^{\,3}(1-\phi)}{\phi^3(1-\phi_0)} \frac{1+\dfrac{d_g}{d_p}\dfrac{\sigma}{1-\phi_0}}{1+\dfrac{\sigma}{1-\phi_0}} \tag{2.18}$$

Where subscript 0 denotes the initial condition. This equation can be used to calculate the pressure drop or flow resistance in the frac-pack under high Reynolds number flow conditions. The following equation shows a pressure drop and flow resistance calculation example for the frac-pack or filter segment *i*:

$$R_{fp}\Big|_i = \frac{-\Delta P_{fp}\Big|_i}{q_{fp}\Big|_i} = \frac{\Delta x}{q_{fp}\Big|_i}\left(\frac{\mu u_s}{k} + \beta_F \rho u_s^2\right) \tag{2.19}$$

Where $R_{fp}|_i$ is the flow resistance in frac-pack or filter segment *i*, and *k* is the permeability calculated by the permeability decline model in Sharma et al. (2000).

In Figure 2.16, the above results are applied to a numerical model of filtration in a core and compared with experimental data. The experiments were conducted with 40/60 proppant and u_s=0.06m/s. First, a model with a correction to λ_0, Eq. (2.14) and deposition-dependent filtration coefficient model, Eq. (2.7) was used without considering the non-Darcy effect on filtration. This is shown as a dashed line in the figure. In addition, the model also applying the non-Darcy effect is shown as a solid line. Due to the initial high filtration coefficient, the initial pressure increase is high. But with declining filtration coefficient at later times, the pressure drop across the filter was stabilized. The model with the non-Darcy effect resulted in a better match with experimental data. It indicates that the pressure drop by the non-Darcy effect and its contribution in filtration are not negligible.

2.6.3 Effect of Experimental Models on Injection Simulation

By applying the results in this work to Suri & Sharma (2010)'s frac-packed well model, we investigated how the filtration in the frac-pack changes the well performance

and fracture dimensions. In Figure 2.17, we compared simulation results using filtration coefficients from this work, from Rajagopalan & Tien (1976)'s model without corrections, and from Suri & Sharma's model. When filtration in the frac-pack is accounted for, the pressure change and the injectivity were controlled strongly by the degree of filtration in the frac-pack. The injectivity declined at a slower rate when the filtration coefficient was calculated with the correlation suggested in this work. The effect of high fluid velocity in the frac-pack was a major factor impacting the simulation results. The extent of filtration in the frac-pack changes the dimensions of the fracture as well. In a high filtration environment, particle plugging in the frac-pack can widen the existing frac-pack and cause a redistribution of the proppant. The pressure distribution shows the effect of the channel created by filtration. Depending on the degree of filtration in the frac-pack, the width and the channel length can change significantly as shown here. The change in the pressure and fracture dimensions are both strongly dependent on the filtration parameters chosen for the frac-pack.

Experimental observations and models proposed in this work will also be applicable to proppants in frac-packs in producing wells. The solid particles depositing in producing well frac-packs would be solid particles containing fines produced from the near-well formations instead of the suspended particles in injection water. The productivity decline caused by the filtration can be predicted, as in the case of injectivity, if operators analyze the produced fines.

2.7 CONCLUSION

The degree of particle plugging in frac-packs has a strong influence on the performance of frac-packed injectors. The selection of proppant sizes and water quality specifications are very important design parameters affecting injectivity decline. To reliably predict the injectivity of a frac-packed well, we measured the particle filtration

behavior over a range of fluid velocities for proppant packs. Improved empirical models are proposed to better estimate the filtration coefficient. Some of main findings in this work are summarized below:

- Initial filtration coefficients for large proppants were experimentally found to be similar to the predictions from an existing model, but measurements for small size proppants were smaller than model predictions. An empirical correction was developed to properly predict the filtration coefficient for high velocity flow in frac-packs based on our experimental results.
- The filtration coefficient at high fluid velocities is found to be mainly a function of fluid velocity and particle-to-grain (suspended solid particles-to-proppant) size ratio. The observed deviation from the model was also a function of the same parameters.
- The filtration coefficient decreases with time (or with increasing amount of deposited particles). A model for this time dependence is also presented based on the experimental data.
- A model is presented to account for the effect of deposited particles on non-Darcy flow in the frac-pack.
- The impact of changes in the filtration coefficient on the injectivity and fracture dimensions were shown by applying these findings to a comprehensive injector model.

Based on the results presented in this chapter, operators can better specify injection water quality, design injection facilities and frac-pack completions that will allow stable injectivities in long-term water injection projects.

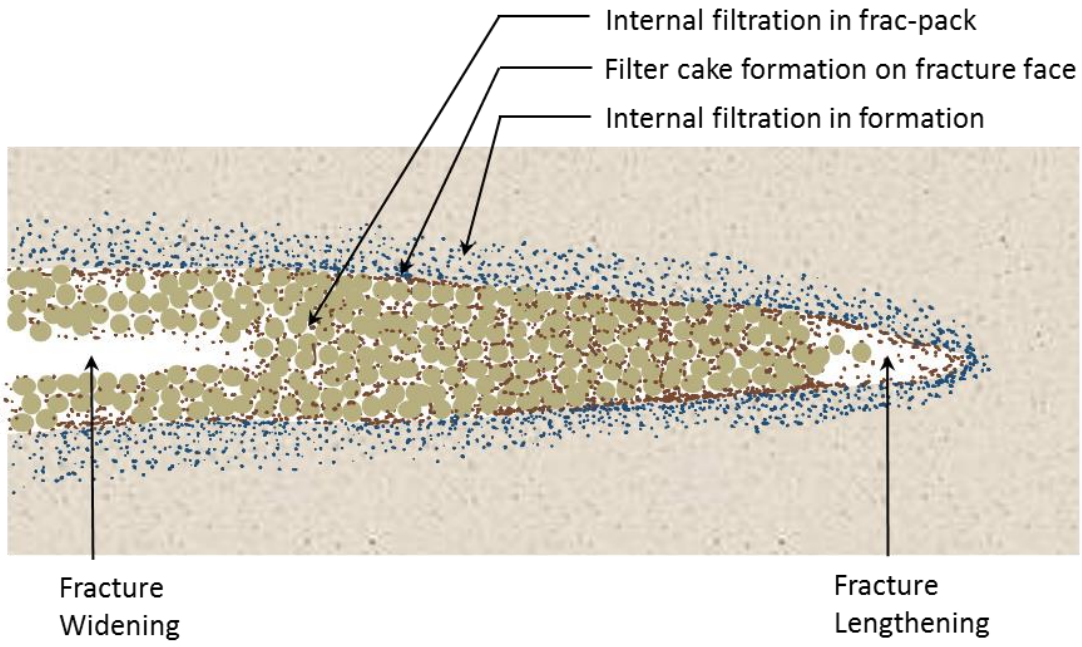

Figure 2.1: Various modes of filtration in frac-packs and adjacent formation. Frac-pack can widen and lengthen in time to affect the filtration.

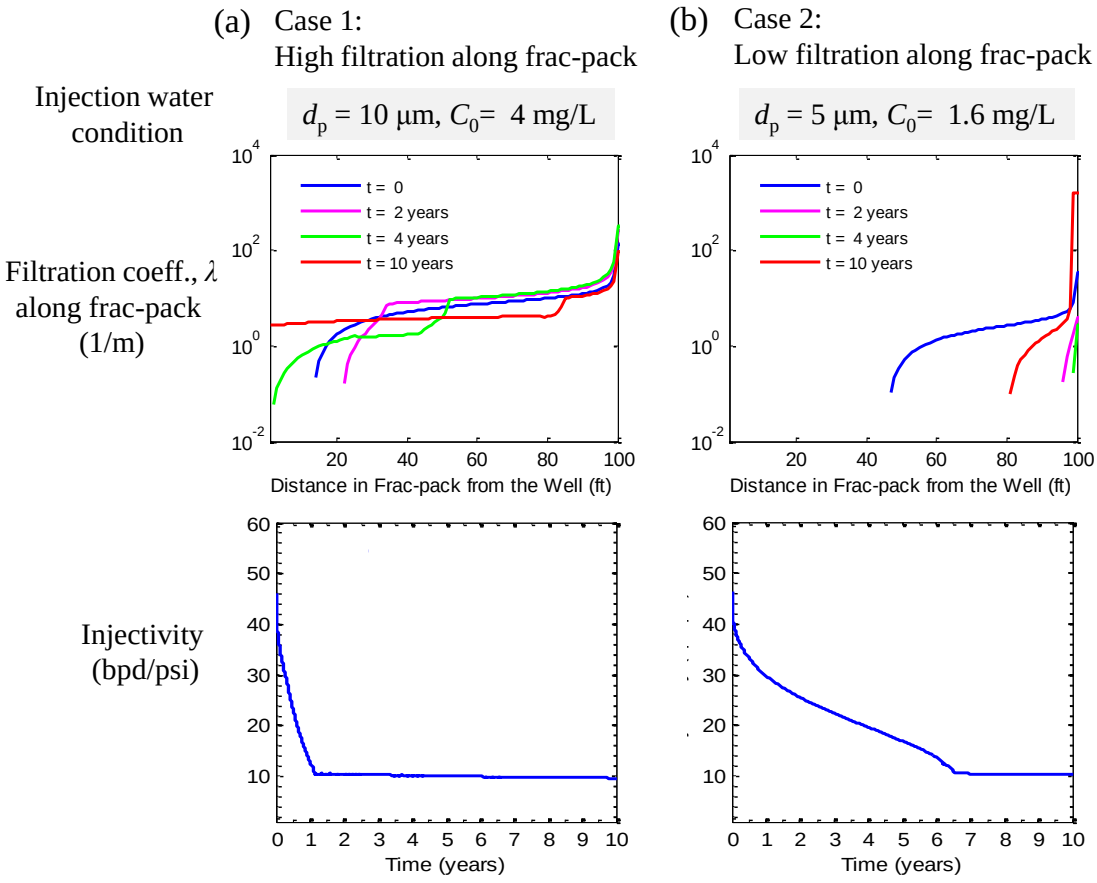

Figure 2.2: Comparison of injectivities in simulations with high and low degree of filtration in frac-pack. Filtration was controlled by injection water qualities, and filtration coefficients were predicted by Rajagopalan & Tien's model.

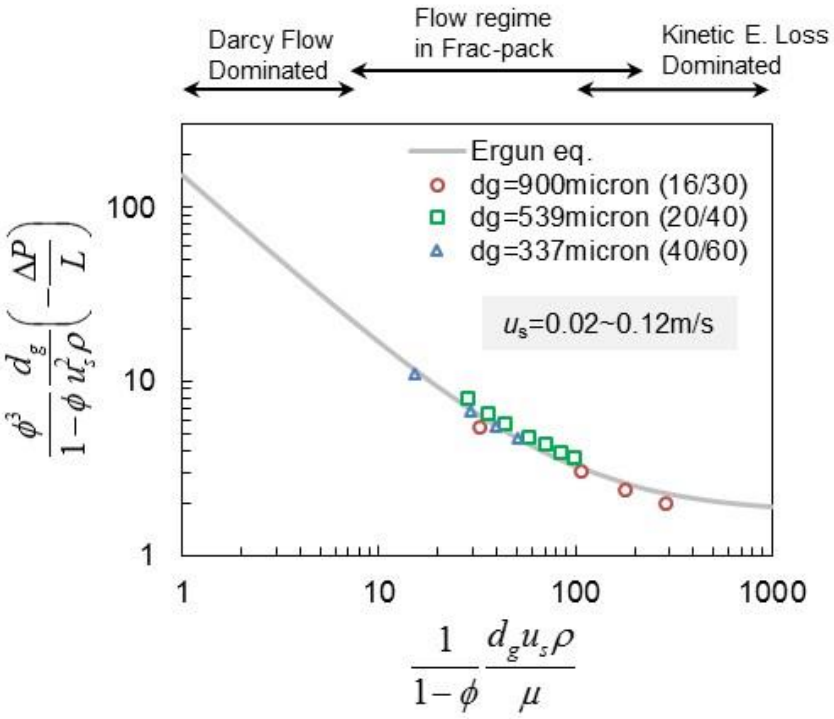

Figure 2.3: Non-Darcy behavior of steady-state pressure drops across proppant pack. The *x*-axis indicates modified Reynolds number, and the *y*-axis indicates modified friction factor.

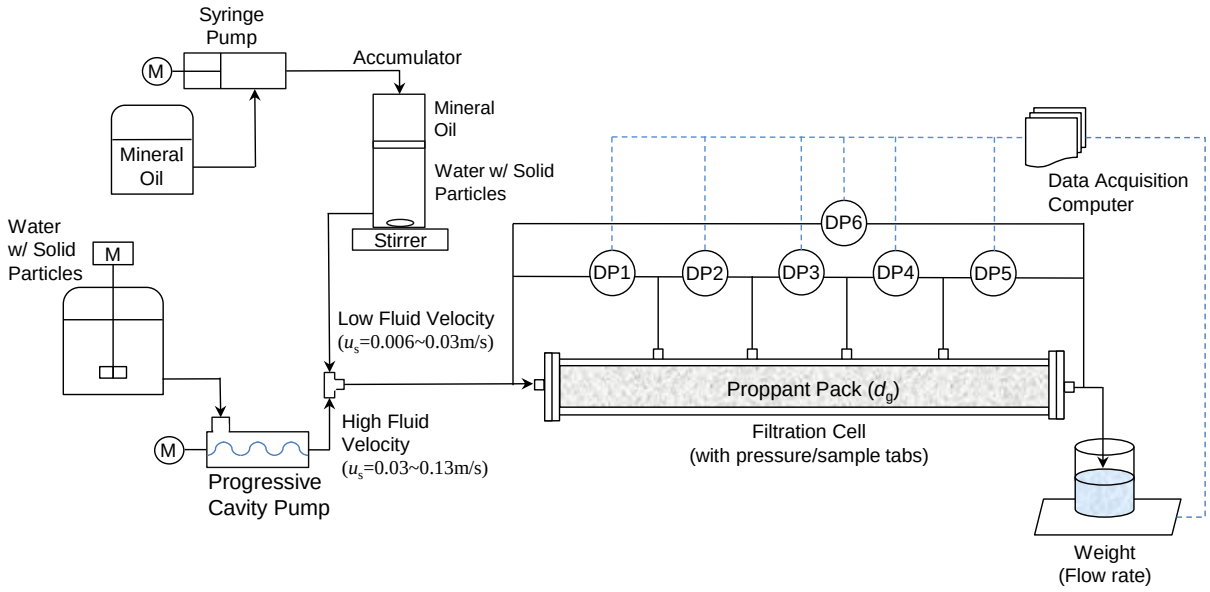

Figure 2.4: Experimental setup. For a low fluid velocity, a syringe pump was used to displace water with particles. A progressive cavity pump was used for direct injection of water with particles into the filtration cell for high fluid velocity.

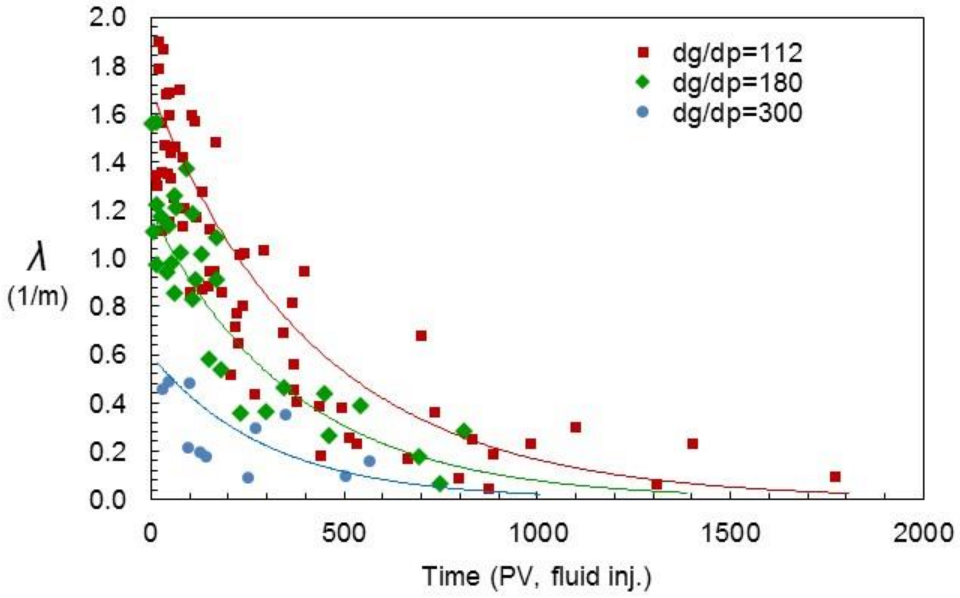

Figure 2.5: Filtration coefficient changing with time for different proppant sizes. Note that there are multiple data sets of experiments for different fluid velocities in each group. This figure shows the method of estimation for the initial filtration coefficient. Higher filtration coefficients were measured for the smaller diameter proppant.

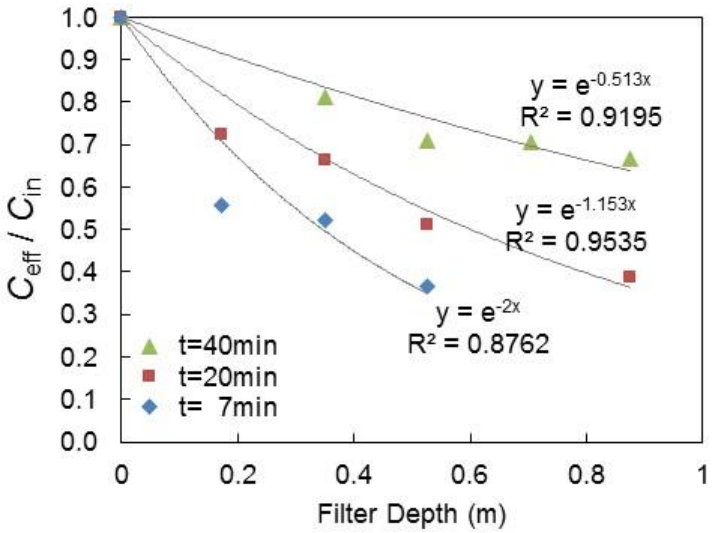

Figure 2.6: Effluent concentration ratio to inlet for different filter depth with time. The exponents of trend lines indicate filtration coefficients at specific time. Data are measured at u_s=4.5 cm/s with the grain size of d_g=0.539mm.

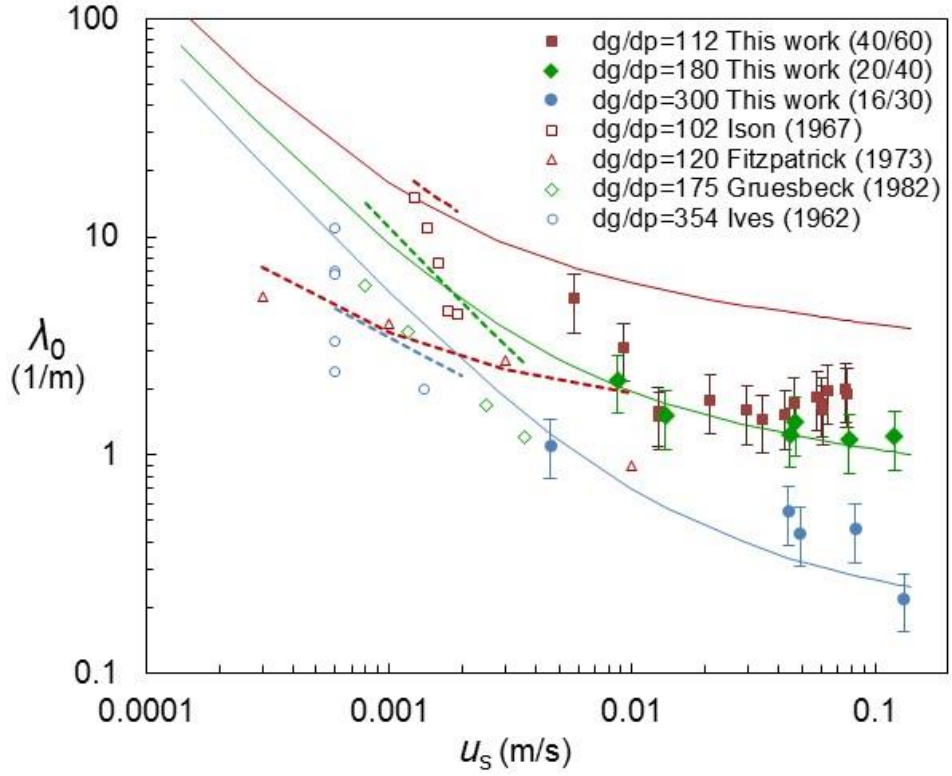

Figure 2.7: Initial filtration coefficient measurements compared with the model prediction values. Solid dots are measured values in this work, and the hollow dots are measurements from previous work. They are compared with Rajagopalan and Tien's model predictions, which are represented as lines. The same color lines and dots are to be compared. The model predictions for previous work were also shown as dotted lines. Each color represents a similar particle to grain size ratio.

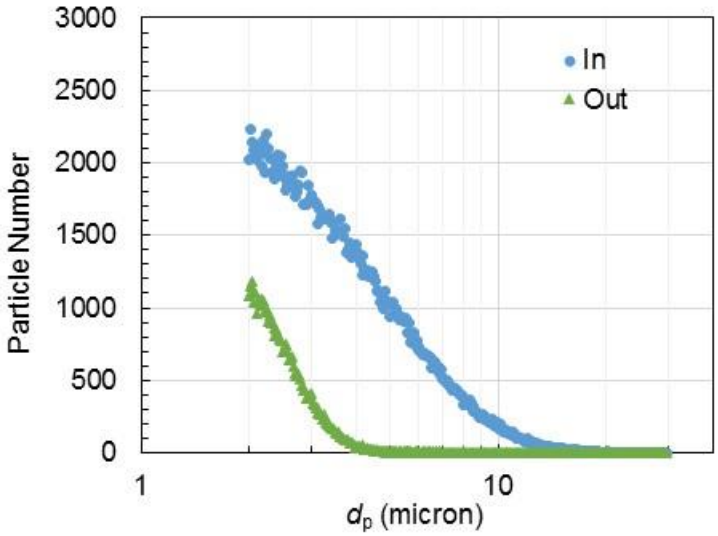

Figure 2.8: Typical particle size distribution of filter inlet and outlet samples. Each measured volume was 2000μL. Note that there are 300 bins between 2 and 30 microns, and logarithms of particle size bins are equally spaced.

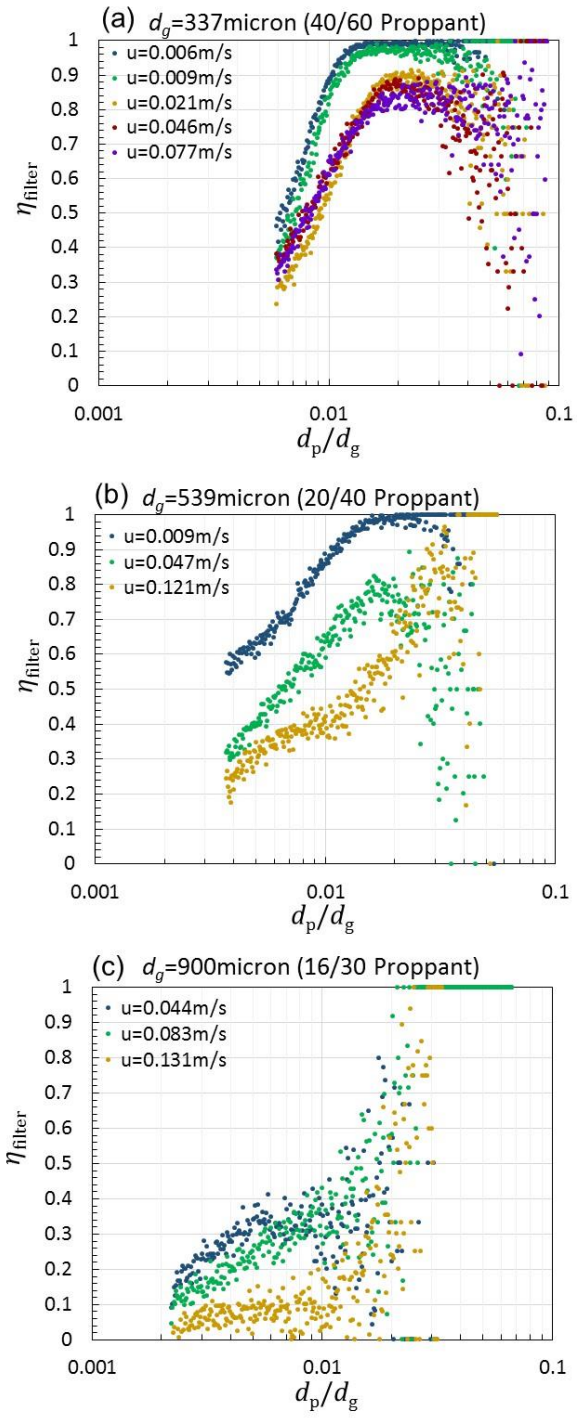

Figure 2.9: Distribution of filter collection efficiency versus particle-to-grain size ratio plotted for different fluid velocities in various proppants used as grains. (a) 40/60, (b) 20/40, and (c) 16/30 proppant were used as filter medium. Filter collection efficiency does not decrease with increasing fluid velocity above 0.021m/s in (a).

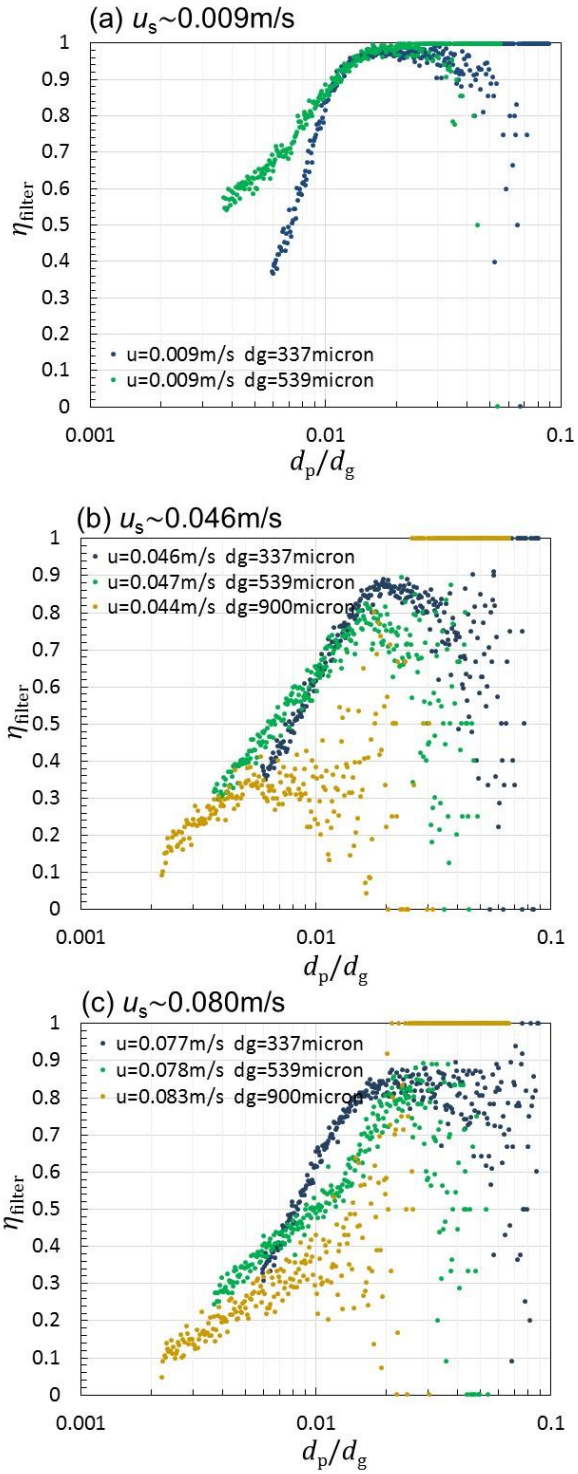

Figure 2.10: Filter collection efficiency versus particle-to-grain size ratio. Each figure shows groups for different fluid velocities: (a) 0.009m/s, (b) 0.046m/s and (c) 0.080m/s.

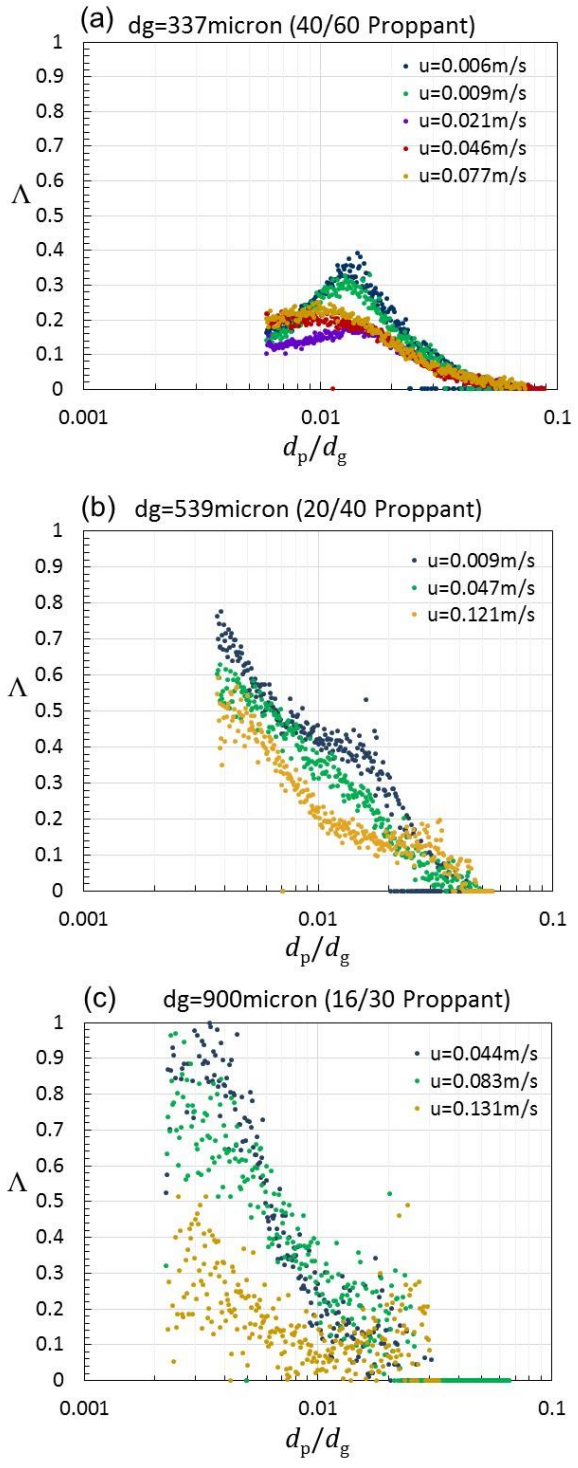

Figure 2.11: Effective collector number ratio versus particle-to-grain size ratio shown for different filter (proppant) size. Proppant sizes of (a) 40/60, (b) 20/40, and (c) 16/30 were used for various fluid velocities.

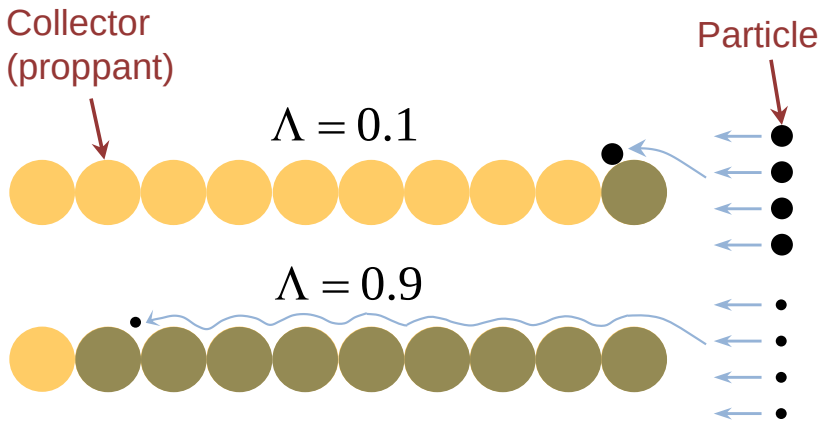

Figure 2.12: Conceptual explanation on the effective collector number ratio. Large particles are captured at the entrance of the filter leading to small Λ. Small particles are more evenly captured throughout the filter resulting in large Λ.

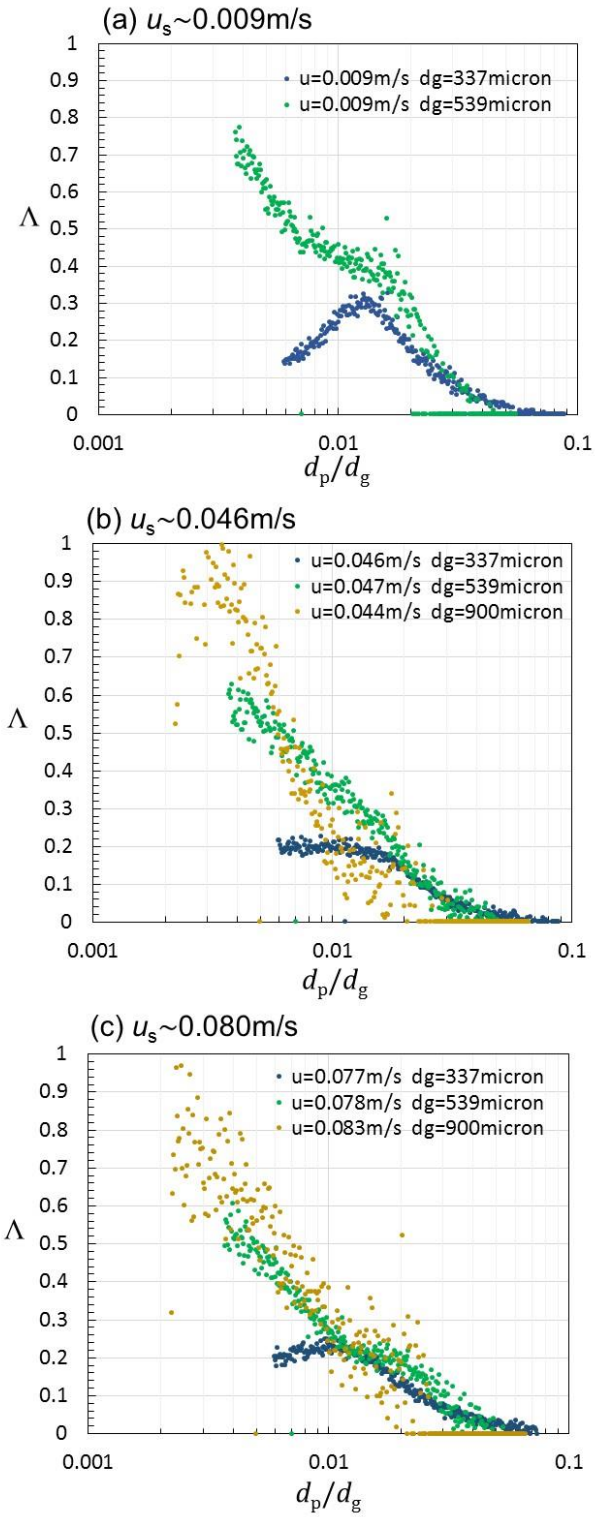

Figure 2.13: Effective collector number ratio versus particle-to-grain size ratio plotted for different velocity groups: (a) 0.009m/s, (b) 0.046m/s and (c) 0.080m/s

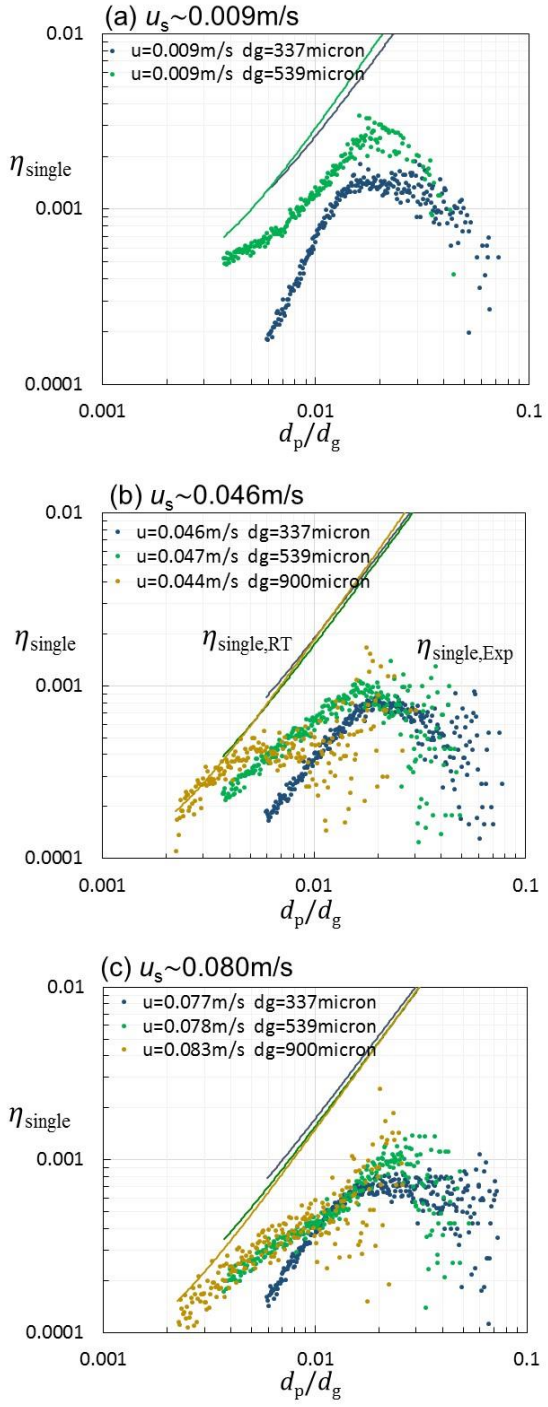

Figure 2.14: Single collector efficiency predicted from experiments ($\eta_{single,Exp}$) compared with single collector efficiency calculated from Rajagopalan & Tien's model ($\eta_{single,RT}$) shown as lines. The single collector efficiencies were plotted vs particle-to-grain size ratio for different velocity groups: (a) 0.009m/s, (b) 0.046m/s and (c) 0.080m/s

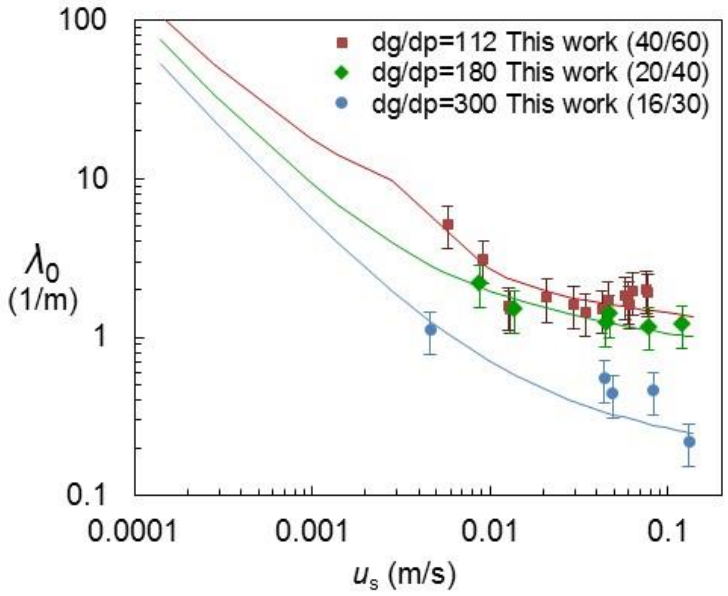

Figure 2.15: Corrected predictions for initial filtration coefficients compared with measurements.

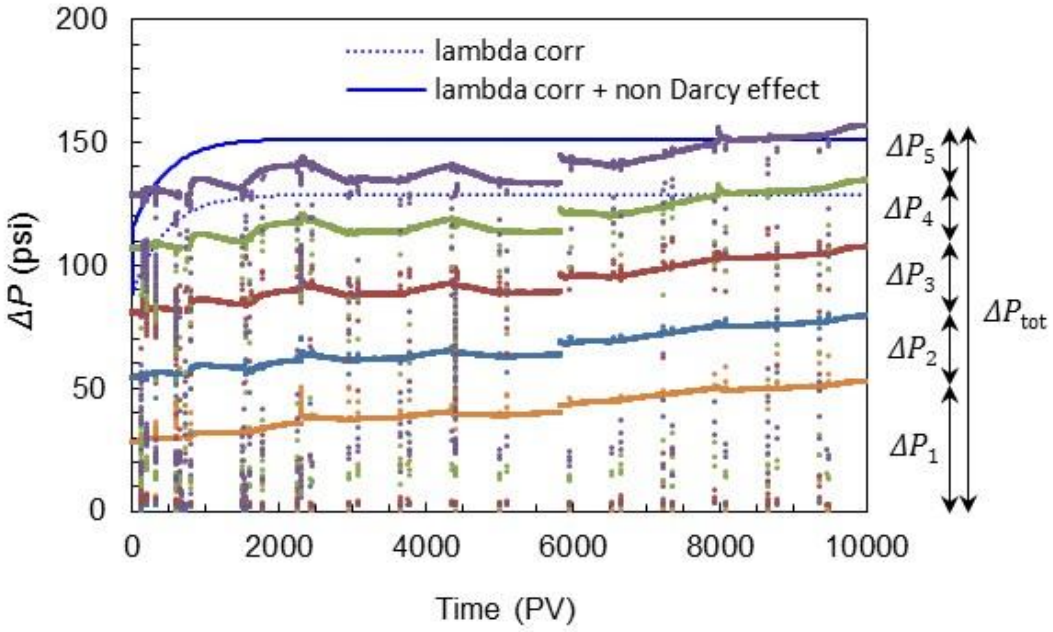

Figure 2.16: Pressure drops across proppant pack. Experimental values show pressure drops for each segment. Model predictions were compared with experimental values. Dashed line is a pressure drop from corrected filtration coefficient. Solid line includes non-Darcy effect as well.

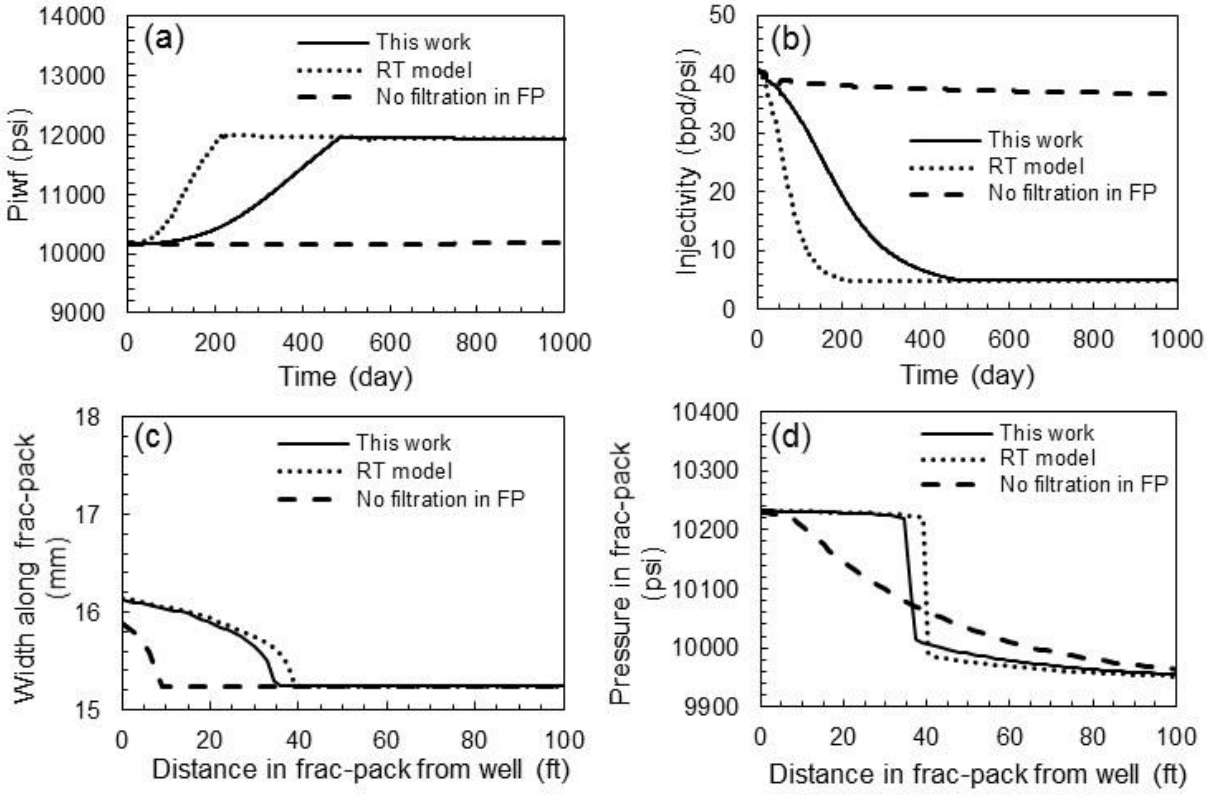

Figure 2.17: Comparison of simulation results using filtration coefficients in this work, Rajagopalan & Tien's model without correction, and velocity correction factor, VCF=0 (no filtration) in Suri & Sharma (2010). (a) injection well bottomhole pressure with time, (b) injectivity with time, (c) frac-pack width along frac-pack from the well at t=1000days, and (d) pressure in the frac-pack vs distance from the well at t=1000days. In (a) and (b), fracture widening effect was turned off to show the effect of filtration in frac-pack alone.

Nomenclature

A_s	=	Specific surface area per unit solid volume, L^{-1}, m^{-1}
B	=	Empirical Parameter in Eq. (2.8), −
C	=	Concentration of solid particles, −, ppmv
d_g	=	Diameter, grain, L, m
d_p	=	Diameter, particle, L, m
k	=	Permeability, L^2, m^2
K	=	Empirical Parameter in Eq. (2.8), −
L	=	Length, filter, L, m
n_{eff}	=	Effective collector number, −
ΔP	=	Pressure drop, $mL^{-1}t^{-2}$, Pa
q	=	Flow rate, volumetric, L^3t^{-1}, $m^3 \cdot s^{-1}$
R	=	Flow resistance, $mL^{-4}t^{-1}$, $Pa \cdot s \cdot m^{-3}$
t	=	Time, t, s
u_s	=	Superficial (Darcy) velocity, Lt^{-1}, $m \cdot s^{-1}$
$u_{s,cr}$	=	Critical superficial velocity, Lt^{-1}, $m \cdot s^{-1}$
v_{cr}	=	Critical interstitial velocity, Lt^{-1}, $m \cdot s^{-1}$
Δx	=	Length of core segment or frac-pack segment, L, m
β_F	=	Inertial parameter in Forchheimer eq., L^{-1}, m^{-1}
η	=	Collection efficiency, −
η_{filter}	=	Collection efficiency, filter, −
η_{single}	=	Collection efficiency, single collector, −
λ	=	Filtration coefficient, L^{-1}, m^{-1}
λ_0	=	Filtration coefficient of clean bed, L^{-1}, m^{-1}
$\lambda_{0,RT}$	=	Initial filtration coefficient by RT model, L^{-1}, m^{-1}
Λ	=	Effective collector number ratio, −
μ	=	Viscosity, $mL^{-1}t^{-1}$, $Pa \cdot s$
ρ	=	Density, fluid, mL^3, $kg \cdot m^3$
σ	=	Specific deposit, −
ϕ	=	Porosity, −

References

Barkman, J. H., & Davidson, D. H. 1972. Measuring Water Quality and Predicting Well Impairment. *Journal of Petroleum Technology*, **24** (7): 865–873. http://dx.doi.org/10.2118/3543-PA

Cushing, R. S., & Lawler, D. F. 1998. Depth Filtration: Fundamental Investigation through Three-Dimensional Trajectory Analysis. *Environmental Science & Technology*, **32** (23): 3793–3801. http://dx.doi.org/10.1021/es9707567

Ergun, S. 1952. Fluid Flow Through Packed Columns. *Chemical Engineering Progress*, **48** (2): 89–94.

Fitzpatrick, J. A., & Spielman, L. A. 1973. Filtration of Aqueous Latex Suspensions Through Beds of Glass Spheres. *Journal of Colloid and Interface Science*, **43** (2): 350–369. http://dx.doi.org/10.1016/0021-9797(73)90382-2

Gruesbeck, C., & Collins, R. E. 1982. Entrainment and Deposition of Fine Particles in Porous Media. *Society of Petroleum Engineers Journal*, **22** (6). http://dx.doi.org /10.2118/8430-PA

Happel, J. 1958. Viscous Flow in Multiparticle Systems: Slow Motion of Fluids Relative to Beds of Spherical Particles. *AIChE Journal*, **4** (2): 197–201. http://dx.doi.org/10.1002/aic.690040214

Ison, C. R. 1967. *Dilute Suspensions in Filtration*. University of London, London, England.

Ives, K. J. 1962. Filtration using Radioactive Algae. *Transactions of the American Society of Civil Engineers*, **127** (3): 372–385.

Maroudas, A., & Eisenklam, P. 1965. Clarification of Suspensions: A Study of Particle Deposition in Granular Media: Part I—Some Observations on Particle Deposition. *Chemical Engineering Science*, **20** (10): 867–873. http://dx.doi.org/10.1016/0009-2509(65)80083-5

Perkins, T. K., & Gonzalez, J. A. 1985. The Effect of Thermoelastic Stresses on Injection Well Fracturing. *Society of Petroleum Engineers Journal*, **25** (1): 78–88. http://dx.doi.org/10.2118/11332-PA

Rajagopalan, R., & Tien, C. 1976. Trajectory Analysis of Deep-Bed Filtration with the Sphere-in-Cell Porous Media Model. *AIChE Journal*, **22** (3): 523–533. http://dx.doi.org/10.1002/aic.690220316

Sharma, M. M., Pang, S., Wennberg, K. E., & Morgenthaler, L. N. 2000. Injectivity Decline in Water-Injection Wells: An Offshore Gulf of Mexico Case Study. *SPE Production & Facilities*, **15** (1): 6–13. http://dx.doi.org/10.2118/60901-PA

Sharma, M. M., & Yortsos, Y. C. 1987. Transport of Particulate Suspensions in Porous Media: Model Formulation. *AIChE Journal*, **33** (10): 1636–1643. http://dx.doi.org/10.1002/aic.690331007

Shumbera, D., Ritter, D., Ellis, R., Jannise, R., et al. 2003. Improved Water Injector Performance in a Gulf of Mexico Deepwater Development Using an Openhole Frac Pack Completion and Downhole Filter System: Case History. Paper SPE 84416 presented at the SPE Annual Technical Conference and Exhibition, 5-8 October 2003, Denver, Colorado. http://dx.doi.org/10.2118/84416-MS

Suarez-Rivera, R., Stenebråten, J., Gadde, P., & Sharma, M. 2002. An Experimental Investigation of Fracture Propagation During Water Injection. Paper SPE 73740 presented at the International Symposium and Exhibition on Formation Damage Control, 20-21 February 2002, Lafayette, Louisiana. http://dx.doi.org /10.2118/73740-MS

Suri, A., & Sharma, M. 2010. A Model for Water Injection Into Frac-Packed Wells. *SPE Reservoir Evaluation & Engineering*, **13** (3): 449–464. http://dx.doi.org /10.2118/110084-PA

Suri, A., Sharma, M., & Moreno, J. M. M. 2010. Injectivity of Frac-Packed Wells: A Case Study of the Guando Field. Paper SPE 125897 presented at the SPE International Symposium and Exhibiton on Formation Damage Control, 10-12 February 2010, Lafayette, Louisiana, USA. http://dx.doi.org/10.2118/125897-MS

Tufenkji, N., & Elimelech, M. 2004. Correlation Equation for Predicting Single-Collector Efficiency in Physicochemical Filtration in Saturated Porous Media. *Environ. Sci. Technol.*, **38** (2): 529–536. http://dx.doi.org/10.1021/es034049r

Wennberg, K. E. 1998. *Particle Retention in Porous Media: Applications to Water Injectivity Decline*. NTNU - Norwegian University of Science and Technology, Trondheim, Norway.

Yao, K.-M., Habibian, M. T., & O'Melia, C. R. 1971. Water and Waste Water Filtration. Concepts and Applications. *Environmental Science & Technology*, **5** (11): 1105–1112. http://dx.doi.org/10.1021/es60058a005

Chapter 3 : Generation and Filtration of O/W Emulsions in Porous Media

3.1 INTRODUCTION

3.1.1 Summary

Produced water typically contains oil-in-water (O/W) emulsions. These emulsions can be removed by surface facilities before injection, but it is difficult to remove them completely. Water containing dilute O/W emulsions can be re-injected into formations for waterflooding or pressure maintenance. These oil droplets can plug the pore space in porous media. If this occurs in the near-well or near-fracture region, the performance of injection wells can decline rapidly which may lead to costly remediation processes.

The other important aspect of emulsion flow in porous medium is that the residual oil phase can be displaced at high-velocities when the formation contains a residual oil saturation. During this process of oil displacement or capillary desaturation, displaced oil forms O/W emulsion droplets that participate in the plugging processes. These processes of generation and filtration of O/W emulsions occur simultaneously in the porous media, especially at near-wellbore flow conditions.

This chapter focuses on an experimental understanding of how oil droplets can be generated by viscous flow, and then plug pore throats. The rate of generation and filtration of oil droplets were quantified based on experimental observations in this work. By experimental observations and relevant models, a comprehensive model of O/W emulsion flow in porous media can be developed to more precisely predict the near-well formation damage caused by produced water re-injection (PWRI) and the subsequent performance of injection wells.

3.1.2 Water Injectivity Decline by O/W Emulsions

As reviewed in Chapter 1, when produced water is re-injected into the subsurface formation, the most critical problem is the injectivity decline of the well. There have been field reports in which the injectivity declined by more than half in a few weeks or months. The origin of this injectivity decline is primarily solid particles, O/W emulsion droplets and microbes, depending on the source of water. For produced water, O/W emulsion is the primary cause of plugging. Coleman & McLelland (1994) reported the oil content to be 50 to 500 mg/L in the produced water measured at the injection facility before treatment. The oil droplets are typically lowered to 20 to 50 ppmv by treatment processes, but this concentration of oil droplets still damages the pore spaces near the wellbore, and the results are quite sensitive to the presence of surfactants or corrosion inhibitors.

Several experimental and field studies indicate that oil droplets in injection water can lead to significant permeability declines. Hsi et al. (1994) reported a PWRI field case in the Prudhoe Bay in which they installed on-site coreflooding equipment, and verified that permeability damage was higher when injection water was not filtered. Many other coreflood experiments also show that injection of oil droplets can reduce the core permeability. Zhang et al. (1993) experimentally investigated the formation damage caused by oily water and solids. They indicated that the extent of the permeability damage depends on the size and concentration of oil and solids, and the damage by individual components was different from the damage caused by the presence of both oil droplets and solid particles.

van den Broek et al. (1999) performed core-floods with water containing solid particles and oil droplets. Injection of solids-containing water led to severe permeability damage near the inlet section of the core, but the injection of oil-containing water led to permeability damage over the entire section of the core. The mixture of solid and oil

droplets led to higher permeability damage than the combined damage of the individual components. Darwish et al. (1999) also observed that oil droplets can lead to higher permeability damage than HPAM polymer. Al-Abduwani et al. (2001) conducted a visual observation of produced-water injection into a sandstone specimen by using an electron microprobe. In this work, however, deposition mechanisms were not clearly depicted in the electron microprobe images.

Ali et al. (2007) compared declines in permeability when only O/W emulsions were used in core-flood experiments and when O/W emulsions were used together with hematite particles. They indicated a much more severe permeability decline occurred when emulsions were mixed with solid particles. Ochi et al. (2007) conducted core-flood experiments of dilute oil droplet solutions and measured outlet concentration and droplet sizes. They also observed the permeability declines caused by trapping and suggested an empirical permeability change model and well-scale models. Buret et al. (2008) also measured fluid resistances caused by oily water filtration in grain-packing. They reported higher permeability decline compared to solid particle filtration due to the uniform deposition along the packing because of oil droplets naturally deforming while flowing through pore spaces.

The above experiments on permeability damage caused by oil droplets were conducted with water (or brine)-saturated cores. Mendez (1999) was the first to show that the presence of residual oil saturation can substantially impact the behavior of permeability damage. She showed that oil droplets were generated from the residual oil phase, and the subsequent plugging made permeability declines steeper. In her work, the oil droplet concentration, the emulsifier concentration, injection flow rates and formation permeability were shown to have an important effect on the permeability reduction of cores with residual oil saturation.

Because of the ability of O/W emulsions to plug pore spaces, they have been used as fluid-loss-control agents and plugging agents in completion fluids. Al-Riyamy & Sharma (2004) studied the mechanisms controlling filtration and fluid leak-off of O/W emulsions containing solid particles. They experimentally investigated the effect of both external and internal filtration of O/W emulsions containing solid particles. Emulsified drilling fluid, which is the oil-based mud, utilizes the same properties of emulsions that plug pore spaces even though there are differences in emulsion concentrations. The formation damage during drilling stages caused by emulsions in drilling fluids can be found in Fjelde (2009).

3.1.3 Objectives

It is of critical importance to understand the flow behavior of dilute O/W emulsions in porous media with a residual oil saturation. The generation and filtration of emulsion droplets are critical factors needed to predict emulsion flow behavior. The objective of this chapter is to experimentally measure the rate of generation and filtration of O/W emulsions in a porous medium. These experimental observations can be implemented in an existing macroscopic material balance model for emulsion flow in a porous medium with residual oil saturation. For the rate of generation, the size and concentration of O/W emulsions generated at different capillary number were investigated. This trend is formulated into an empirical model. For the filtration behavior of O/W emulsions, synthetic dilute O/W emulsions were injected into granular packs saturated with water to measure the filtration coefficient. The filtration coefficient was measured for various capillary numbers, grain sizes, and fluid velocities. The measurements were compared to known models, and the characteristic behavior for O/W emulsion filtration were analyzed. It was determined that the physics of filtration of O/W emulsions was different from solid particle filtration.

3.2 MODELS FOR O/W EMULSION FLOW IN POROUS MEDIA

3.2.1 Material Balance of Flowing Dilute Oil Droplets in Porous Media

Numerous researchers have built models to describe the flow of O/W emulsions in porous media. The initial models focused on predicting the pressure drops caused by O/W emulsion flow. These models focus on the fact that O/W emulsions tend to decrease the effective viscosity of the oil phase. This group of models addressed understanding the static behavior of emulsion flow. This approach is also called a homogenous model that assumes the emulsion is a continuum where the emulsion-rock surface interaction is not accounted for. Devereux (1974a, 1974b) built a model accounting for capillary effects by modifying Buckley-Leverett's theory with a retardation factor for the emulsion phase. Devereux then conducted an experiment varying pressure drops and emulsion concentration. Alvarado & Marsden Jr. (1979) built a model for O/W emulsion flow through a porous media and a capillary tube. They also conducted emulsion flow experiments changing core permeability, flow velocity and the rheological properties of emulsions.

Another modeling approach is based on conventional filtration theory and macroscopic material balance of oil droplets. The material balance for the particulates is written assuming a single-phase fluid. The same formulations can be written for the filtration of dilute O/W emulsions. Emulsions are assumed to be stable and behave as solid particles while flowing through the pore-space. Soo & Radke (1986) and Soo et al. (1986) developed a macroscopic material balance model for flowing dilute oil droplets through a porous medium with a single phase fluid. Their model is based on the same filtration theory described in the previous chapter. It utilizes the filtration coefficient, λ for the rate of particle deposition. An example of the application of these models can be found in Hofman (1990) and Hofman & Stein (1991). Based on filtration models, permeability decline was predicted and matched to calculation results from the model.

In addition to trapping of O/W emulsions, the generation of O/W emulsions from the residual oil saturation needs to be accounted for in the macroscopic material balance. This work was done by Mendez (1999). This model provides a proper material balance specific to the flow of oil droplets in porous media, because oil droplets flow and exhibit different behavior than solid particles when residual oil exists. The trapping and generation of oil droplets can be experimentally measured, and these findings can be implemented into an oil-droplet flow model. This model also accounts for the impact of the residual oil phase. Emulsions can be generated from the oil phase at high capillary numbers, and this provides additional sources of droplets for subsequent filtration. The work in this chapter is based on a model first proposed by Mendez (1999) and the details will be explained in following sections.

After Mendez (1999)'s work, there were studies to investigate the effect of residual oil on permeability damage and its associated mechanisms. Vaz Jr. et al. (2006a) and Vaz Jr. et al. (2006b) built an analytic model to predict the permeability impairment in a core with oil saturation by assuming a simple linear behavior in the filtration coefficient. They showed the pressure drop may not be significant when the relative permeability to water increases by the detachment of oil droplets. However, this may not be consistent with experimental results under certain conditions. Ali et al. (2009) investigated the effect of residual oil on hematite particle filtration. They observed a deeper invasion of particles into the core. But the pressure drop was not significantly affected by the presence of the oil phase. Saraf et al. (2010) conducted an experiment in which hematite particles were injected into cores with residual oil, and they then measured the amount of internal deposition by CT scan. Their results also show that the deposition is dispersed through longer depths of the core when residual oil was present and they showed agreement with effluent break-through models based on deep-bed filtration theories.

There are different approaches other than filtration theory to describe the retention of O/W emulsions in the porous medium. Jin & Wojtanowicz (2014) used a Langmuir isotherm to describe the rate of emulsion capturing in the oil phase. The deposition process of flowing emulsions was assumed to be an adsorption process. This model has an advantage that it can be analytically simplified, but has a disadvantage in that the isotherm may not address the physics of oil droplet filtration adequately. They also pointed out that experiments and theories are required for the high velocity conditions encountered in the near-well region.

3.2.2 Deep-Bed Filtration of O/W Emulsions and its Mechanisms

The main cause of the injectivity decline during oily-water injection is the deposition of oil droplets and associated increase in flow resistances near the injection well. In this section, the deep-bed filtration process of O/W emulsions is reviewed in more detail.

The filtration of O/W emulsions occurs primarily in the near-well and near-fracture regions. These flow conditions are of our interest. As described in the previous chapter, the linear (superficial or Darcy) velocity of 1 to 10 cm/s is the typical range of fluid velocity encountered in a fracture. The fluid velocity in the matrix near the injector is slower than this. Typically, the range of linear velocity in the near well region is from 0.1 to 1 cm/s. In the far-field region, the linear velocities are lower than these values. Many of the previous filtration experiments were conducted in the range of low fluid velocities that correspond to those encountered in the far-field region. The filtration experiments conducted in this chapter are focused on the linear velocity conditions in the order of 0.1 to 1 cm/s which represent near-well or near-fracture conditions.

Straining and interception were investigated as main mechanisms of oil droplet filtration in this study. In the conventional theory of filtration of solid particles, different modes of filtration mechanisms were explained based on interaction forces, size ratio and

particle trajectory along the grain. The particle is assumed to be smaller than the grain (collector), and mechanisms of particle transportation and deposition on the grain were explained by interception, sedimentation, and diffusion (Yao et al., 1971). Later, in a similar manner but for a broader range of size-ratio of oil-droplet to grain, Soo & Radke (1986) explained two main mechanisms of O/W emulsion filtration. In case the particle size is small when compared to the grain (or pore throat) size, the main trapping mechanism is interception. Droplets are attached to the grain surface by electrical, van der Waals, gravitational and hydrodynamic forces. In contrast, when the particle size is comparable to the grain size, the main trapping mechanism is straining. Straining is a process of droplet trapping in a pore constriction. Detailed explanations of these mechanisms can be found in Herzig et al. (1970) and Pang & Sharma (1997). Buret et al. (2010) also presented experimental data of oil droplet filtration based on both mechanisms and identified severe permeability declines in straining-dominated deposition regimes.

Filtration of oil droplets in porous media is different from that of solid particles. Some oil droplets can coalesce with the residual oil phase. This will eventually increase the oil saturation. The remaining portion of deposited oil droplets, however, will contribute to the porosity and permeability decline. The coalescence fraction can be experimentally estimated from pressure drops. However, more investigation is required to understand the factors that control the fraction of drops that coalesce during the filtration of oil droplets.

3.2.3 Generation of O/W Emulsions by Capillary Desaturation

When the pressure gradient across a porous medium with residual oil saturation is high enough, oil droplets are created from the residual oil phase by a snap-off mechanism. This phenomenon can occur simultaneously with the filtration of O/W emulsion droplets. Oil droplets in the injected water can be trapped in the pore, and generated droplets can also be trapped in the same way. The generated oil droplets will contribute to the

permeability impairment.

The process of decreasing oil saturation induced by high capillary number conditions is known as the capillary desaturation. Lake (1989) summarized the mechanisms and experimental observations of capillary desaturation. Experimental observations are available on the relationship between residual wetting or non-wetting phase saturation and the capillary number. A residual saturation can be lowered by high viscous forces when the viscous forces overcome the capillary forces. When oil is the de-saturating phase, the reduced oil saturation can be represented by a function of the capillary number:

$$S_{or} = S_{or}^{h} + \frac{S_{or}^{l} - S_{or}^{h}}{1 + TN_{Ca}} \tag{3.1}$$

Where S^{h}_{or} and S^{l}_{or} are residual oil saturations respectively at high and low capillary numbers. T is an empirical parameter, and N_{ca} is the capillary number defined as $\mu u/\sigma$. μ is the viscosity of the displacing fluid, u is the superficial velocity, and σ is the oil-water interfacial tension.

Despite displaced oil droplets affecting the flow behavior, once they are generated, no systematic observation has been conducted on the characterization of displaced oil droplets. The size distributions and concentration of generated oil droplets are of our interest in this work, because they will be additional sources that plug the core. The quantification of the generated droplet sizes and concentrations is one of the objectives of this work. In this section, the capillary desaturation process is briefly introduced.

Oil droplets are generated by a snap-off mechanism at high capillary number conditions (Peters, 2012). When an oil droplet is forced to move through a pore throat, the droplet breaks up after exiting the pore throat. At the neck of the constriction, if the capillary pressure at the entrance is larger than the capillary pressure at the exit, the oil

droplet can emerge from the pore throat. This condition can be written as:

$$\sigma\left(\frac{1}{r_1}-\frac{1}{r_2}\right)>\frac{2\sigma}{r_3} \tag{3.2}$$

where r_1 and r_2 are principal radii at the pore throat, and r_3 is the radius of oil droplet protruding to the pore body before the break-up (shown in the schematic in Figure 3.1). σ is the interfacial tension between the oil and the water. When the viscous force on a trapped oil phase is large enough to overcome the capillary force, the interface proceeds into the constriction until the droplet emerges. The snap-off of the droplet will follow. When the oil saturation is larger than the residual oil saturation at a low capillary number, the oil phase is connected throughout the porous medium. Once this continuous oil phase is displaced by high viscous forces, the oil phase will be disconnected. Then the oil ganglia can mobilize and break up repeatedly into O/W emulsion droplets. This procedure occurs in sequence through multiple pore constrictions which makes it difficult to describe the generated droplet size or concentration based on a single snap-off process.

Mendez (1999) postulated that the rate of oil-droplet generation has a first-order kinetics with respect to the amount of oil displaced:

$$r_{gen}=\frac{1}{v_D}\frac{d\sigma_{gen}}{dt}=u\frac{k_{gen}}{v_D}\left(S_o-S_{or}\right) \tag{3.3}$$

where r_{gen} is the rate of generation of oil droplets by viscous and buoyancy forces in a unit of number of droplets per unit bulk volume, σ_{gen} is the specific droplet generation in a unit of generated volume of droplets per unit bulk volume. k_{gen} is the rate constant for droplet generation and has units of reciprocal of the length, and v_D is the volume of a single oil droplet. All generated droplets are assumed to be the same size. If S_o is the same as S_{or} under low capillary-number conditions, no oil droplets will be generated. The dependency of k_{gen} on S_o and S_{or} is difficult to experimentally measure, because the volume of oil

displaced which contributes to emulsions is difficult to measure. In this work, the rate is assumed as independent of ($S_o - S_{or}$), and the zeroth-order relation to ($S_o - S_{or}$) is postulated:

$$r_{gen} = u \frac{k_{gen}}{v_D} \tag{3.4}$$

Where the unit of k_{gen} is (number of generated droplets)/(length·pore volume) in our zeroth-order relation.

k_{gen} can be measured experimentally and is dependent on interfacial properties in a complicated manner. Because of this, it is important that the rate of generation be measured with the actual porous medium and the fluids of interest. However, there are no previous measurements that can be used for such an analysis. Only similar cases of emulsion generation were found for phenomenon in surface facilities. van der Zande et al. (2001) reported experimental observations of emulsion generation in the surface facilities operating at high shear rate conditions, e.g., choke valves. Experiments on similar phenomena pertinent to choke valves can be found in Dalmazzone et al. (2005).

The generation process can significantly be affected by the type of oil phases. Crude oil contains natural surfactants. The generated droplet sizes and concentrations can vary substantially even with trace amounts of natural surfactants in the crude oil. Mendez (1999) showed that different crude oil types (present as a residual oil phase) can lead to different permeability declines. This was primarily caused by various degrees and sizes of oil droplet generation from crude oils used in the experiments.

3.2.4 Comprehensive Model for Emulsion Generation and Filtration in Porous Media with Residual Oil

Mendez (1999) built a macroscopic material balance model for O/W emulsion flow through a porous medium with residual oil saturation. Trapping and generation of emulsions are accounted for in this model. In this section, this model is summarized to

provide a background of measurements for trapping and emulsion generation. The measurements shown in this chapter can be directly used for this model. The model is assumed to be one-dimensional, and the core is assumed to be in a horizontal position without a gravity effect. Incompressible fluid phases and a homogeneous porous medium is assumed. The droplets are assumed to be of a single uniform size.

The material balance for emulsion droplets is written as:

$$\phi \frac{\partial C_o}{\partial t} + u \frac{\partial C_o}{\partial x} = -u\lambda C_o + u \frac{k_{gen}}{v_D} \tag{3.5}$$

Where C_o is the emulsion concentration with a unit of number of droplets per unit pore volume. v_D is the volume of an emulsion droplet. The terms on the left represent accumulation and convection, and the terms on the right represent the trapping and generation of droplets. Initial and boundary conditions are:

$$C_o = C_{oin} \quad \text{at} \quad x = 0 \ \text{and} \ t > 0$$

$$C_o = 0 \quad \text{at} \quad t = 0 \ \text{and} \ x > 0$$

The material balance for the oil phase can be written as:

$$\phi \frac{\partial S_o}{\partial t} + u \frac{\partial f_o}{\partial x} = u\lambda C_o v_D p - u k_{gen} \tag{3.6}$$

Where f_o is the fractional flow of the oil phase, and p is the fraction of coalesced droplets which becomes a part of the residual oil phase (some fraction of the trapped droplets). The left side of the equation represents accumulation and convection of the oil phase, and the right side represent the coalesced and generated droplets. When S_o is below S_{or}, the fractional flow term will disappear. The relevant initial condition is:

$$S_o = S_{or} \quad \text{at} \quad t = 0 \ \text{and} \ x > 0$$

Some portion (p) of the droplets will coalesce with the residual oil phase. These

droplets increase the oil saturation, but will not contribute to reducing permeability. However, the remaining portion $(1-p)$ of trapped droplets will plug pores and reduce permeability. The rate of trapping of emulsion droplets is separately written as a first-order rate expression:

$$v_D \frac{\partial C_o^t}{\partial t} = u\lambda C_o v_D (1-p) \tag{3.7}$$

Where $C_o{}^t$ is the concentration of trapped oil droplets (number of droplets per unit bulk volume). p becomes 0 when all the deposited emulsion droplets contribute to reducing permeability, and p becomes 1 when they all coalesce with the residual oil phase. The initial condition is:

$$C_o{}^t = 0 \quad \text{at} \quad t = 0 \ \text{and} \ x > 0$$

The above three relationships define the material balances. There are also relations to define the effect of the emulsion deposition on porosity and permeability.

$$\phi = \phi_o - C_o^t v_D \tag{3.8}$$

$$k_d = k_{dp} k_{ds} k_{dt} = \frac{\phi^3 (1-\phi_o)^2}{\phi_o{}^3 (1-\phi)^2} \left(\frac{1 + \dfrac{C_o^t v_D}{1-\phi_o}}{1 + \dfrac{d_g}{d_e} \dfrac{C_o^t v_D}{1-\phi_o}} \right)^2 \frac{1}{1+\beta C_o^t v_D} \tag{3.9}$$

Where k_{dp}, k_{ds} and k_{dt} represent ratios of reduced permeability caused by a reduction of porosity, an increase in surface area, and an increase in tortuosity respectively. The reduced permeability can be calculated by multiplying k_d with the initial permeability.

The filtration coefficient can change with depositions of oil droplets. The change can be determined empirically. Mendez (1999) proposed the following correlation:

$$\lambda = \lambda_o \left(1 - \alpha \frac{C_o^t}{C_{oin}} \right) \tag{3.10}$$

The initial filtration coefficient can be estimated by the models introduced in the previous chapter. The empirical parameter, α, can be a function of droplet size distribution, pressure gradient, pore size distribution and other surface interaction force parameters.

3.3 EXPERIMENTAL

3.3.1 Materials and Setup

The experimental setup in Figure 3.2 was designed to measure the rate of oil droplet generation and filtration. It supplements the setup in the previous chapter to be able to create and measure the residual oil saturation and create O/W emulsions at various fluid velocities. Oil, water and O/W emulsions can be separately pumped into cells filled with sand. Sampling ports from the inlet and the outlet of the cell enabled us to take samples to measure the emulsion size distribution and concentration. Pressure drops can be measured from the cell and its pressure taps, so researchers can acquire pressure distributions along the cell. The cell is a horizontal, cylindrical tube filled with sand.. Cells with lengths of 10.3, 20.7, 40 and 87 cm and inner diameter of 0.95 cm were used. Typically, a shorter cell was used when a higher degree of filtration was expected.

The different types of porous media used were Ottawa sand, Series F-95, Ottawa sand with US mesh sizes of 80/100, 40/60, 20/40, and 16/30 CarboHSP proppant. Their diameters, $d_{g,50}$ were 96, 166, 336.5, 538.7 and 899.5 μm respectively, and all were water-wet. Sands were vibration-packed in the cell and flushed with distilled water at a linear velocity with a range of 5 to 15 cm/s to remove any particles or debris on the surface. To make the residual oil saturation, distilled water (pH 6.0 and ionic strength of 0.016 M) and Exxsol D110 de-aromatized mineral oil (kinematic viscosity 3.43cSt at 25˚C) were used for the water and oil phase respectively. They were also used for the synthesis of dilute

O/W emulsion solutions. Interfacial tension was measured for this water-oil system. The pendant drop method (Ramé-Hart goniometer) was used, and the interfacial tension was found to be 35.02 dynes/cm by averaging multiple measurements.

To accommodate various flow rate conditions, two pumps were used. For linear velocities ranging between 0.03 and 0.13 m/s, a Moyno progressive cavity pump A4015 was used. For lower velocities of 0.006 to 0.03 m/s, a DCI VPA syringe pump series 16 was used. Rosemount pressure transducers were used for monitoring differential pressures throughout the filtration cell. The emulsion concentration and size distributions were measured using a Coulter counter, Multisizer 3 from Beckman Coulter. Accumulators were used to pump emulsions and oil as necessary.

3.3.2 O/W Emulsion Synthesis

When O/W emulsion droplets were generated by a high velocity flow in a porous medium, no emulsifier was necessary. However, for the filtration experiments using O/W emulsions, dilute emulsion solutions were synthesized using an emulsifier. Xiameter OFX-0193, a silicone polyether copolymer was used as the emulsifier. A 0.62% oil and 0.08% emulsifier in weight fractions were mixed with water and processed by an ultrasonic homogenizer, Branson Sonifier 250. In approximately three minutes of homogenizing time, stable emulsion solutions can be created. This solution was diluted between 1:10 to 1:20 with water to make emulsion solutions simulating produced water with a concentration between 30 to 50 ppmv at the inlet of the filtration cell.

3.3.3 Procedure

By applying a high velocity flow of water to sand-packs saturated with residual oil, emulsions were generated, and then their sizes and concentrations were measured. This procedure was repeated for various sizes of sands and fluid velocity to investigate their

effects. First, the sand-pack was flushed with distilled water at high flow rates of 5 to 15 cm/s to remove any particles on the surface. Oil was pumped at a low speed (0.1cm/s) to establish a residual water saturation. Then, water was pumped at the same low speed to establish the residual oil saturation. The displaced volumes were recorded for each of the stages of injection to calculate the residual water and oil saturations. Dead volumes, including tubing to fluid collection points, were calculated and appropriately subtracted from collection volumes. Then, water was pumped at various higher speeds to observe capillary desaturation. Once pumping started, pressure drops across the sand-pack stabilized within 1 to 2 minutes. Pumping continued for about 6 pore volumes after the stabilization. The displaced fluids were sampled at regular time intervals. Samples were analyzed using a Coulter counter and microscope to determine emulsion size distributions and concentrations. This procedure was repeated for various sand grain sizes.

In a separate set of experiments, filtration experiments using synthetic O/W emulsions were conducted. Synthetic O/W emulsions were prepared and placed in the accumulator with a magnetic stirrer to maintain an even concentration during the filtration process. Water was pumped into the accumulator. The water displaced the emulsion to the sand-pack (filtration cell) at a constant superficial (Darcy) velocity. As the filtration progressed with time (pumped pore volumes), samples were taken at the inlet and outlet of the cell at different times. Coulter counter measurements were repeated to obtain a consistent concentration from the sample by measuring a statistically sufficient number of droplets. This was achieved by measuring 6,000 μL of each sample. This method for Coulter counter measurement was the same as that of the previous chapter. This experiment was repeated with different size of sands, and some modifications were applied as necessary. For example, sampling tabs in the middle of the cell were used to investigate the changes along the cell depth.

3.4 RATE OF GENERATION OF O/W EMULSIONS IN POROUS MEDIA

3.4.1 Residual Saturation during Capillary Desaturation

One of the main objectives of this experiment was to understand the rate of emulsion generation under near-well conditions, because these generated particles can participate in further filtration processes. The capillary desaturation experiment was conducted, and the displaced fluid was analyzed for emulsion sizes and concentration. The relationship of residual saturation and capillary number can be compared with a typical capillary desaturation curve (Lake, 1989). The sand-pack with residual oil saturation was displaced by water at high fluid velocities. The displaced volumes for each fluid velocity stage were recorded and residual oil saturations at each stages were calculated. In Figure 3.4, oil saturations for different sand sizes are shown to correlate to the capillary number which represents the ratio of viscous to local capillary forces. The capillary number is defined as:

$$N_{ca} = \frac{u_s \mu}{\sigma} \tag{3.11}$$

where u_s is the superficial velocity of water, μ is the viscosity of water, and σ is the water-oil interfacial tension. From this figure, the observed capillary desaturation with a small size sand matches the typical behavior. The range of capillary numbers where desaturation occurs are between 10^{-5} and 10^{-2}. However, the larger grains show smaller values in the desaturation curve then those typically found in literature. It is considered that, along with viscous forces, the effect of body forces (typically gravity for single phase and buoyancy for two phase) acting on the non-wetting phase blobs are also crucial for the large size grains. In this case, buoyancy needs to be accounted for along with the viscous force. The Bond number represents the ratio of the body-force to the local capillary forces, and it is typically defined as:

$$N_{bo,k} = \frac{kg(\rho_w - \rho_o)}{\sigma} \tag{3.12}$$

The above two numbers are the ratios of forces promoting the displacement of the non-wetting phase to the entrapping force, which is the capillary force. The trapping number is the sum of these two numbers. This represents the ratio of the displacing forces (buoyancy and viscous forces) to the entrapping forces (local capillary forces) depending on the direction of each force (Pope et al., 2000).

$$N_{tr,k} = \frac{\left|\bar{\bar{k}} \cdot \left(\bar{\nabla}\Phi + g\left(\rho_w - \rho_o\right)\bar{\nabla}D\right)\right|}{\sigma} \tag{3.13}$$

where Φ is the flow potential accounting for gravity and D is the depth to the datum. In cases with simpler flow directions, the definition of the trapping number can be simplified to:

$$N_{tr,k} = \sqrt{N_{ca}{}^2 + N_{bo,k}{}^2} \quad \text{for horizontal flow} \tag{3.14}$$

$$N_{tr,k} = N_{ca} + N_{bo,k} \quad \text{for vertical flow} \tag{3.15}$$

Experiments in this work were conducted under horizontal flow directions.

For the definition of the Bond number when dealing with a porous medium, permeability typically has been used for the square of the characteristic length. In this work, another characteristic length available is the diameter of the generated emulsion droplets. The diameter of droplets increased with increasing sand-pack permeability, and this observation will be explained later. The Bond number and relevant trapping number can be defined by using the generated emulsion droplet diameter:

$$N_{bo,de} = \frac{d_e^2 g(\rho_w - \rho_o)}{\sigma} \tag{3.16}$$

$$N_{tr,de} = \sqrt{N_{ca}{}^2 + N_{bo,de}{}^2} \tag{3.17}$$

For the smaller-size sands which were used for the experiments, $N_{bo,k}$ and $N_{bo,de}$ are negligible compared to N_{Ca}. However, for larger-size sands and low velocities, they become comparable to N_{Ca}. In these cases, the trapping numbers are used instead of the capillary number. These results were shown in Figure 3.4b and c. The empirical correlation for S_{or} and $N_{tr,de}$ can be written as:

$$S_{or} = 0.014 + \frac{0.290 - 0.014}{1 + 6.40 \times 10^3 N_{tr,de}} \tag{3.18}$$

The desaturation curves more closely follow a trend with trapping number. The trend in capillary desaturation curve shows a better match, especially when the emulsion diameter is used. This indicates that, for the grain sizes larger than 0.1mm, the buoyancy effect as a displacing force is comparable to the effect of viscous displacement and may not be ignored. For the rest of this work, $N_{tr,de}$ is used instead of N_{ca}.

3.4.2 Sizes of Generated Emulsions during Capillary Desaturation

Size distributions of generated emulsions. In this section, it was experimentally verified that O/W emulsion droplets can be generated during the capillary desaturation processes in a porous medium. The droplets were generated from displacement of oil ganglia. The discharged fluid was analyzed within the trapping number range of 10^{-5} and 10^{-2}. Visual inspection by microscope shows the O/W emulsions with various sizes, as in Figure 3.3a. The emulsion sizes observed were in the order of 1 to 50 microns. They are spherical, and, in the figure, they are compared to the synthetic O/W emulsion droplets. The shapes and sizes of generated and synthetic emulsions were not seen to be substantially different.

The generated emulsions were analyzed by a Coulter counter to investigate their

size distribution and concentration. Figure 3.5 shows the emulsion size distributions for samples taken under various flow conditions. Two different sizes of sand are used as the porous medium. For each experimental set, the flow rate was varied to see the effect of the trapping number on size distributions. In experiments with larger grain, the size of emulsions were larger. In the sand-pack with a smaller grain, smaller droplets were generated. In both grain sizes, the lower flow rates (small trapping number) resulted in larger size droplets. As the trapping number increased, smaller droplets were generated. One possible explanation of this is that if there are various sizes of pore throats in the porous medium and snap-off is the mechanism of oil-droplet generation, oil droplet generation occurred from the larger pore throats under the lower trapping number conditions. At the higher flow velocity, the oil droplets were generated from the smaller pore throats. This behavior was observed in both sand-packs with large- and small-size sands.

Normalized size distributions. The generated droplet size increases with increasing sand (or pore) sizes. A more generalized behavior can be understood by looking at the normalized size distributions. To investigate this proportionality, the particle size distributions were plotted as the size of droplets divided by the grain size (d_e/d_g) in Figure 3.6. It is clearly seen that the droplet size distributions acquired from different sand-packs were the same for the same trapping number conditions (Figure 3.7). The trapping number had the same effect as explained above for the regular size distributions, and is also shown in Figure 3.6. Importantly, the normalized size distributions overlapped for the same trapping number in experiments with different sand sizes. This indicates that the ratio of generated emulsion-to-grain sizes is primarily a function of the trapping number. At low trapping numbers, droplets with a large d_e/d_g are generated, and at high trapping numbers, droplets with small d_e/d_g are generated.

Representative emulsion sizes. Representative emulsion sizes are acquired from the size distributions. The 50-percentile values of emulsion diameters in differential volume distributions were used as the representative emulsion sizes. The emulsion sizes from experiments with various sand sizes and trapping numbers are presented in Figure 3.8a. The generated emulsion droplets were larger in the larger size sands, and smaller at the higher trapping number conditions. The representative sizes of emulsion droplets were between 5 to 30 μm in the experimental conditions. The normalized droplet size (d_e/d_g) is plotted in Figure 3.8b. The trend of the normalized droplet size versus the trapping number shows a correlation with less dependency on the sand-grain size. The normalized size distribution showed a strong correlation with the trapping number. Assuming the normalized size is a function of the trapping number and grain sizes, a better representation for the normalized droplet size was considered in Figure 3.8c. The figure shows that a normalization in terms of $d_e/d_g^{0.67}$ results in a better dependency on trapping number by the following empirical correlation:

$$d_e = d_g^{0.67}\left(-0.155\log_{10} N_{tr,de} - 0.059\right) \tag{3.19}$$

where d_e and d_g is in units of μm. This correlation offers a quick estimation of the size of the generated droplet size within the experimental conditions of this report. The parameter $d_e/d_g^{0.67}$ can be understood as one of the characteristic parameters during the snap-off process. The physical reasons and implications of this empirical relation are not investigated here and require additional research.

3.4.3 Rate of Generation of Emulsions during Capillary Desaturation

Concentrations of generated droplets were also measured during capillary desaturation experiments. The concentrations were measured for 0 to 6 pore volumes (PV) of injection after the stabilization of the pressure drop. Concentrations of samples taken

during 0 to 6 PV were averaged. The concentrations of generated emulsions are shown in Figure 3.9a at various trapping number conditions conducted with various sand-grain sizes. Higher concentrations of emulsion droplets were generated at higher trapping number and in experiments with larger sand-grain sizes.

Because shorter sand-packs were used for experiments with finer sand-grains, the concentration of generated emulsions required a normalization to the length of sand-packs. The concentrations were divided by sand-pack lengths and C_e/L, i.e., the normalized concentrations, are plotted in Figure 3.9b. This C_e/L is the rate constant of emulsion generation, k_{gen} for zeroth-order generation rate expression used in Eq (3.4). The normalized concentrations of generated emulsions were less dependent on sand-pack grain sizes. The values plotted closely to each other; hence, the generated concentration per unit length was primarily a function of the trapping number. There was still a tendency to show a dependency on the grain sizes, however, because the sizes of the droplets generated through small grains were small.

This size-dependency of normalized concentrations of generated emulsions indicates that the introduction of size term is required. The emulsion-generation terms in Eq. (3.5) and (3.6) indicate that k_{gen}/v_D may be significant, which is a generation rate constant in terms of droplet numbers. The generated droplet diameter (d_e) and the volume of generated droplets (v_D) were shown in the previous section. By using these two measured parameters, k_{gen}/v_D and k_{gen}/d_e were plotted for various trapping numbers and sand-grain sizes in Figure 3.10. k_{gen}/v_D and k_{gen}/d_e represent the characteristic rate constants of O/W emulsion generation in high-velocity flows. Terms in the balance equations (3.5) and (3.6) for flowing droplets and oil-phase saturation use k_{gen}/v_D as a characteristic rate constant. However, the results shown in Figure 3.10 indicate that k_{gen}/d_e may explain the rate of emulsion generation better than k_{gen}/v_D because of it having less dependency on the size of

sand-grains. The empirical correlation for k_{gen}/d_e and $N_{tr,de}$ can be constructed from the data presented here:

$$\frac{k_{gen}}{d_e} = 2.50 \times 10^3 N_{tr,de}^{0.85} \tag{3.20}$$

where k_{gen} is in units of ppmv/m and d_e is in units of μm. Based on these empirical correlations in Eq. (3.19) and (3.20), the sizes and rates of emulsion droplet generation can be predicted only by the grain size and trapping number (both of which are known for a given reservoir and injection conditions). The results were shown in Figure 3.11.

The concentrations of generated emulsions change with time and location in the sand-pack. Figure 3.12 shows the concentrations of generated emulsions in samples taken at 0 to 2 PV, 2 to 4 PV, and 4 to 6 PV. They are shown for various fluid velocities, and in all the cases, the concentration of emulsion generation decreased with time. The concentrations along with the sand-pack lengths are shown in Figure 3.13. It was evident that the generated concentration increased with the length of the sand-pack. The proportionality of concentration with lengths, however, was not constant for all the cases with different velocities. This was primarily due to the experimental design and procedures. Samples were taken sequentially from the outlet to the inlet, hence the rate of generation may have been changed while samples were taken between samplings. A different design and procedure would be required to minimize this effect.

3.5 RATE OF FILTRATION OF INJECTED O/W EMULSIONS IN POROUS MEDIA

3.5.1 Initial Filtration Coefficient and Filtration Mechanisms

The degree of filtration of O/W emulsion droplets through a porous medium is an important factor in predicting the injectivity decline during produced water re-injection. The degree of filtration can be quantified by the filtration coefficient. In this section, the

filtration coefficient of synthetic O/W emulsion droplets in sand-packs was measured. No oil saturation was created in the porous medium to measure the filtration coefficient in the clean sands. Approaches to measure the filtration coefficient in the previous chapter were also used for oil-droplet filtration. In the previous chapter, the velocity conditions of interest were that of frac-packs, which have a superficial velocity of 1 to 10 cm/s. For the oil-droplet filtration, the fluid velocity conditions in the near-well or near-fracture are considered. In this case, the superficial velocity is 0.1 to 1 cm/s.

Synthetic O/W emulsion droplets with concentrations between 30 to 50 ppmv were pumped into sand-packs (filtration cell). Concentrations at the inlet and outlet of the sand-pack were measured. Measurements were taken at various times, and the change in filtration coefficient was extrapolated to the start time to get the initial filtration efficient at t=0. Experiments were repeated at various fluid velocities with various sand-grain sizes so that the initial filtration coefficients can be calculated for respective conditions. The results were compared with predictions by Rajagopalan & Tien (1976)'s model as in Figure 3.14.

The initial filtration coefficients measured at superficial velocities between 0.1 to 1cm/s were comparable to model predictions. Generally, they were slightly lower than the model predictions, but they were in good agreement within the experimental conditions. The reason that measurements were lower than the predictions could be the detachment of emulsion droplets that were previously deposited. Also, importantly the initial filtration coefficient exhibited less dependency on the fluid velocity in the filtration through small sands. In larger grain sands, the initial filtration coefficient decreases with the increasing fluid velocity; however, this behavior diminishes as the grain size decreases. There are models to predict the initial filtration coefficient in Happel's cell, as explained in the previous chapter. These models predict the interception mechanism, but straining is not

predicted. In this work, it was postulated that the portion of emulsion deposition by a straining mechanism occurs at a higher degree through the small size of sands, and the dependency on fluid velocity was weaker for filtration in smaller grains.

It can be estimated from Buret et al. (2010) that interception is dominant when d_g/d_p is larger than 50, and straining is dominant when d_g/d_p is smaller than 15. In sand-packs with a sand diameter of 0.166mm, based on Buret's explanation, approximately over 10 μm oil droplets will be deposited by the straining mechanism. With a typical oil droplet size distribution of produced water, portions of droplets over 10 μm are not negligible. With the current synthetic oil droplets, a larger portion of droplets in 0.166 mm sands can be deposited by the straining mechanism. Hence, in Figure 3.14, the dependency of the initial filtration coefficient on the fluid velocity may vary with grain sizes. This indicates that under the current experimental conditions, interception and straining are the primary mechanisms in large and small sand sizes respectively.

3.5.2 Filtration Along Filter Depth

Concentrations of oil droplets at various filter-depths normalized to the inlet concentration (C_{eff}/C_{in}) were shown for different filtration times in Figure 3.15. When the filtration coefficient is constant throughout the sand-pack, C_{eff}/C_{in} declines exponentially along the depth. This behavior was observed in the filtration of solid particles in the previous chapter. In the filtration of oil droplets here, the exponential decline of the concentration ratio along the depth was observed; however, the decline exponent was not uniform. The decline was higher near the inlet, indicating higher deposition near the inlet. This may be caused by different deposition mechanisms. Near the inlet, straining and interception may occur simultaneously to increase the degree of filtration. Another possibility is that deposited oil droplets may detach in the middle of sand-packs. Further research is needed to explain this behavior, but this observation indicates that the filtration

of oil droplets is different when compared to the filtration of solid particles.

3.5.3 Change in Filtration with Time

The effect of previous deposition on the change in filtration coefficient was investigated by measuring the filtration coefficient as it changes with time. Measurements conducted for sand-packs of various sizes are plotted in Figure 3.16. In Figure 3.16a, it was observed that the filtration coefficient declines with time for 0.293 and 0.539 mm sand-grains. This dependency on previous deposition was also observed in the filtration of solid particles in the previous chapter. The same filter medium was used here, and similar behavior was observed. The dependency on time is subject to change depending on the filter medium, particle types and other flow conditions. The filtration conditions used for oil droplets here led to similar behavior in terms of dependency on pre-existing deposits.

When smaller sand-grain was used for the medium, different behavior was observed. As can be seen in Figure 3.16b, the filtration coefficient in the sand-pack with d_g=0.166mm decreased to a negative value after initially showing a high degree of filtration. This indicates that the outlet concentration was larger than the inlet concentration. The initially deposited droplets accumulated to construct a larger oil ganglia than the suspended droplets. These oil ganglia can eventually create small oil droplets by a snap-off mechanism after being continuously exposed to high velocity flows. In smaller sand-grains, this mechanism has a higher chance of occurring. More initial deposition can occur by straining rather than by interception in sand packs with smaller grains. This can initiate the detachment of oil droplets. This is more likely to happen in smaller grains.

3.5.4 Detachment of Oil Droplet During Filtration

The observation of the detachment of emulsions from pre-deposited droplets was investigated further. In the previous chapter, the concept of the collection efficiency was

introduced. The filter collection efficiency shows the ratio of deposition for injected droplets of different sizes. In Figure 3.17, the filter collection efficiencies at the beginning of filtration were compared for various linear velocities for a sand size of d_g=0.293mm. The large size of droplets over 10 μm injected were almost completely captured through the filter. Smaller size droplets were captured less. With increasing fluid velocity, the collection efficiencies decreased, and this was consistent with the initial filtration coefficient decreasing as fluid velocity increased. This trend of collection efficiency remains the same with increasing velocity, which implies that the mechanism of filtration is primarily interception under this condition. This is the same behavior that was observed in the filtration of solid particles in the previous chapter. In Figure 3.18, the collection efficiency for the same grain size at various filtration times is shown. This figure shows a clear trend that the collection efficiency decreases with filtration time. This is consistent with the previous observation that the filtration coefficient decreases with time.

The same filtration experiments were conducted with a smaller sand-grain size (d_g=0.166mm). The collection efficiencies of the filter at the initial time with various velocities were shown in Figure 3.19, and the change in the collection efficiency with filtration time at a constant velocity is shown in Figure 3.20. The initial collection efficiency at low flow rates shows the same trend as in the larger grain experiments; however, the collection efficiencies at higher velocities show a dip in the trend for larger size droplets between 20 and 30 μm. This is caused by a high concentration of large droplets in the outlet of the sand-pack, indicating that detachment can occur simultaneously with the filtration process under high-velocity conditions.

This was also observed in the trend of collection efficiencies over time. In Figure 3.20, the net generation of emulsion is higher at later times of filtration. The collection efficiencies for larger droplet sizes show negative values which indicate that pre-deposited

oil droplets are detached at later times. Experiments were not continued for longer amounts of time to verify if this behavior continued. However, within the experimental time shown above, the detachment behavior was more noticeable with time. The droplet distributions at the inlet and outlet were compared in Figure 3.21. This corresponds to collection efficiencies shown for PV=189 and 946 in Figure 3.20. The detached droplet size distribution curves are wide in their shapes, but a substantial portion of droplets between 20 and 30 μm were detached. This size range is comparable to the pore throat size of this specific sand grain.

3.5.5 Permeability Decline During Filtration of Oil Droplets

Permeability decline caused by filtration of oil droplets was investigated in this section. Pressure drops along the sand-pack were measured during the filtration processes. The permeability ratio was calculated by the pressure drop assuming Darcy's law in the sand-pack. Dilute solutions of oil droplets were injected into sand-packs, some saturated with only water and some with a residual oil saturation. The results of an extensive series of permeability decline experiments can be found in Mendez (1999). This study differs from Mendez's work in that it uses sand-packs that contain large-size grains as compared to the actual rock cores studied in Mendez's work. This difference in the experimental conditions caused different results, which can be understood based on different primary filtration mechanisms.

With sand-packs initially saturated with only water, the permeability decline ratios measured in this work are shown in Figure 3.22. Permeabilities declined to 70 to 90 percent of their initial values within about 300 pore volumes of injection. In sand-packs with smaller grains, the permeability declined more rapidly due to the higher filtration coefficient (Figure 3.22a). When fluid velocities were varied with d_g=0.096mm sands (Figure 3.22b), the permeability decline did not show a significant difference. It was

previously shown that the straining mechanism occurs more significantly in sand-grains of this size, and the filtration coefficient is not affected by fluid velocities.

When sand-packs were saturated with residual oil saturation, permeability declines were less than those of water-saturated sand-packs, as in Figure 3.23. Under high velocity conditions, the permeability did not decline and maintained its initial value. When interception is the primary mechanism of droplet deposition, the contribution of droplet generation and subsequent deposition of generated oil droplets does not significantly reduce the permeability. Instead, rates of deposition and generation of droplets are balanced to maintain a constant permeability for the sand-packs.

Both mechanisms of straining and interception were considered to contribute to the permeability decline within the experimental conditions in this work. However, the permeability decline observed here is not as significant as what was observed by Mendez (1999) where the permeability declines were more than 50% of the initial permeability values. The difference is that the porous medium had a relatively higher permeability in this study. Because of this, the contribution of the interception mechanism was higher. In Mendez (1999)'s experiment, however, straining was the primary mechanism of deposition. It was shown that the threshold of permeability that can lead to a very rapid decline in permeability is around 1 Darcy, assuming typical conditions of produced water re-injection. In Figure 3.24, the typical trends of permeability decline in lower permeability cores by Mendez (1999) were compared. In lower permeability cores, especially with residual oil saturation, the permeability declined rapidly.

3.6 CONCLUSION

In this chapter, the flow of O/W emulsions in porous media was investigated, with an emphasis on near-well or near-fracture conditions. The rate of generation and filtration of oil droplets when a porous medium is saturated with water or residual oil were

experimentally measured. The impacts of fluid velocity and sand-grain sizes on the rate of droplet generation and filtration were presented. Some of important findings in this chapter are:

- An experimental setup was designed to measure rates of generation and filtration of dilute oil-droplet solution, and experiments were conducted under flow conditions encountered in near-well or near-fracture regions.
- A trapping number using the diameter of generated droplets characterizes the capillary desaturation process well.
- The size of generated oil droplets under high velocity conditions is primarily a function of the trapping number.
- The rate of oil-droplet generation under high velocity conditions is primarily a function of the trapping number and the size of the generated droplet.
- Smaller droplets are generated when the sand grain size is smaller. The size of the generated oil droplets is a function of the capillary number and the sand grain size and can be estimated by empirical correlations presented in this work.
- Straining is the primary filtration mechanism in porous media with low permeabilities (Lower than 1 Darcy). In larger sand-grains (higher permeability sand packs and frac packs), interception is the primary mechanism for trapping, for the typical size of oil-droplets in produced water.
- In the filtration processes under high-velocity conditions with small sand-grain porous media containing oil, a high degree of droplet generation occurs simultaneously with filtration.
- The predictive model for the initial filtration coefficient can be applied to predict the rate of filtration of oil droplets, especially when interception is the primary filtration mechanism.

- Permeability decline occurs more rapidly in flow conditions when straining becomes the more important filtration mechanism.

Based on experimental observations presented here, our understanding of the flow of O/W emulsion droplets in porous media with a residual oil saturation has been improved substantially. These findings and empirical relations will be used in models for injection wells into which produced water is being injected.

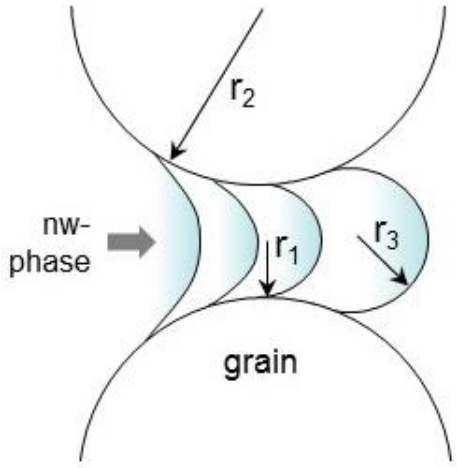

Figure 3.1: Schematic diagram of snap-off mechanism.

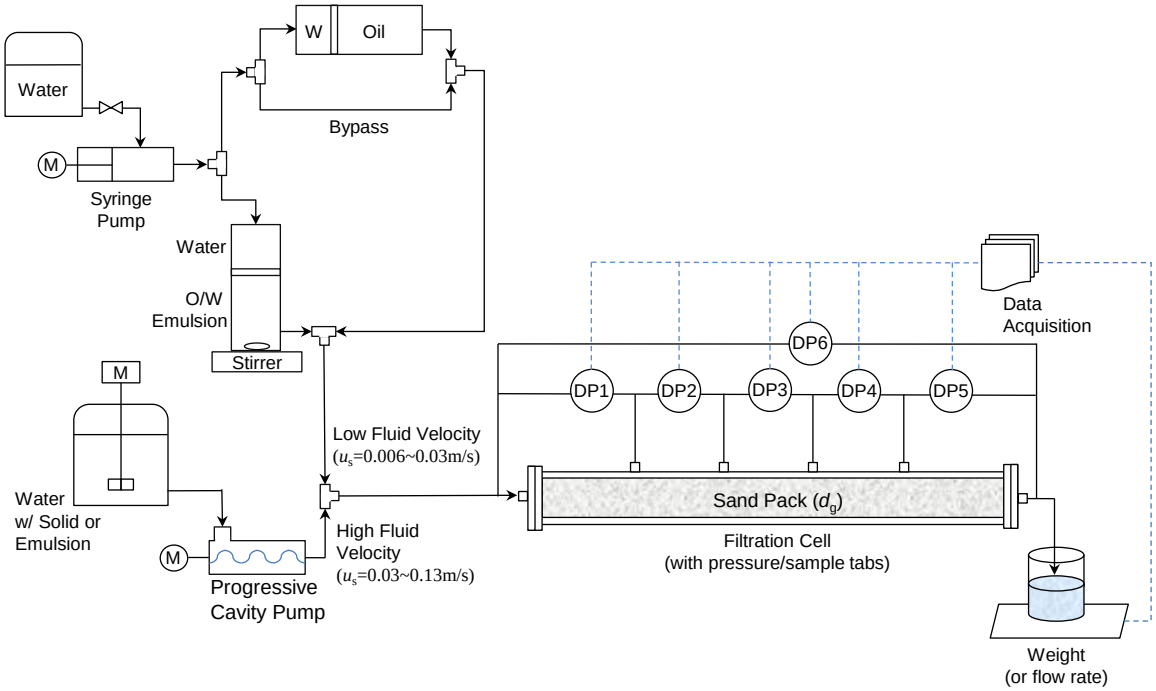

Figure 3.2: Experimental setup for capillary desaturation and filtration of O/W emulsion droplets.

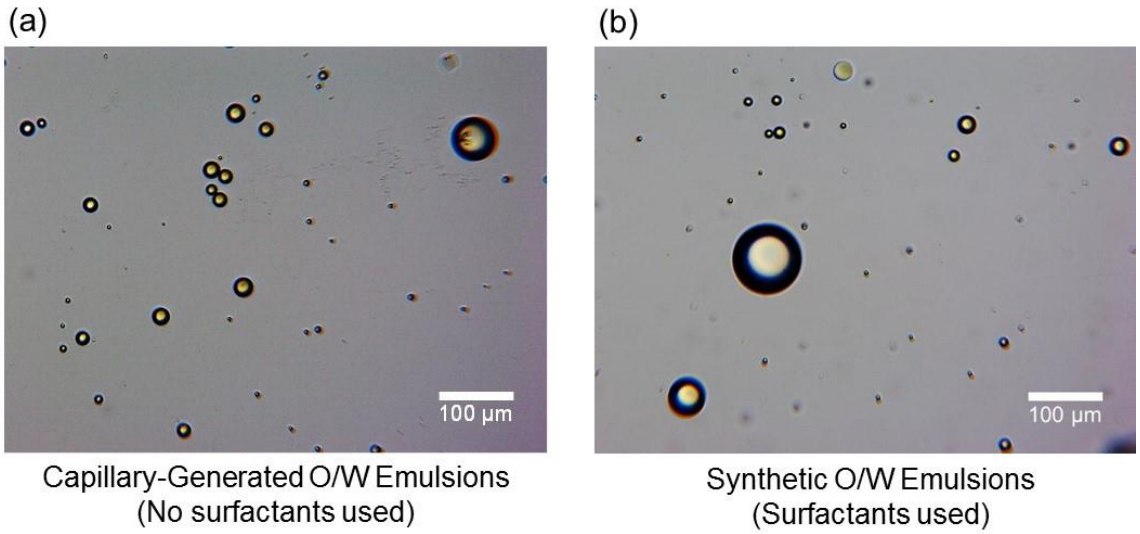

Figure 3.3: Microscope images of (a) O/W emulsion droplets created by high capillarity. (b) Synthesized O/W emulsion droplets.

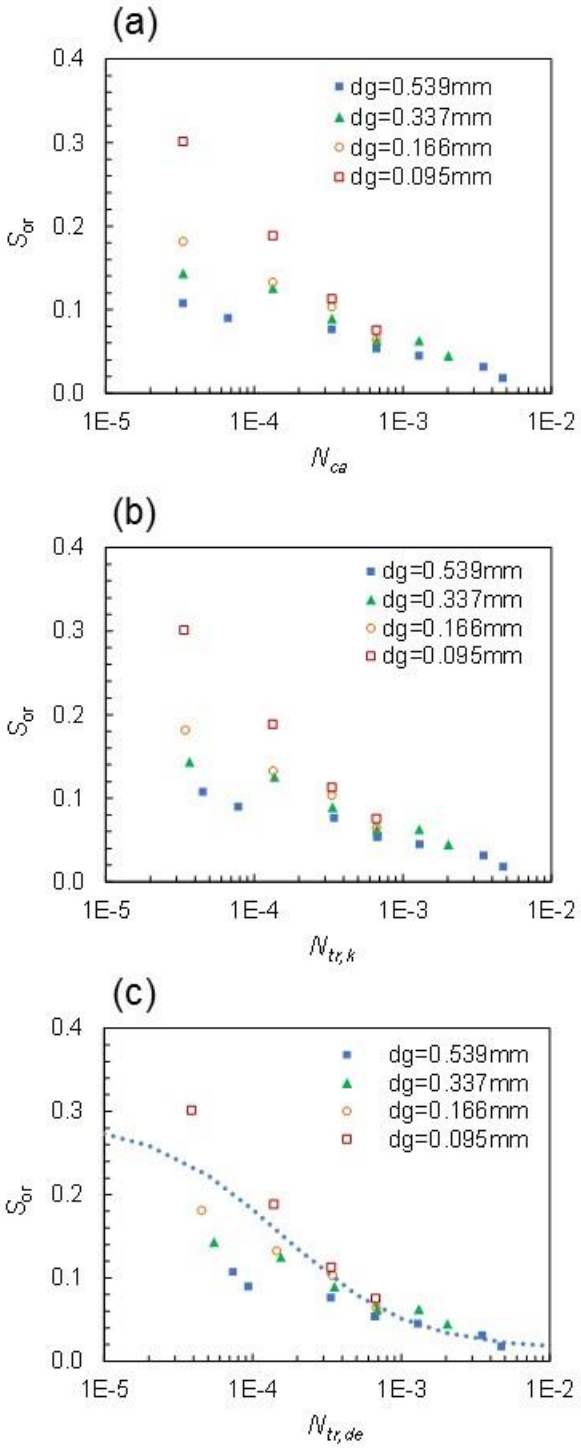

Figure 3.4: Capillary desaturation curve. Residual oil saturations are plotted to: (a) Capillary number, (b) Trapping number defined with permeability, and (c) Trapping number defined with emulsion droplet diameter.

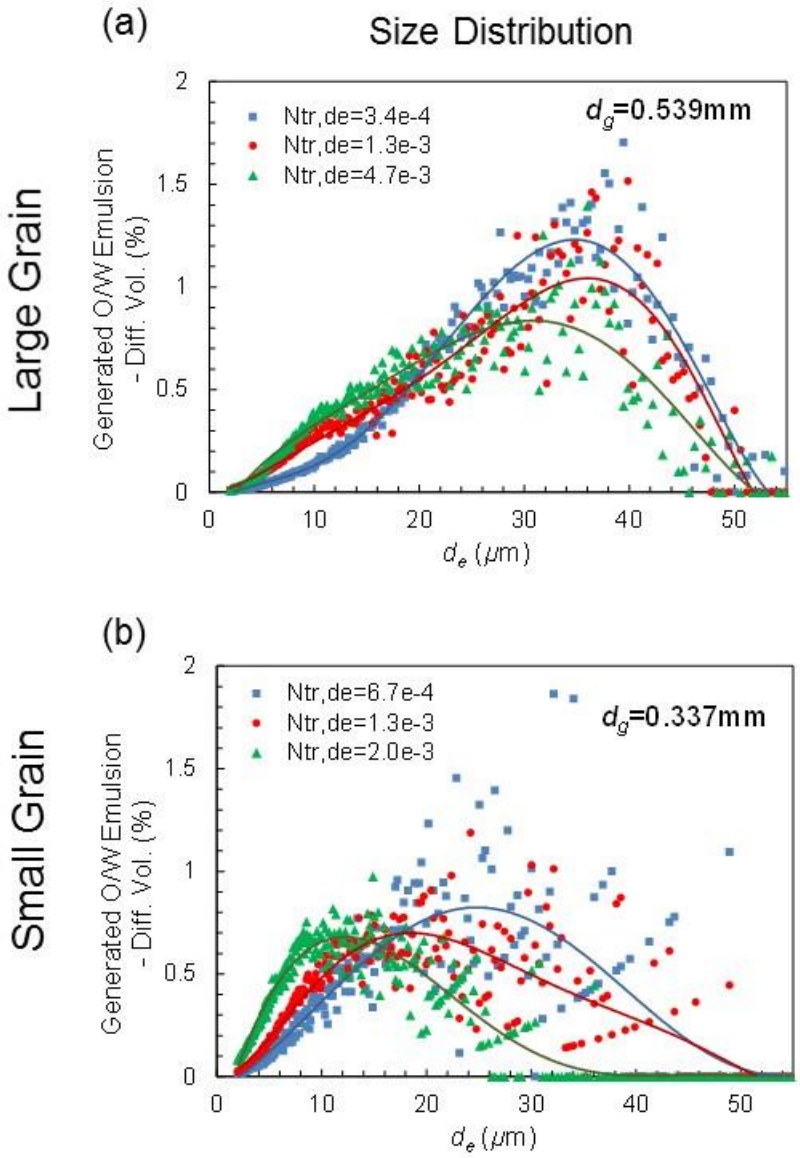

Figure 3.5: Size distribution of capillary-generated emulsion droplet diameter. The y-axis value is the differential volume percentage for corresponding droplet diameter. Experiments are with sand grain sizes of (a) d_g=0.539mm, (b) d_g=0.337mm.

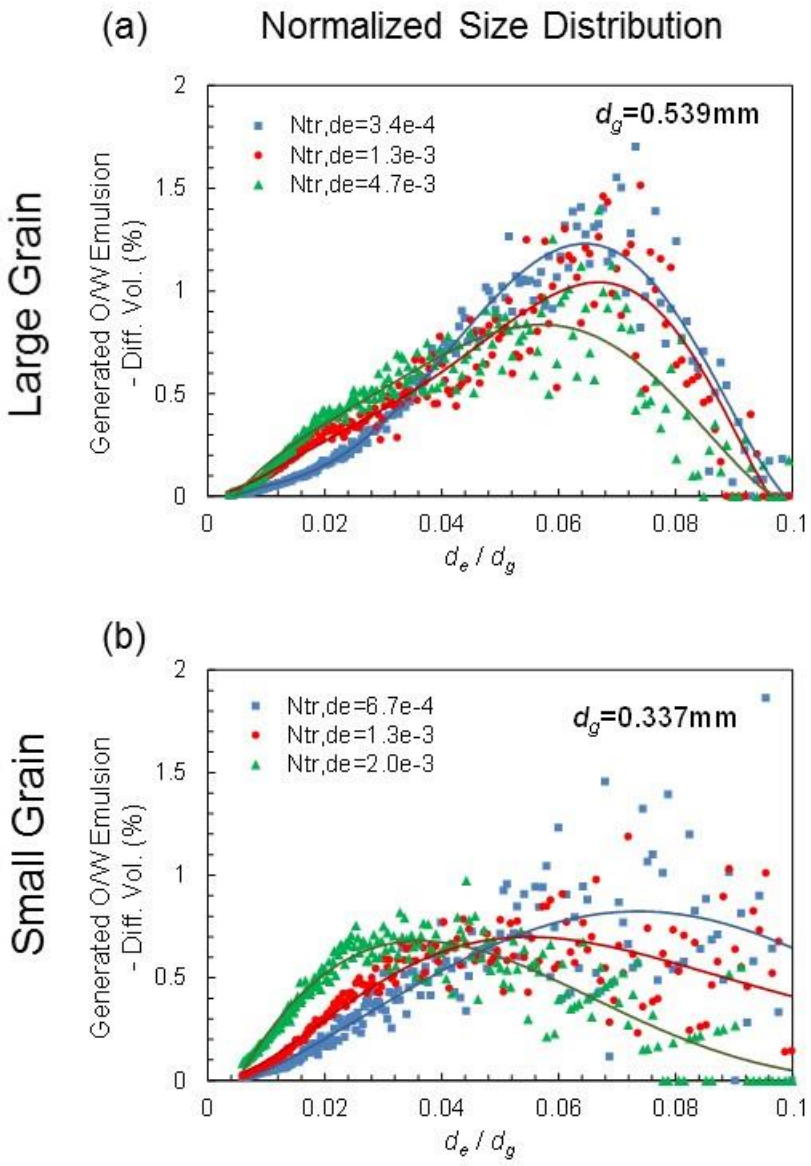

Figure 3.6: Normalized size distribution of capillary-generated emulsion droplet diameter divided by sand-grain sizes. The y-axis value is the differential volume percentage for the corresponding droplet diameter. Experiments are with sand-grain sizes of (a) d_g=0.539mm, (b) d_g=0.337mm.

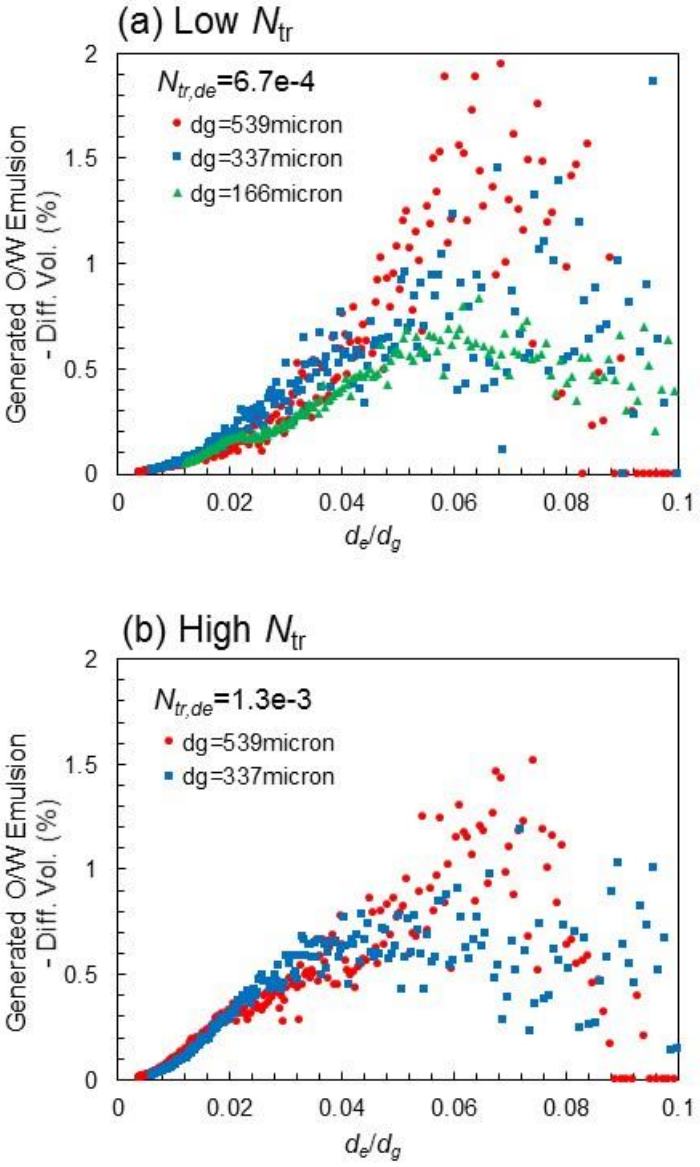

Figure 3.7: Size distributions in differential volume percentage of generated emulsion droplets. Distributions using various sand-grains were compared at (a) low, and (b) high trapping number conditions.

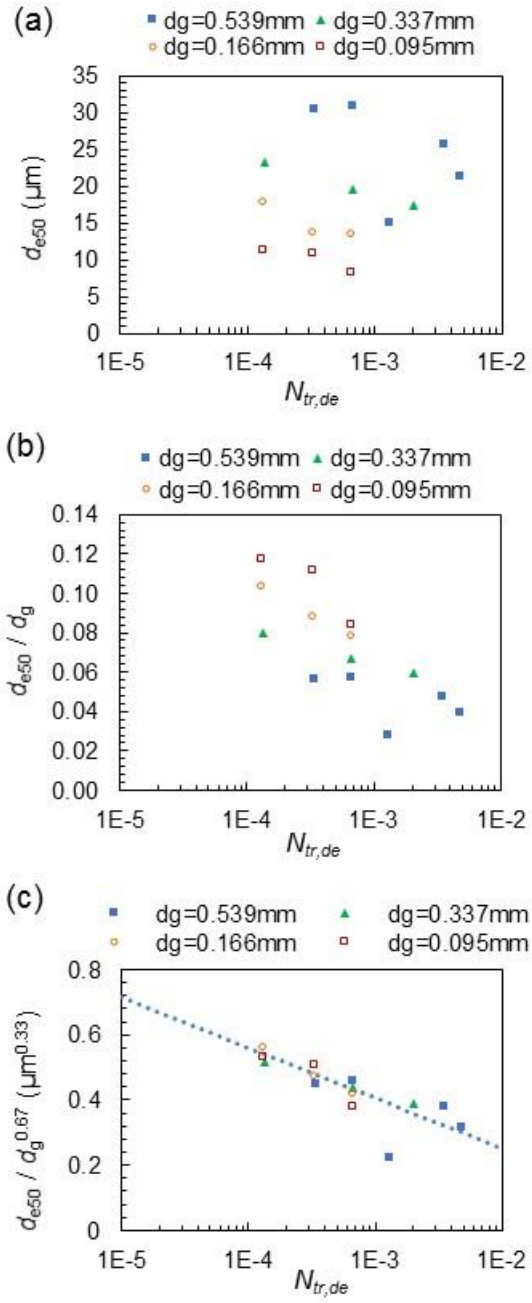

Figure 3.8: (a) Generated emulsion sizes in 50 percentile diameter of differential-volume distribution. (b) d_{e50} normalized by sand-grain sizes. (c) d_{e50} normalized by $d_g^{0.67}$.

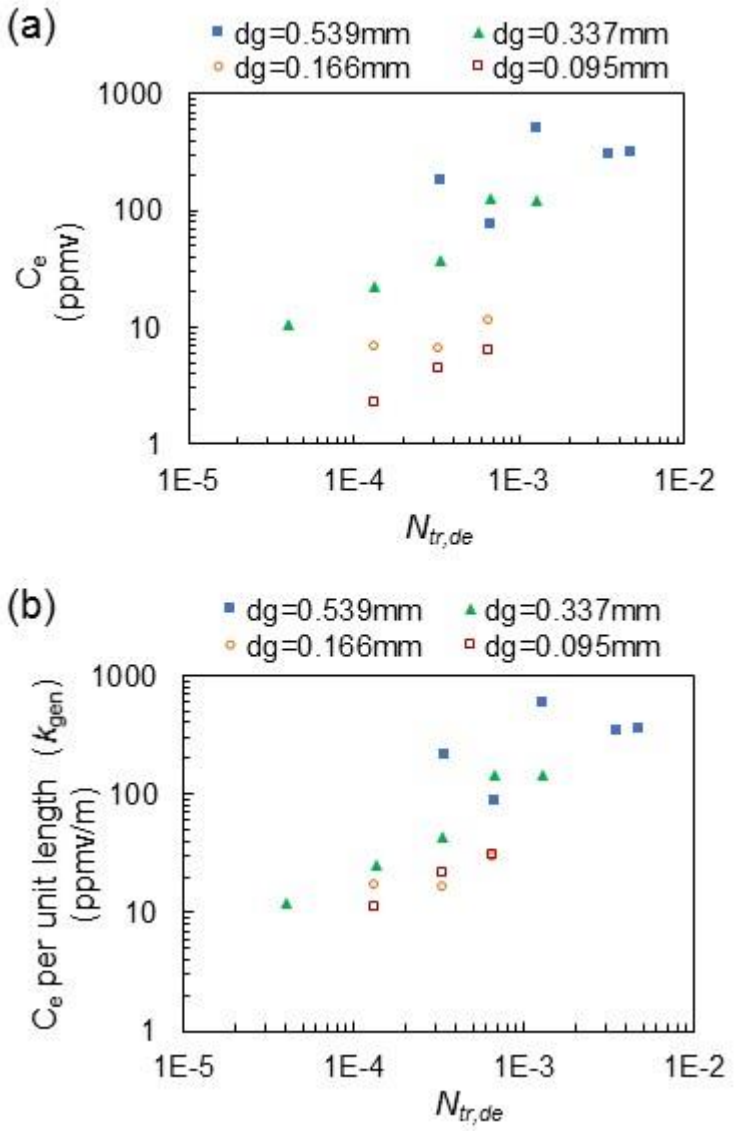

Figure 3.9: (a) Concentration of generated emulsion droplets (C_e) in ppmv. Average of measurements of samples from 0 to 6 PV. (b) Emulsion generation rate constant ($k_{gen}=C_e/L$).

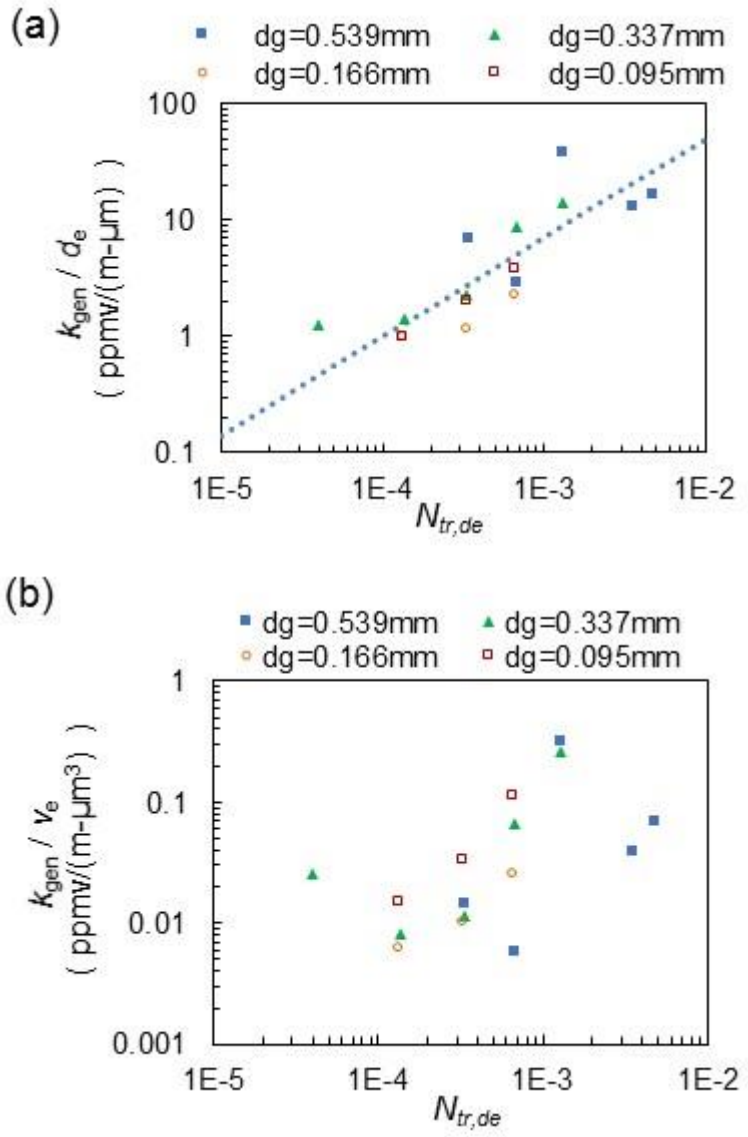

Figure 3.10: (a) k_{gen} divided by measured emulsion droplet diameter.
(b) k_{gen} divided by measured emulsion droplet volume.

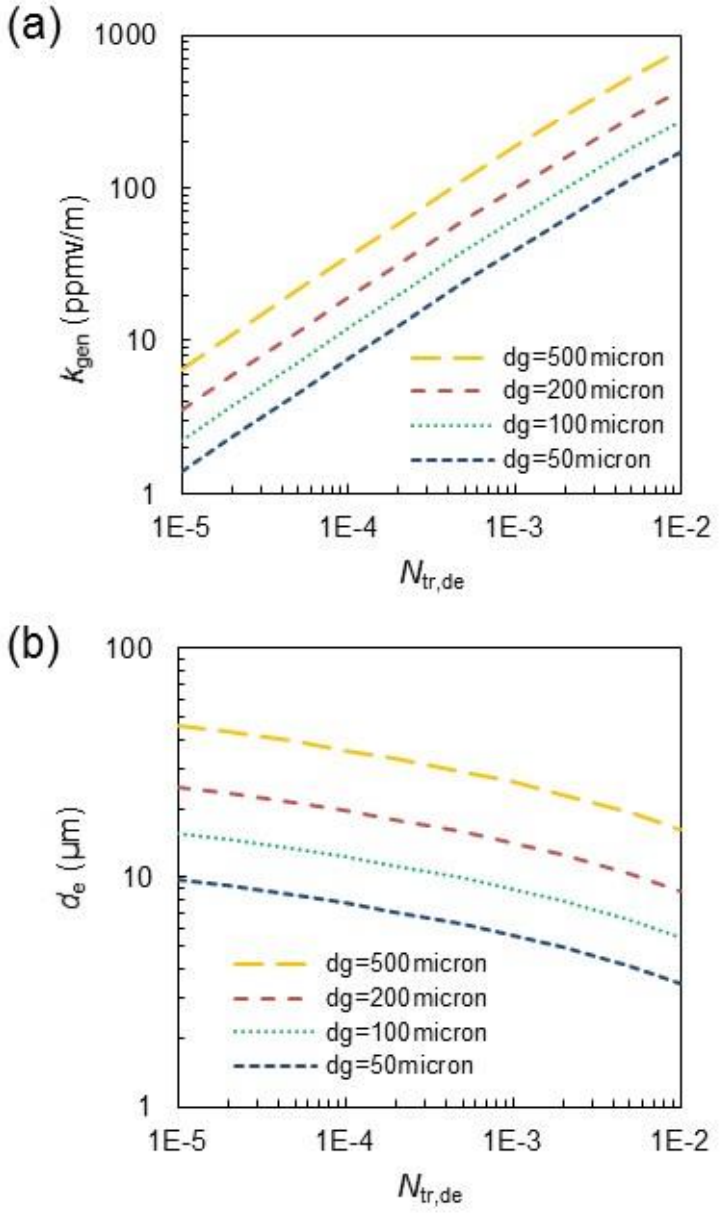

Figure 3.11: (a) Rate constant of emulsion generation based on zeroth-order rate expression, (b) Size of generated emulsion droplet.

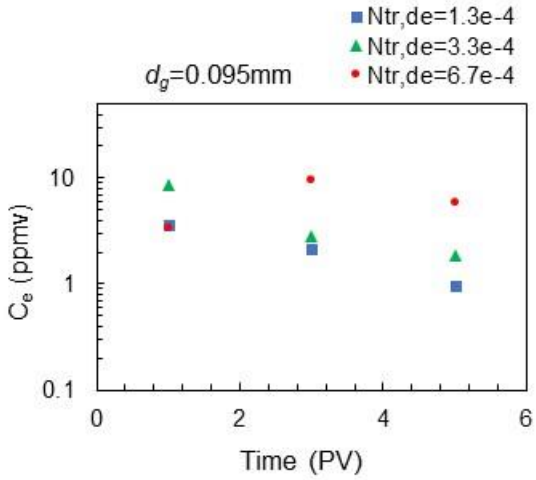

Figure 3.12: Changes in concentrations of generated emulsions with time. Time (PV) was measured after the flow stabilization.

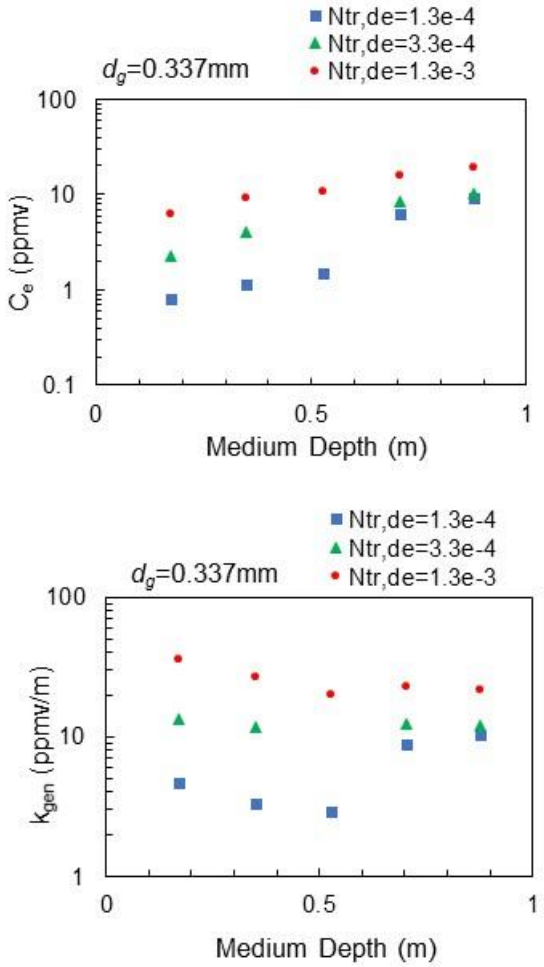

Figure 3.13: (a) Concentration of generated emulsions along the depth of the medium (sand-pack), (b) Rate constants of emulsion generation along the depth of the medium.

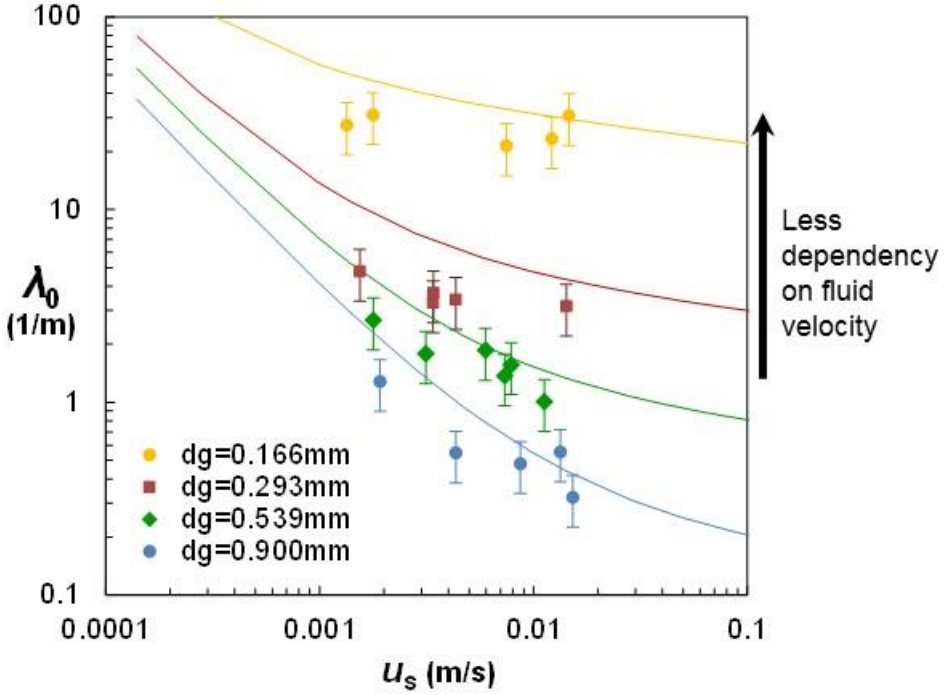

Figure 3.14: Initial filtration coefficient of dilute O/W emulsion droplets through sand-packs. Lines are predictions by Rajagopalan & Tien (1976)'s model for each sand-grain sizes.

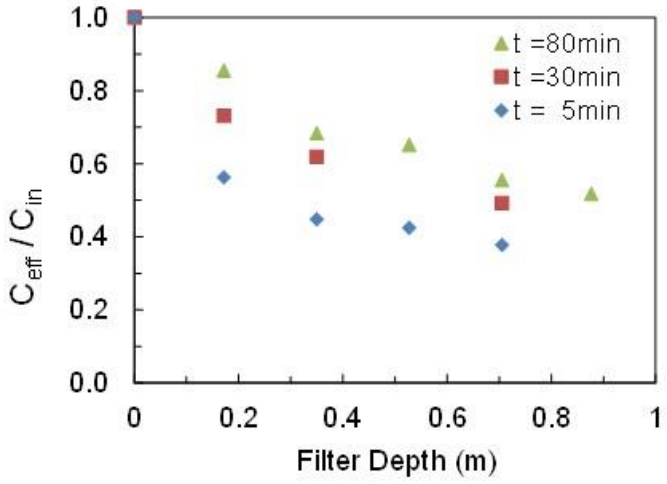

Figure 3.15: Ratio of concentrations at outlet to inlet dilute O/W emulsion flow along the depth of sand-pack.

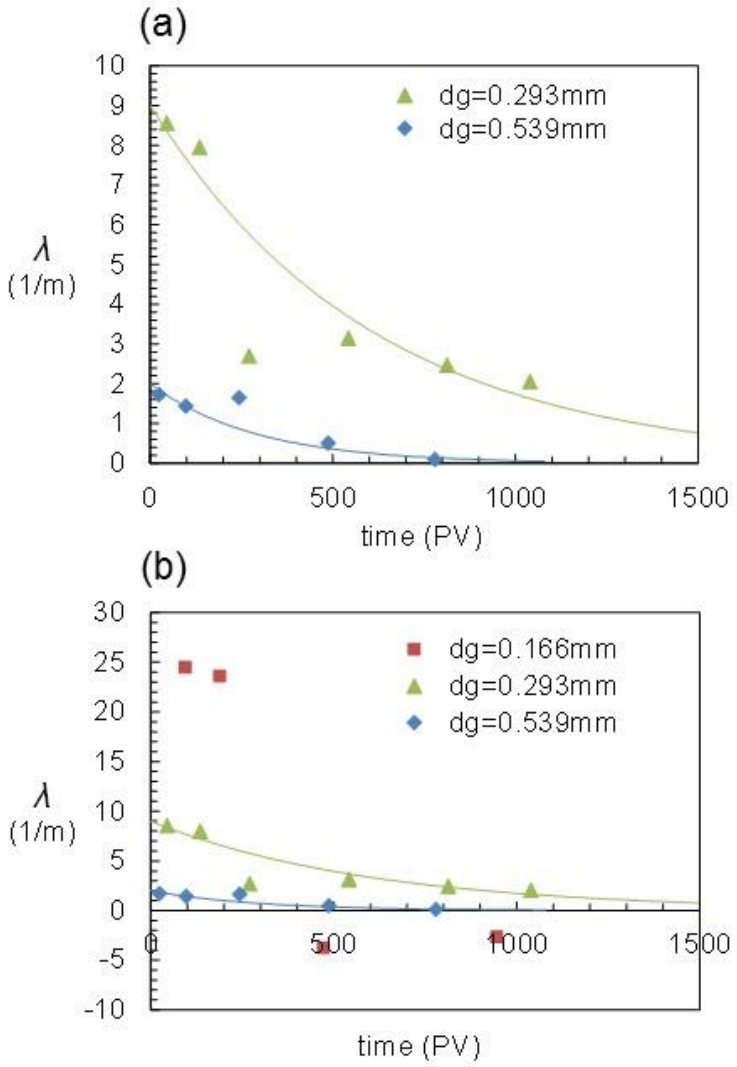

Figure 3.16: Effect of deposition on filtration coefficient. Changes in filtration coefficient are shown with time (injected pore volumes) for different sand-grain sizes. (a) d_g=0.293 and 0.539 mm, (b) d_g=0.166 mm is shown additionally with grains in (a), and it shows the net generation of emulsions.

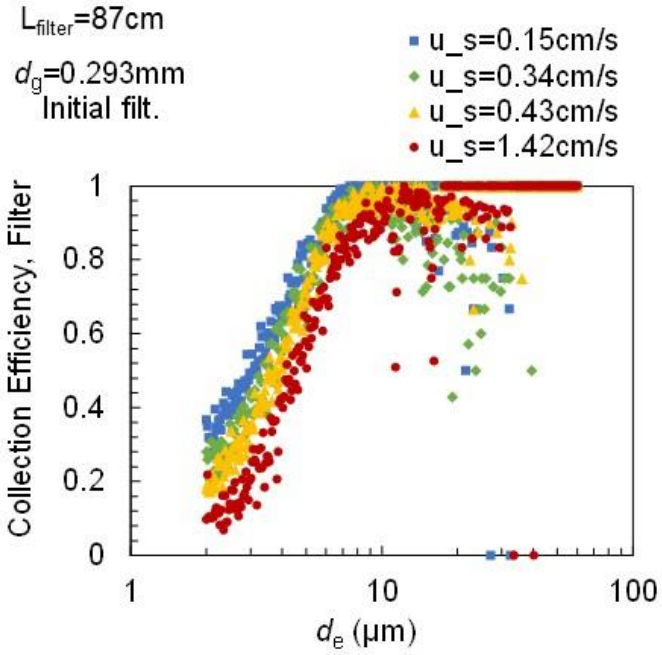

Figure 3.17: Collection efficiency of sand-pack for various sizes of emulsion droplets at different fluid velocities (d_g=0.293mm, samples were taken at the beginning.).

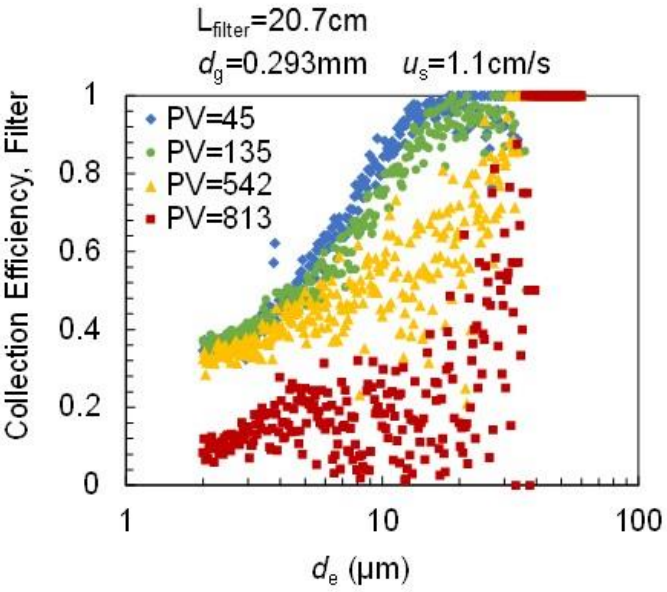

Figure 3.18: Collection efficiency of sand-pack with various injected pore-volumes in larger grain size (d_g=0.293mm).

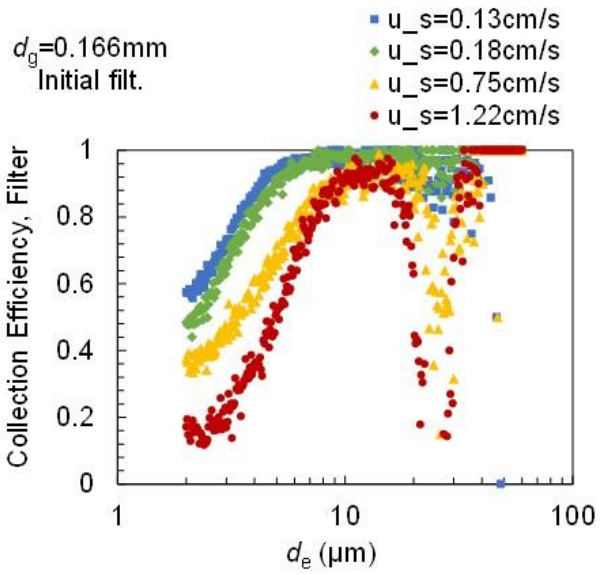

Figure 3.19: Collection efficiency of sand-pack for various size of emulsion droplets at different fluid velocities (d_g=0.166mm, samples were taken at the beginning).

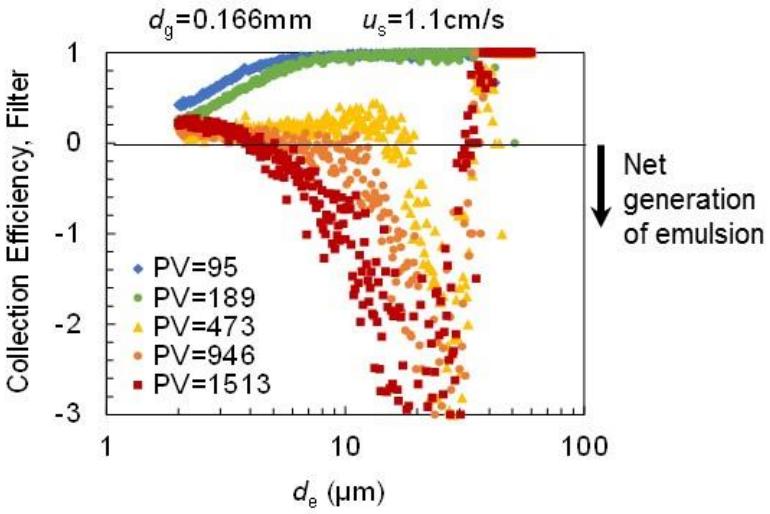

Figure 3.20: Collection efficiency of sand-pack with various injected pore-volumes in smaller grain size (d_g=0.166mm).

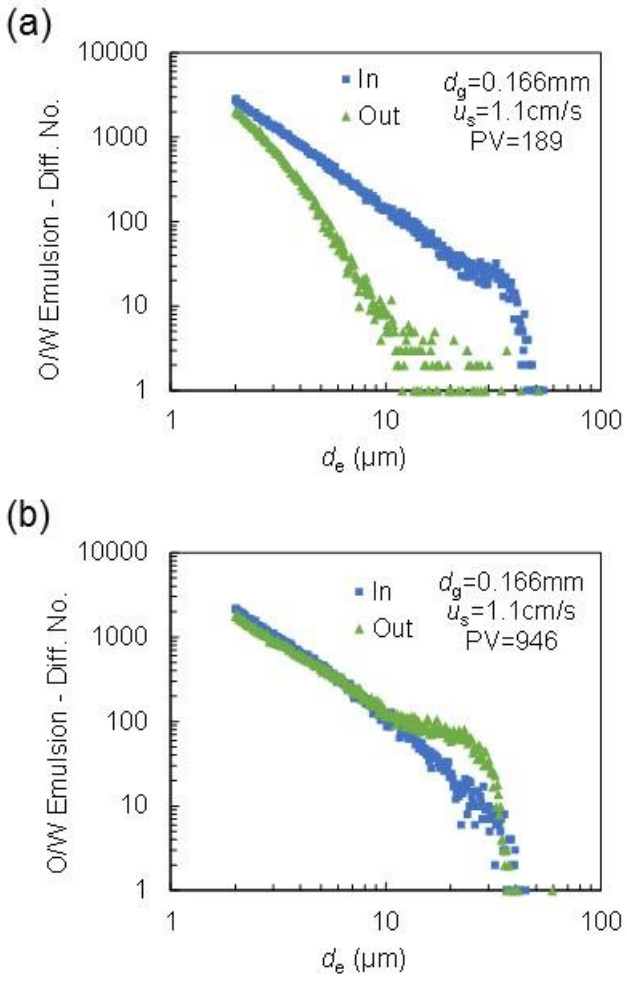

Figure 3.21: Emulsion size distributions in inlet and outlet emulsion solutions. (a) at early stage of filtration (PV=189), (b) at late stage of filtration (PV=946).

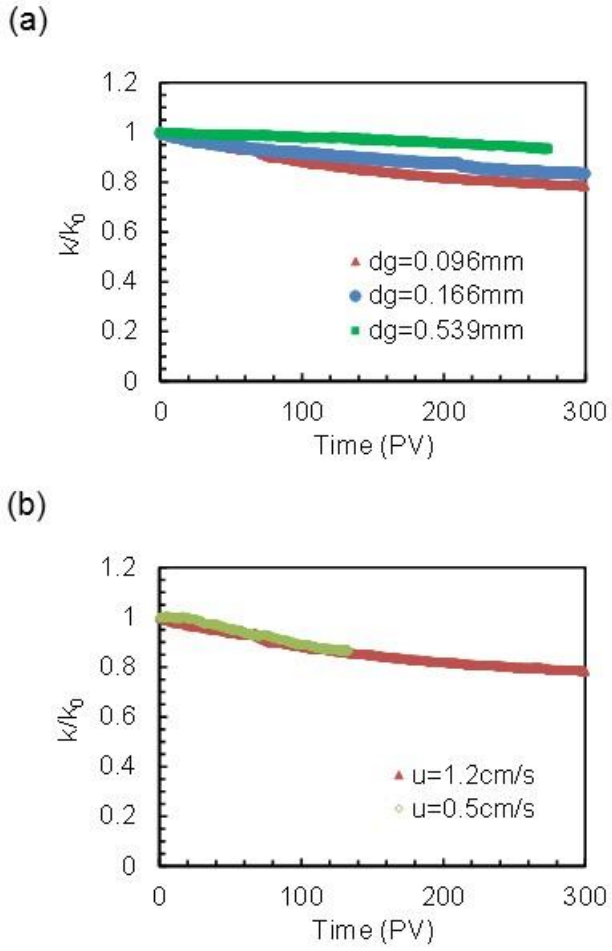

Figure 3.22: Permeability decline by filtration of oil droplets. $S_{o,init}$=0. (a) effect of grain size (u_s=1.2cm/s), (b) effect of fluid velocity (d_g=0.096mm).

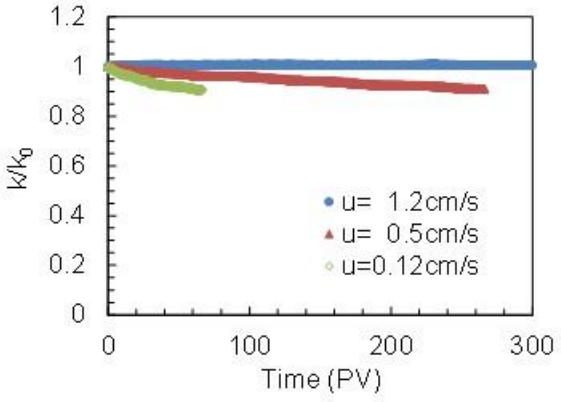

Figure 3.23: Permeability decline during filtration of dilute O/W emulsions at various fluid speed. (d_g=0.166mm and $S_{o,init}$=S_{or})

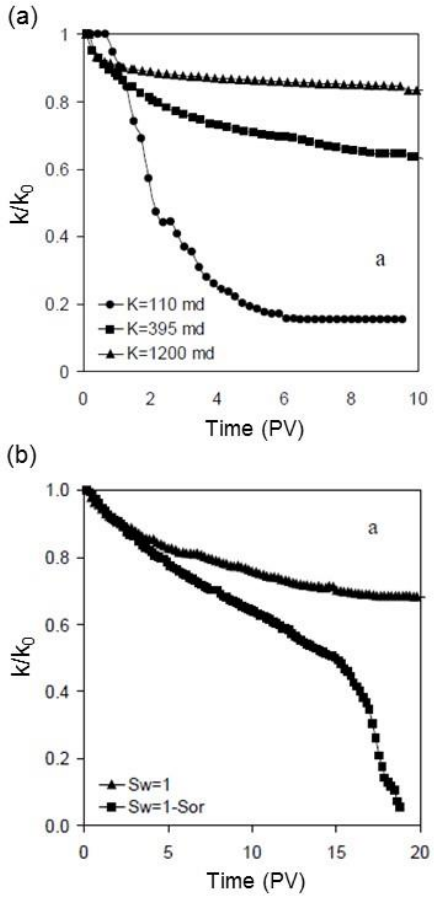

Figure 3.24: Permeability decline by injection of O/W emulsion droplets in lower permeability cores. (a) effect of core permeability, (b) effect of initial saturation (from Mendez, 1999).

Nomenclature

C_{eff} = Concentration of emulsion droplets, effluent
C_{oin} = Concentration of oil droplets in injection water
C_o^t = Concentration of trapped oil droplets
d_e = Diameter, emulsion, L^1, m
d_g = Diameter, grain, L^1, m
f_o = Fractional flow of the oil phase
k = Permeability, L^2, Darcy
k_d = Permeability decline ratio, −
k_{gen} = Rate constant for droplet generation
N_{bo} = Bond number, −
N_{ca} = Capillary number, −
N_{tr} = Trapping number, −
p = Fraction of coalesced droplets which becomes the residual oil phases among the trapped droplets
ΔP = Pressure drop, $mL^{-1}t^{-2}$, Pa
r_{gen} = Rate of generation of oil droplets
S^h_{or} = Residual oil saturations at high trapping number, −
S^l_{or} = Residual oil saturations at low trapping number, −
S_o = Oil saturation
S_{or} = Residual oil saturation
T = Empirical parameter in residual saturation equation
u_s = Superficial (Darcy) velocity, L^1t^{-1}, m/s
v_D = Volume of a single oil droplet
α = Empirical parameter in filtration coefficient change with deposition
β = Damage factor in permeability damage, −
λ = Filtration coefficient, L^{-1}, m^{-1}
λ_0 = Filtration coefficient of clean bed, L^{-1}, m^{-1}
μ = Viscosity, $mL^{-1}t^{-1}$, Pa·s
ρ = Density, fluid, mL^{-3}, $kg \cdot m^{-3}$
σ = Interfacial tension, m^1t^{-2}, dyne/cm
σ_{gen} = Specific droplet generation
Φ = Flow potential accounting for gravity, $mL^{-1}t^{-2}$, Pa
ϕ = Porosity, −

References

Al-Abduwani, F. A. H., W.M.G.T. van, den, & Currie, P. K. 2001. Visual Observation of Produced Water Re-Injection Under Laboratory Conditions. Paper SPE 68977 presented at the SPE European Formation Damage Conference, 21-22 May 2001, The Hague, Netherlands. http://dx.doi.org/10.2118/68977-MS

Ali, M., Currie, P. K., & Salman, M. 2007. Permeability Damage Due to Water Injection Containing Oil Droplets and Solid Particles at Residual Oil Saturation. Paper SPE 104608 presented at the SPE Middle East Oil and Gas Show and Conference, 11-14 March 2007, Kingdom of Bahrain. http://dx.doi.org/10.2118/104608-MS

Ali, M., Currie, P., & Salman, M. 2009. The Effect of Residual Oil on Deep-Bed Filtration of Particles in Injection Water. *SPE Production & Operations*, **24** (1): 117–123. http://dx.doi.org/10.2118/107619-PA

Al-Riyamy, K., & Sharma, M. 2004. Filtration Properties of Oil-in-Water Emulsions Containing Solids. *SPE Drilling & Completion*, **19** (3): 164–172. http://dx.doi.org/10.2118/89015-PA

Alvarado, D. A., & Marsden Jr., S. S. 1979. Flow of Oil-in-Water Emulsions Through Tubes and Porous Media. *Society of Petroleum Engineers Journal*, **19** (6): 369–377. http://dx.doi.org/10.2118/5859-PA

Buret, S., Nabzar, L., & Jada, A. 2008. Emulsion Deposition in Porous Media : Impact on Well Injectivity. Paper SPE 113821 presented at the Europec/EAGE Conference and Exhibition, 9-12 June 2008, Rome, Italy. http://dx.doi.org/10.2118/113821-MS

Buret, S., Nabzar, L., & Jada, A. 2010. Water Quality and Well Injectivity: Do Residual Oil-in-Water Emulsions Matter? *SPE Journal*, **15** (2): 557–568. http://dx.doi.org/10.2118/122060-PA

Coleman, J. R., & McLelland, W. G. 1994. Produced Water Re-Injection; How Clean is Clean? Paper SPE 27394 presented at the SPE Formation Damage Control Symposium, 7-10 February, Lafayette, Louisiana. http://dx.doi.org/10.2118/27394-MS

Cortis, A., & Ghezzehei, T. A. 2007. On the transport of emulsions in porous media. *Journal of Colloid and Interface Science*, **313** (1): 1–4. http://dx.doi.org/10.1016/j.jcis.2007.04.021

Dalmazzone, C., Noïk, C., Galinat, S., Masbernat, O., et al. 2005. Flow of a Concentrated Oil-Water Dispersion Through a Restriction. Paper BHR-2005-D2 presented at the 12th International Conference on Multiphase Production Technology, 25-27 May, Barcelona, Spain. Retrieved from https://www.onepetro.org/conference-paper/BHR-2005-D2

Darwish, M. I. M., van Boven, P., Hensens, H. C., & Zitha, P. L. J. 1999. Porous Media Flow of Oil Dispersions in Polymers. Paper SPE 56741 presented at the SPE Annual Technical Conference and Exhibition, 3-6 October, Houston, Texas. http://dx.doi.org/10.2118/56741-MS

Devereux, O. F. 1974a. Emulsion flow in porous solids: I. A flow model. *The Chemical Engineering Journal*, **7** (2): 121–128. http://dx.doi.org/10.1016/0300-9467(74)85005-7

Devereux, O. F. 1974b. Emulsion flow in porous solids: II. experiments with a crude oil-in-water emulsion in porous sandstone. *The Chemical Engineering Journal*, **7** (2): 129–136. http://dx.doi.org/10.1016/0300-9467(74)85006-9

Fjelde, I. 2009. Formation Damage Caused by Emulsions During Drilling With Emulsified Drilling Fluids. *SPE Drilling & Completion*, **24** (02): 222–228. http://dx.doi.org/10.2118/105858-PA

Herzig, J. P., Leclerc, D. M., & Goff, P. L. 1970. Flow of Suspensions through Porous Media—Application to Deep Filtration. *Industrial & Engineering Chemistry*, **62** (5): 8–35. http://dx.doi.org/10.1021/ie50725a003

Hofman, J. A. M. H. 1990. *Flow of Dilute Emulsions Through Porous Media*. University of Eindhoven.

Hofman, J. A. M. H., & Stein, H. N. 1991. Permeability Reduction of Porous Media on Transport of Emulsions Through Them. *Colloids and Surfaces*, **61** (4): 317–329. http://dx.doi.org/10.1016/0166-6622(91)80318-I

Hsi, C. D., Dudzik, D. S., Lane, R. H., Buettner, J. W., et al. 1994. Formation Injectivity Damage Due to Produced Water Reinjection. Paper SPE 27395 presented at the SPE Formation Damage Control Symposium, 7-10 February, Lafayette, Louisiana. http://dx.doi.org/10.2118/27395-MS

Jin, L., & Wojtanowicz, A. K. 2014. Development of Injectivity Damage Due to Oily Waste Water in Linear Flow. Paper SPE 168130 presented at the SPE International Symposium and Exhibition on Formation Damage Control, 26-28 February, Lafayette, Louisiana, USA. http://dx.doi.org/10.2118/168130-MS

Lake, L. W. 1989. *Enhanced Oil Recovery*. Prentice Hall Incorporated.

Mendez, Z. 1999. *Flow of Dilute Oil-in-Water Emulsions in Porous Media*. The University of Texas at Austin.

Ochi, J., Detienne, J.-L., & Rivet, P. 2007. Internal Formation Damage Properties and Oil-Deposition Profile Within Reservoirs During PWRI Operations. Paper SPE 108010 presented at the European Formation Damage Conference, 30 May-1 June 2007, Scheveningen, The Netherlands. http://dx.doi.org/10.2118/108010-MS

Pang, S., & Sharma, M. M. 1997. A Model for Predicting Injectivity Decline in Water-Injection Wells. *SPE Formation Evaluation*, **12** (3): 194–201. http://dx.doi.org /10.2118/28489-PA

Peters, E. J. 2012. *Advanced Petrophysics: Volume 2: Dispersion, Interfacial Phenomena/Wettability, Capillarity/Capillary Pressure, Relative Permeability*. Greenleaf Book Group.

Pope, G. A., Wu, W., Narayanaswamy, G., Delshad, M., et al. 2000. Modeling Relative Permeability Effects in Gas-Condensate Reservoirs With a New Trapping Model. *SPE Reservoir Evaluation & Engineering*, **3** (02): 171–178. http://dx.doi.org /10.2118/62497-PA

Rajagopalan, R., & Tien, C. 1976. Trajectory Analysis of Deep-Bed Filtration with the Sphere-in-Cell Porous Media Model. *AIChE Journal*, **22** (3): 523–533. http://dx.doi.org/10.1002/aic.690220316

Saraf, A., de Zwart, A., Currie, P., & Ali, M. A. J. 2010. Analysis of the Effect of Residual Oil on Particle Trapping During Produced-Water Reinjection Using X-Ray Tomography. *SPE Journal*, **15** (4): 943–951. http://dx.doi.org/10.2118/122137-PA

Soo, H., & Radke, C. J. 1986. A Filtration Model for the Flow of Dilute, Stable Emulsions in Porous Media—I. Theory. *Chemical Engineering Science*, **41** (2): 263–272. http://dx.doi.org/10.1016/0009-2509(86)87007-5

Soo, H., Williams, M. C., & Radke, C. J. 1986. A Filtration Model for the Flow of Dilute, Stable Emulsions in Porous Media—II. Parameter Evaluation and Estimation. *Chemical Engineering Science*, **41** (2): 273–281. http://dx.doi.org/10.1016/0009-2509(86)87008-7

Spielman, L. A., & Goren, S. L. 1972. Theory of Coalescence by Flow through Porous Media. *Industrial & Engineering Chemistry Fundamentals*, **11** (1): 66–72. http://dx.doi.org/10.1021/i160041a011

Van den Broek, W. M. G. T., Bruin, J. N., Tran, T. K., van der Zande, M. J., et al. 1999. Core-Flow Experiments With Oil and Solids Containing Water. Paper SPE 54769 presented at the SPE European Formation Damage Conference, 31 May-1 June, The Hague, Netherlands. http://dx.doi.org/10.2118/54769-MS

Van der Zande, M. J., Janssen, P. H., & van den Broek, W. M. G. T. 2001. Size of Oil Droplets Under High-Water-Cut Conditions. Paper SPE 67250 presented at the SPE Production and Operations Symposium, 24-27 March, Oklahoma City, Oklahoma. http://dx.doi.org/10.2118/67250-MS

Vaz Jr., A., Bedrikovetsky, P., Furtado, C. J., Siqueira, A., et al. 2006a. Effects of Residual Oil on Reinjection of Produced Water. Paper SPE 100341 presented at the SPE Europec/EAGE Annual Conference and Exhibition, 12-15 June 2006, Vienna, Austria. http://dx.doi.org/10.2118/100341-MS

Vaz Jr., A., Bedrikovetsky, P., Furtado, C. J., Siqueira, A., et al. 2006b. Injectivity Impairment Due to Residual Oil Mobilisation (Treatment of Laboratory Data). Paper SPE 100391 presented at the SPE Asia Pacific Oil & Gas Conference and Exhibition, 11-13 September 2006, Adelaide, Australia. http://dx.doi.org /10.2118/100391-MS

Yao, K.-M., Habibian, M. T., & O'Melia, C. R. 1971. Water and Waste Water Filtration. Concepts and Applications. *Environmental Science & Technology*, **5** (11): 1105–1112. http://dx.doi.org/10.1021/es60058a005

Zhang, N. S., Somerville, J. M., & Todd, A. C. 1993. An Experimental Investigation of the Formation Damage Caused by Produced Oily Water Injection. Paper SPE 26702 presented at the Offshore Europe, 7-10 September, Aberdeen, United Kingdom. http://dx.doi.org/10.2118/26702-MS

Chapter 4 : Development of a 3-D Fracture Model for Water Injectors

4.1 INTRODUCTION

4.1.1 Fracture Height Growth

The process of fracture growth induced by long-term water injection is different than the process of hydraulic fracturing. Injection well fracturing is caused by particle plugging due to solids in the injected water and thermal stress changes due to the injection of large volumes of cold water. The traditional (Carter's) fluid leak-off model is not appropriate for water injection wells due to the above effects.

As in hydraulic fracturing, researchers need to predict fracture dimensions and the leak-off behavior in order to understand the injectivity. This data is the basis for water quality specifications and the subsequent design of the water treatment facility. Fracture growth into bounding layers, when not properly addressed, can significantly distort all aspects of the mechanical and fluid flow behavior. A shale breach into the adjacent layers, however, cannot be properly predicted by a constant height fracture growth model, e.g., PKN model. When water is injected into multiple layers, complicated *in situ* stress conditions require the utilization of a 3-D fracture growth model.

4.1.2 Containment of Fracture Growth

Because of the reasons stated above, there have been studies to investigate the fracture growth into bounding layers. Simonson et al. (1978) studied containment of hydraulic fractures. They based their study on linear elastic fracture mechanics formulations. They studied the effects of differing materials, stress variation between layers and the pressure gradient by fracturing fluids. van Eekelen (1982) started to look into the

shape of fracture penetration into bounding layers. In most cases, the fracture penetrated into the bounding layers, and the depth of penetration was determined by differences in modulus and *in situ* stresses. Prediction of penetration depending on stiffness and *in situ* stress are presented based on a simple fracture geometry with penetration. Fung et al. (1987) also used a semi-analytic approach to upgrade previous relations of a vertical fracture's extent in an arbitrary horizontal stress distribution in multiple layers. These models became the basis for pseudo-three-dimensional fracture growth models that explicitly predict fracture height.

Clifford et al. (1991) extended a 3-D fracture growth model in water injectors. They focused on changes in thermal stresses and consequent fracture growth. However, filtration and relevant leak-off calculations were not applied. van den Hoek (2005) calculated the dimensions and degree of containment of waterflood-induced fractures based on pressure transient analysis. Interpretation methods for falloff tests in fractured water injectors are presented in his study. The fracture-height recession from the breach into bounding layers as well as the length recession was accounted for in this model.

In fracture growth models for hydraulic fracturing or waterflood-induced fracturing, determining the growth into bounding layers involves understanding multiple parameters. Because of this, analytic solutions make the models complicated, and a numerical model may not address all the proper assumptions required. Garcia et al. (2013) used a discrete element model (DEM) to focus on fracture growth behavior at the interface of layers. They identified four growth patterns: straight-crossing, arresting, T-shaped propagation, and fracture re-initiation with an offset.

There have also been experimental investigations on fracture containment issues. Teufel & Clark (1984) conducted an experiment in which they propagated hydraulic fractures in layered rocks. By investigating the fracture shapes created, they demonstrated

that the interfacial shear strength and the stress contrast between the target and bounding layers have the most significant impact on determining if a fracture will breach the bounding layers. Mechanical properties, including the modulus, did not significantly affect the results. However, the stress contrast between layers is critical.

4.1.3 Fluid Leak-off

Carter (1957)'s leak-off model is a conventional fluid leak-off (fluid loss) model for hydraulic fracturing simulations. Many commercial fracturing simulations assume the leak-off coefficient to be constant and use it to calculate the leak-off rate in the fluid material balance. This coefficient is usually specified based on the field injection test or estimated from the reservoir and injection properties. The constant leak-off coefficient from hydraulic fracturing, when used for the water injection projects, may not represent the proper leak-off behavior due to the long-term buildup of internal and external filter cakes. Hence, to calculate the proper leak-off behavior for water injection induced fractures, particle plugging, stress changes and fracture mechanics should be comprehensively taken into account. The leak-off coefficient of water injection fractures needs to change with time, because the effect of the particle plugging and the *in situ* stress change will vary over the long period of injection. This also requires the leak-off rate to be calculated during the entire period of water injection.

4.1.4 Water Injection Models with Constant Height (2-D) Fracture Growth

Suri et al. (2011) built the latest injection well model by making improvements to Pang & Sharma (1997) and Wennberg & Sharma (1997)'s comprehensive water injector model, which was based on Perkins & Gonzalez's (1985) model. Their models calculate the filtration of solids and oil droplets, reservoir fluid flow, fracture propagation and poro-thermo-elastic stress changes.

The permeability reduction model proposed by Pang & Sharma (1997) predicts the permeability profiles based on the amount of particle plugging on the fracture face. An internal filtration model was used to calculate permeability reduction and was improved by Gadde & Sharma (2001). These models use the macroscopic material balance of the accumulated solid particles near wells and fractures. The degree of filtration is calculated using the filtration coefficients predicted by Rajagopalan & Tien (1976).

To find the fluid flow and relevant pressure drops for composite reservoir zones, researchers use the infinite conductivity solution by Gringarten et al. (1974). Assuming a vertical fracture with two wings, the dimensions and pressure drops of the stepwise fluid and thermal fronts can be analytically calculated. The fluid and thermal fronts are assumed to be ellipses confocal with the fracture. For the fracture growth calculation used in water injection models, Perkins & Gonzalez (1985) analytically predicted the changes in the *in situ* stress caused by thermo- and poro-elastic effects induced by long-term injection. They introduced a 2-D fracture propagation model to calculate the fracture length induced by water injection.

These models were combined into a semi-analytical model to simulate fractured or unfractured vertical open-hole gravel-packed wells, cased and perforated wells, horizontal wells with transverse or longitudinal fractures (Suri & Sharma, 2009), and vertical frac-packed wells (Suri & Sharma, 2010).

4.1.5 Fracture Growth Criteria in the 2-D Model

The water injection model by Suri et al. (2011) describes fracture propagation using a 2-D model. This model was used as a reference model for the new 3-D model. Specifically, its particle plugging, reservoir fluid flow, and stress change models are used as parts of the new model. Its fracture growth model has been substantially changed and is reviewed here for comparison. The fracture is assumed to initially grow as an enlarging

penny-shaped crack. Once the height of the fracture reaches the height of the formation, it is assumed to be confined between the bounding formations. The fracture tip is assumed to be circular while it is growing, but the fracture height remains constant. Griffith (1921) energy balance theory was used for mode I fracture propagation in a plane strain condition. This condition applies to fractures with a penny-shaped crack tip.

$$K_I = K_{Ic} \tag{4.1}$$

where K_I is a stress intensity factor in mode I fractures and K_{Ic} is a critical stress intensity factor in mode I fractures. A previously existing crack propagates when K_I exceeds K_{Ic}. By definition, both terms can be written as follows:

$$\frac{2}{\pi}\Delta\sigma_I\sqrt{\pi r_f} = \sqrt{\frac{2\gamma E}{1-\nu^2}} \tag{4.2}$$

where γ is a specific surface energy, and E is Young's modulus. The driving stress of mode I fractures, $\Delta\sigma_I$, can be expressed in terms of the fracture propagation pressure, P_{frac} and the *in situ* stress, $S_{h\min}$.

$$\Delta\sigma_I = P_{frac} - S_{h\min} \tag{4.3}$$

By using this definition and rearranging the equation, the fracture propagation pressure can be calculated:

$$P_{frac} = S_{h\min} + \sqrt{\frac{\pi\gamma E}{2\left(1-\nu^2\right)r_f}} \tag{4.4}$$

The penny-shaped fracture tip radius, r_f in the above equation can be replaced with the fracture height, $h_f/2$, once the top and bottom of the fracture tip reaches the bounding layers. The square root term in the above equation is practically negligible compared to the $S_{h\min}$ value. Then, the fracture propagation at the tip occurs when the tip pressure exceeds

the $S_{h\min}$ value. This is certainly the case for low moduli rocks such as poorly consolidated sands. When the stress contrast between the target and bounding layers is large enough to contain the fracture, the 2-D fracture growth criteria serves as a good model for waterflood-induced fracturing.

4.2 MODEL FORMULATION

4.2.1 Features and Assumptions of the Model

The objective of the new water injection model is to predict the well's injectivity decline by addressing the combined effect of the fracture geometry in 3-D, the degree of the particle plugging, and the change in the *in situ* stress caused by poro- and thermo-elastic effects. There are several assumptions made in the calculations:

- The reservoir is homogeneous and isotropic.
- The fracture is a single, vertical, bi-winged fracture. ($S_{\text{vert}} > S_{\text{horiz}}$)
- The degree of particle plugging is uniform over the entire fracture face.
- The fluid loss is one-dimensional and perpendicular to the fracture face.
- Darcy's law is valid in the reservoir.
- The fluid displacement and the temperature profile in the reservoir are piston-like.
- Heat conduction between layers is neglected.
- Water injection rate is constant.

Based on the above assumptions, the simulation model is composed mainly of two modules: the fracture propagation module and the formation damage module. The formation damage module is composed of particle filtration, reservoir fluid flow, and stress change calculations. This module eventually calculates the fluid leak-off coefficient, which is used in the fracture propagation module for the next time step. The schematic calculation sequence is shown in Figure 4.1.

The model grid blocks are the finite element mesh composed of the regular triangular elements in the middle of the fracture and the singular quadrilateral elements at the fracture tip. The fracture propagation module calculates the fracture width, pressure, and leak-off rate at specific nodes of the mesh. The fracture propagation distance, relevant time step and remeshing calculations are also conducted. Based on the fracture calculation at a specific propagation time step, the formation damage module calculates both internal and external particle filtration on the fracture face with the transition time calculation. The calculated particle concentrations converted to resistances in the reservoir fluid flow calculations. These resistances are converted to the leak-off coefficient, which are used for the fracture propagation calculation for each time step.

The following sections explain the formulations and numerical schemes used in the fracture propagation module and the formation damage module.

4.2.2 Material Balance in the Fracture

The material balance equation can be written for the entire fracture and also in differential form. First, the overall material balance for the fracture and the injected fluid can be written as:

$$V_{inj} = V_{frac} + V_L \tag{4.5}$$

where V_{inj} is the cumulative volume of water injection, V_{frac} is the fracture volume and V_L is the cumulative leak-off volume. In this equation, the cumulative injection volume is simply the flow rate multiplied by the injection time when the injection flow rate is maintained constant.

$$V_{inj} = q_{inj} \cdot t_{inj} \tag{4.6}$$

Meanwhile, for the time duration of Δt, the material balance for the fluid in a fracture is:

$$q_{inj} \cdot \Delta t = \Delta V_{frac} + q_L \cdot \Delta t \tag{4.7}$$

The leak-off flow rate for the short period of time step can be assumed:

$$q_L(t) = q_{inj} - \frac{\Delta V_{frac}}{\Delta t} \tag{4.8}$$

For any specific time step, the leak-off flowrate, $q_L(t)$ can be calculated with this equation assuming that it is constant within that time step. This will serve as one way to calculate the average leak-off rate. It will then be compared with $q_L(t)$, which is calculated from the formation damage module.

The differential form of the material balance equation is used in the fracture propagation module based on Yew (1997), Gu (1987) and Ouyang (1994)'s model. The fracture width is narrow compared to the areal dimension of the fracture. This leads researchers to assume that the pressure in the fracture is dependent on the *x* and *y* directions (area), but not the *z* direction (width). The velocity components of *x* and *y* directions are only accounted for in the fracture, and the fluid flow in the *z* direction is taken as the fluid leak-off. The fluid is assumed to be Newtonian and incompressible. The material balance equation for the control volume, which has dimensions of Δx, Δy and $w(x,y)$ inside the fracture, is:

$$-\frac{\partial q_x}{\partial x} - \frac{\partial q_y}{\partial y} - q_L = \frac{\partial w}{\partial t} \tag{4.9}$$

where q_x and q_y are then related to the fluid pressure, $P(x,y)$ inside the fracture:

$$\frac{\partial}{\partial x}\left(\frac{w^3\,\partial P}{12\mu\,\partial x}\right) + \frac{\partial}{\partial y}\left(\frac{w^3\,\partial P}{12\mu\,\partial x}\right) = \frac{\partial w}{\partial t} + 2 \cdot u_L(t,x,y) \tag{4.10}$$

where *w* is the width of the fracture at a specific location, q_L is the volumetric leak-off rate and u_L is the linear leak-off rate. Using the finite element formulation, the equation can be transformed to the following matrix equations.

$$[K]\{P\} = -\{f_L\} - \{f_w\} + \{f_p\} \tag{4.11}$$

where the detailed derivation of the formulation can be found in Yew (1997), Gu (1987) and Ouyang (1994).

4.2.3 Fracture Mechanics

The fracture mechanics in the model is based on linear elastic fracture mechanics. The fracture opening equation is required along with the fluid flow equation to calculate the fracture geometry and pressure distribution in the fracture model. Economides & Nolte (2000) stated that the width, *w*, near the tip of a stress-free crack is a function of the stress intensity factor, $K_{I,}$ for the plain strain assumption.

$$w(r) = \frac{4(1-\nu)}{G} K_I \sqrt{\frac{r}{2\pi}} \tag{4.12}$$

where *r* is the inward normal distance from the fracture front. The definition of the stress intensity factor, K_I, can be used to give the following equation including the stress and the pressure terms.

$$w(r) = \frac{4\sqrt{2}}{\pi} \frac{1-\nu}{G} \left(P - S_{h\min}\right) r \tag{4.13}$$

This relation was formulated for arbitrarily shaped fractures in an infinite elastic medium by Bui (1977):

$$-P(x,y) + S_{h\min}(x,y) = \frac{G}{4\pi(1-\nu)} \int_{\Omega} \left[\frac{\partial}{\partial x}\left(\frac{1}{r}\right)\frac{\partial w}{\partial x'} + \frac{\partial}{\partial y}\left(\frac{1}{r}\right)\frac{\partial w}{\partial y'} \right] dx'dy' \tag{4.14}$$

Gu (1987) and Yew (1997) reformulated the above equation into a weak form:

$$\begin{aligned} &\frac{G}{4\pi(1-\nu)} \int_{\Omega}\int_{\Omega} \frac{1}{r}\left(\frac{\partial v}{\partial x}\frac{\partial w}{\partial x'} + \frac{\partial v}{\partial y}\frac{\partial w}{\partial y'} \right) dxdydx'dy' \\ &\qquad = \int_{\Omega} \left\{ P(x,y) - S_{h\min}(x,y) \right\} v\left(x,y\right) dxdy \end{aligned} \tag{4.15}$$

where the test function, $v(x,y)$ is a continuous function which satisfies that the fracture width is zero at the fracture tip. It is notable that the singular term $1/r$ was moved to the test function, $v(x,y)$. The opening displacement equation can also be transformed into the following form by the finite element formulation:

$$[A]\{w\} = \{f\} \tag{4.16}$$

It is again recommended to refer to Yew (1997), Gu (1987) and Ouyang (1994) for the detailed finite element formulation, the algorithms and the iterative method schemes for the fracture width, pressure and propagation calculations.

4.2.4 Fracture Propagation

One of the assumptions of the previous 2-D fracture model by Suri et al. (2011) is that all the fluid injected leaks off. This assumption is valid as the fracture efficiency (fracture volume divided by injected volume), which is commonly calculated for hydraulic fracturing jobs, is almost zero when calculated for water injection projects. Instead, the fracture lengths are calculated by an iteration method which satisfies the fracture propagation criteria at the fracture tip, as explained in Section 4.1.5. In contrast, the 3-D fracture growth model generally does not use this assumption, and the fluid loss (the leak-off flowrate) calculation is required, as well as the fracture propagation criteria.

Based on the finite element formulation for the fluid flow equation in a fracture and the fracture opening equation, Yew (1997) and Gu (1987) developed an iterative scheme for the 3-D fracture propagation calculation for hydraulic fracturing simulations. Their fracture propagation model was modified and used as a fracture propagation module in this work. The original model works for time scales of hydraulic fracturing, normally about an hour. Hence, the model was modified to accommodate the time scale of water injection, which normally extends to several years. The other major change in the model was

estimation of the leak-off coefficient which was specified by the user in the previous model. In the new model, it is calculated by the formation damage module. The leak-off coefficient varies with time as it is dependent on the degree of the formation damage which is affected by the history of the fracture growth.

In the fracture propagation criteria, stress intensity factors at the mesh points of the fracture tip are compared with their critical value, the fracture toughness. The process is composed of: (i) discretization of the material balance equation in the time domain, (ii) solving for the pressure and width by Picard iterative method, and (iii) fracture front movement calculation by the stress intensity factor. In this first part of the process, the discretization of the material balance in the time domain is combined with the global mass balance equation for the entire fracture. By combining Eq. (4.7) and (4.11), the time step is implicitly decided during the iterative scheme. In the second step, the resulting time step becomes the basis for solving the width and pressure. Then, the convergence is tested during the Picard iterative scheme for the solution of the pair of the width and pressure equations. Finally, once the fracture width is calculated for the fracture mesh, the stress intensity factor is again calculated from Eq. (4.12). In the course of the propagation, if the fracture is assumed to be stationary for a short period of time, the incremental stress intensity factor can determine at each node the tip propagation distances from its critical value, $K_I - K_{IC}$ (Mastrojannis et al., 1980).

$$\Delta d = \frac{K_I - K_{IC}}{K_{IC} + \frac{S_{tip} H_l}{\sqrt{h_d}}} \tag{4.17}$$

where S_{tip} is the local *in situ* stress at the tip, H_l is the local fracture height, and h_d is the depth of the fracture in the high *in situ* stress layer.

Another factor that affects fracture propagation is the initial condition of the net

pressure in the fracture mesh at the moment the fracture begins to propagate. In Gu and Yew's 3-D hydraulic fracturing simulation, the initial net pressure condition may have a limited effect on fracture propagation as the fracture is normally growing from the beginning of the injection in hydraulic fracturing. However, in many water injection projects, we need to precisely predict when the fracture starts to grow and this time may vary from minutes to years. The new model calculates the time when the fracture starts to grow. By using the simple fracture growth criteria of a 2-D model, the timing of the fracture initiation can be determined. The particle plugging, the *in situ* stress change and the fracture propagation pressure in the well and/or the initial fracture (if it is a fractured well) are calculated before the fracture starts to grow. The fracture starts to grow when the fracture tip pressure exceeds the fracture propagation pressure. The net pressure distribution in the fracture is estimated by the linear interpolation between the wellbore and fracture tip pressure, and supplied to the 3-D fracture growth calculations as the initial condition of fracture growth.

4.2.5 The Adaptive Leak-off Calculation

In many fracturing simulations, the leak-off coefficient is specified by the user and remains constant during the injection period. However, this assumption is not valid for water injection simulations because the leak-off behavior is a strong function of the formation damage which changes significantly over the long time of the injection. It is also dependent on the fracture growth behavior. Hence, the leak-off rate and the relevant leak-off coefficient must be calculated at each time step.

A 2-D analytical radial flow reservoir model (Figure 4.2) and the formation damage model near the fracture faces were used to calculate the leak-off rate, q_L at a certain time step. With a known reservoir boundary pressure, P_e, the pressure drops for each fluid flow region were calculated by the following equations:

$$\Delta P_1 = q_L R_1 = q_L \frac{\mu_o}{2\pi k k_{ro} h} \ln\left(\frac{2r_e}{a_2 + b_2}\right) \tag{4.18}$$

$$\Delta P_2 = q_L R_2 = q_L \frac{\mu_{wr}}{2\pi k k_{rw} h} \ln\left(\frac{a_2 + b_2}{a_1 + b_1}\right) \tag{4.19}$$

$$\Delta P_3 = q_L R_3 = q_L \frac{\mu_{wi}}{2\pi k k_{rw} h} \ln\left(\frac{a_1 + b_1}{a_0 + b_0}\right) \tag{4.20}$$

$$\Delta P_4 = q_L R_4 = q_L \frac{\mu_{wi}}{2\pi k k_{rw} h} \ln\left(\frac{a_0 + b_0}{L_f}\right) \tag{4.21}$$

where, ΔP_1 is a pressure rise between the water flood front and the far-field drainage boundary. ΔP_2 is a pressure increase between the connate water flood front and the injected water flood front. ΔP_3 is a pressure increase between the injected water flood front and the thermal front. ΔP_4 is a pressure increase between the thermal front and the fracture.

A pressure increase across a skin damage on the fracture face, ΔP_s, can be obtained from the particle filtration and permeability reduction model (Pang and Sharma, 1997; Saripalli et al., 1999; Sharma et al., 2000). It is composed of the flow resistances of the internal filtration of particles in the matrix near the fracture face and the external filter cake formation on the fracture face.

$$\begin{aligned} \Delta P_s &= q_L R_s \\ &= q_L \left(\max\left(R_{\text{int}} - R_{undamaged}, 0\right) + R_c\right) \\ &= q_L \left(\max\left(\frac{\mu_{wi}}{A_f} \int_0^{L_{DZ}} \frac{dx}{k(x)} - \frac{\mu_w L_{DZ}}{A_f k}, 0\right) + \frac{\mu_w h_c}{A_f k_c}\right) \end{aligned} \tag{4.22}$$

Then, the pressure drop from the reservoir boundary to the fracture tip can be calculated by combining the above equations leading to an explicit expression for the leak-off rate at a certain time.

$$\begin{aligned}\Delta P_{tip-e} = P_{tip} - P_e &= \Delta P_1 + \Delta P_2 + \Delta P_3 + \Delta P_4 + \Delta P_s \\ &= q_L \left(R_1 + R_2 + R_3 + R_4 + R_s \right)\end{aligned} \tag{4.23}$$

$$q_L(t) = \frac{P_{tip} - P_e}{R_1 + R_2 + R_3 + R_4 + R_s} = \frac{P_{frac} - P_e}{R_1 + R_2 + R_3 + R_4 + R_s} \tag{4.24}$$

By explicitly solving the resistances with the superficial velocity and fracture length from the previous time step, the leak-off rate is obtained by Eq. (4.24). This can be used to calculate the leak-off coefficient, C_L at a specific time by assuming Carter's fluid loss correlation (for comparison with classical models).

$$C_L(t) = \frac{q_L(t)}{A_f(t)}\sqrt{t} \tag{4.25}$$

The validity of the Carter's correlation will be discussed later. At this stage, this leak-off coefficient is assumed to represent the degree of fluid loss based on the uniform leak-off assumption over the entire area of the fracture. This coefficient becomes useful as the leak-off calculation is dependent on time and location when used in a 3-D fracture propagation module. The fluid-loss calculation in the fracture propagation module is based on the equation shown below:

$$u_L(x, y, t) = \frac{C_L(t)}{\sqrt{t - \tau(x, y)}} \tag{4.26}$$

The resulting linear leak-off velocity is directly used for the material balance equation in 3-D fracture propagation models. After substituting the leak-off rate in Eq. (4.10), the pressure distribution and width are obtained from the fracture propagation module.

4.3 MODEL ALGORITHM

4.3.1 Method for Time Step Handling

The new injection well model is composed of two calculation modules: the fracture

growth module and the formation damage module. The fracture growth calculation requires a discrete time step which starts from the moment the fracture growth criterion is met at the tip. The resulting time step (days or months) can be relatively long when the fracture growth rate is low. However, the particle plugging model requires the calculation for the duration before fracture growth, and it needs a smaller time step than that of the fracture propagation module. We used two different time steps for the respective modules, as shown in Figure 4.3. The variables and results of each module were interchanged as necessary.

Before fracture initiation, the formation damage module is run to predict the fracture initiation time. After fracture initiation, the fracture module calculates the fracture propagation time step. The resulting fracture geometry and an incremental time, Δt_n^{3D} from the fracture propagation module is now used for the formation damage module. For the time step duration recently calculated from the fracture propagation module, the formation damage module calculates the change in the reservoir fluid flow, stress changes, and particle plugging. This requires smaller time steps as the particulate plugging model needs cumulative information with time-dependent properties, e.g., flow resistances in the reservoir, thermal- and poro-elastic stress changes with time. The increment in the time step of the formation damage module, Δt^{2D} is a constant value smaller than Δt^{3D}. The leak-off coefficient is calculated when $t^{2D}=t^{2D}_{n,final}$ for the next time step of the 3-D fracture module. This scheme properly computes the fluid leak-off during the most recent fracture propagation time step.

4.3.2 Calculation Algorithm

The main algorithm is described in Figure 4.4. At the beginning of the simulation, the time when the fracture starts to propagate is calculated. The fracture propagation module is not used at this stage. The particle plugging, thermal and poro-elastic stress change and the reservoir flow resistances are calculated to check whether the *in situ* stress

condition is above the fracture initiation pressure. The equations in Section 4.2 are used for the reservoir flow resistance calculation, permeability reduction, and stress change models. The 2-D fracture propagation criterion in Section 4.1 is used to determine the fracture initiation as well. When the fracture is initiated either from the un-fractured or fractured well, the fracture propagation module begins from the fracture initiation time.

After fracture initiation, the simulation algorithm uses the 3-D propagation module as an outer loop and the formation damage module an inner loop. As shown in Figure 4.1, the fluid losses are determined for the following fracture growth calculation based on the leak-off coefficient from the particle filtration model of the previous time step. The fluid flow equations and the fracture width calculation are performed by the iterative scheme as described in Section 4.2.4 to give the time and location dependent fluid loss rate. Subsequently, the fracture propagation distances at the tip, the new dimensions and the pressure of the fracture are determined. In this iterative scheme, the time step corresponding to fracture growth is calculated.

The discrete fracture growth requires calculating the necessary changes in the formation damage properties, the stress condition, and the reservoir fluid flow during each time step of the fracture propagation module. To address variations within one time step of the fracture propagation module, the formation damage module uses a refined time step that is smaller than that of the fracture propagation module. The fracture dimensions are linearly interpolated for the refined time step as the dimension information is necessary for calculating particle plugging and the flow resistances. The validity of the linear interpolation will be shown by the simulation results. This intermediate calculation is important as the change in it determines the subsequent leak-off coefficient for the outer loop calculation. The leak-off coefficient is now used for the subsequent time step’s fluid flow equation in the fracture propagation module. The necessary parameters for the fluid

flow and fracture opening formulation are prepared for the fracture growth module in the following time step. This procedure will be repeated until the simulation ends.

4.4 RESULTS AND DISCUSSION

4.4.1 Effect of Fracture Penetration into Bounding Layers

The new model was tested by using typical parameters of a water injection project. The results of the new model are compared with the model by Suri et al. (2011) which utilizes the 2-D fracture propagation scheme for a water injection project. The previous 2-D model uses the same formation damage model as the current 3-D model; however, it does not employ the algorithm or leak-off calculation explained in the previous sections.

The base case undergoes the following procedure. The injection well was assumed to be initially a fractured vertical well with an initial length of 100 ft and a height of 150 ft. The initial shape of the fracture was assumed to be circular. The fracture width at initiation was calculated by a 3-D model with the pressure distribution at the moment of fracture initiation. The stress contrast was 200 psi to the bounding layers to ensure fracture containment. The input parameters in Table 4.1 are the injection fluid, reservoir, thermal and mechanical properties used for the base case simulation.

The fracture initiation time for this specific case was predicted to be about 0.6 years, shown in Figure 4.5. The fracture length grows from 100 to about 300 ft over fifteen years. However, the 2-D model predicted the fracture growth to be about 350 ft in the same time duration. The length predicted by the 3-D model was generally shorter than that predicted by the 2-D model. This is believed to be due to the stricter fracture propagation criteria of the 3-D model in which the stress intensity factors along the tip are compared with their critical values. In Figure 4.6, the bottom-hole pressure is shown as well as the fracture tip pressure. In the 2-D model, the fracture tip pressure is almost the same as the minimum *in*

situ stress. This is in accordance with the 2-D fracture propagation criteria as explained in Section 4.1.5. In the 3-D model, the fracture criterion is independent of this global criterion, but the stress intensity factors are compared locally and thus more strictly than in the 2-D model. The 3-D model's shorter length leads to thicker external filter cake deposition. The pressure drop across the thicker filter cake in the 3-D model was higher than in the 2-D case. In some cases, this can increase the bottom-hole pressure to be higher in the 3-D model than in the 2-D simulation. If the 3-D fracture length is shorter than the 2-D, the opposite result is expected, and the 3-D bottom-hole pressure would be lower than that of the 2-D.

The injectivity is directly predicted from the bottom-hole pressure. Before fracture initiation, the injectivity normally decreases, and the rate of decrease is a function of the particle plugging of the well. After fracture initiation, the newly propagated area of the fracture is subject to additional particle plugging, and the injectivity is stabilized. The stabilized injectivity and the time of the stabilization is a strong function of the injection water quality and formation properties. The injection water quality can be specified to maintain the high injectivity as long as possible. Specification of the water quality is one of the most important recommendations that can be derived from the injection well model.

4.4.2 Leak-off Behavior

The leak-off coefficient calculated by the formation damage module, which includes the particle filtration model, the reservoir fluid flow model, and the stress change model, is a crucial parameter for the 3-D fracture propagation model. The leak-off coefficient, C_L, by definition, is only valid when assuming that Carter's correlation is valid. The calculated leak-off coefficient is dependent only on time and based on the assumption of the formation damage module that the fluid loss is uniform along the fracture face. But, by using the leak-off coefficient, the 3-D fracture propagation module generates the linear

fluid loss rate, $u_L(t,x,y)$, which is dependent on time and location in the fracture.

The leak-off coefficient was calculated in two ways. The coefficient from the formation damage module, which was actually used during simulation, was compared with the coefficients calculated from the simulation results, shown in Figure 4.6. The coefficients acquired from the simulation results are not used for any part of the simulation and are not important in the simulation procedure. They were calculated from the average leak-off rate in Eq. (4.8) for comparison purposes only. They represent the ratio of the fluid loss to the injection flow rate. They can be understood as the reference values used to check whether the formation damage module plays a significant role in the overall fracture model. In Figure 4.6, the difference between the leak-off coefficients from the formation damage module and the simulation results represents the significance of the formation damage module in water injection fracturing. The change in magnitude of the calculated coefficient over time results in a significant change in fracture dimensions when it is assumed to remain constant.

When the change in the average linear fluid loss velocity over time is investigated, the validity of the Carter's model can be addressed. Carter's model assumes that the velocity change is inversely proportional to the square root of time. In Figure 4.6, the fluid loss flux computed from the formation damage module was best fit with an exponent of approximately 0.4 for water injection simulations. Some other simulations in the following figures also showed exponent values lower than 0.5. The lower exponents result in lower values of linear leak-off velocity than those from the exponent of 0.5. This is the combined effect of the additional fluid resistance caused by particle filtration into the reservoir rock, reservoir fluid flow, and stress changes, which tend to be significant over the long time scale of water injection. While this is of a critical importance when waterflood-induced fractures are simulated, this effect may not be significant in hydraulic fracturing.

4.4.3 Application of Adaptive Leak-off Model in Hydraulic Fracturing

The adaptive leak-off calculation was applied to investigate the leak-off behavior in hydraulic fracturing simulation. The same calculation and algorithm was used based on the particle plugging model, reservoir fluid flow model, and the stress change model. For this problem, the injection time is many orders of magnitude shorter and the effect of reservoir fluid flow and thermal stress change were negligible, but the transition from internal to external filtration affected the trend in the leak-off coefficient over time, as shown in Figure 4.7. However, the leak-off coefficient remained relatively constant compared to the water injection cases. The order of magnitude of the leak-off coefficient predicted was lower than that estimated for water injection, and it was close to typical values measured in hydraulic fracturing. There were no significant differences between the coefficients from the leak-off calculation module and the results of the simulation. The exponent of the correlation between leak-off flux and time was approximately 0.5. This is very close to the exponent of the traditional Carter's correlation. Therefore, the fluid leak-off behavior predicted from the new model when applied to hydraulic fracturing resulted in a result that was very similar to Carter's model. This indicates that the leak-off behavior during long term water injection is different than leak-off during hydraulic fracturing. The adaptive (or time-dependent) leak-off model in this work can be used to estimate the leak-off coefficient when a value is not available from laboratory or field tests. It is important to note that in our simulations presented here, slick water was assumed to be the injection fluid. If any other fluids with different rheology and wall-building properties are used, the result may deviate from Carter's correlation. This requires further investigation.

4.4.4 Effect of Water Quality on Fracture Growth

The effect of the injection water quality, *in situ* stress, and reservoir properties was investigated. Different simulation cases were run to observe the sensitivity of the model to

injection and reservoir properties including the particle concentration in the injection water, the stress contrast between sand and bounding layers, and the formation permeability. The parameters changed are summarized in Table 4.3.

The effect of the particle concentration in the injection water is shown in Figure 4.8. The particle concentration directly affects the cumulative amount of particles and the filtration properties on the fracture face. Higher concentrations of particles in the injection water led to a quicker decline of the injectivity and earlier fracture initiation, as expected. The bottom-hole pressure is expected to be higher for a higher concentration of solids in the injection water. As a consequence, longer fractures are expected. Conversely, a lower concentration of particles leads to a higher fluid loss. The exponents for Carter's correlation were approximately 0.4, but no specific correlation with the solids concentration was seen in the results.

4.4.5 Effect of Reservoir Permeability on Fracture Growth

The formation permeability was another factor that affects the injectivity and leak-off behavior, as shown in Figure 4.9. The differences in permeability led to different fracture lengths and injectivities. In higher permeability formations, the fluid loss to the fracture was lower and the stabilized injectivity was higher. The leak-off coefficient was dependent on the permeability, and the exponents for the leak-off correlations were also approximately 0.4.

Compared with the sensitivity to the water quality, the fracture initiation time was less sensitive to the formation permeability when the other parameters are the same. The fracture length, however, was affected by the formation permeability. In both cases, the leak-off behavior shows typical values for waterflood-induced fractures. Hence, the filtration during long-term injection is the main component of leak-off behavior.

4.4.6 Effect of Stress Contrast between Target and Bounding Layers

The fracture dimensions generated with different *in situ* stress conditions are compared in Figure 4.10. In the Base Case simulation, the stress contrast between the target and bounding layer was 200 psi, which ensured fracture containment within the target layer. When the stress contrast was lowered to 50 psi, the fracture was predicted to breach the bounding layers. In Figure 4.11, the stress contrast is lower than the previous case. Under these stress conditions, the breaching of the fracture into the bounding layers occurred when the stress contrast was lowered to 56 psi. The relevant net pressure in the fracture is shown in Figure 4.12. The threshold value of the stress contrast used to determine fracture breaching cannot be predicted by any rule of thumb. In Figure 4.13, under higher stress conditions, the breach occurred at a stress contrast of around 100 psi. The impact of other rock mechanical properties are analyzed in the following section.

The effects of fracture breaching and fluid loss into the bounding layer are effectively addressed by a 3-D fracture model. The pressure and width distributions can be calculated during the propagation process. When the fracture dimension changes because of different stress conditions, the exposed fracture area and particle filtration also changes. This will lead to changes in fluid loss behavior in the fracture which can be accounted for by the model.

4.4.7 Effect of Mechanical Properties on Fracture Growth

The effects of Young's modulus, E and fracture toughness, K_{Ic} on the fracture shape were investigated. Based on the relations of linear elastic fracture mechanics, the fracture toughness was estimated when Young's modulus values were varied, and these combinations of E and K_{Ic} were simulated:

$$K_{Ic} = \sqrt{\frac{2\gamma E}{1-\nu^2}} \tag{4.27}$$

where γ is the specific surface energy and ν is Poisson's ratio. Specific surface energy, γ=50Pa·m and Poisson's ratio, v=0.3 were used to calculate the fracture toughness. The resulting fracture shapes with widths are plotted in Figure 4.14. Figure 4.15 shows the corresponding net pressure distributions. If the rock is soft, with a low Young's modulus, the width becomes large and the net pressure becomes small. In harder rock, the simulation showed higher net pressure and a smaller width. Fracture growth into the bounding layer was not observed, indicating that fracture containment is more controlled by the stress contrast.

However, when the stress contrast is low enough for the fracture to grow into the bounding layers, the mechanical properties can impact the degree of growth into the bounding layers. In Figure 4.16, when the stress contrast is approximately 100 psi, the stress intensity factor played a significant role in changing the fracture height growth. The 3-D fracture simulation allowed us to investigate the impact of various parameters on fracture containment.

4.5 CONCLUSION

Traditional hydraulic fracture models use a constant leak-off coefficient. In this research, we used an alternative approach. First, the leak-off coefficient was made time-dependent, based on a detailed filtration model that accounts for the formation of internal and external filter cakes. The 3-D fracture module and the leak-off calculation module were combined using a special time-step handling mechanism.

The major findings of this work are:

- The leak-off coefficient during water injection fracturing can change with time, depending on the particle filtration behavior.
- The time exponent in Carter's leak-off correlation is shown to be approximately 0.4 when used for water injection fracturing, which is lower than the conventional value

of 0.5.

- The adaptive (time-dependent) leak-off calculation was used for hydraulic fracture simulation and the results suggest that the conventional (Carter's) leak-off calculation is appropriate for this application.
- The adaptive, filtration model based, leak-off calculation can be used independently for estimating the leak-off coefficient from the injection water and reservoir properties, without specifying a leak-off coefficient *a priori*.
- The 3-D fracture model is shown to properly address fracture growth into the bounding layers.

This model can be used for specifying injection water quality in the field with complicated *in situ* stress conditions. Based on the injector performance, operators can properly select injection water treatment facilities and minimize well treatment costs. The model can also provide improved estimates of the leak-off coefficient for the design of hydraulic fracturing treatments.

This simulation has been applied to actual field simulations. Simulation results for 3-dimensional fracture growth can provide strategies for injection rates and water treatment specifications during the design stage of waterflooding projects. During operational stages of waterflooding, the history of injection rates and its transient effects on fracture height containment can be investigated to specify future injection strategies.

Table 4.1: Differences between the new model, Gu (1987); Yew (1997) model, and Suri et al. (2011) model.

	New Model	Gu et al.	Suri et al.
Applications	Water inj., Hyd. frac. with slick water	Hyd. frac.	Water inj.
Leak-off			
C_L calculation	Adaptive	Constant	$q_L=q_{inj}$
C_L assumption	Dependent on t,x,y	Dependent on t,x,y	Dependent on t, Uniform in x,y
Formation dm. calc., Rsvr. fluid flow, Stress change calc.	Yes	No	Yes
Fracture propagation			
Material balance in the fracture	Yes	Yes	No
Frac. dimension	3-D	3-D	2-D
l_f	Calc. $\Delta t,\Delta d$ Based on FEM	Calc. $\Delta t,\Delta d$ Based on FEM	Find l_f such that $P_{tip}=P_{frac}$

Table 4.2: Input parameters of the base case model.

Parameter	Value	
Inj. Fluid and Filtration Properties		
Injection rate	35000	bbl/d
Injection water density	1.023	g/cc
Inj. water viscosity at $T=T_{inj}$	0.494	cp
Inj. water viscosity at $T=T_{rsvr}$	0.283	cp
Density of particles in Inj. Water	1.05	g/cc
Conc. of particles in Inj. Water	10	ppm
Size of particles in Inj. Water	10	micron
Filter cake permeability	0.005	md
Well and Reservoir Properties		
Well type	Vertical	
Well radius	4.8	inch
Reservoir drainage radius	3000	ft
Initial reservoir pressure	10000	psi
Min. horiz. stress in inj. layer	13500	psi
Stress contrast to adj. layers	200	psi
Layer height	150	ft
Permeability, horiz.	200	md
Permeability, vert.	20	md
Porosity	0.25	-
Thermal Properties		
Reservoir temperature	230	˚F
Injected water temperature	140	˚F
Specific heat of water	0.966	Btu/lbm-˚F
Specific heat of oil in reservoir	0.591	Btu/lbm-˚F
Specific heat of reservoir rock	0.191	Btu/lbm-˚F
Linear coeff. of thermal expansion of rock	8.0×10^{-6}	in/in-˚F
Rock Mechanical Properties		
Mineral grain density	165.4	lbm/ft3
Poisson's ratio	0.3	-
Compressibility of rock grains	1.52×10^{-7}	1/psi
Compressibility of formation	5.0×10^{-6}	1/psi
Young's modulus	1000000	psi
Min. *In situ* horiz. stress	13500	psi
Specific surface energy	50	Pa·m
Fracture toughness	702.0	psi√in

Table 4.3: Parameters changed for sensitivity studies.

No.	Parameter	Value
1	Size of Particles in inj. Water	1 ppm
2	Size of Particles in inj. Water	5 ppm
3	Size of Particles in inj. Water	10 ppm
4	Size of Particles in inj. Water	30 ppm
5	Stress Contrast	200 psi
6	Stress Contrast	50 psi
7	Matrix Permeability	20 md
8	Matrix Permeability	100 md
9	Matrix Permeability	200 md

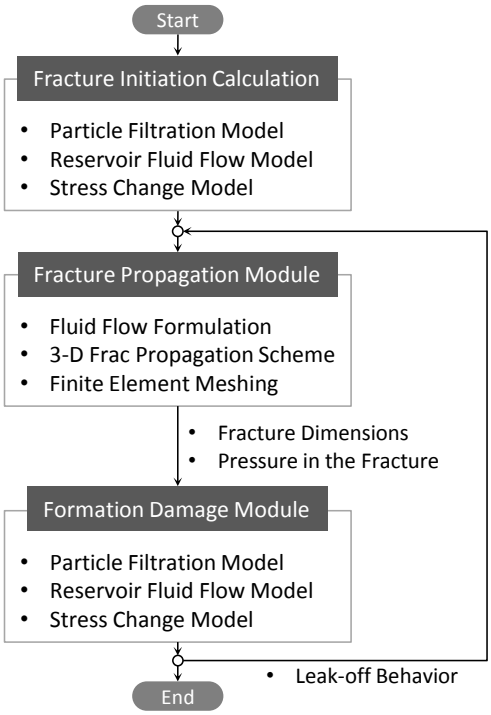

Figure 4.1: Simulation flow chart.

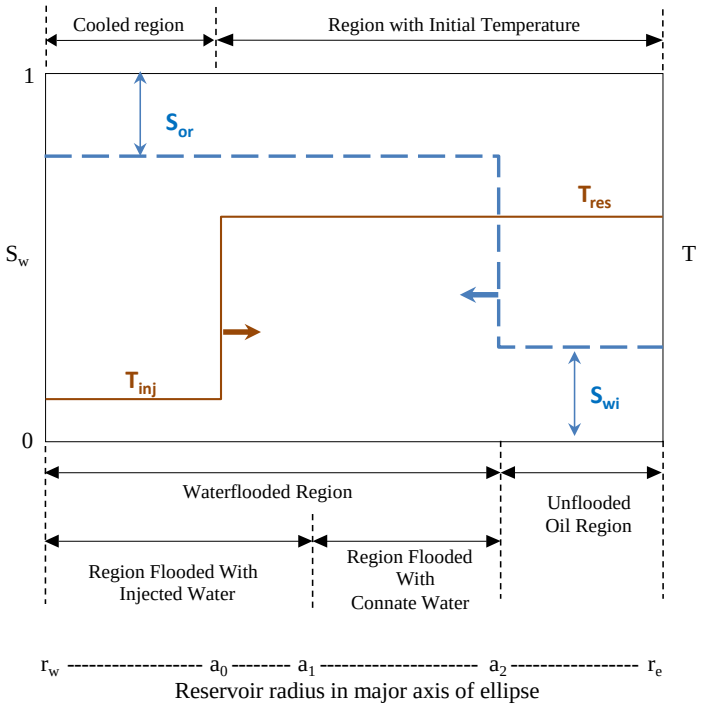

Figure 4.2: Water saturation and temperature profile in the reservoir model.

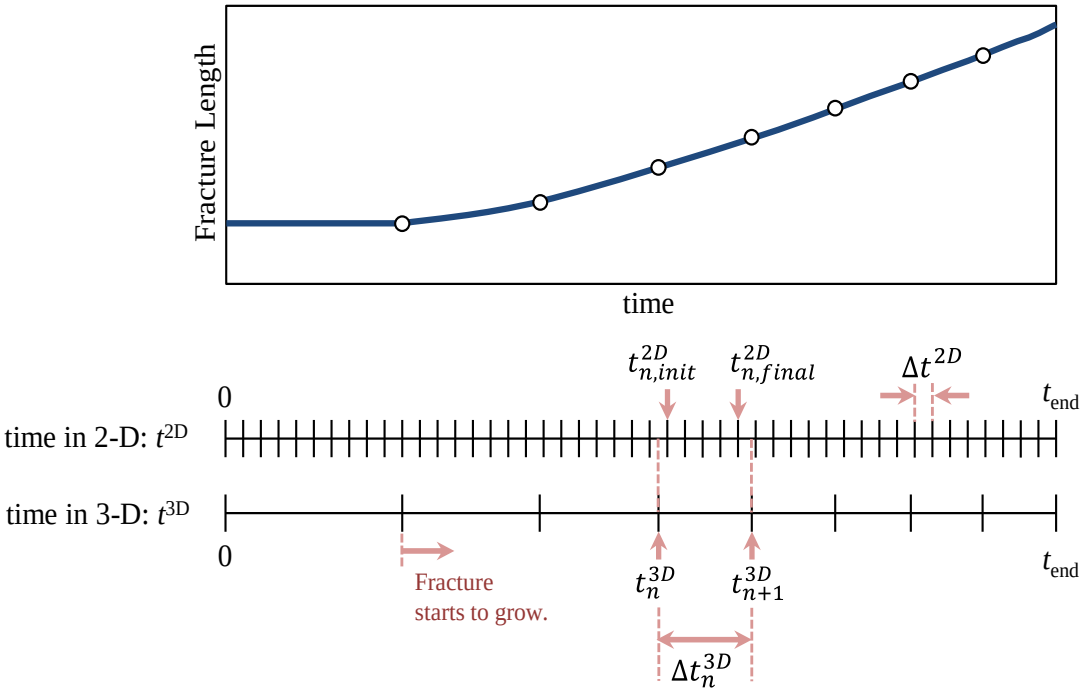

Figure 4.3: Time steps used in the simulation. The time step in 2-D, $t^{2\text{-D}}$ is for the calculation of the particle plugging model, reservoir fluid flow, and stress changes. The time step in 3-D, $t^{3\text{-D}}$ is for the calculation of fracture propagation.

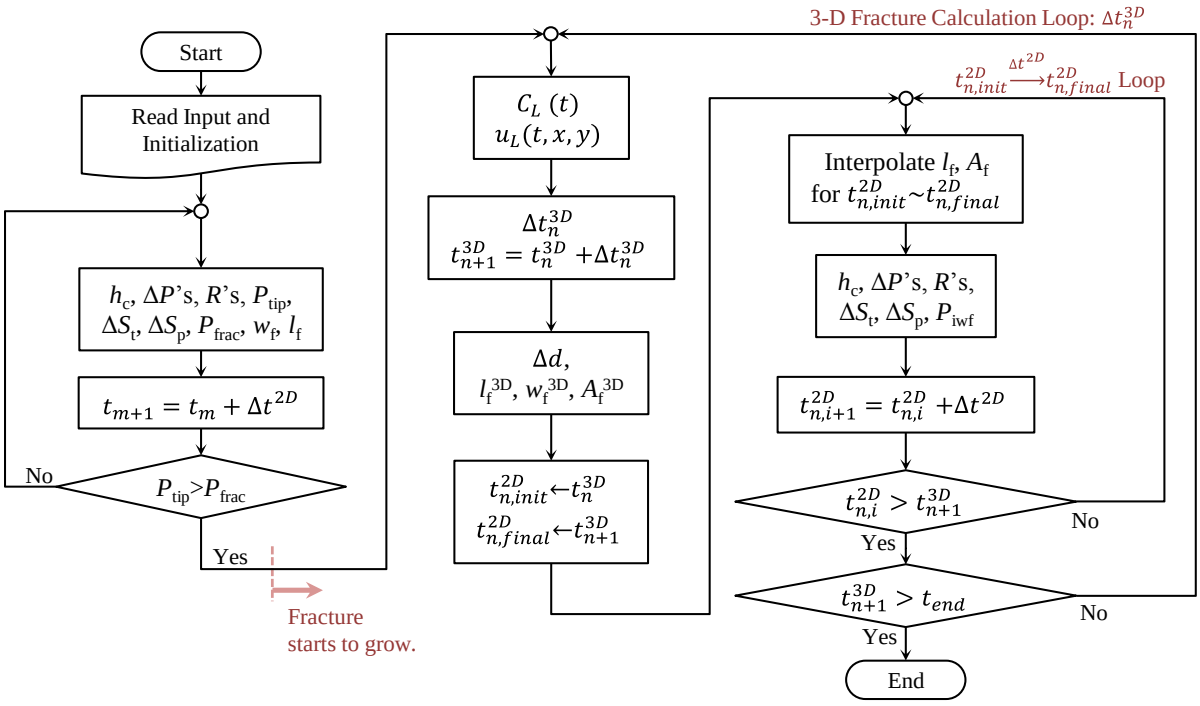

Figure 4.4: Main Algorithm. The outer loop conducts calculations for the fracture propagation (for time step $t^{3D}{}_n \rightarrow t^{3D}{}_{n+1}$) and the inner loop calculates the particle plugging model, fluid flow equations in the reservoir, and the stress changes for the time steps ($t^{2D}{}_{n,\text{init}} \rightarrow t^{2D}{}_{n,\text{final}}$).

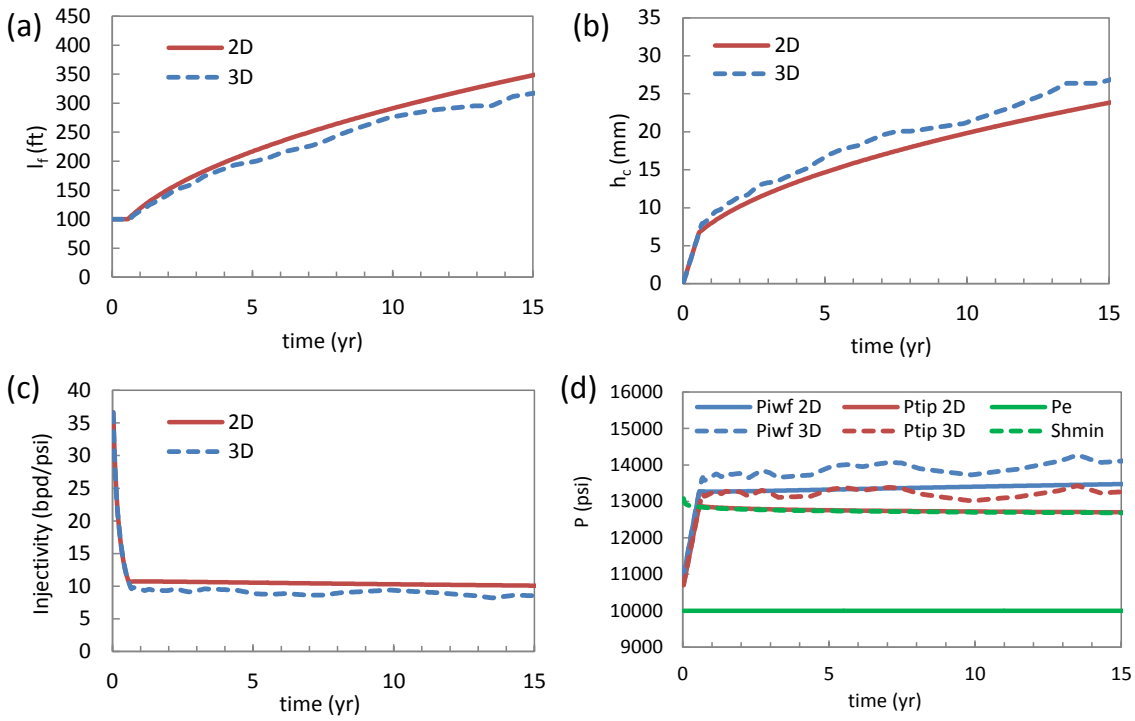

Figure 4.5: Results of the base case model. (a) Fracture half-length with time. (b) Thickness of the external filter cake on the fracture faces. (c) Injectivity of the well. (d) Flowing injection bottom-hole pressure and fracture tip pressure compared to the minimum horizontal stress and the reservoir boundary pressure. The results were compared to those of a water injection well model with 2-D fracture propagation.

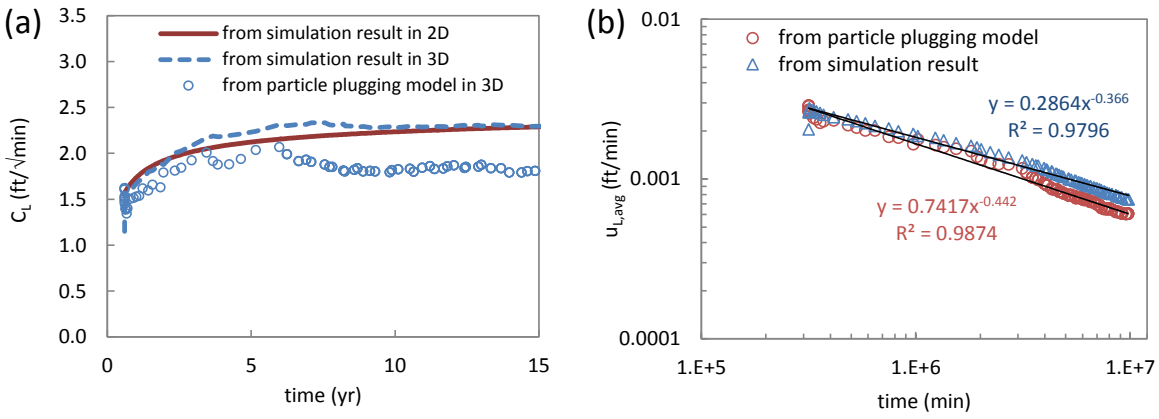

Figure 4.6: The leak-off behavior from the base case results. (a) The leak-off coefficient used in Carter's leak-off equation. The leak-off coefficient calculated from the particle plugging model is compared to the effective leak-off coefficients calculated from the simulation results. The coefficients from simulation results bears no physical significance, but the differences indicate the particle plugging model made the leak-off coefficient less than the traditional model.

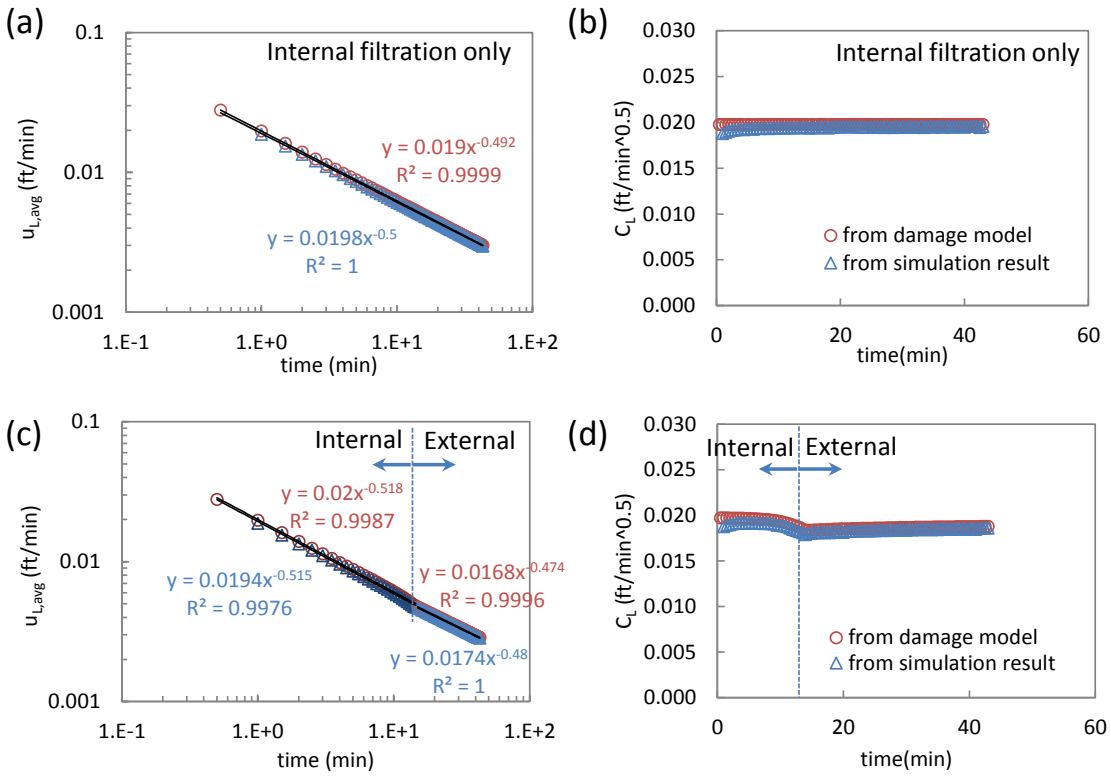

Figure 4.7: Leak-off behavior calculated by the adaptive leak-off model for a hydraulic fracturing simulation. (a, b) Only the internal filtration was simulated. (c, d) The transition from internal to external filtration was simulated. For all cases, leak-off behavior from the adaptive leak-off calculation and simulation results follows the conventional Carter's leak-off correlation.

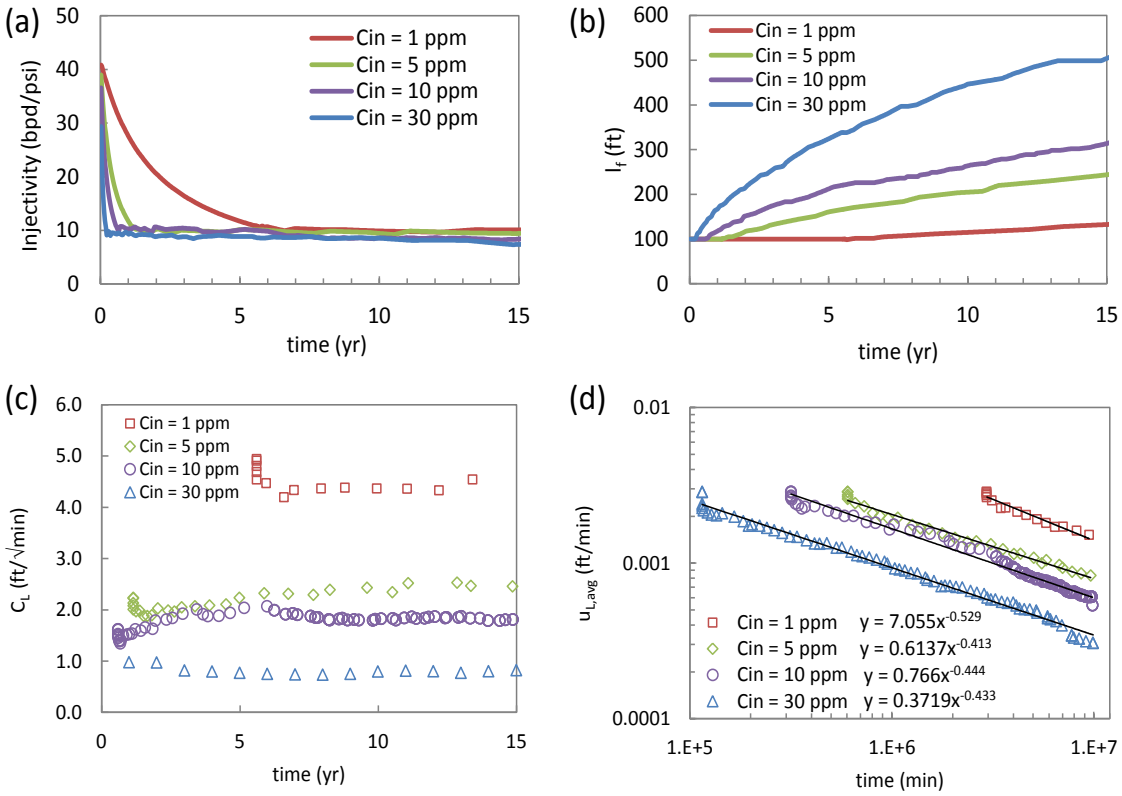

Figure 4.8: The effect of the injection water quality on (a) injectivity, (b) fracture length, and (c, d) leak-off behavior. Higher particle concentration in the injection water led to less leak-off and higher rate of fracture growth.

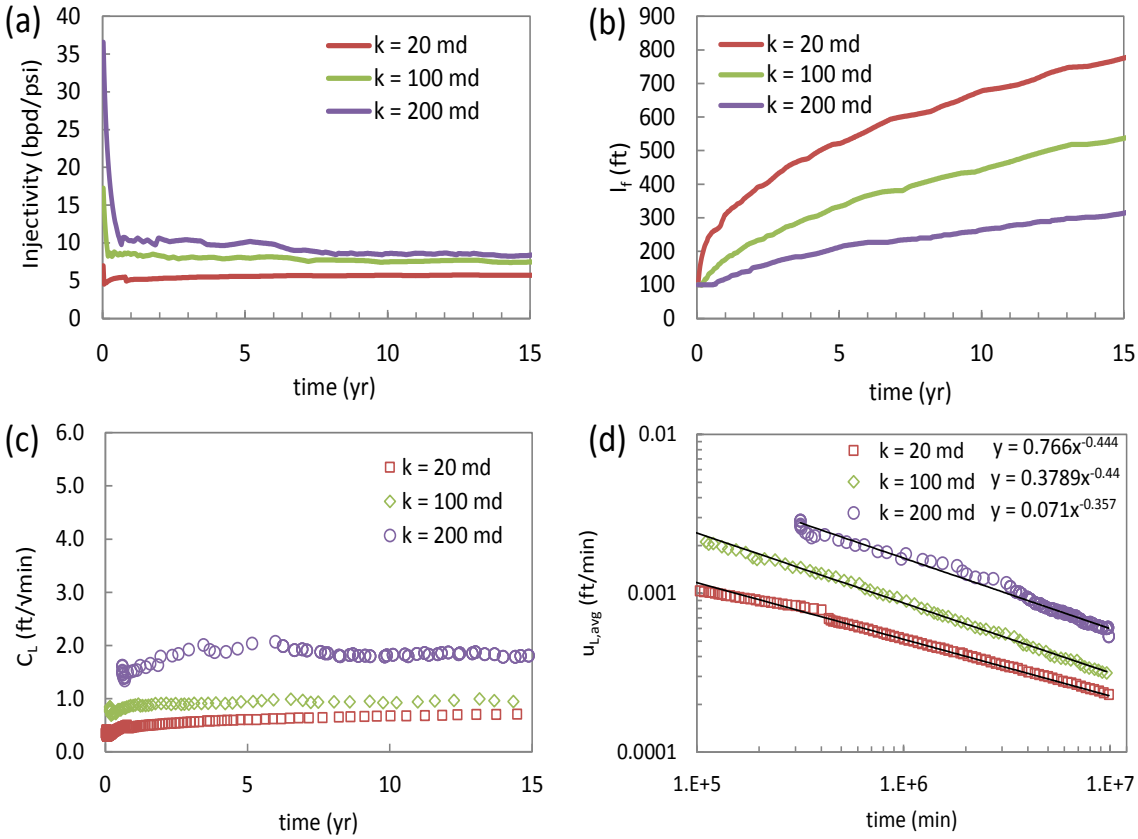

Figure 4.9: The effect of the initial permeability of the formation on (a) injectivity, (b) fracture length, (c, d) leak-off behavior. Higher matrix permeability in the injection water led to higher leak-off and a slower rate of fracture growth.

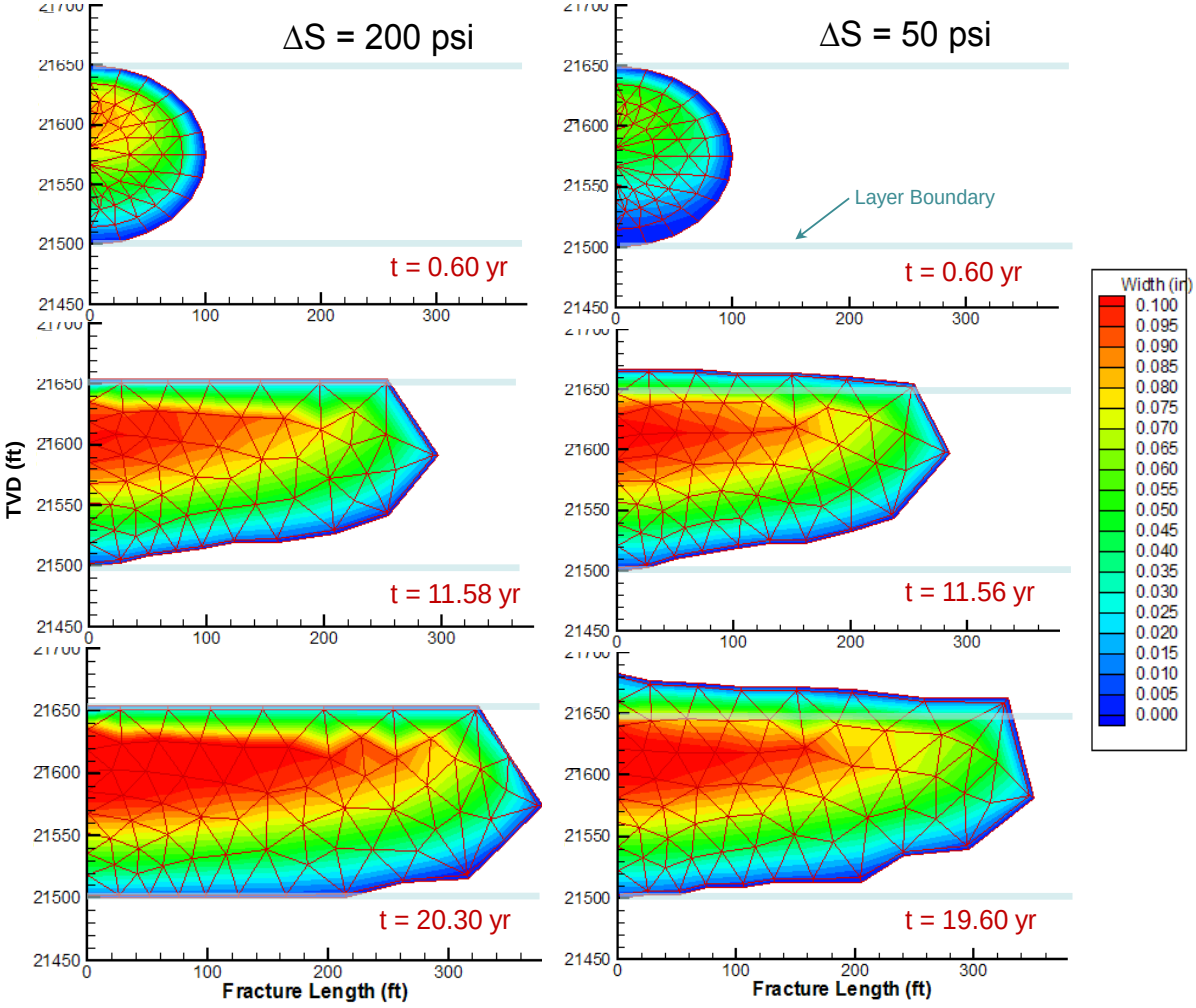

Figure 4.10: Effect of the stress difference between the sand and bounding layers on the fracture dimensions. Higher stress contains the fracture within the sand layer, but the fracture breaches into the bounding layers when the stress contrast is lower.

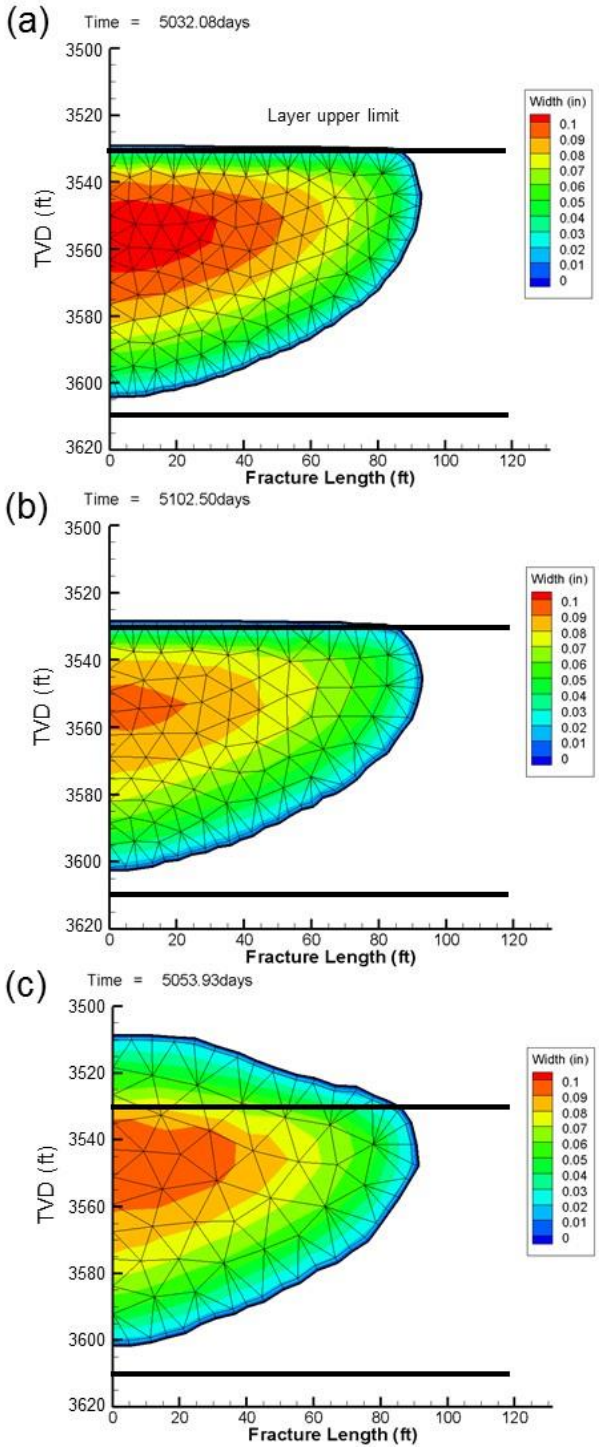

Figure 4.11: Effect of stress contrast between target and bounding layers on fracture shape and width. Fracture shapes at $t \approx 5000$days are shown. (a) Stress contrast is 282 psi, (b) 141 psi and (c) 56psi.

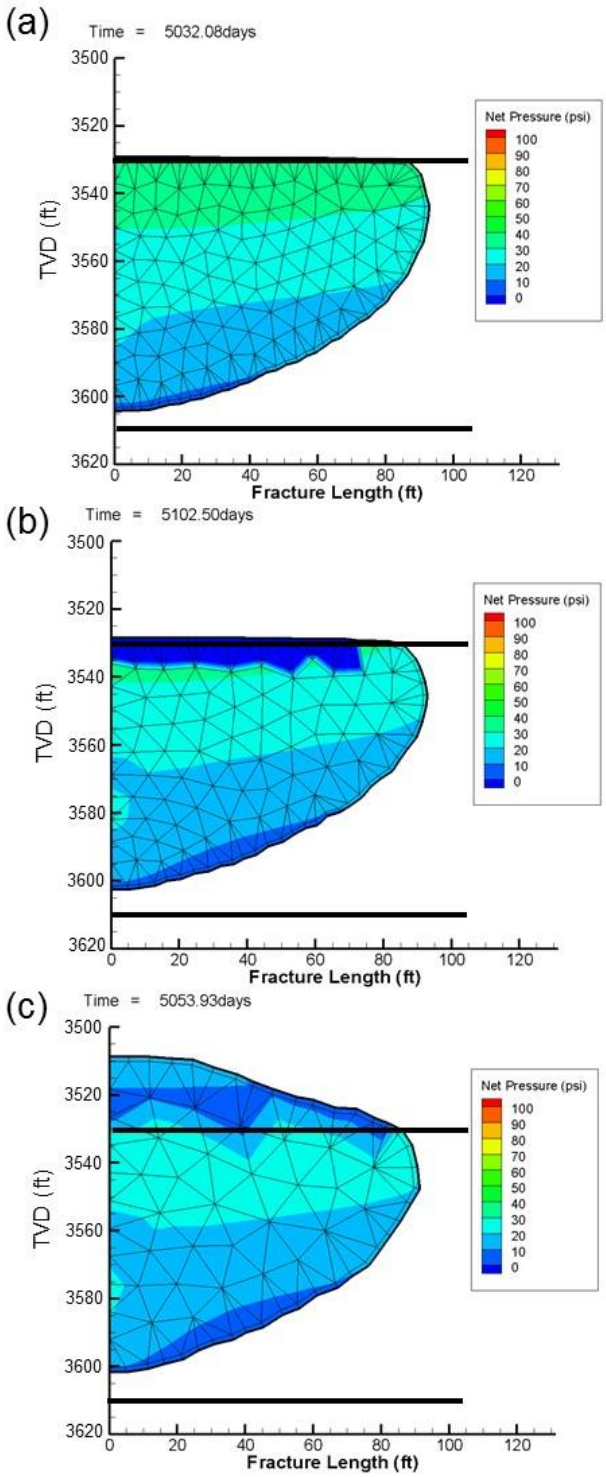

Figure 4.12: Effect of stress contrast between target and bounding layers on fracture shape and width. Fracture shapes at t≈5000days are shown. (a) Stress contrast is 282 psi, (b) 141 psi and (c) 56psi.

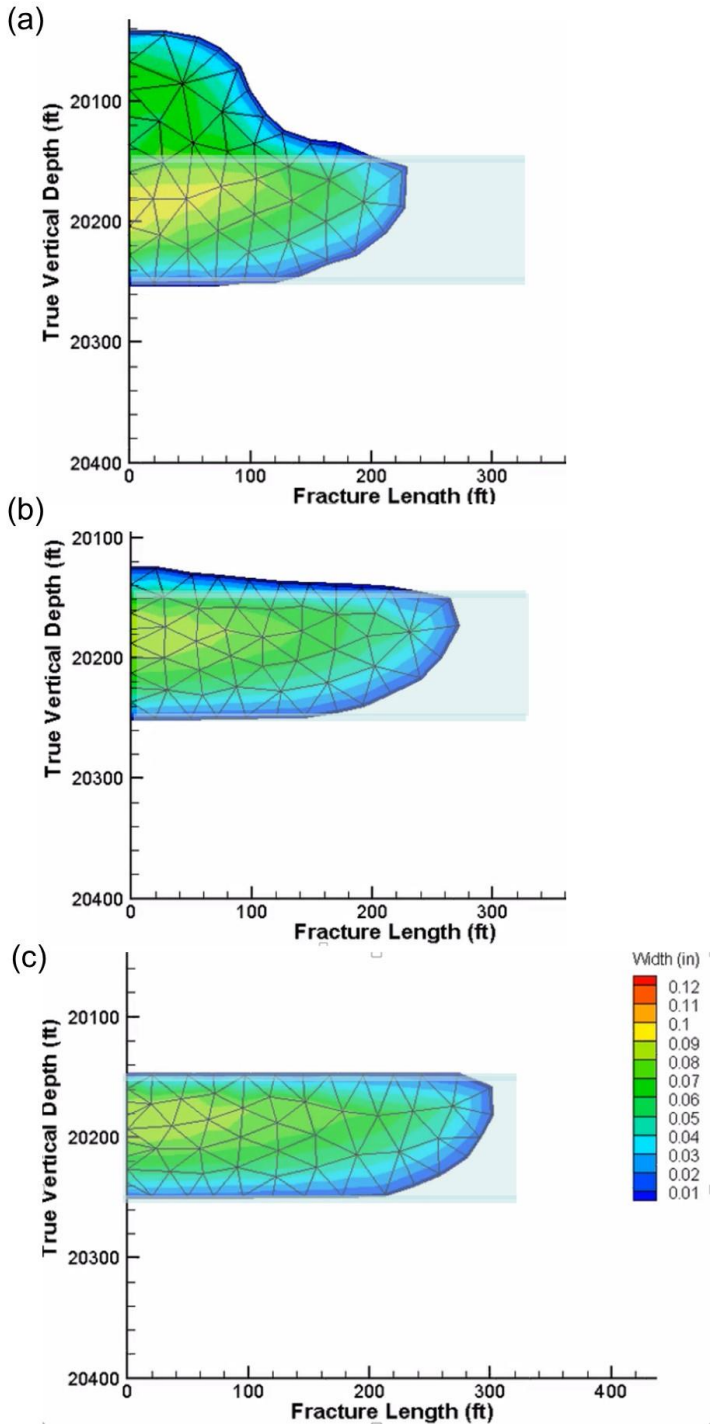

Figure 4.13: Effect of stress contrast between target and bounding layers. Fracture shapes are at $t \approx 10$yrs. (a) Stress contrast is 98psi, (b) 112psi and (c) 200psi.

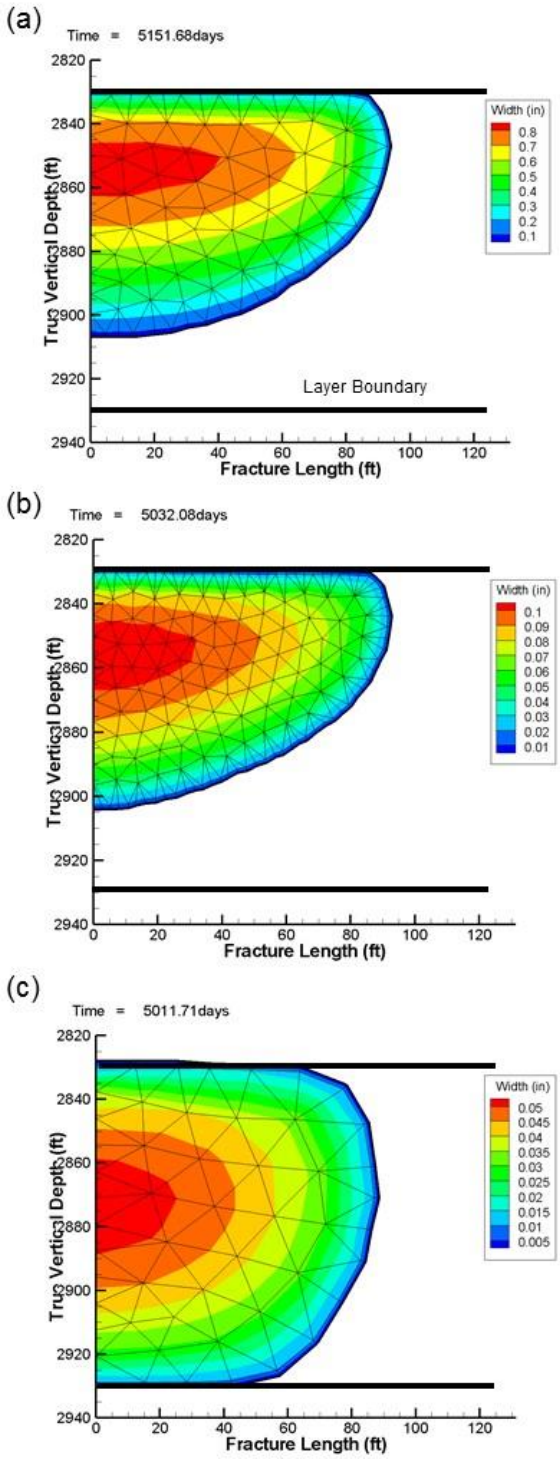

Figure 4.14: Effect of Young's modulus and fracture toughness on fracture width. (a) E=32500psi, K_{Ic}=144psi·√in, (b) E=325000psi, K_{Ic}=450psi·√in, and (c) E=3250000psi, K_{Ic}=1440psi·√in

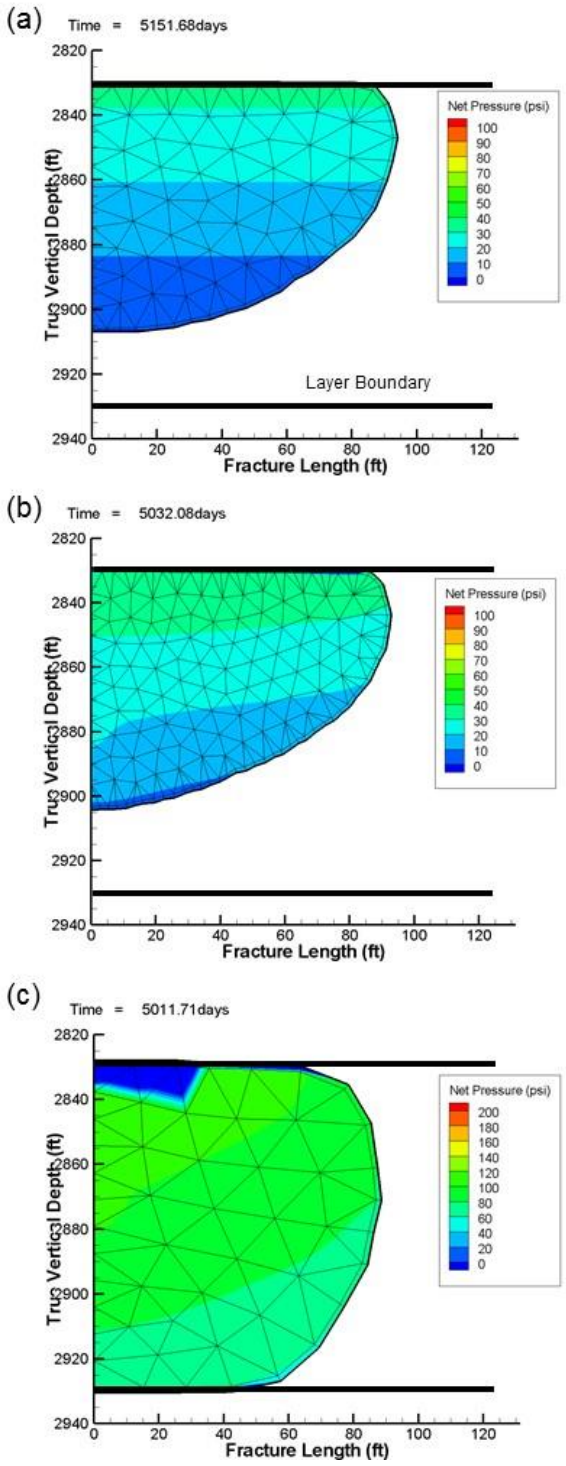

Figure 4.15: Effect of Young's modulus and fracture toughness on fracture width. (a) E=32500psi, K_{Ic}=144psi·√in, (b) E=325000psi, K_{Ic}=450psi·√in, and (c) E=3250000psi, K_{Ic}=1440psi·√in

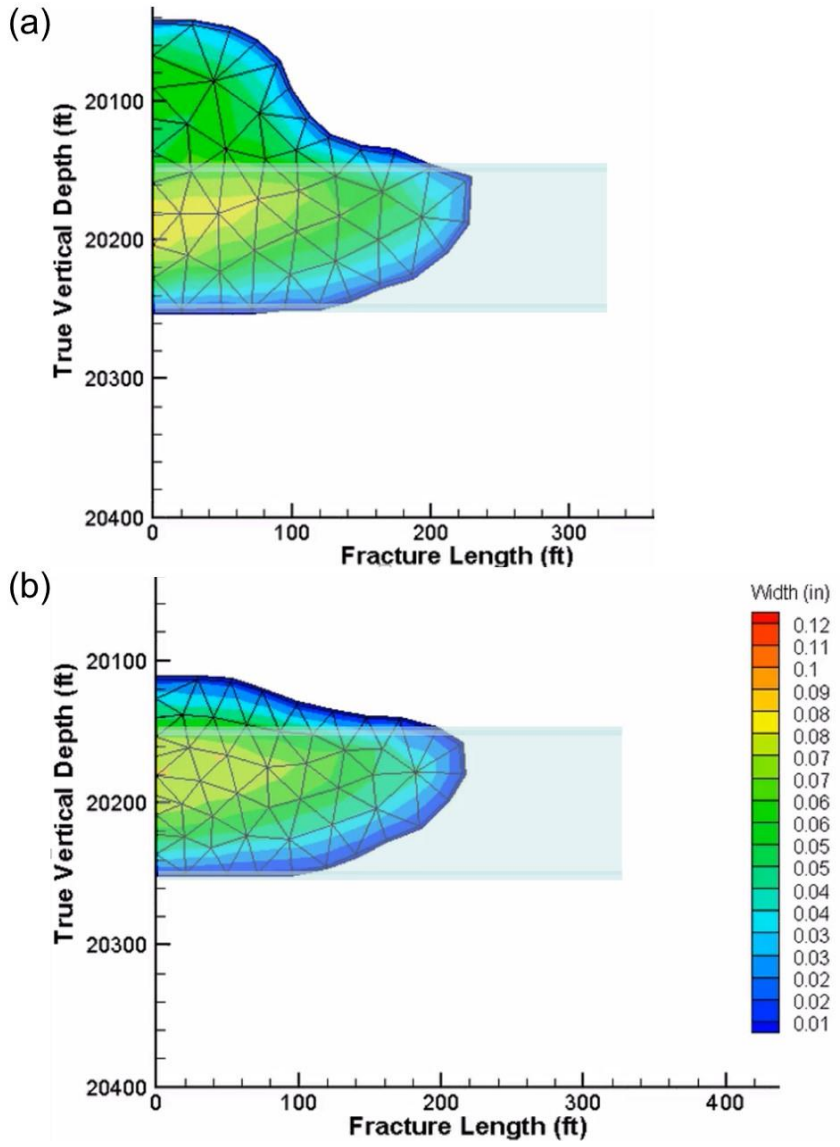

Figure 4.16: Effect of the stress intensity factor on fracture shape. Stress contrasts between target and bounding layers were 98 psi for both cases. Fracture shapes are at $t \approx$ 10yrs. (a) K_{Ic}=900psi·√ft and (b) K_{Ic}=1000psi·√ft

Nomenclature

A_f = Area of fracture face, L^2, ft^2

a_0 = Major axis of the thermal front ellipse, L^1, ft

a_1 = Major axis of the waterflood front ellipse, L^1, ft

b_0 = Minor axis of the thermal front ellipse, L^1, ft

b_1 = Minor axis of the waterflood front ellipse, L^1, ft

C_L = Leak-off coefficient in Carter's correlation, $L^1t^{-0.5}$, ft/√min

Δd = Increment frontal displacement of fracture node, L^1, ft

E = Young's modulus, $m^1L^{-1}t^{-2}$, psi

G = Shear modulus, $m^1L^{-1}t^{-2}$, psi

h_c = Thickness of external filter cake, L^1, mm

h_d = depth of the fracture in the high *in situ* stress layer, L^1, m

H_l = Local fracture height, L^1, m

I = Injectivity ($=q_{inj}/(P_{iwf}-P_e)$), $m^2L^1t^1$, bpd/psi

k = Permeability of formation, L^2, Darcy

k_c = Permeability of filter cake, L^2, Darcy

K_I = Stress intensity factor, $m^{1.5}L^{-1}t^{-2}$, psi√in

K_{IC} = Critical stress intensity factor, $m^{1.5}L^{-1}t^{-2}$, psi√in

k_{ro} = Relative permeability to oil, −

k_{rw} = Relative permeability to water, −

L_{DZ} = Depth of internal damaged zone, L^1, m

L_f = Fracture length, L^1, m

P = Pressure, $m^1L^{-1}t^{-2}$, psi

P_e = Pressure at reservoir boundary, $m^1L^{-1}t^{-2}$, psi

P_{frac} = Fracturing pressure at the tip of 2-D fracture, $m^1L^{-1}t^{-2}$, psi

P_{iwf} = Flowing injection pressure at bottom-hole, $m^1L^{-1}t^{-2}$, psi

P_{tip} = Pressure at fracture tip, $m^1L^{-1}t^{-2}$, psi

ΔP_1 = Pressure rise between connate waterflood front and reservoir boundary, $m^1L^{-1}t^{-2}$, psi

ΔP_2 = Pressure rise between connate waterflood front and injected waterflood front, $m^1L^{-1}t^{-2}$, psi

ΔP_3 = Pressure rise between injected waterflood front and thermal front, $m^1L^{-1}t^{-2}$, psi

ΔP_4 = Pressure rise between thermal front and the fracture, $m^1L^{-1}t^{-2}$, psi

ΔP_s = Pressure increase by particle deposition on fracture face, $m^1L^{-1}t^{-2}$, psi

q_{inj} = Injection flowrate, L^3t^{-1}, bbl/d

q_L = Volumetric leak-off flowrate, L^3t^{-1}, bbl/d

R_1 = Fluid flow resistance corresponding to ΔP_1, $m^{-2}L^{-1}t^{-1}$, psi/bpd

R_2 = Fluid flow resistance corresponding to ΔP_2, $m^{-2}L^{-1}t^{-1}$, psi/bpd

R_3 = Fluid flow resistance corresponding to ΔP_3, $m^{-2}L^{-1}t^{-1}$, psi/bpd

R_4 = Fluid flow resistance corresponding to ΔP_4, $m^{-2}L^{-1}t^{-1}$, psi/bpd

r_f = Radius of circular fracture tip, L^1, m

R_{int} = Fluid flow resistance by internal filter cake, $m^{-2}L^{-1}t^{-1}$, psi/bpd

R_s = Fluid flow resistance corresponding to ΔP_s, $m^{-2}L^{-1}t^{-1}$, psi/bpd

R_{und} = Fluid flow resistance of undamaged zone, $m^{-2}L^{-1}t^{-1}$, psi/bpd

S = Total stress, $m^1L^{-1}t^{-2}$, psi

S_{hmin} = Minimum horizontal *in situ* stress, $m^1L^{-1}t^{-2}$, psi

S_{tip} = local *in situ* stress at the tip, $m^1L^{-1}t^{-2}$, psi

t_{inj} = Injection time, t^1, min

t_n^{2D} = Simulation time used in formation damage module, t^1, s

t_n^{3D} = Simulation time used in fracture growth module, t^1, s

u_L = Linear velocity of fluid leak-off, L^1t^{-1}, ft/min

V_{frac} = Volume of the fracture, L^3, ft^3

V_{inj} = Cumulative injection volume, L^3, ft^3

V_L = Cumulative leak-off volume, L^3, ft^3

w = Fracture width, L^1, inch

γ = Specific surface energy, m^1t^{-2}, Pa·m

μ = Viscosity, $m^1L^{-1}t^{-1}$, Pa·s

μ_o = Viscosity of oil, $m^1L^{-1}t^{-1}$, Pa·s

μ_{wi} = Viscosity of water at injection temperature, $m^1L^{-1}t^{-1}$, Pa·s

μ_{wr} = Viscosity of water at reservoir temperature, $m^1L^{-1}t^{-1}$, Pa·s

ν = Poisson's ratio, −

σ = Effective stress, $m^1L^{-1}t^{-2}$, psi

$\Delta\sigma_I$ = Driving stress of mode-I fracture (net pressure), $m^1L^{-1}t^{-2}$, psi

References

Abou-Sayed, A. S., Sinha, K. P., & Clifton, R. J. 1984. Evaluation of the Influence of *In situ* Reservoir Conditions on the Geometry of Hydraulic Fractures Using a 3-D Simulator: Part 1-Technical Approach. Paper SPE 12877 presented at the SPE Unconventional Gas Recovery Symposium, 13-15 May 1984, Pittsburgh, Pennsylvania. http://dx.doi.org/10.2118/12877-MS

Bui, H. D. 1977. An Integral Equations Method for Solving the Problem of a Plane Crack of Arbitrary Shape. *Journal of the Mechanics and Physics of Solids*, **25** (1): 29–39. http://dx.doi.org/10.1016/0022-5096(77)90018-7

Carter, R. D. 1957. Appendix I - Derivation of the General Equation for Estimating the Extent of the Fractured Area. *Optimum Fluid Characteristics for Fracture Extension by G.C. Howard and C.R. Fast*, Drilling and Production Practice (pp. 261–269). American Petroleum Institute.

Clifford, P. J., Berry, P. J., & Gu, H. 1991. Modeling the Vertical Confinement of Injection-well Thermal Fractures. *SPE Production Engineering*, **6** (04): 377–383. http://dx.doi.org/10.2118/20741-PA

Economides, M. J., & Nolte, K. G. (Eds.). 2000. *Reservoir Stimulation* (3rd ed.). John Wiley & Sons.

Fung, R. L., Vilayakumar, S., & Cormack, D. E. 1987. Calculation of Vertical Fracture Containment in Layered Formations. *SPE Formation Evaluation*, **2** (04): 518–522. http://dx.doi.org/10.2118/14707-PA

Gadde, P., & Sharma, M. 2001. Growing Injection Well Fractures and Their Impact on Waterflood Performance. Paper SPE 71614 presented at the SPE Annual Technical Conference and Exhibition, 30 September-3 October 2001, New Orleans, Louisiana. http://dx.doi.org/10.2118/71614-MS

Garcia, X., Nagel, N., Zhang, F., Sanchez-Nagel, M., et al. 2013. Revisiting Vertical Hydraulic Fracture Propagation Through Layered Formations – A

Numerical Evaluation. *47th U.S. Rock Mechanics/Geomechanics Symposium*. Paper ARMA 13-203 presented at the 47th U.S. Rock Mechanics/Geomechanics Symposium, 23-26 June, San Francisco, California. Retrieved from https://www.onepetro.org/conference-paper/ARMA-2013-203

Griffith, A. A. 1921. The Phenomena of Rupture and Flow in Solids. *Philosophical Transactions of the Royal Society of London. Series A, Containing Papers of a Mathematical or Physical Character*, **221** (582-593): 163–198. http://dx.doi.org/10.1098/rsta.1921.0006

Gringarten, A., Henry J., R., & Raghavan, R. 1974. Unsteady-State Pressure Distributions Created by a Well With a Single Infinite-Conductivity Vertical Fracture. *Society of Petroleum Engineers Journal*, **14** (4): 347–360. http://dx.doi.org/10.2118/4051-PA

Gu, H. 1987. *Study of Propagation of Hydraulically Induced Fractures*. The University of Texas at Austin, USA.

Mastrojannis, E. N., Keer, L. M., & Mura, T. 1980. Growth of Planar Cracks Induced by Hydraulic Fracturing. *International Journal for Numerical Methods in Engineering*, **15** (1): 41–54. http://dx.doi.org/10.1002/nme.1620150105

Ouyang, S. 1994. *Propagation of Hydraulically Induced Fractures with Proppant Transport*. The University of Texas at Austin, USA.

Pang, S., & Sharma, M. M. 1997. A Model for Predicting Injectivity Decline in Water-Injection Wells. *SPE Formation Evaluation*, **12** (3): 194–201. http://dx.doi.org /10.2118/28489-PA

Perkins, T. K., & Gonzalez, J. A. 1985. The Effect of Thermoelastic Stresses on Injection Well Fracturing. *Society of Petroleum Engineers Journal*, **25** (1): 78–88. http://dx.doi.org/10.2118/11332-PA

Rajagopalan, R., & Tien, C. 1976. Trajectory Analysis of Deep-Bed Filtration with the Sphere-in-Cell Porous Media Model. *AIChE Journal*, **22** (3): 523–533. http://dx.doi.org/10.1002/aic.690220316

Saripalli, K., Bryant, S., & Sharma, M. 1999. Role of Fracture Face and Formation Plugging in Injection Well Fracturing and Injectivity Decline. Paper SPE 52731 presented at the SPE/EPA Exploration and Production Environmental Conference, 1-3 March 1999, Austin, Texas. http://dx.doi.org/10.2118/52731-MS

Sharma, M. M., Pang, S., Wennberg, K. E., & Morgenthaler, L. N. 2000. Injectivity Decline in Water-Injection Wells: An Offshore Gulf of Mexico Case Study. *SPE Production & Facilities*, **15** (1): 6–13. http://dx.doi.org/10.2118/60901-PA

Simonson, E. R., Abou-Sayed, A. S., & Clifton, R. J. 1978. Containment of Massive Hydraulic Fractures. *Society of Petroleum Engineers Journal*, **18** (01): 27–32. http://dx.doi.org/10.2118/6089-PA

Suri, A., & Sharma, M. 2009. Fracture Growth in Horizontal Injectors. Paper SPE 119379 presented at the SPE Hydraulic Fracturing Technology Conference, 19-21 January 2009, The Woodlands, Texas. http://dx.doi.org/10.2118/119379-MS

Suri, A., & Sharma, M. 2010. A Model for Water Injection Into Frac-Packed Wells. *SPE Reservoir Evaluation & Engineering*, **13** (3): 449–464. http://dx.doi.org/10.2118/110084-PA

Suri, A., Sharma, M., & Peters, E. 2011. Estimates of Fracture Lengths in an Injection Well by History Matching Bottomhole Pressures and Injection Profile. *SPE Reservoir Evaluation & Engineering*, **14** (4): 385–397. http://dx.doi.org/10.2118/132524-PA

Teufel, L. W., & Clark, J. A. 1984. Hydraulic Fracture Propagation in Layered Rock: Experimental Studies of Fracture Containment. *SPE Journal*, **24** (01): 19–32. http://dx.doi.org/10.2118/9878-PA

Van den Hoek, P. J. 2005. Dimensions and Degree of Containment of Waterflood-Induced Fractures from Pressure Transient Analysis. *SPE Reservoir Evaluation & Engineering*, **8** (05): 377–387. http://dx.doi.org/10.2118/84289-PA

Van Eekelen, H. A. M. 1982. Hydraulic Fracture Geometry: Fracture Containment in Layered Formations. *Society of Petroleum Engineers Journal*, **22** (03): 341–349. http://dx.doi.org/10.2118/9261-PA

Wennberg, K. E., & Sharma, M. M. 1997. Determination of the Filtration Coefficient and the Transition Time for Water Injection Wells. Paper SPE 38181 presented at the SPE European Formation Damage Conference, 2-3 June 1997, The Hague, Netherlands. http://dx.doi.org/10.2118/38181-MS

Yew, C. H. 1997. *Mechanics of Hydraulic Fracturing*. Gulf Professional Publishing.

Chapter 5 : Stress Reorientation in Waterflooded Reservoirs

5.1 INTRODUCTION

5.1.1 Summary

Waterflooding significantly changes the magnitude and orientation of reservoir stress states. This chapter presents a new coupled simulator that incorporates two-phase flow and thermo-poro-elastic behavior. The simulation was applied to waterflooding well patterns and it indicates significant stress reorientation over a large spatial extent in the field. Simulations also show the complexity of thermal stresses in different well patterns. The model is applied to horizontal wells, allowing researchers to investigate the impacts of stress reorientation on fracture growth, reservoir sweep, and oil recovery.

The model was validated with known solutions by comparing stresses, pressures and fluid saturations. It was then applied to different vertical well patterns. The combined effect of poro-thermo-elastic stresses are shown to provide critical information about sweep efficiencies which have significant impacts on waterflood design and management. Estimates of recovery factors, infill-well designs, and injection-induced fracture orientations are critically affected by the reoriented stress state. The reservoir heterogeneity and natural fracture stimulation are important in altering stress reorientation and oil recovery.

The model clearly shows that stress-reorientation during waterflooding is not a near-well phenomenon, but instead occurs on a field scale. Even for simple five-spot models, the complete reversal between the maximum and minimum horizontal stress directions occurs far away from wells. The contrast between horizontal stresses also significantly changes, indicating where natural fracture networks are likely to be stimulated.

Fracture propagation based on reoriented stress field indicates that well locations and patterns can significantly impact oil recovery. By using the same model for horizontal well patterns, similar effects are demonstrated.

Stress reorientation and subsequent non-planar fracture growth is extremely important in predicting secondary and tertiary oil recovery. The simulations presented here can be used to specify well spacing and patterns to improve reservoir sweep. *In situ* stresses are reoriented by the pore pressure, temperature, and fracture growth of different well configurations. These factors determine the direction of injection-induced fractures. Simulation results that systematically show the impact of this stress reorientation on oil recovery under different reservoir, fluid conditions and well patterns are presented in this research.

5.1.2 Motivation

The injection and production activities during waterflooding operations can substantially change the pressure, temperature and water-oil-gas saturations of the field. Along with the changes in these properties, the multiphase flow on a field scale can also significantly change the *in situ* stress state in waterflooded reservoirs. The fluid production and injection can change both the magnitudes and the directions of the stress in an oilfield.

It is important that operators have this stress information on a real-time basis so they can estimate the fracture growth induced by the injectors. The reoriented stress status will determine the fracture direction and dimensions which may differ from the far-field stress state. It will also determine how natural fractures will be stimulated. When an infill well is located, the effect of injection and production on *in situ* stresses needs to be assessed. The wellbore stability calculation needs to be based on the stress status of where the well was located at the time of drilling. If an infill well is to be stimulated with a fracture, both the direction and magnitude of the stress need to be assessed. This allows operators to

predict the shape and dimension of the fractures.

In this chapter, the flow, geomechanics and energy balance of an immiscible, slightly compressible two-phase flow in porous medium will be examined. The new simulation calculates changes in pressure, water-oil saturations, temperature, deformation, and stress when waterflooding reservoirs. The simulator will be validated with known solutions for thermo- and poro-elastic stress changes. Stress changes in simple well patterns, e.g., five-, nine-spot, line-drive well patterns, are assessed so we can investigate the fluid injection-production effect. Horizontal well pairs and multiple injection-production wells were also tested to act as more realistic field cases.

5.1.3 Factors Controlling Stress Reorientation

Subsurface stress states can be changed by three main effects: poroelastic, thermo-elastic, and mechanical effects. The poroelastic effect mainly comes from the pressure gradient created by fluid injection and production. Along with poroelastic effects, the temperature difference between the injection fluid and the reservoir induces thermo-elastic changes in the subsurface stress state. In most cases, the injection fluid temperature is lower than the reservoir temperature. This thermal effect causes the rock formation near the injectors to contract and the magnitude of stress to decrease. Another effect that can change the subsurface stress condition is the mechanical effect caused by a fracture opening or other type of rock failure or deformation. In this study, we simulate the impact of each one of these effects but mainly investigate poro- and thermo-elastic effects.

Increased pore-pressure induces an increase in the compressive stress. If pore pressure is lowered, the compressive stress state is relieved to a lower value. Higher temperature injection leads to a higher compressive stress, while a lower temperature injection leads to a lower stress. Fracture opening will lead to a locally higher stress in a direction perpendicular to the fracture faces. If the vertical-direction stress is high enough

to be the highest principal stress direction despite the above effects, horizontal stresses will mainly reorient in the horizontal plane. The directions of maximum and minimum horizontal stresses, S_{Hmax} and S_{hmin} will change. For example, the direction of S_{Hmax} near the hot-water injector will reorient radially to the well.

Roussel & Sharma (2011) examined the stress reorientation caused by a fracture opening when fracturing horizontal wells in shale reservoirs. In their study, the stress induced by the creation of propped fractures in horizontal wells was calculated using a 3-dimensional (3D) numerical model. The extent of S_{Hmax} reorientation between fractures was shown to control the stimulation effectiveness. The poroelastic effect caused by production and the mechanical effect from the propped fracture were critical factors in predicting the *in situ* stress state.

In addition to these factors, the thermal effect on stress reorientation is important in maintaining the reservoir pressure and disposing water into the subsurface when water injection is continued for several years. In typical operating conditions, the injection water temperature is lower than that of the formation. The cold-water injection relieves near-well compressive stresses. The extent of the stress change is dependent not only on the injection-reservoir temperature difference, but also on operational conditions, such as injection rates and well types. As the effects of poroelasticity and thermoelasticity change the magnitude and direction of the stress in a competing manner, they both need to be accounted for when calculating the stress state during waterflooding.

Despite the importance of the subject, stress reorientation in waterflooding reservoirs has not been researched extensively. Studies on stress reorientation have focused more on unconventional plays, i.e., low-permeability reservoirs. One such study for unconventional plays is refracture optimization by Roussel & Sharma (2012). They conducted simulations using poroelastic and mechanical effects on stress reorientation to

optimize the candidate-well selection and the timing of a refracturing operation. Fredrich et al. (1996) applied a field-scale multi-well finite-element geomechanical model to suggest production-injection strategies to reduce well casing damage induced by reservoir compaction. Even though these studies are missing some critical components that may be more important in waterflooding stress-reorientation, e.g., multiple injector-producer or thermoelasticity, they provided insight and models to clarify how the *in situ* stress changes with pore-pressure changes, fracture growth, and injection-production activities.

5.1.4 Previous Studies on Impact of Fracture Growth and Stress Changes on Waterflooding

Researchers have investigated the effect of long-term production and injection on the sweep efficiency in waterflooding reservoirs. Many studies focused on the change to the sweep pattern of waterflooding reservoirs caused by fracture growth. Dikken & Niko (1987) investigated the effect of waterflood-induced fracture propagation on reservoir sweep. The fracture growth was, in many waterflooding cases, controlled by thermal effects. Garon et al. (1988) conducted simulations of thermally-induced fracturing in Prudhoe Bay and showed the importance of thermal effects. Stevens et al. (2000) also discussed the role of thermal fracturing in horizontal wells. Because waterflooding requires predictions of multiple physical effects, there have been attempts to simultaneously simulate these factors as in Settari & Warren (1994). Many coupled fluid-geomechanics simulations were developed and used for reservoir management.

Gadde & Sharma (2001) investigated the role of injection induced fractures on waterflooding oil recovery efficiency. They showed that the growth of such fractures could be adequately modeled using an explicit formulation that coupled fracture growth to the change in pressure due to injected solids. Fracture growth was shown to have a significant impact on oil recovery in multi-layered reservoirs. The stress field in the reservoir was not

computed.

Researchers also investigated changes in the stress-field during waterflooding. Wright et al. (1994) indicated large changes in a local stress-field due to a waterflooding pressure-gradients in a low-permeability diatomite field. Estimated stress changes were compared to the fracture mapping that had been done using tiltmeters. Their field history made it clear that the role of stress reorientation was critical to the success of secondary oil recovery. In their continuing work (Wright et al., 1995), stress reorientation was explained by three mechanisms: reservoir compaction, poroelastic effects, and fault-slip effects. The reservoir compaction was created mainly by production and the thermal effect of cold water injection. Their work was not validated with a numerical simulation approach, but research on stress states during waterflooding started to draw the industry's attention. Their work showed that designing a well pattern without considering the reoriented stress field can potentially lead to an unswept corridor of oil.

Another work that utilized field-scale geomechanics in waterflooding is the research completed by Dons et al. (2007). They showed that the seismic responses induced by fluid substitution and pressure gradients during long-term waterflooding can be interpreted as rock hardening and softening. This is a good example of the effect of fluid injection spanning field-wide stress changes. The acoustic impedance variation in their study clearly showed the fluid displacement to be dependent on reservoir, rock, fluid properties and operational conditions. They indicated that the fracture induced by water injection was also a critical factor in affecting the impedance variation.

Well configurations and patterns are known to be important factors in waterflood management. Minner et al. (2002) showed that fracture orientations depend critically on the pattern of injectors and producers and their interactions, based on the concept of stress reorientation. The results showed that hydraulic fracture azimuth variability was smaller in

infill wells located along injectors when compared to those located near producers. In their stress reorientation calculations, the stress reorientation primarily occurred near producers. Their work emphasized the importance of well configurations and patterns.

Optimizing the reservoir-management strategy based on induced-fracture prediction is considered to be important. Ovens et al. (1998) evaluated fracture orientations and dimensions by tracer injection, saturation log, water-cut monitoring, and injection fall-off surveys in the waterflooded field. They were able to see the effect of injector-producer interaction on fracture propagation geometry. The estimated fracture-orientations were used for producer placement and reservoir-sweep predictions. van den Hoek et al. (2008) also showed a waterflooding optimization process to estimate dynamically-induced fractures during waterflooding.

The above work showed that stresses can reorient significantly in a field, with these changes being induced both by pressure gradients and by thermal effects. It was also shown that the resulting fracture reorientations and sweep efficiencies can change the recovery efficiencies. This is critical for waterflood project management. The studies highlighted above provide practical insights into the applicability of stress management and its impact on field economics. Based on these insights, more systematic approaches are suggested in this work that can address the impact of stress changes based on a new geomechanical simulator.

5.1.5 Coupled Fluid-Geomechanics Simulation Approaches

Since the 1990's, interest has developed in stress management focusing on unconventional resources. Accordingly, coupled simulations to calculate fluid-flow and stress-state have been developed. These simulations solve reservoir stresses and deformations together with conventional reservoir flow simulations. Such models can be categorized into explicitly-coupled, iteratively-coupled, and fully-coupled simulations.

Dean et al. (2006) compared these different techniques in the coupling methods of reservoir fluid flow and geomechanics.

Koutsabeloulis & Hope (1998) created a fully and partially coupled reservoir simulation that deals with stress, multi-phase fluid flow, and thermal effects. Work by Tran et al. (2002) is an example of an iteratively-coupled reservoir-geomechanics simulation. L. K. Thomas et al. (2003), Kim, Moridis, Yang, et al. (2012), and Kim, Moridis, & Rutqvist (2012) also suggested coupled flow-geomechanics simulations.

Some simulation approaches include additional features specific to their applications. Chen & Teufel (2000) applied coupled flow-geomechanics simulations to naturally fractured reservoirs. Monteagudo et al. (2011) extended the capability of a fully-coupled simulation for two-phase flow, which was then applied to a discrete fracture network. In some cases, induced fractures were simulated along with geomechanics simulations. Ji et al. (2004) presented methods to model a propagating fracture on the platform of a coupled reservoir-geomechanics simulation. They incorporated fracture grids into the reservoir domain by modifying its transmissibilities. The fracture was estimated to propagate in a pre-defined direction and planar. Hustedt et al. (2005) modeled fractures induced by water injection. They developed a reservoir simulator and a fracture simulator, and then explicitly coupled the two modules. They had the same limitation in the fracture shape with Ji et al. (2004)'s work. In their continuing research, Hustedt et al. (2008) applied their model to a waterflooded field example. They predicted that the well patterns will affect the fracture geometry and directions, but did not use the concept of stress reorientation in this work.

5.2 MODEL DEVELOPMENT

5.2.1 Features

To properly calculate stress changes caused by injection and production of fluids in reservoirs, it is essential to build a multi-phase and multi-well reservoir simulation model which can account for the following:

- Multiphase fluid flow
- Poro-elasticity
- Thermo-elasticity
- Effect of mechanical rock failure on reservoir stresses
- Pressure- and rate-constrained well model
- 3D discretization
- Fracture propagation

A simulation model that handles these factors can serve as a general fluid-geomechanics simulation. In this chapter, we build a general model that is capable of accounting for these important subsurface phenomena. Some of the above factors are inter-related and a simulation model should handle all of the above factors simultaneously in a properly coupled manner. The model is designed so that some of features may be turned off depending on the specific application so that the speed of the simulation can be maximized.

A general purpose reservoir-fluid-geomechanics simulation can serve as a starting point for many specific applications. It can also supplement many reservoir simulation or field operational and management applications. Some examples of the simulation's applications are:

- Flow-back of fracturing fluid
- Stress reorientation by multi-phase injection/production
- Fracture growth during waterflooding

- Productivity calculation of stimulated wells
- Reservoir fluid-flow calculation coupled with fracture propagation
- Shale resources with gas-condensate
- Reservoir compaction and surface subsidence

5.2.2 Methodology

A coupled flow-geomechanics simulation was developed for the two-phase flow of slightly compressible fluids in reservoirs. The formulation was based on the strong forms of the two-phase flow, energy balance, and stress equations. Equations were discretized by the finite volume method. Then, an extended version of the IMPES (Implicit-Pressure, Explicit-Saturation) algorithm was utilized to couple these equations. The fluid pressures and saturations of each phase in the reservoir were calculated, as well as the temperature value, displacement (rock deformation) vector and stress tensor in reservoirs. The simulation was compared with known analytic solutions as a validation process. The pressure and saturations were compared with Buckley-Leverett solutions for 1-dimensional (1D) flow. The simulation results of water saturation profiles at various dimensionless times were very similar to the corresponding Buckley-Leverett solutions. Stress reorientation in single wells were compared with known behavior in reservoirs. More complicated waterflooding well-pattern models were also created, and their results were qualitatively analyzed.

This chapter outlines a first attempt to create a general-purpose multiphase-geomechanics reservoir simulation using OpenFOAM, a computational fluid dynamics package by OpenCFD Ltd. (ESI Group). The package is a library of continuum mechanics solutions written in C++. FOAM stands for Field Operation And Manipulation. The main feature of OpenFOAM is that it provides the discretization of partial differential equations in strong forms based on the finite volume method. It has other important functions,

including:

- Meshing capability
- Extensive range of numerical and interface features
- Extendibility to implement multiple models
- Easy applicability to avoid complex discretization
- Existing reference applications

Partial differential equations that solve pressure, saturations, temperature, displacement, and stress were formulated in the applicable forms for OpenFOAM. Algorithms were created to allow us to fully utilize the above features of the program.

5.2.3 Assumptions

This simulation can be applied to the water-oil two-phase fluid flow in reservoirs. The formulation was based on 3D arbitrary geometry. The assumptions used for the derivation of two-phase formulation are:

- The reservoir is non-isothermal.
- Fluids are immiscible and slightly compressible two-phases of liquids, typically oil and water.
- Fluid pressures in reservoirs are maintained above the bubble-point pressure, and no gas phase exists in reservoirs.
- Any simple shape of grids can be used. Rectangular and triangular meshes were used.
- A full permeability tensor can be used.
- There is no interaction of the fluid with the rock (solid) component.

The assumptions used for development methodology are:

- An IMPES formulation is used.
- An arbitrary number of wells and locations can be used.

- Wells can be injectors or producers.
- Well constraints of water rate, oil rate, and total liquid rate or pressure are individually defined for each recurrent scheme.
- Varying grid block sizes in any direction can be specified.
- Varying permeability in any direction can be used.
- Varying porosity and temperature for each cell can be used.
- The initial state of deformation (displacement) is zero.

The codes are composed of pre-processing codes, the main code, and post-processing codes. Pre-processing codes are used to read input parameters and convert units to SI units. The main program algorithm was composed of a non-recurrent section and a recurrent section. The non-recurrent section was developed to initialize data, such as converting data into the proper form in vectors or matrix. The calculations of transmissibilities on grid faces are conducted in the non-recurrent section as well. In the recurrent section, the transmissiblity matrix, T, is established for each recurrent section while the well constraints are changed. In the main time-step loop, the forcing function is made, and the pressure at the new time level, P^{n+1}, is calculated by matrix inversion. The water saturation, S_w^{n+1}, is then calculated explicitly from the pressure.

5.2.4 Two-Phase Fluid Flow in Reservoirs

Immiscible and slightly compressible two-phase flow in porous media is described here. Basic mass conservation equations, as described in Lake (1989), were used to solve for the pressure and water saturation in the reservoir during injection and production activities. In IMPES (implicit pressure, explicit saturation) reservoir simulations, the mass conservation equations for water and oil phases are written individually and added to give the pressure equation:

$$\phi c_t \frac{dP}{dt} + \vec{\nabla} \cdot \left(-\overline{\overline{\lambda_w}} \cdot \vec{\nabla} P \right) + \vec{\nabla} \cdot \left(-\overline{\overline{\lambda_o}} \cdot \vec{\nabla} P \right) = B_w \overline{q_w} + B_o \overline{q_o} - \frac{\partial}{\partial t} \left(\vec{\nabla} \cdot \vec{U} \right) \qquad (5.1)$$

Where c_t is a total compressibility. $\overline{\overline{\lambda_w}}$ and $\overline{\overline{\lambda_o}}$ are the relative mobility tensors of water and oil phase respectively. B_w and B_o are the formation volume factors of water and oil phases, which are functions of pressure, and $\vec{U}$ is the displacement vector. $\overline{q_w}$ and $\overline{q_o}$ are the injection or production rate per unit bulk volume. Positive values of these rates indicate fluid injection and negative values indicate fluid production. The mass conservation of water phase can also be written as:

$$\phi \frac{dS_w}{dt} + \phi S_w \left(c_g + c_w \right) \frac{dP}{dt} + \vec{\nabla} \cdot \left(-\overline{\overline{\lambda_w}} \cdot \vec{\nabla} P \right) = B_w \overline{q_w} \qquad (5.2)$$

This equation can be solved explicitly based on the results of the above pressure equation. Viscosities and formation volume factors can be treated as a function of pressure and/or temperature. A shear-rate dependent viscosity model can be applied as well for modeling polymer injection.

5.2.5 Energy Balance for Two-Phase Flow in Reservoirs

The energy balance for water-oil two-phase flow in reservoirs can be written by modifying the general energy balance equation in a porous medium (Lake, 1989):

$$\begin{aligned} \rho_b C_{pb} \frac{dT}{dt} = {} & k_b \nabla^2 T - \rho_w C_{pw} \overrightarrow{u_w} \cdot \vec{\nabla} T - \rho_o C_{po} \overrightarrow{u_o} \cdot \vec{\nabla} T \\ & + \rho_w C_{pw} \overline{q_w} \left(T - T_{ref} \right) + \rho_o C_{po} \overline{q_o} \left(T - T_{ref} \right) \end{aligned} \qquad (5.3)$$

Where ρ_b is the bulk density, and C_{pb} is the bulk heat capacity. k_b is the bulk heat conductivity. They all can be calculated as the volumetric average of fluids and grains. The subscripts of *w* and *o* indicate the water and oil phase values respectively. The linear velocity of each phase, $\overrightarrow{u_w}$ and $\overrightarrow{u_o}$, can be derived from the calculated pressure using Darcy's law.

5.2.6 Poro- and Thermo-Elasticity Model Coupled with Two-Phase Flow

Biot (1941)'s theory of poroelasiticity acts as the starting point for calculating the geomechanical response of reservoir stress states caused by fluid injection-production activities. Biot's theory was refined and utilized for soil and rock mechanics by Rice & Cleary (1976) and Detournay & Cheng (1993). This study's formulations of poroelasticity and thermoelasticity are based on Jaeger et al. (2007). Zimmerman (2000) also presented formulations of linearized poroelasticity and thermoelasticity. In Zimmerman's work, it was noted that mechanical deformation has a strong effect on pressure, but it does not considerably influence the temperature.

The *in situ* stress and displacement of reservoirs by non-isothermal, two-phase fluid flow are calculated by poro- and thermo-elasticity theories. The volumetric strain tensor, $\overline{\overline{\varepsilon}}$ is defined through the displacement vector, $\vec{U}$, by the strain-displacement relation:

$$\overline{\overline{\varepsilon}} = \frac{1}{2}\left[\nabla\vec{U} + \left(\nabla\vec{U}\right)^{T}\right] \tag{5.4}$$

In this study, the reservoir is assumed to initially be at an undisturbed initial compressive state; hence, $\vec{U}$ is a zero vector at the initial reservoir stress state of $\overline{\overline{S}} = \overline{\overline{S}}_{initial}$. The change in the total stress, $\overline{\overline{S}}$ in tensor form, is defined by a differential form of the stress-strain law with pressure and thermal effects:

$$\Delta\overline{\overline{S}} = \lambda \mathrm{tr}\left(\overline{\overline{\varepsilon}}\right) I + 2\mu\overline{\overline{\varepsilon}} - \alpha\left(P - P_i\right) I - \alpha_T\left(3\lambda + 2\mu\right)(T - T_i) I \tag{5.5}$$

Now, the stress equilibrium equation can be written as:

$$-\nabla\cdot\Delta\overline{\overline{S}} = -\nabla\cdot\left[\lambda \mathrm{tr}\left(\overline{\overline{\varepsilon}}\right) I + 2\mu\overline{\overline{\varepsilon}} - \alpha\left(P - P_i\right) I - \alpha_T\left(3\lambda + 2\mu\right)(T - T_i) I\right] = 0 \tag{5.6}$$

Where the sign convention is that compressive stress states have negative values. The effective stress, $\overline{\overline{\sigma}}$ is defined as $\overline{\overline{\sigma}} = \overline{\overline{S}} + \alpha P I$. In this study's figures, some total stress values in compressive states are displayed as positive values to show their magnitude. In

addition, λ, Lamě's first parameter and μ, Lamě's second parameter (or shear modulus) are defined by the following equations:

$$\lambda = \frac{E\nu}{(1+\nu)(1-2\nu)} \tag{5.7}$$

$$\mu = G = \frac{E}{2(1+\nu)} \tag{5.8}$$

where E is Young's modulus and ν is Poisson's ratio. They are treated as mechanical properties which are not affected by pressure or temperature.

5.2.7 Finite Volume Discretization

The finite element method has been extensively used for stress analysis, and the finite volume method has been more often used for fluid flow simulations (Jasak & Weller, 2000). In many cases, the finite volume method involves integrating governing equations and using the segregated solution procedure with iterative coupling between individual solution parameters. This work uses the finite volume method, as this research necessitates solving for multiple unknowns. The fundamental discretization methods of solution domain and governing equations is well described in Jasak (1996) and Weller et al. (1998). Their approach was used to develop the platform for OpenFOAM, the open-source library used in this work. Classes of OpenFOAM are created here based on their discretization methods, which this work used in the environment of object-oriented programming.

In this study, general polyhedrons are used to discretize the solution domain. Cartesian grid blocks are used for the basic validation problems shown in this chapter. This work also uses some examples of arbitrary unstructured meshes. When any type of general polyhedral shapes are used for solutions, all variables to be solved are defined under the same mesh structures. Figure 5.1 shows a typical shape of general polyhedral control volume. P is a computational point which is located at the centroid of the control volume.

All of the unknowns are calculated at the location of P. N is the centroid location of the neighboring cell. S is the face area vector, which is normal to the interface shared by contacting grid cells, which has a magnitude of face area. The value at the interface can also be interpolated by various schemes in this work.

The governing equations in the form of partial differential equation (PDE) are discretized by the finite volume method. In this procedure, any non-linear terms of PDE's are linearized before discretization. Then, integrals of PDE written in weak forms are applied over the time-step between t and $t+\Delta t$ and the control volume. Then, the volume integral is converted to a surface integral form by Gauss' theorem. The surface integral can be found by calculating the discrete sums of interface values. Finding interface values require differencing schemes which use cell centroid values of P and N. Central, upwind, and blended differencing methods are available in OpenFOAM to calculate the values on interfaces. For Laplacian terms, typically in diffusion equations, the gradient of values of interfaces are required. To build a reservoir simulation, this study mainly used the central differencing, and the upwind scheme was used for necessary parameters. The upwind scheme will be further explained in later sections. For temporal discretization, Explicit, Euler-implicit, and Crank-Nicholson methods are available. In this work, the Euler-implicit method was used for all temporal discretizations.

5.2.8 Algorithm

IMPES (Implicit Pressure, Explicit Saturation) and fully implicit methods have been typically used as the main algorithms in a conventional multi-phase reservoir simulation that solves for pressure and saturations. Thomas (1981) explained that IMPES involves eliminating the saturation terms from the flow equation to solve for either pressure or flow potential. Saturation then is explicitly solved for by referring back to the pressure equation. Typically, compared to a fully implicit method, IMPES methods have less

numerical diffusion. A fully implicit method, however, is generally more stable. The stability of IMPES can be improved by applying an upwind scheme, as the numerical diffusion can be compensated for by the IMPES formulation. The simulation developed in this work is one of many extended versions of IMPES methods. This simulation uses a method suitable for OpenFOAM as it inherently uses the segregated solution algorithm. The implicitness can be increased by applying iterative schemes in OpenFOAM, which can improve the stability and compensate for any issues caused by the loose coupling between the solutions of each parameter.

Various coupling methods are available for solving for geomechanical, fluid flow and well activities together. Samier et al. (2006) and Samier et al. (2008) discussed the iterative schemes for coupling geomechanics with reservoir simulation. Coupling methods can be: loose coupling, one-way coupling, and implicit-iterative coupling. Researchers can choose which to use based on whether reservoir and geomechanical properties are solved simultaneously and whether the geomechanical calculation is fed back to petrophysical properties, e.g., porosity and permeability. Many geomechanical coupling methods utilize the explicit-iterative coupling method.

In this simulation, an explicit method based on IMPES was used. The pressure solution by Eq. (5.1) is used to solve for the pressure within the domain. Then, water saturation is subsequently solved for by Eq. (5.2), and temperature can be solved for by Eq. (5.3). The pressure and temperature distribution in the domain can then be used to calculate poro-thermo-elastic responses. The displacement equation is solved by using Eq (5.6), and then the stress is solved by Eq. (5.5). The principal stress directions and magnitudes are also calculated from the stress tensor to show stress reorientation. The sequence of solutions is summarized in Figure 5.2. We apply a time step handling method and interpolation schemes, described in a later section of this chapter, to ensure the stability

of the sequence of solutions for PDEs. The segregated manner used to solve for each PDE can be also iteratively coupled in OpenFOAM as necessary. When the mechanical effect on stress reorientation is significant, for example when we are simulating fracture growth or fault slippage, iterative coupling between pressure and displacement calculations is recommended. When a large deformation in the reservoir is expected, as in a reservoir subsidence simulation, the deformation term in the pressure equation is relatively significant.

In the example solutions in this study, all the cases were solved within a reasonable calculation time, i.e., typically in several minutes to an hour with a personal computer. This explicit algorithm was also applied to unstructured meshes in 2D reservoirs and the calculation results were found to be physically reasonable.

5.2.9 Rock-Fluid Interaction, Well Models and Boundary Conditions

This simulation uses well models with rate- or pressure-constraint conditions. For water injection simulations, constant-rate injection and constant-pressure production models were mainly used. For the well-index calculation in structured meshes, two well models were used in the simulation. They are Peaceman (1983)'s well model and the semi-steady state equation model. The calculated well index, J_l, was used as a transfer function between the pressure and rate values of the well, depending on which value was needed. From Peaceman (1983)'s well model, the viscosity term in the denominator is moved to the relative mobility term. The J_l values for each well cell can be calculated as:

$$J_\ell = \frac{2\pi k_{i_\ell, j_\ell} h_{i_\ell, j_\ell}}{\left[\frac{1}{2}\ln\left(\frac{r_{o\ell}^2}{r_{w\ell}^2}\right) + \frac{1}{4} + s_\ell\right]} \tag{5.9}$$

where the subscript l indicates the index of the well. The permeability term in each model was calculated by the harmonic mean of horizontal direction permeability components, k_{xx}

and k_{yy} when the wellbore is along the *z*-direction. r_o is the equivalent radius of the well block. It is estimated from parameters in the mesh geometry:

$$r_{ol} = 0.28 \frac{\left[(k_{yl} / k_{xl})^{1/2} \Delta x_l^{\,2} + (k_{xl} / k_{yl})^{1/2} \Delta y_l^{\,2} \right]}{(k_{yl} / k_{xl})^{1/4} + (k_{xl} / k_{yl})^{1/4}} \tag{5.10}$$

Well models for non-rectangular polyhedral finite volume cells were used for unstructured meshes, as in Chen & Zhang (2009). The equivalent radius of the well block can be estimated with the following equation:

$$r_{ol} = \sqrt{\frac{A_l}{\pi}} \tag{5.11}$$

Here A_l is the area of the well block plane perpendicular to the wellbore direction. This model is applicable for a 2D unstructured grid block mesh. When the horizontal permeability anisotropy is significant, a more complex model is required.

For the outer boundary, a no-flow boundary condition for the fluid flow was used. Pressure gradients were set to zero. For the energy balance equation, temperatures were also set to have a zero-gradient at the boundary. Generally, no energy transfer is assumed, but it can be calculated in case energy loss to bounding layers are important. For stress conditions, no-displacement and constant traction boundary conditions were used for the field-scale simulations. It is essential that the domain size is large enough to not have any boundary effects. Two simulations with no-displacement and constant-traction boundaries can be compared with increasing domain sizes. Then, the size of the domain above which no differences in results are seen can be selected to serve as the domain size. Certain cases require a symmetry boundary condition for displacement. For example, a quarter of a five-spot well pattern was assumed to have a fixed location (no displacement) at their corners. The displacement in the perpendicular direction to the boundary was set to zero, but the boundary was allowed to deform in the direction parallel to the boundary.

5.2.10 Numerical Schemes and Adjustable Time-Step Methods

In finite volume discretization, the relative mobility of water and oil needs to be implemented at the interface of cells. These values can be interpolated from the values of adjacent cell grid centroids. In the IMPES simulation, upstream weighting (also called upwinding or upstream differencing) is known to be conditionally stable, as in Aziz & Settari (1979). In developing this simulation, the relative mobility terms were calculated using the first-order upstream weighting method.

$$\lambda_{rw,S} = \begin{cases} \lambda_{rw,P} & \text{for } \Phi_P \geq \Phi_N \\ \lambda_{rw,N} & \text{for } \Phi_P < \Phi_N \end{cases} \tag{5.12}$$

where λ_{rw} are the relative mobility of water at surface (S), current cell (P), and neighbor cell (N). Φ is the flow potential accounting for gravity. For the oil phase, the same scheme is used. This upwind differencing scheme helps to guarantee that the solution is bounded. The value at the interface of cells is determined by the flow direction (determined by the higher flow potential). This effectively introduces (or increases) the numerical diffusion in the calculated solutions. IMPES methodology, however, has less numerical diffusion than the fully-implicit method. In effect, the two methodologies trade off stability for numerical dispersion of the resulting shock-front caused by the hyperbolic nature of the equations. In this simulation, first-order upwinding sufficiently ensured the stability of structured and unstructured grid systems. Second-order upstream weighting schemes are available, but they were not used here.

During the development of this simulation, it was noted that instability caused by incorrectly applying upstream weighting was distinctly observed in the saturation results, because the saturation equation is hyperbolic. The temperature equation also has this characteristic and requires the upwinding scheme. Temperature profiles caused by fluid convection can show sharp fronts. For this reason, thermal reservoir simulations utilize

upwinding techniques in semi-implicit algorithms, as in Zheng & Buchanan (2013). For temperature calculations, the temperature gradients in the convection terms of Eq. (5.3) required the upwinding scheme. The upwinding scheme can be written for temperature in a manner similar to Eq. (5.12).

Normally, the IMPES-based simulations require a smaller time step than the fully implicit method. The stability criteria based on the Courant number can be used to estimate the time step; however, in later stages of simulation, a time-step handling mechanism is required to speed up the calculation. In this simulation, the time-step was adaptively updated based on the maximum change of water saturation in the field. The stability of water saturation is primarily governed by wave front propagation during injection. This tends to govern the overall stability of the simulations, and hence was chosen for the adaptive time-step modification algorithms.

$$\Delta t^{(n+1)} = \frac{\Delta S_{w,tol}}{\left|\Delta S_{w,\max}^{(n)}\right|} \Delta t^{(n)} \tag{5.13}$$

Where $\Delta t^{(n+1)}$ is the following time-step size, and $\Delta S_{w,tol}$ is the user-specified tolerance in water saturation change. $\left|\Delta S_{w,\max}^{(n)}\right|$ is the maximum change of the water saturation in the current time-step. When the saturation change becomes larger than the tolerance value, the time-step becomes smaller to prevent instability. The initial time step after each well operation change needs to be sufficiently small. The tolerance value can normally be set to between 0.0005 and 0.003.

5.3 MODEL IMPLEMENTATION

5.3.1 Validation of Fluid Flow Model with Analytic Solution

To validate the developed simulation's results, we tested a 1-D reservoir (or core) with a producer and an injector. The results from the simulation were compared with the

results of well-known analytical Buckley-Leverett solutions. The material balance of a two-phase fluid flow in 1D geometry can be written for a water phase as:

$$\phi \frac{\partial S_w}{\partial t} + u \frac{\partial f_w}{\partial x} = 0 \tag{5.14}$$

where f_w is the fractional flow for water. Assuming no capillarity and no gravity effects, the fractional flow for water can be written:

$$f_w(S_w) = \frac{1}{1 + \frac{k_{ro}\mu_w}{k_{rw}\mu_o}} \tag{5.15}$$

It can be further shown that the velocity of a specific saturation front in a 1D flow is proportional to the derivative of f_w with respect to S_w. In the following equation, both terms indicate the velocity of the saturation front.

$$\left.\frac{\partial x}{\partial t}\right|_{S_w} = \frac{u}{\phi}\left(\frac{df_w}{dS_w}\right) \tag{5.16}$$

The waterflooding front has a shock front, when the f_w versus S_w curve has concave-up and convex-up portions in its shape, as in Figure 5.3. This front can be described by a tangent condition. This condition is that the slope that connects S_{wr} and S_{wf} in f_w vs. S_w curve is the same as the slope at S_{wf}. S_{wf} is the shock front saturation. This determines the value of S_{wf} and can be written as:

$$\frac{\Delta f_w}{\Delta S_w} = \left.\frac{df_w}{dS_w}\right|_{S_w = S_{wf}} \tag{5.17}$$

Once the velocity of the shock front is determined, we can calculate the time required for the shock front to approach to the end of the core. At that breakthrough time, the water saturation profile versus the distance can be calculated for different saturations. The fractional flow curve is shown in Figure 5.3. The shock front velocity can be

analytically acquired based on the tangent condition. Then, the dimensionless distance, x_D can be calculated with the saturation velocity, df_w/dS_w and dimensionless time, t_D. This result is shown in Figure 5.4. This figure also shows the water saturation at the same t_D, as derived from simulation results. The simulation's results also show the numerical dispersion. This led to the earlier breakthrough seen in the simulation results when compared to the analytic Buckley-Leverett solution. Except for a slight time discrepancy for breakthrough, the simulation very closely matched the analytic saturation profile. The simulation was numerically stable with the given parameters.

5.3.2 Stress Reorientation in Single Wells

Stress reorientation by injection and production from a single well was investigated as a validation of the simulation's stress and displacement calculation. Poroelasticity and thermoelasticity are analogous to each other (Norris, 1992), and their contributions to stress-strain relation are independently linear in pressure and temperature terms. In this simulation, their contributions can be separately turned on and off. It was intended that their individual effects would be investigated separately, and their simultaneous effects could be applied to actual simulations.

Jin et al. (2000) investigated the production-induced stress sensitivity caused only by poroelastic effects. Commercial geomechanics and reservoir simulations were coupled explicitly. The relationship of production and stress state led to different field-development strategies, but a simplified relationship between them was not determined. Chen & Teufel (2001) discussed reservoir stress changes induced by production and injection. They built an idealized single-well case, and showed the poroelastic effect of production and injection separately by qualitative Mohr's circle analysis. In 2-D vertical well cases, they showed that the production decreases radial and mean horizontal stresses (stresses become less compressive), and injection leads to the opposite result (stresses become more

compressive). Roussel et al. (2013) calculated the injection and production-induced stress changes, and then visualized the stress directions and magnitudes. The idea was that near-well stresses reorient in terms of their magnitude and direction by production and injection. Both properties will affect the geometry of fractures if infill wells are drilled in the stress-reoriented area.

The above studies do not show thermoelastic or thermo-poro-elastic effects, so this dissertation investigates the stress reorientation near a single injection or production well. Poroelastic effects on an injector and a producer were separately tested in single-phase fluid flow. The injection temperature was varied to see its effect on thermoelasticity. The thermo-poro-elastic effects on stress reorientation in the injectors was also shown. The domain selected was large enough to not have the boundary effect. Input parameters used in these simulations are summarized in Table 5.2. Six different cases were simulated:

A. Injection at q_{inj} =100 bbl/day: Isothermal poroelastic effects only.
B. Production at P_{wf} =4000 psi: Isothermal poroelastic effects only.
C. Injection of 293K fluid into 353K reservoir: Thermoelastic effects only.
D. Injection of 353K fluid into 293K reservoir: Thermoelastic effects only.
E. Injection of 293K fluid into 353K reservoir: Poro-thermo-elasticity.
F. Injection of 353K fluid into 293K reservoir: Poro-thermo-elasticity.

Poroelasticity. From these simulations, the individual effects of temperature and pressure gradient change on the principal stress directions were analyzed. In cases A and B with only the poroelastic effect being tested, shown in Figure 5.5 and 5.6, the fluid injection leads to the reorientation of $S_{\text{H}max}$ to a radial direction, and the fluid production led to stresses being reoriented in the ortho-radial (orthogonal to radial) direction confocal to the producer. This was caused by injection increasing the near-well stress magnitude, and production decreasing it. The displacement or rock deformation was towards the producers

and away from the injectors, as expected.

These observations can also be explained by the stress equilibrium equation. We consider an infinitesimal reservoir portion in a cylindrical coordinate system shown in Figure 5.7. Assume that there is an injection well at the origin of the cylinder, and the outer perimeter is assumed to be production wells. There are no changes in pressure along the θ-direction. The pressure gradient in the radial direction is shown in Figure 5.7. Assuming that initial stress states is isotropic ($S_{rr,init} \approx S_{\theta\theta,init}$) and only poroelasticity is taken into account, Eq. (5.6) can be written as:

$$\nabla \cdot \overline{\overline{\sigma}} = \alpha \nabla \cdot (PI) \tag{5.18}$$

In the cylindrical coordinate system, this equation can be written for r and θ directions:

$$\frac{1}{r}\frac{\partial}{\partial r}(r\sigma_{rr}) + \frac{1}{r}\frac{\partial \sigma_{r\theta}}{\partial \theta} - \frac{\sigma_{\theta\theta}}{r} = \alpha \frac{\partial P}{\partial r} \tag{5.19}$$

$$\frac{1}{r}\frac{\partial}{\partial r}(r\sigma_{r\theta}) + \frac{1}{r}\frac{\partial \sigma_{\theta\theta}}{\partial \theta} + \frac{\sigma_{r\theta}}{r} = \alpha \frac{\partial P}{\partial \theta} \tag{5.20}$$

By assuming $\partial/\partial\theta$ to be zero, Eq. (5.19) can be rearranged to:

$$\sigma_{rr} - \sigma_{\theta\theta} = -r\frac{\partial \sigma_{rr}}{\partial r} + \alpha r \frac{\partial P}{\partial r} = -r\frac{\partial S_{rr}}{\partial r} \tag{5.21}$$

This relation indicates which direction of stress is larger depending on S_{rr} gradient in r direction. Near an injection well, $\partial S_{rr}/\partial r$ is positive, and $\sigma_{\theta\theta}$ is larger than σ_{rr}. This leads to the magnitude of S_{rr} being larger than $S_{\theta\theta}$ in a compression-negative convention. Based on the same logic, near production wells, negative $\partial S_{rr}/\partial r$ values lead to $S_{\theta\theta}$ being larger than S_{rr}. These relations provide a theoretical background for the observations of stress reorientation in single vertical wells near injectors and producers: Fluid injection leads to the reorientation of S_{Hmax} in the radial direction, and fluid production leads to an ortho-radial direction confocal to the producer. Researchers can apply this theoretical explanation

to thermoelasticity cases by replacing the pressure terms with temperature terms. It should be noted that the absolute magnitude of both total stresses (radial and tangential) around an injection well will generally be higher than around a producing well since the pore pressure is higher. This implies that producing wells (low total stress) will act as attractors for hydraulic fractures even if the direction of the maximum stress is ortho-radial immediately around the well.

Thermoelasticity. Results for cases C and D are shown in Figure 5.8 and 5.9. In these cases, a hot fluid is injected into a cold reservoir, and a cold fluid is injected into a hot reservoir respectively. The hot fluid injection leads to radial reorientation of S_{Hmax}. In the case of cold fluid injection, S_{Hmax} becomes ortho-radial to the well. This is caused by the stress magnitude increasing in the case of hot fluid injection, and the stress decreasing during the cold fluid injection. This is similar to what occurred in the previous poroelastic cases. In cases with typical injection/production rates or typical temperature differences between injection water and the reservoir, however, the extent of reorientation can differ significantly for both poroelastic and thermoelastic cases.

These phenomena differ in the nature of the PDE's they are controlled by. The pressure equation is a diffusion (parabolic) equation, but the temperature equation is a wave (hyperbolic) equation. The pressure gradient disperses over a wider range than the temperature front. The degree of propagation of each depends on the matrix permeability and thermal conductivity; however, temperature propagation incurs a step-wise profile and does not extend as far as the pressure propagation under typical conditions. The pressure and temperature changes near the wellbore are shown in Figure 5.12. The figure shows that the spatial extent of temperature and pressure changes are directly related to the extent of stress reorientation. This can also be verified by investigating the stress magnitudes in x and y directions in Figure 5.13, where the magnitude of stress changes and their spatial

extent is clearly shown.

In applications to actual field simulations, heat losses to the over- and under-burden can be significant depending on layer properties. In simulations shown here, a plane-strain condition was applied and heat loss to the over- and under-burden was not accounted for. The areal distribution of the stress field was primarily calculated in 2-dimensional reservoirs in this study. For 3-dimensional simulations, including multiple layers will be required to calculate the heat loss and its associated effect on stress reorientation. The current formulation shown in the previous sections can handle 3-dimensional simulations. Simulations of the energy balance for 3-dimensional reservoirs with multiple layers can be conducted and validated with known analytic solutions, e.g., Marx & Langenheim (1959) model, in a future study.

Poro-thermo-elasticity. The combined effect of poroelastic and thermoelastic effects on stress reorientation is shown in Figure 5.9 and 5.10. In the hot fluid injection case, the poro- and thermo-elastic effects make the stresses reorient in the same direction, radially. The extent of reorientation is mostly influenced by the poroelastic effect, in this case. However, in cold fluid injection, the poroelastic effect changes S_{Hmax} radially, but the thermoelastic effect changes it ortho-radially. In that case the two effects create competing results. In the near-well region, when the magnitude of stress decrease caused by the thermoelastic effect is larger than the poroelastic effect, the S_{Hmax} direction becomes ortho-radial, dominated by the thermal effect. The far-field region, however, is not affected by the thermo-elastic effect, and shows that it is dominated by the poroelastic effect.

5.4 DISCUSSION

5.4.1 5-Spot Waterflooding Well Pattern

As part of the simulation, stress reorientation in a 5-spot waterflooding well pattern

is investigated. As in the previous section, poroelastic, thermoelastic, and poro-thermo-elastic effects are shown individually for easy comparison. The input parameters are summarized in Table 5.3. A quarter section of the five-spot well pattern was simulated by assuming symmetry condition at the boundaries. Subsequent figures are represented with well locations and initial horizontal stress directions, as in Figure 5.14. The injection well was constrained with a constant injection rate of 10,000 bpd, and the production well was constrained with 5,000 psi of bottom-hole pressure. The production rates of the water and oil phases were calculated, as in Figure 5.15. The change in water and oil production rates show the water breakthrough at around t =520 days. Other assumptions are as follows:

- The vertical stress was set high enough so that it could remain the highest principal stress.
- The same well patterns were assumed to continue infinitely.
- A no-flow boundary condition was assumed for both phases.
- A no-heat-flux boundary condition was assumed.
- Symmetric displacement was assumed at boundaries: The displacement component perpendicular to the boundary is 0, and the parallel component is calculated. The displacement vector at each corner is 0.
- The traction conditions at the boundaries were calculated.

The purpose of these assumptions is to build a simulation that represents a unit section of a typical waterflooded reservoir with multiple wells in a regular pattern. Using these assumptions, the stress reorientation in a typical five-spot well pattern can be inspected, and the different impacts of poroelastic, thermoelastic and their combined effects were compared. In subsequent figures, snapshot images of different properties are shown at 200 and 600 days, which is before and after water-breakthrough.

Pressure and temperature. The pressure gradient was established by fluid injection

and production in the entire area of the well pattern with symmetry at the boundaries (Figure 5.16). The pressure distribution is dispersive while the temperature distributions show clear step-wise fronts (Figure 5.17). This is because two are solved in different types of PDE's. The pressure equation is a diffusion equation, and the temperature equation is a wave equation. Depending on fluid injection rates and heat capacities of the fluid and the matrix, the speed of the temperature front may vary. Typically the temperature front is comparatively slower than the fluid displacement front in waterflooding conditions.

Saturations. The change in water saturation and the displacement of oil by water is seen in a typical waterflooding sweep pattern. The water breakthrough is shown in a saturation map in Figure 5.18 and 5.19. These figures can be compared with the production rates of each phase in Figure 5.15. In these figures, the fluid linear-velocity vectors are shown for water and oil phases over time. The fluid linear-velocity of water and oil vary from the front to the back of the water saturation front. The linear velocities of each phase are high in the near-well regions. These observations correspond to the production rates of each phase during pre- and post-water-breakthrough.

Stresses and displacement. We also investigated the poro- and thermo-elastic responses in a 5-spot waterflooding well pattern. Compared to single well cases, the individual effects for an injector and a producer are combined by the pressure distributions along the flow paths between wells. The magnitude and directions of rock displacement, the maximum horizontal stress direction and difference of maximum and minimum horizontal stresses are shown in:

- Figure 5.20 and Figure 5.21: Effect of poroelasticity only
- Figure 5.22 and Figure 5.23: Effect of thermoelasticity only
- Figure 5.24 and Figure 5.25: Effect of both poro- and thermo-elasticity

Poroelasticity. In the poroelastic cases, the injected fluid deformed the reservoir

rock in an outward direction from the injector. Rock displacements near the producer are toward the well. The resulting reoriented S_{Hmax} directions become radial near the injector, and ortho-radial near the producer. This behavior is similar to the single well cases. When the fluid flows from injector to producer, the pressure gradients are created throughout the field. Accordingly, the stresses reorient in the region where the pressure gradient is generated. In many cases, this is most of the areal region of 5-spot well pattern. This is an important difference from single well cases: Stresses reorient on a field-wide scale during waterflooding; they are not limited to the near-well region.

In the upper-left corner of the simulated well-pattern domain, the S_{Hmax} direction very quickly reoriented to 90˚ from the initial state. This is the combined effect of the injector and the producer, which changes S_{Hmax} to the same direction, i.e., radial for the injector and ortho-radial for the producer, for that location in the well pattern. The same effect applies to the lower-right corner. In this case though, the resulting directions are the same as the initial S_{Hmax} direction, so S_{Hmax} direction does not turn here. This effect is represented clearly under the current boundary conditions that assume symmetry. In actual field cases, this assumption is more applicable to wells located in the center of a continuous set of well patterns. Center wells in a 5-spot well pattern will have a wide stress reorientation region caused by this phenomenon. In the case of wells located in the outer region of the well patterns, the effect is smaller. The stress reorientation will be more similar to the single well case in the outer regions of continuous well pattern.

Thermoelasticity. In the case of thermoelasticity, the effect of the cooled region is dominant, and it can change the stress of the outer regions that are still at the initial temperature. The contraction of the cooled region causes the rock displacement direction to be toward the injection well. The magnitude of rock displacement is the largest at the temperature fronts, and its magnitude is larger than that of the poroelastic effect. The

reoriented stress field can be divided largely into two regions, which correspond with regions with decreased (cooled region) and initial (outer region) temperatures. In the cooled region, magnitudes of both S_{xx} and S_{yy} decrease by cooling, meaning the principal stress directions do not turn from the initial state. In the outer region, the contracted (cooled) region effectively pulls the reservoir toward the injector while the well pattern boundaries are fixed. Then, the $S_{\mathrm{H}max}$ directions reorient ortho-radially to the injection well. When this effect overcomes the horizontal stress difference, the $S_{\mathrm{H}max}$ direction in the lower-right corner reorients 90˚ from the initial state, while that of the upper-right corner remains in its initial direction. This thermoelastic effect is a field-wide phenomenon, not a near-well phenomenon, unless it is the boundary region of a continuous well pattern.

Poro-thermo-elasticity. As shown in simulations for individual effects, poroelastic and thermoelastic effects reorient the stress field in different directions. To predict the actual stress reorientation when waterflooding a reservoir, the two effects must be accounted for simultaneously. Figure 5.24 and 5.25 show how the two effects compete and their combined effect on stress reorientation. The displacement vectors show how two distinctive regions are created by poro- and thermo-elasticity. With typical injection and reservoir temperature conditions, rock deformation near the injection well is dominated by the thermoelastic effect, which is caused by contraction by cold water injection. Near the production well, the poroelastic effect is stronger than the thermoelastic effect, and as a result, the reservoir is pulled toward the producer. Therefore, in typical waterflooding, injectors and producers pull the reservoir toward themselves by thermal and pore-pressure effects respectively. The boundaries of these two regions propagate from injectors to producers in a similar pattern as temperature front propagation. The magnitude of displacement is typically larger in the thermoelastic case than the poroelastic case. The magnitude of poro-thermo-elastic displacement is smaller than in the thermoelastic only

case because the poroelastic effect relieves the contraction.

Stress reorientation regions. The stress direction change in the poro-thermo-elastic case also shows the combined effect. Stress reorientation regions can be typically divided into three different regions. The cooled (contracted) region (region i) near the injector shows lower horizontal stress contrast and S_{Hmax} alignment in the radial direction. Beyond the cooled region, the contraction of the near-injector causes ortho-radial alignment of S_{Hmax} to the injector (region ii), as can be seen from thermoelastic case. The near-producer region (region iii) exhibits the ortho-radial S_{Hmax} alignment to the producer as a typical poroelastic effect. Generally, the reorientation of the stress direction in the overall field is controlled by the injector's thermal effect. The poroelastic effect is more dominant only in the near-producer region.

The horizontal stress contrast is generally very large in region (ii). In this region, the pulling effect from region (i) only relieves the stress magnitude in the radial direction. The stress magnitude of the ortho-radial direction component is high due to the poroelastic pushing effect from the injector. If a fracture is induced from the injector, the fracture can grow along any arbitrary direction in the cooled region, because the reoriented direction of the stress is radial to the injector. The reduced horizontal stress contrast can also enhance the stimulation of natural fractures. The induced fracture growth may be a more complex shape with local heterogeneity, along with pre-existing natural fracture networks. It can be inferred that stimulations from near-injector fractures will be effective in the cooled region. This induced-fracture, however, will turn its direction when it grows beyond the cooled region. In region (ii), the stress direction will now be ortho-radial to the inner region. It is possible for fractures to turn 90 degrees from their previous propagation directions. This phenomenon is enhanced by the high stress contrast in region (ii). Stimulation by an induced fracture near the injectors can be trapped at the temperature propagation front. This

is a dynamic process in which the reoriented stress at the fracture tip will decide how the fracture grows.

5.4.2 9-Spot Waterflooding Well Pattern

In 9-spot waterflooding well patterns, the different well configurations lead to a different stress reorientation map. Simulations were set up based on the previous 5-spot well pattern case. All the parameters used in 5-spot simulations were used in the 9-spot simulations for consistency. In a single 9-spot well pattern unit, there are three injection wells, located at the corners. To make the overall injection rate consistent, an injection rate of 3,333 bbl/day was used instead of the 10,000 bbl/day rate used in the 5-spot well pattern case. The domain size of the unit well pattern simulated was identical to that used in the 5-spot case. The same fluid, thermal and mechanical properties were used. Both poro- and thermo-elasticity were simulated which allowed us to compare the stress reorientations of the different well patterns. Pressure, water saturation, and temperature distributions are shown in Figures 5.27, 5.28 and 5.29. These figures show a reasonable pressure distribution and fluid and temperature sweep patterns for the 9-spot well pattern.

As observed for the 5-spot well patterns, poro- and thermo-elasticity also impact the stress reorientation on a field scale in a 9-spot well pattern case. The reservoir displacement near the injectors is controlled primarily by the thermal effect of cold-water injection, as in Figure 5.30. The remaining field, however, shows displacement toward the production well indicating that the poroelastic effect and fluid movement in the reservoir are dominant here. The magnitude of displacement caused by the thermal effect is larger than that caused by the pressure gradient. The influence of the individual well on the near-well displacement is the same as what had been observed in previous simulations.

The S_{Hmax} direction in 9-spot well pattern waterflooding is shown in Figure 5.31. The three regions for stress reorientation shown in a 5-spot well pattern are also seen in

this well pattern. They are: (i) thermally contracted region at injection temperature, (ii) outer region with ortho-radial S_{Hmax} reorientation to injector at initial temperature, and (iii) a region with an ortho-radial reorientation to the producer. Region (i) and (ii)'s areas are comparatively smaller than the same areas in the 5-spot well pattern cases. The smaller areas are caused by the lower injection rate per well. The lower rate led to a smaller area of stress reorientation when the regions' areas in the two patterns were compared. Areas with reoriented stress are located in near-well regions, which caused the stress-reorientation region in the overall field to be less than that of the 5-spot well pattern. The S_{Hmax} direction in region (ii), the outer region of the injectors, is ortho-radially oriented to the injectors. The contracted inner area, region (i), has the injector at the upper-left corner turned 90˚ in the S_{Hmax} direction, and no S_{Hmax} direction change in the far-field direction for the other two injectors. The injection-induced fracture growth will follow these S_{Hmax} directions. When fractures are induced outward to region (i), the fractures will tend to turn along the reoriented S_{Hmax} direction in the region (ii), which will significantly change the sweep pattern. The change in the horizontal stress contrast will again affect the stimulation of natural fractures. The near-injector regions will be influenced by the lowered stress contrast, which is caused by the thermal effect. Hence, the high degree of stimulation of natural fractures near the injectors will effectively increase injectivity during long-term water injections.

5.4.3 Line-drive Waterflooding Well Pattern

In the line-drive well pattern, similar approaches as those described in previous sections were used to investigate the stress state induced during waterflooding. The producers were constrained by the bottom-hole pressure. Because there are two producers in a single unit of the well pattern, the injection rate per well was constrained with the rate of 10,000 bbl/day to make the field injection rate per producer consistent with the

previously described cases. Pressure, water saturation, and temperature distribution at 200 and 600 days are shown in Figures 5.33, 5.34 and 5.35. Again, typical pressure profiles and sweep patterns of fluid phase and temperature were simulated for the line-drive well pattern.

Behavior similar to that found in the previous cases in reservoir displacement was observed in this case, as shown in Figure 5.36. The thermal effect dominates the deformation results in the largest field area, and especially in the region oriented toward the injectors. The poroelastic displacement was smaller than the thermoelastic effect. The S_{Hmax} direction during line-drive waterflooding is shown in Figure 5.37. The three different stress reorientation regions, as explained in previous sections, were also observed in the line-drive well patterns. Again, the stress reorientation was mostly controlled by the thermal effect near the injectors. One notable behavior in the line-drive case is that the horizontal stresses in the middle of the reservoir along the initial S_{Hmax} direction were almost completely reversed. This is caused by the geometry of this well pattern. Well locations and the resulting stress reorientation are symmetric along this stress reversal region. At this symmetric center of the well pattern domain, the reservoir is pulled toward both sides by thermal and poroelastic contraction. This pulling makes the stress magnitude less compressive, and the S_{Hmax} direction turns 90˚ from its initial direction. If infill wells are drilled between injectors or producers after a certain stage of waterflood, tensile fractures from these infill wells can grow along the reoriented direction. This may improve the sweep efficiency if infill wells are placed with proper timing during waterflooding. This simulation is essential in predicting the effect of reoriented stresses when infill drilling is conducted.

5.4.4 Stress Reorientation in Single Horizontal Well

In a single vertical well, fluid injection reorients the S_{Hmax} direction radially and the

fluid production ortho-radially, as explained in previous sections. This is conceptually shown in Figure 5.38a. When the fluid is injected and produced through the lateral section of the horizontal well with open-hole completions, stress reorientation may not resemble that of a vertical well. The stress direction does not orient radially or ortho-radially concentric to the horizontal well lateral. One may not apply the simple principle of a vertical well to a horizontal well case. It is important to separately simulate stress reorientation near a single horizontal injector and a producer.

The simulation was set up with the parameters shown in Table 5.4. These values were used for the following horizontal well pair simulations as well. A single horizontal injector or producer in a homogeneous reservoir was simulated here. The vertical stress was assumed to be large enough to remain the largest principal stress while stresses were changed, so we paid special attention to the change in horizontal stresses. A 2-D reservoir was built based on the assumption that stress variation in the reservoir height direction is negligible.

The general reorientation in the S_{Hmax} direction for the horizontal injector and producer are shown in Figure 5.38b. Only poroelasticity was accounted for in this figure, and the initial S_{Hmax} direction is perpendicular to the well direction. In the region outward from the heel or toe of the horizontal lateral section, the S_{Hmax} direction reorients in a similar manner (as vertical wells): Injection turns S_{Hmax} radially, and production turns S_{Hmax} ortho-radially. Along the horizontal well lateral section, however, S_{Hmax} reoriented parallel to the injector, and perpendicular to the producer. Similar changes in the stress direction were previously reported in Minner et al. (2002), Rod & Jorgensen (2005) and Roussel & Sharma (2010).

This was caused by changes in the stress magnitude in the horizontal well's direction (S_{yy} in this case) increasing more in the injector, and decreasing more in the

producer than the corresponding changes of stress magnitude in the direction perpendicular to the well (S_{xx} in this case). In injectors, the stress became more compressive along the horizontal injector direction. In producers, the compressive stress was more relieved by production along the horizontal producer direction than the stress relief perpendicular to the well lateral.

This phenomenon near a horizontal well or a series of fluid sources, such as a fracture, was totally different from what was observed in a vertical well. One may think that this is counter-intuitive, but it can be explained by poroelasticity equations. This observation can be simply stated as follows: A line of fluid sources (or sinks) increases (or decreases) the total stress magnitude more in a direction parallel with the line than in a direction perpendicular to the line. A simple case can be set up with a partial section of a parallel injector and producer, as shown in Figure 5.39. In this infinitesimal portion of the reservoir, there are no changes in the properties in *y*-direction. The pressure gradient is created only in the *x*-direction. The strain-displacement equation can be written as:

$$\overline{\overline{\varepsilon}} = \frac{1}{2}\left[\nabla\vec{U} + \left(\nabla\vec{U}\right)^{T}\right] = \begin{bmatrix} \dfrac{\partial U_x}{\partial x} & \dfrac{1}{2}\left(\dfrac{\partial U_x}{\partial y} + \dfrac{\partial U_y}{\partial x}\right) \\ \dfrac{1}{2}\left(\dfrac{\partial U_x}{\partial y} + \dfrac{\partial U_y}{\partial x}\right) & \dfrac{\partial U_y}{\partial y} \end{bmatrix} \tag{5.22}$$

Where the displacement vector is $\vec{U} = \left(U_x, U_y\right)$. With these assumptions, U_y=0 and $\partial/\partial y$=0. Then, the strain tensor can be simplified to:

$$\overline{\overline{\varepsilon}} = \begin{bmatrix} \dfrac{\partial U_x}{\partial x} & 0 \\ 0 & 0 \end{bmatrix} \tag{5.23}$$

The stress-strain relation can be written for *x*- and *y*-components as:

$$\Delta S_{xx} + \alpha\left(P - P_i\right) = \Delta\sigma_{xx} = \left(\lambda + 2\mu\right)\varepsilon_{xx} + \lambda\varepsilon_{yy} = \left(\lambda + 2\mu\right)\frac{\partial U_x}{\partial x} \tag{5.24}$$

$$\Delta S_{yy} + \alpha\left(P - P_i\right) = \Delta\sigma_{yy} = \lambda\varepsilon_{xx} + \left(\lambda + 2\mu\right)\varepsilon_{yy} = \lambda\frac{\partial U_x}{\partial x} \qquad (5.25)$$

This equation indicates that the effective stresses in x- and y-directions change proportionally to $\partial U_x/\partial x$ with different proportionalities of $(\lambda+2\mu)$ and λ respectively. Based on the assumed geometry, U_x is always positive and $\partial U_x/\partial x$ decreases along the x-direction with a positive intercept value at the injector (Figure 5.39). Hence, in this geometry, $\partial U_x/\partial x$ is positive near the injector and negative near the producer, and $\Delta\sigma_{xx}$ and $\Delta\sigma_{yy}$ change in the same manner as $\partial U_x/\partial x$ near each well. Near the injector, $\sigma_{xx}>\sigma_{yy}$ will be established at steady-state because of the larger proportionality of the x-direction $(\lambda+2\mu)$ than in y-direction (λ). This indicates that σ_{yy} is in a more compressive state than σ_{xx}, leading to a total stress state in which S_{yy} is in a more compressive state than S_{xx}. Consequently, S_{yy} will become S_{Hmax} near the injector, and near the producer, S_{xx} will change to S_{Hmax}.

This phenomenon can also be explained by assuming $S_{xx,init} \approx S_{yy,init}$ and subtracting Eq (5.25) from Eq. (5.24):

$$S_{xx} - S_{yy} = 2\mu\frac{\partial U_x}{\partial x} \qquad (5.26)$$

Near the injector, $\partial U_x/\partial x$ is positive, indicating that $S_{xx}>S_{yy}$ and S_{yy} is more compressive. Near the producer, $\partial U_x/\partial x$ is negative, indicating that $S_{xx}<S_{yy}$ and S_{xx} is more compressive. In summary, the above explanations mathematically state: A line source of injection leads to reorientation of S_{Hmax} in a direction parallel with the source. A line sink of production leads to the S_{Hmax} reorientation in a direction perpendicular to the sink. In thermoelasticity cases, the hot-fluid injection corresponds to the poroelastic injection case, and the cold-fluid injection corresponds to the poroelastic production case.

In simulations, changes in stress magnitudes in x- and y-directions can be verified, as shown in Figure 5.40. S_{yy} increased along the injector and decreased along the producer more than S_{xx} did. Figure 5.41 shows stress reorientation in simulated cases for a single

injector and producer. For injectors, the impacts of individual poroelasticity and thermoelasticity were shown, and both effects were simulated simultaneously so they could be compared. In this specific case, poroelasticity exhibited a dominant effect on stress reorientation. The thermoelastic effect of cold fluid behaves like the poroelastic effect of fluid production. Cold fluid injection relieves compressive stress, especially in the well direction. When poro-thermo-elasticity was accounted for in cold water injection, poroelastic and thermoelastic effects competed with each other to determine the stress reorientation, which depended on reservoir and fluid properties. In horizontal producers, only the poroelastic effect affects the stress reorientation.

5.4.5 Waterflooding in Horizontal Well Pairs

When horizontal wells are used for waterflooding projects, the sweep efficiency can be improved more than when using vertical wells. Open-hole completions are often used and fractures may be induced during waterflooding. The fracture direction can significantly change the sweep patterns. Fractures, transverse or longitudinal to the horizontal well lateral section, may grow depending on the induced stress states. To ensure better reservoir sweep, horizontal injectors and producers are normally used as pairs. Production and injection activities may lead to a different stress reorientation, and the effect of each well may reorient stresses in a complicated manner. In this section, relatively simple models of horizontal well pairs are investigated, and the effects of important parameters are analyzed.

In the simulation, three horizontal wells parallel to each other are considered (Figure 5.42). The injector is located between producers. The injection fluid sweeps the area between wells. The stress reorientation shows a combined effect of the injector and producers, which tend to change the stress direction in different ways. Either the producers or the injector dominate the reoriented stress leading to either a complete stress reversal or

to no changes in the S_{Hmax} direction. This means that induced fractures may grow in a longitudinal direction along the injector, or fractures can grow perpendicularly to the well, which leads to a connection between the injector and the producers. It is necessary to predict stress direction during waterflooding to properly estimate the fracture direction and the subsequent reservoir sweep pattern.

General behavior and operational conditions. Simulation cases with horizontal well pairs were established, and the results were compared with different injection rates while all producers had the same bottom-hole pressure (Figure 5.43). The case with a high injection rate showed the reservoir displacements moving in radial directions without any contraction near the producers. This indicates that, under this simulation condition, the rock deformation occurs in a continuous manner rather than a discrete pattern. In this case, the influence from the injector dominates that of the producers. The S_{Hmax} direction reoriented toward the injector-dominated pattern. The horizontal stress contrast along the injectors increased significantly, indicating that a longitudinal fracture can be induced along the injector.

In the case with a lower injection rate of 15000 bbl/day, the displacement vector field showed two distinctive regions: the injection-induced expanding region (inside) and the production-induced contracting region (outside). The effect of the injector was smaller in the case with the lower injection rate, than that with the higher injection rate. The lowest injection-rate case showed an overall contraction in the field and a much lower degree of stress reorientation. At a later time, the S_{Hmax} direction reoriented along the well in the near-injector area, but this reorientation was negligible when compared to higher-injection rate cases. The horizontal stress contrast was lowered near the injector. If a fracture is induced from the injector, more natural fractures near the injectors can be stimulated in random directions. This may cause the fracture to grow into producers, leading to unfavorable

sweep patterns.

The change in the magnitudes of S_{xx} and S_{yy} explains the stress-direction changing depending on the injection rate. Figure 5.44 shows the stress magnitude along the injector changing with time. The stress magnitude in the well-lateral direction (S_{yy} in this case) increased more in cases with higher injection rates; however, the stress magnitude in the perpendicular direction (S_{xx}) did not change significantly with injection. Hence, there can be a critical value of injection rate above which the stress direction is reversed when other parameters are fixed. As injection rates increase, it is more likely that a longitudinal fracture can be induced along the injector. The stress magnitude along a line between the injector and the producer is shown in Figure 5.45. This also explains the extent of stress reversal in the *x*-direction.

Reservoir, mobility and thermal parameters. The injection rate was not the only parameter that controlled stress reorientation in horizontal well pairs. Various parameters in waterflooding, including reservoir properties, the mobility of the two fluid phases, and thermal properties, can also cause completely different stress states. Understanding these parameters is vital to predicting fracture directions and sweep patterns. In this case study, reservoir permeability, injection fluid viscosity, and reservoir temperature are examined to show their impact on stress reorientation in horizontal well pairs.

In Figure 5.46, the lower reservoir permeability case shows strong reorientation near the injector, indicating that the injector effect is dominant. With higher permeability, however, the stress direction did not rotate. Different viscosities of the injection fluid were also tested, as shown in Figure 5.47. Higher injection fluid viscosity led to stress reorientation, but the stress state did not rotate for the lower viscosity injection fluid. The high-viscosity fluid injection effectively represents a polymer flooding case. The mobility ratio, defined as $k_{rw} \cdot \mu_o / k_{ro} \cdot \mu_w$, is higher in the lower viscosity injection fluid. In a higher

mobility ratio, the water (or polymer) fluid-front shows an earlier breakthrough. This indicates the relatively smaller effect of the injector. In a lower mobility ratio, the fluid-front shape is similar to a step-wise profile. In that case, the injector has a larger effect on stress reorientation.

Finally, the thermal effect is shown in Figure 5.48. The temperature difference between the reservoir and the injection fluid was varied. A higher degree of reservoir cooling tends to reverse a poroelastically-altered stress-direction back to its initial direction in the near-injector area. The extent of the cooled area is only adjacent to the injector, and the outer rotated stress-directions were conserved in this specific case. In the lower temperature difference case, the cooling effect was negligible and the poroelastic effect reversed the stress direction.

5.4.6 Multiple Wells and Application of Unstructured Grids

When the reservoir's geologic structure and its heterogeneity are accounted for in actual field development, well configurations are not designed in a uniform pattern. Instead, wells will be located in asymmetric patterns. The geomechanical responses in a reservoir with multiple wells show the combined effects of all the wells in terms of different fluid and reservoir properties. This combined effect requires a simulation that has more realistic geometries and well locations. The applicability of the current model to multiple wells and the resulting stress reorientation is shown in Figure 5.49 and 5.50. Waterflooding with four injectors in the outer region and four producers in the center was simulated. Poro-thermo-elasticity was applied to calculate geomechanical responses in terms of stress changes.

Reservoir displacements displayed the injectors' and producers' individual effects in some near-well regions. However, the combined effects for multiple wells tended to change the location of the focal points of contraction and expansion away from the well locations. Changes in focal-point locations depend on various reservoir, fluid parameters

and operational conditions. The changes in S_{Hmax} directions also show the individual and combined effects of the wells, depending on their location. The three stress reorientation zones in the five- and nine-spot well patterns are also found here. The induced fractures in this multiple well model can be predicted to turn at the outer zone of the thermal-contraction.

The unstructured grid-block system was tested, and its results were compared with a structured grid-block system in the same Figures. For mesh generation, gmsh, a mesh-generator program by Geuzaine & Remacle (2009) was used. A triangular mesh system with a controllable grid density was generated, and the system of PDE's and discretization methods in the current model were applied to it. The finite volume discretization process explained in the previous section was applied to this triangular mesh system. The results using structured and unstructured mesh were compared and shown to have identical trends of pressure, deformation and stress fields. This unstructured grid system is important in future applications of fracture propagation in arbitrary directions.

5.5 CONCLUSION

The objective of this chapter was to understand the field-scale geomechanical responses caused by injection and production activities during waterflooding in various well patterns. To achieve this goal, a non-isothermal two-phase-flow geomechanical simulator was built. Various representative models for waterflooding well patterns were simulated, and the stress reorientation behavior was interpreted. Some important observations from the model construction and application were:

- Explicitly coupled two-phase flow, energy balance, geomechanics model focusing on stress reorientation calculation was validated using an analytic model and single-well stress reorientation results.
- There are three stress reorientation regions in waterflooding using cold water: a

low-temperature contraction region, an outer initial-temperature contraction region, and a production-dominated region.

- Induced fractures can possibly turn directions in the outer initial-temperature contraction region due to the reoriented stress direction and high horizontal stress contrast.
- Near the horizontal-well-lateral region, the S_{Hmax} direction reorients parallel to the injector (or hot-water injector), and perpendicular to the producer (or cold-water injector). This stress-reorientation trend was explained with poro-thermo-elasticity theories.
- Stress reorientation near the injector of horizontal well pairs is controlled by either the injector or the producer, depending on which one has a stronger effect. The size of the effect depends on fluid, reservoir, and operational parameters.
- Stress reorientation during waterflooding is a field-scale phenomenon and requires simulations reflecting the reservoir, fluid properties and operational conditions.

The new model can be used for various purposes during field development by waterflooding. The primary applications of this model will be to estimate a sweep pattern, to predict the direction of an injection induced-fracture, and to optimize the location of infill wells. Coupling this simulation with a fracture propagation model based on the reoriented stress state would help to better predict the sweep patterns and optimize a waterflooding project.

Table 5.1: Input parameters used for the 1-D waterflooding simulation.

Parameter	Value	
$q_{w,inj}$	10	bbl/d
Length	100	m
Cross-sectional area	4	m^2
Porosity	0.2	-
Permeability	100	md
Viscosity, water	1	cp
Viscosity, oil	5	cp

Table 5.2: Input parameters used for the single well (producer or injector) simulation.

Parameter	Value		Parameter	Value	
Well and Fluid Prop.			Thermal Properties		
Injection rate, water	100	bbl/d	High temperature (inj or prod)	353	K
Prod well BHP	4000	psi	Low temperature (inj or prod)	293	K
Well radius	0.1	m	Specific heat capacity, fluid	4.1	kW/kg-K
Viscosity	1	cp	Specific heat capacity, grain	0.8	kW/kg-K
Reservoir Prop.			Thermal conductivity, fluid	0.58	W/m-K
Init. reservoir pressure	6000	psi	Thermal conductivity, grain	1.7	W/m-K
S_v	13953	psi	Mechanical Properties		
S_{Hmax}	8372	psi	Poisson's ratio	0.3	-
S_{hmin}	8233	psi	Compressibility, fluid	0.4×10^{-9}	Pa^{-1}
Permeability, horiz.	1000	md	Compressibility, grain	2.6×10^{-9}	Pa^{-1}
Porosity	0.2	-	Biot's coefficient	1	-
			Young's modulus	25	GPa

Table 5.3: Input parameters used for waterflood simulation in a quarter 5-spot well pattern.

Parameter	Value		Parameter	Value	
Well and Fluid Prop.			Thermal Properties		
Injection rate, water	10000	bbl/d	Reservoir temperature	353	K
Prod well BHP	5000	psi	Injection temperature	293	K
Well radius	0.1	m	Specific heat capacity, water	4.1	kW/kg-K
Viscosity, water	1	cp	Specific heat capacity, oil	2.4	kW/kg-K
Viscosity, oil	5	cp	Specific heat capacity, grain	0.8	kW/kg-K
Formation vol. factor	$B_i=e^{-ci(P-Pr)}$		Thermal conductivity, water	0.58	W/m-K
Reservoir Prop.			Thermal conductivity, oil	0.15	W/m-K
Lengths in x, y-dir	1000	m	Thermal conductivity, grain	1.7	W/m-K
Layer height	10	m	Mechanical Properties		
Init. reservoir pressure	6000	psi	Poisson's ratio	0.3	-
S_v	13953	psi	Compressibility, water	0.4×10^{-9}	Pa^{-1}
S_{Hmax}	8372	psi	Compressibility, oil	3.0×10^{-9}	Pa^{-1}
S_{hmin}	8233	psi	Compressibility, grain	2.6×10^{-9}	Pa^{-1}
Permeability, horiz.	1000	md	Biot’s coefficient	1	-
Porosity	0.2	-	Young's modulus	25	GPa

Table 5.4: Input parameters used for the single horizontal well simulations.

Parameter	Value		Parameter	Value	
Well and Fluid Prop.			Thermal Properties		
Injection rate, water	5000	bbl/d	High temperature (inj or prod)	353	K
Prod well BHP	800	psi	Low temperature (inj or prod)	293	K
Well radius	0.16	m	Specific heat capacity, fluid	4.1	kW/kg-K
Viscosity	1, 20	cp	Specific heat capacity, grain	0.8	kW/kg-K
Reservoir Prop.			Thermal conductivity, fluid	0.58	W/m-K
Init. reservoir pressure	1100	psi	Thermal conductivity, grain	1.7	W/m-K
S_v	2853	psi	Mechanical Properties		
S_{Hmax}	1950	psi	Poisson's ratio	0.3	-
S_{hmin}	1900	psi	Compressibility, fluid	0.4×10^{-9}	Pa^{-1}
Permeability, horiz.	600	md	Compressibility, grain	2.9×10^{-9}	Pa^{-1}
Porosity	0.28	-	Biot’s coefficient	1	-
			Young's modulus	3	GPa

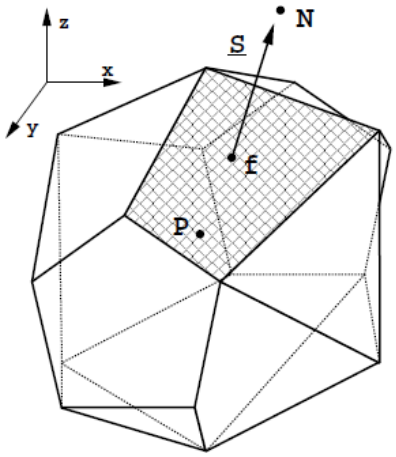

Figure 5.1: Typical control volume of a general polyhedron shape, from Jasak (1996).

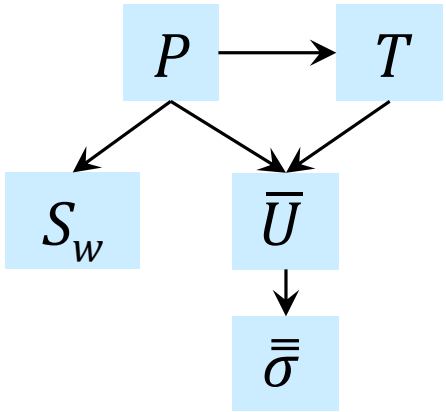

Figure 5.2: Sequence of calculations in the simulation.

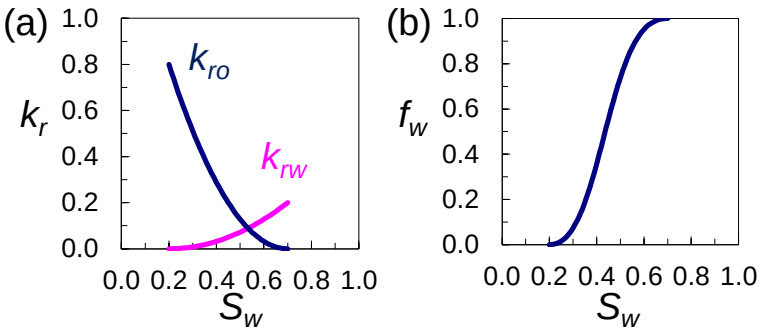

Figure 5.3: (a) Water-oil relative permeability of the simulation case. (b) Fractional flow curve calculated from simulation input properties.

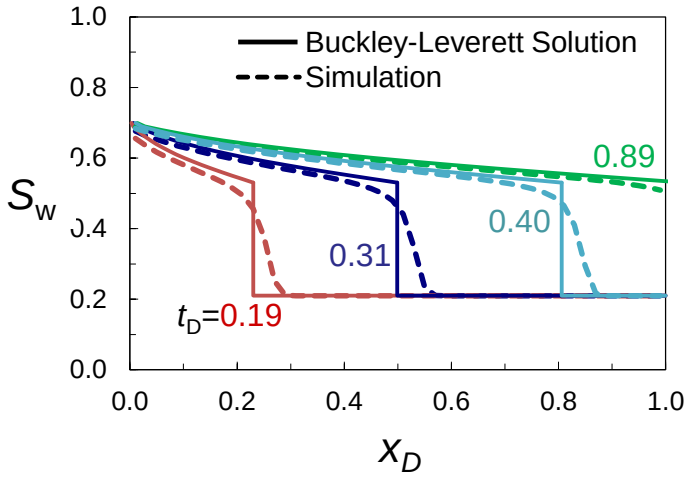

Figure 5.4: Saturation profile vs. dimensionless distance in the core. Simulation results were compared to Buckley-Leverett solution for different dimensionless time.

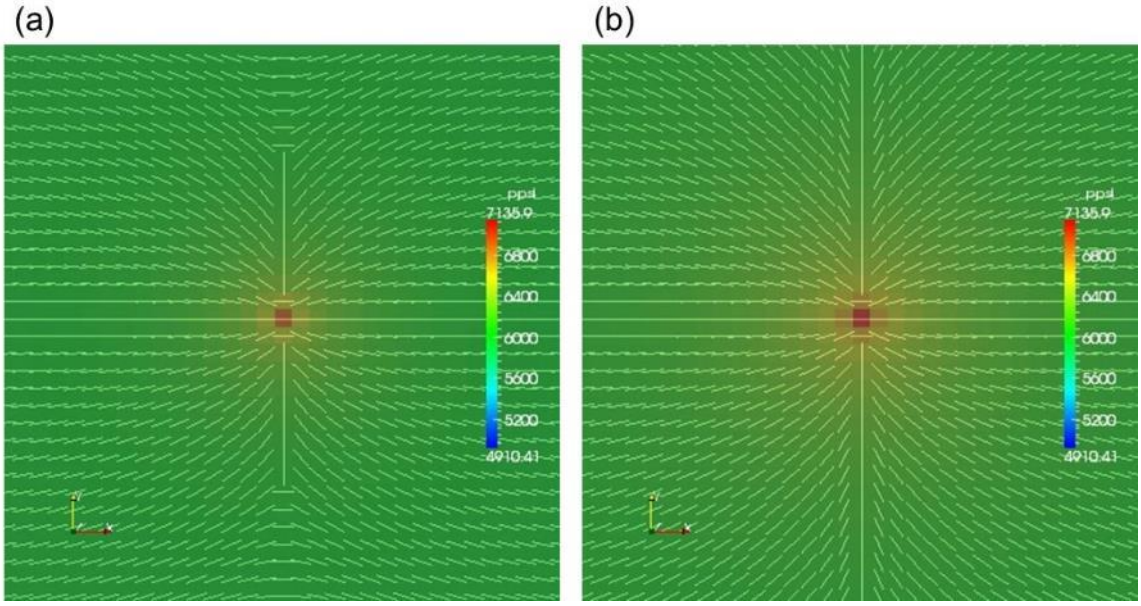

Figure 5.5: Stress reorientation near an injection well. Lines indicate the S_{Hmax} direction (reorientation caused by poroelasticity only). Colors indicate pressure. Length of each side is 640m. (a) t =100days, (b) t =500days.

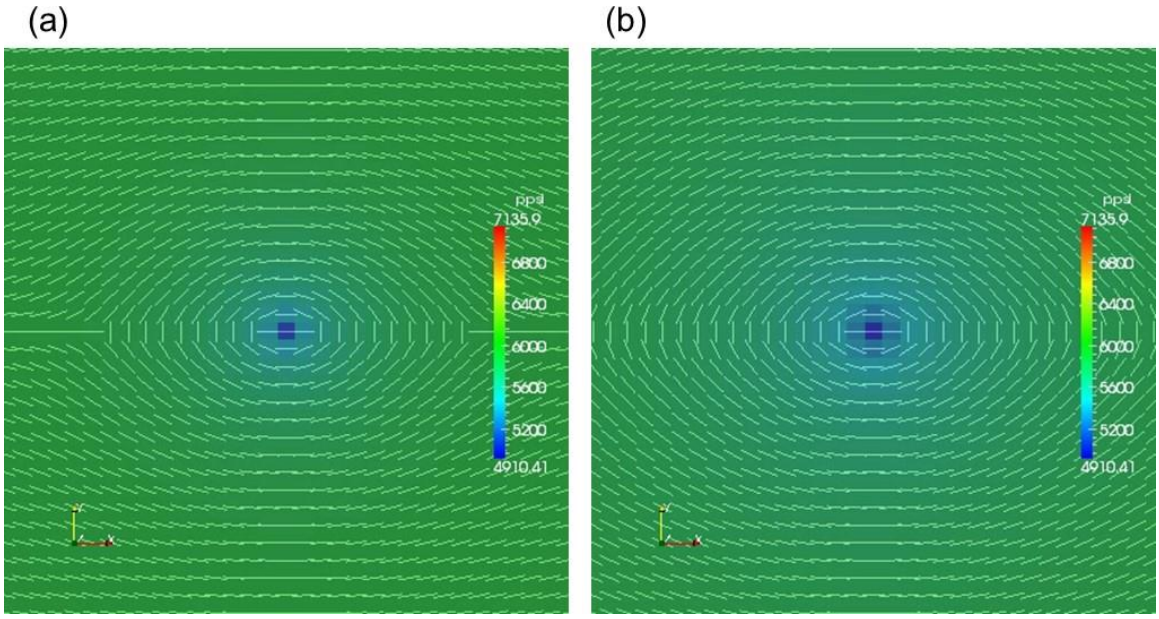

Figure 5.6: Stress reorientation near a production well. Lines indicate the S_{Hmax} direction (reorientation caused by poroelasticity only). Colors indicate pressure. Length of each side is 640m. (a) t =100days, (b) t =500days.

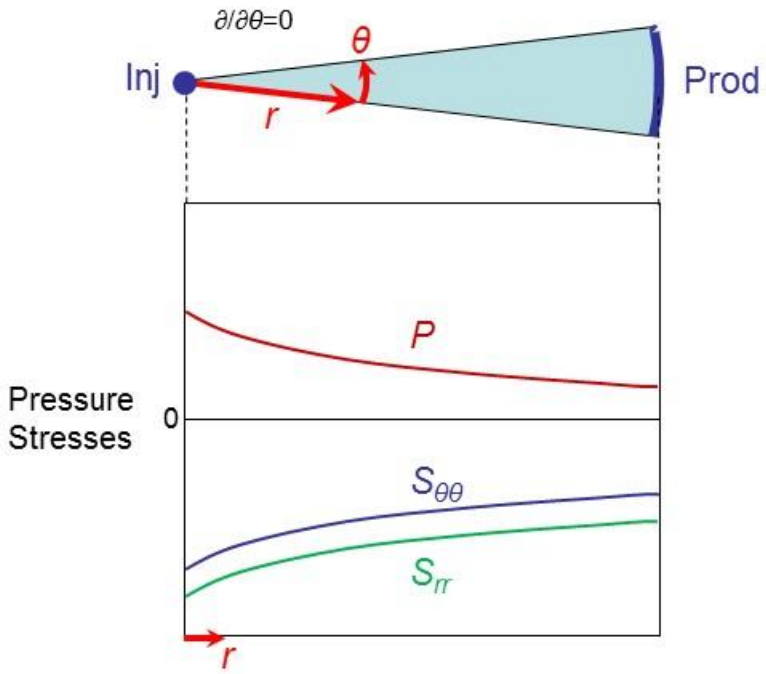

Figure 5.7: Infinitesimal portion of a reservoir in cylindrical coordinates. Fluid injection is a point-source at the origin, and production is along the outer perimeter. Conceptual values of pressure and stresses in r- and θ-directions are shown.

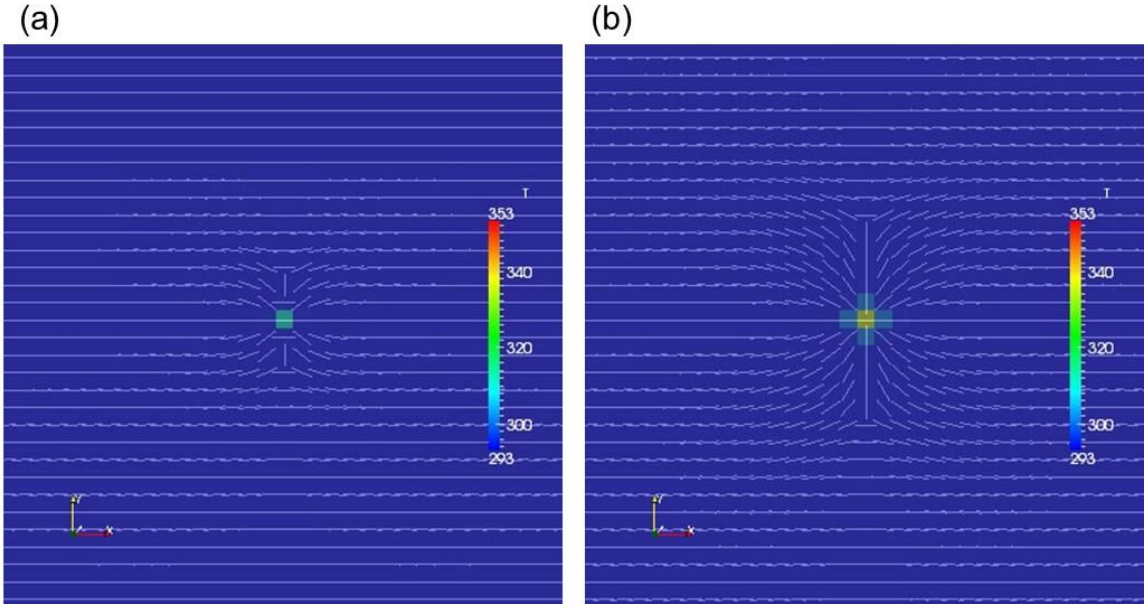

Figure 5.8: Stress reorientation near a hot-fluid injection well. Lines indicate the S_{Hmax} direction (reorientation caused by thermoelasticity only). Colors indicate temperature. Length of each side is 640m. (a) t =100days, (b) t =500days.

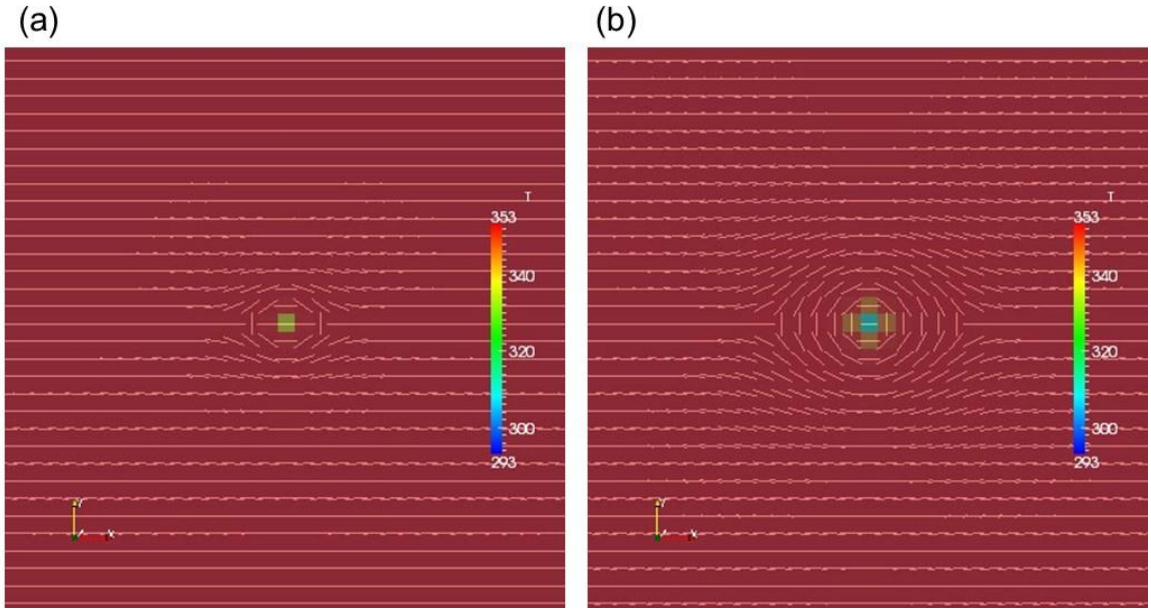

Figure 5.9: Stress reorientation near a cold-fluid injection well. Lines indicate the S_{Hmax} direction (reorientation caused by thermoelasticity only). Colors indicates temperature Length of each side is 640m. (a) t =100days, (b) t =500days.

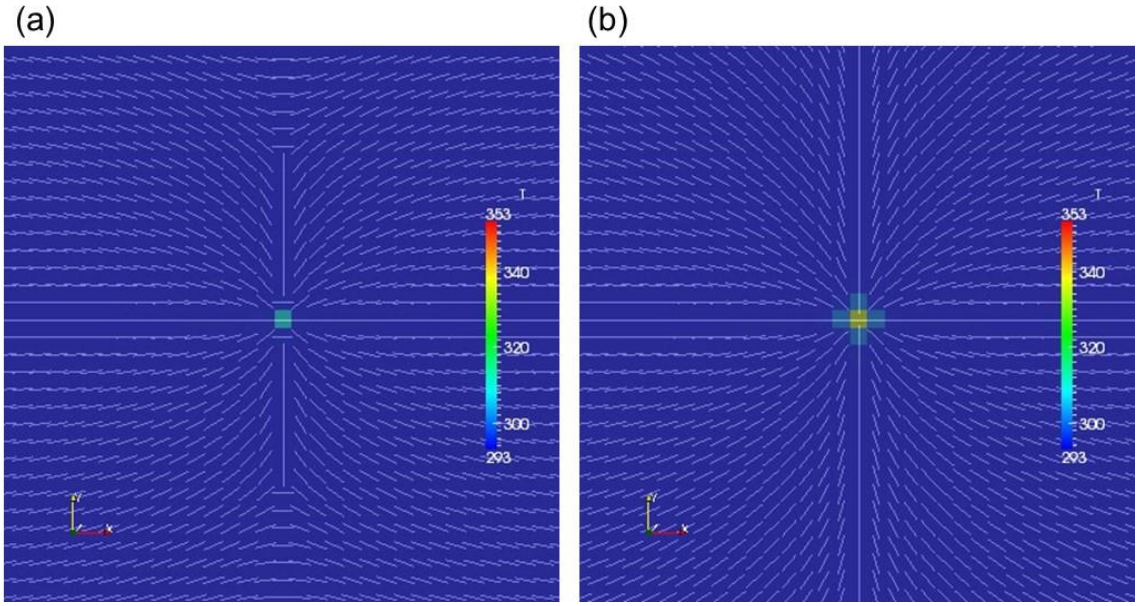

Figure 5.10: Stress reorientation near hot-fluid injection well. Lines indicate the S_{Hmax} direction (reorientation caused by poro- and thermoelasticity). Color indicates temperature. Length of each side is 640m. (a) t =100days, (b) t =500days.

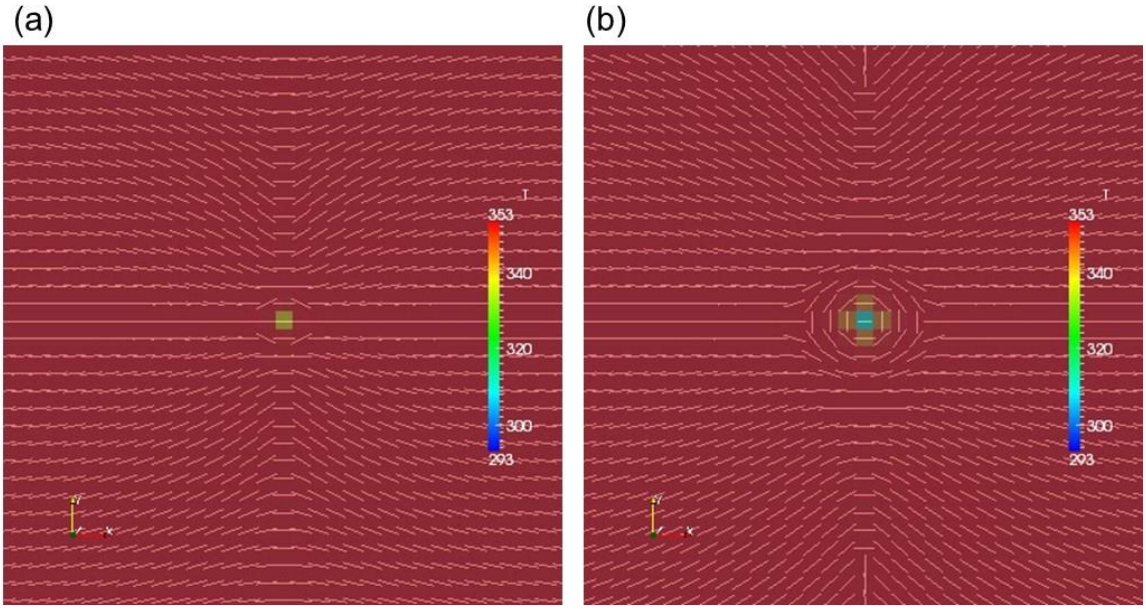

Figure 5.11: Stress reorientation near cold-fluid injection well. Lines indicate the S_{Hmax} direction (reorientation caused by poro- and thermoelasticity). Color indicates temperature. Length of each side is 640m. (a) t =100days, (b) t =500days.

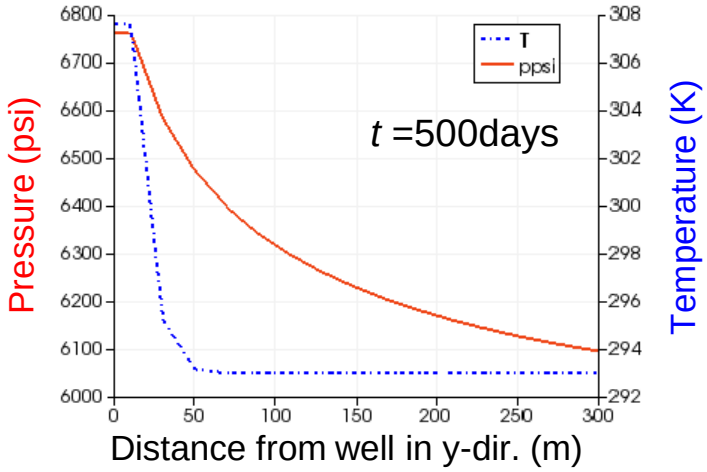

Figure 5.12: Pressure and temperature profile at t =500days in hot-fluid injection case.

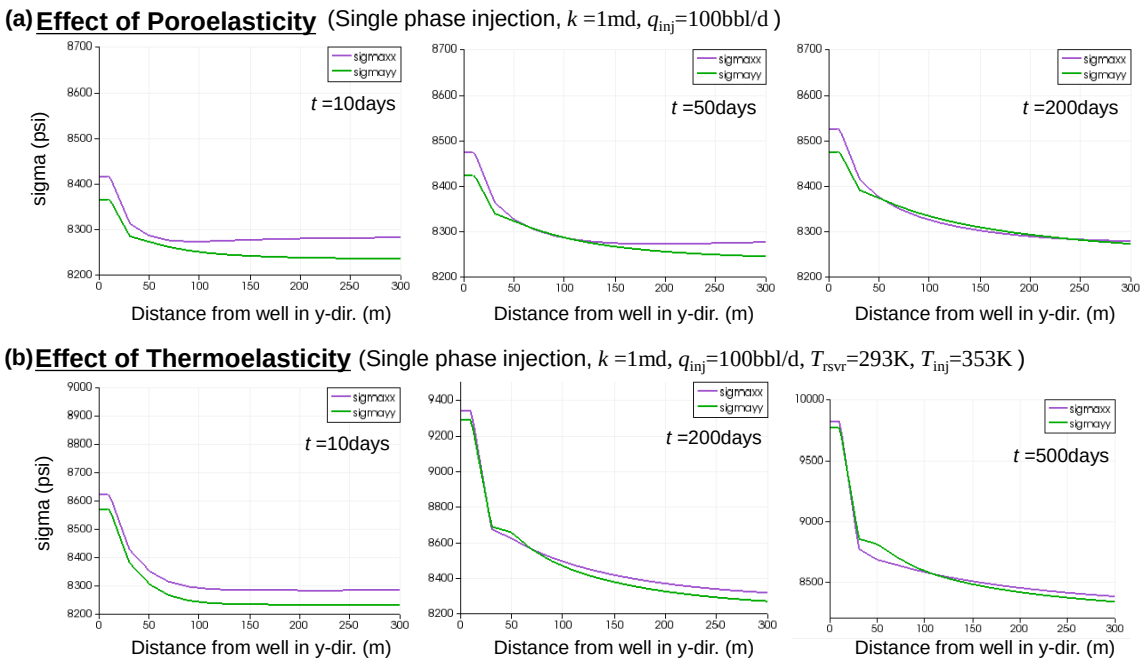

Figure 5.13: Changes in magnitudes of component xx and yy of total stress in simulation cases.

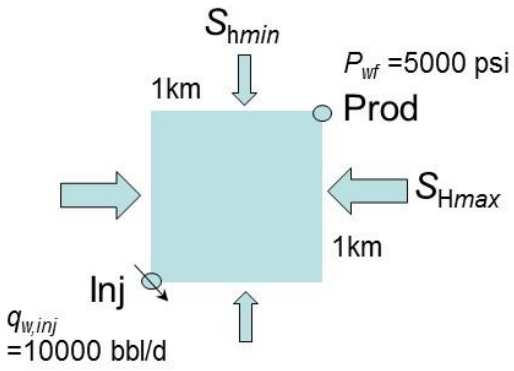

Figure 5.14: Quarter of 5-spot well pattern (1km by 1km). Initial horizontal stress directions are shown.

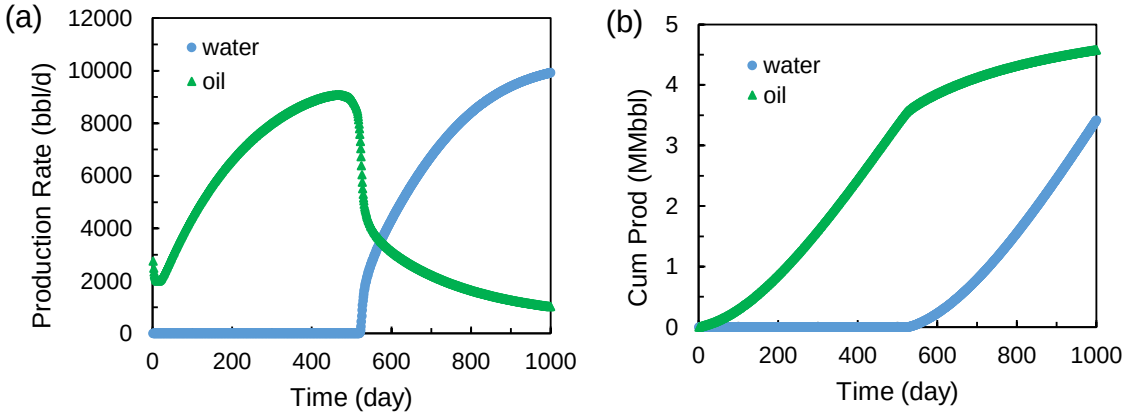

Figure 5.15: Calculated water and oil production in the five-spot well pattern. (a) daily production rate, (b) cumulative production of water and oil.

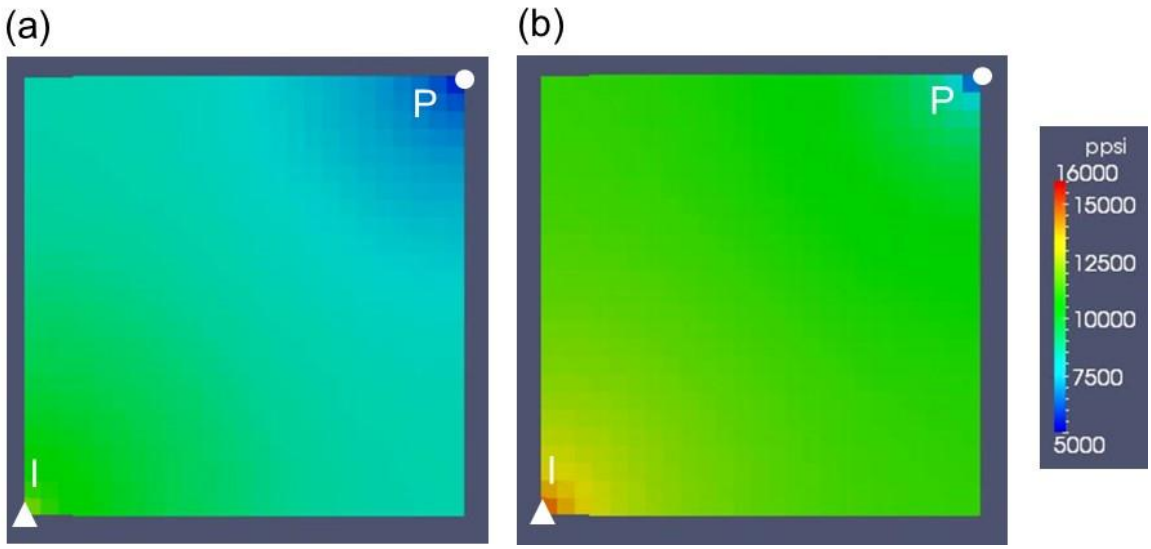

Figure 5.16: Pressure changes in a quarter five-spot well pattern. Pressure is in psi. (a) t =200days, (b) t =600days.

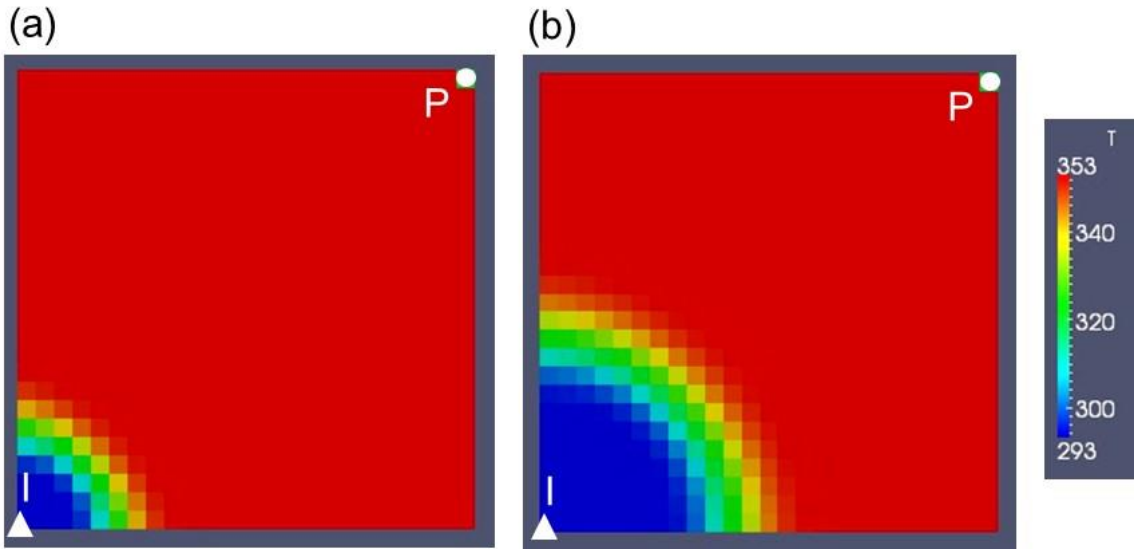

Figure 5.17: Temperature changes in a quarter five-spot well pattern. Temperature is in Kelvin. (a) t =200days, (b) t =600days.

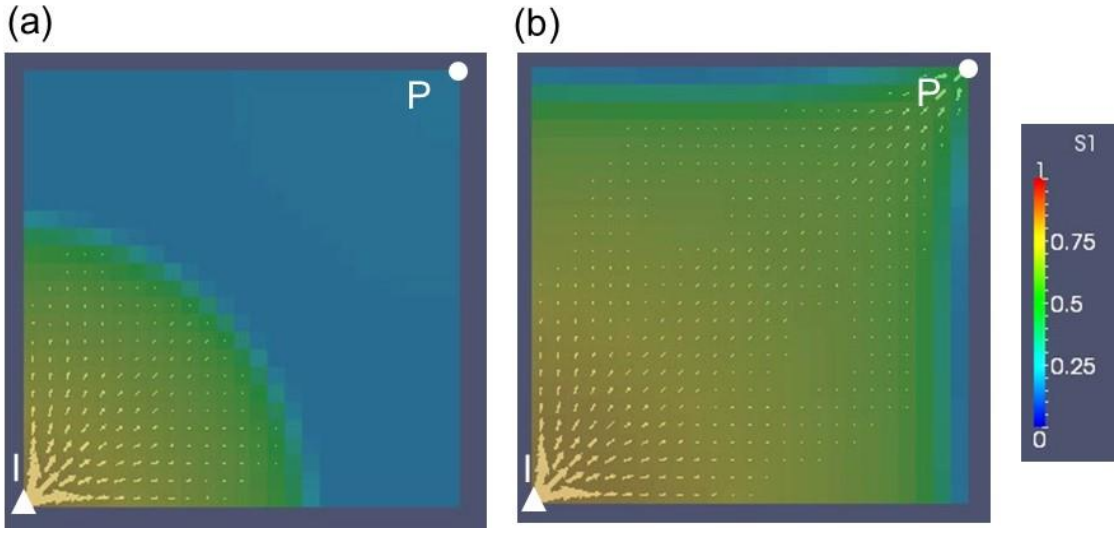

Figure 5.18: Water saturation and water velocity vector changes in a quarter five-spot well pattern. Saturation is in color map and arrows indicate water velocity vectors. (a) *t* =200days, (b) *t* =600days.

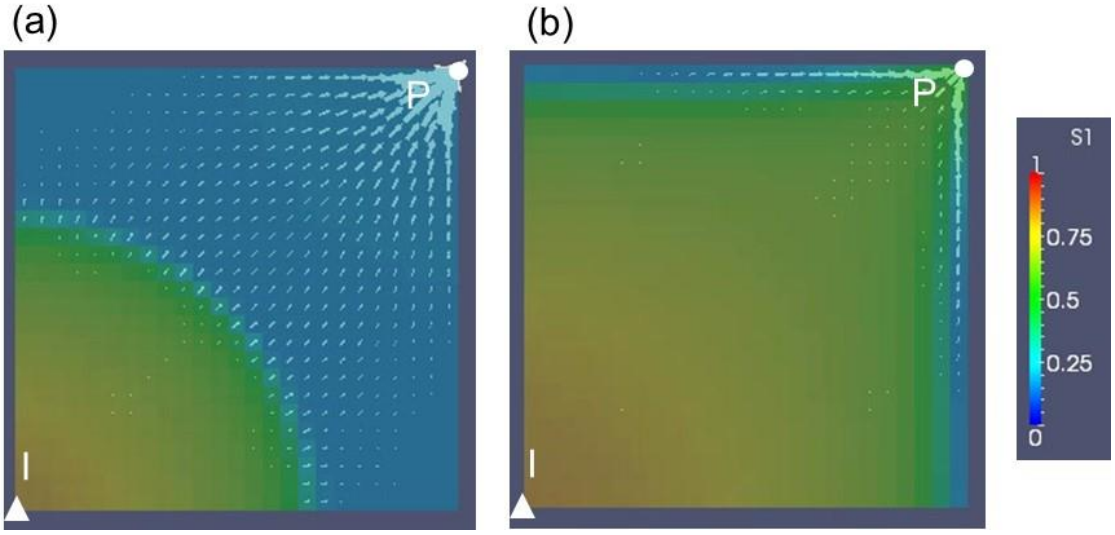

Figure 5.19: Water saturation and oil velocity vector changes in a quarter five-spot well pattern. Saturation is in color map and arrows indicate oil velocity vectors. (a) *t* =200days, (b) *t* =600days.

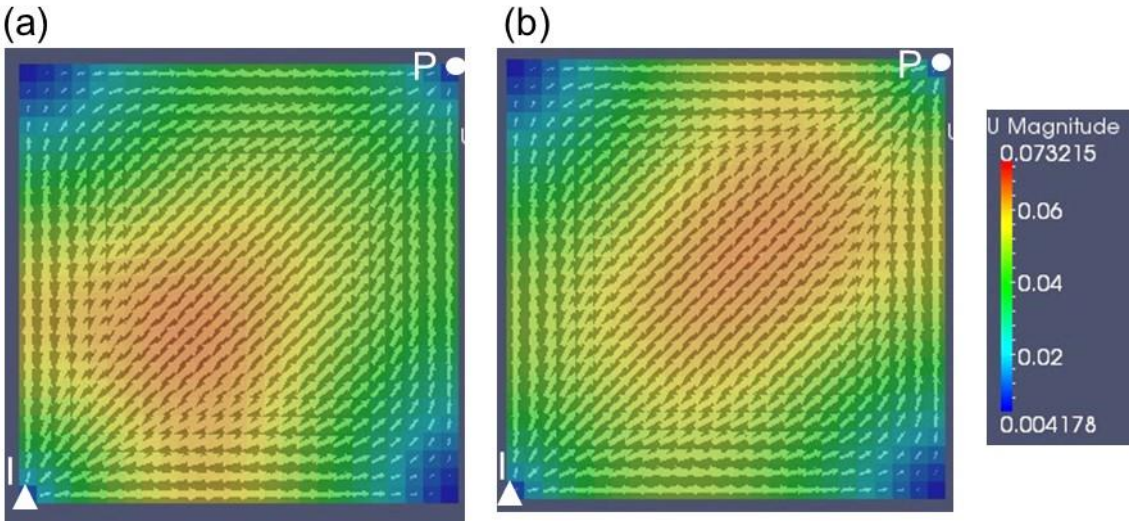

Figure 5.20: Diplacement field for a waterflooded reservoir caused only by poroelasticity in a quarter five-spot well pattern. Arrows indicate the displacement vector. Colors indicate the magnitude of the displacement (in meters). (a) t =200days, (b) t =600days.

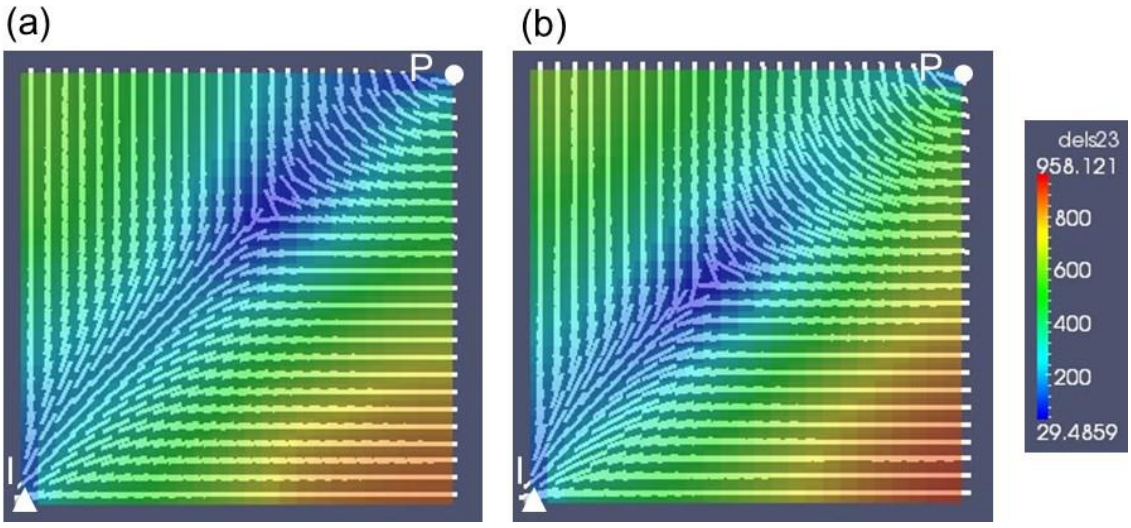

Figure 5.21: Stress reorientation (caused by poroelasticity only) during waterflooding in a quarter five-spot well pattern. Lines indicate the directions of maximum horizontal stress. Colors indicate the differences between maximum and minimum horizontal stresses in psi. (a) t =200days, (b) t =600days.

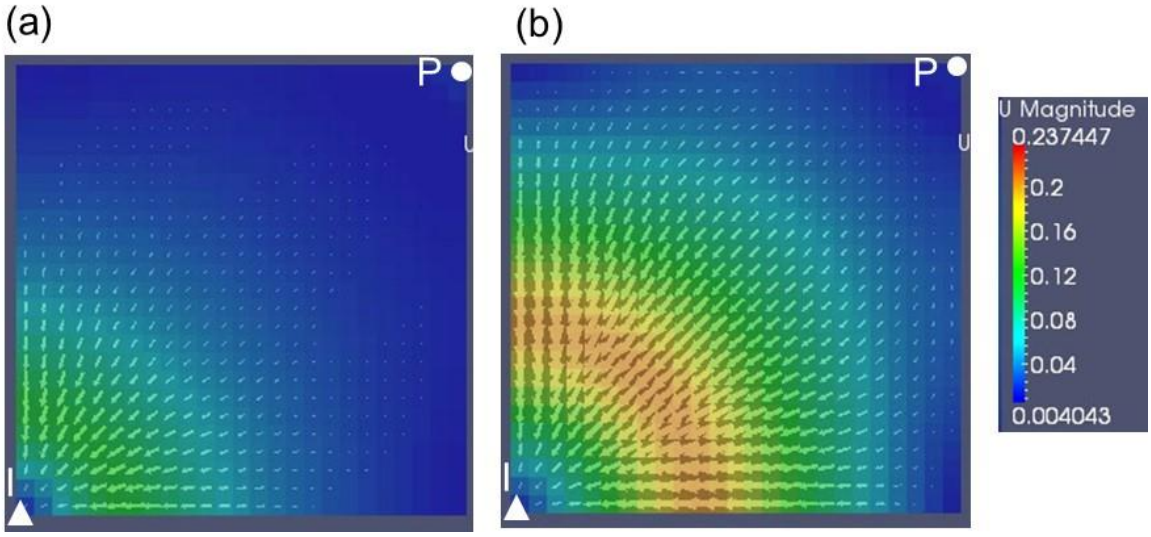

Figure 5.22: Diplacement field for waterflooded reservoirs only by thermoelasticity in a quarter five-spot well pattern. Arrows indicate the displacement vector. Colors indicate the magnitude of the displacement (in meters). (a) t =200days, (b) t =600days.

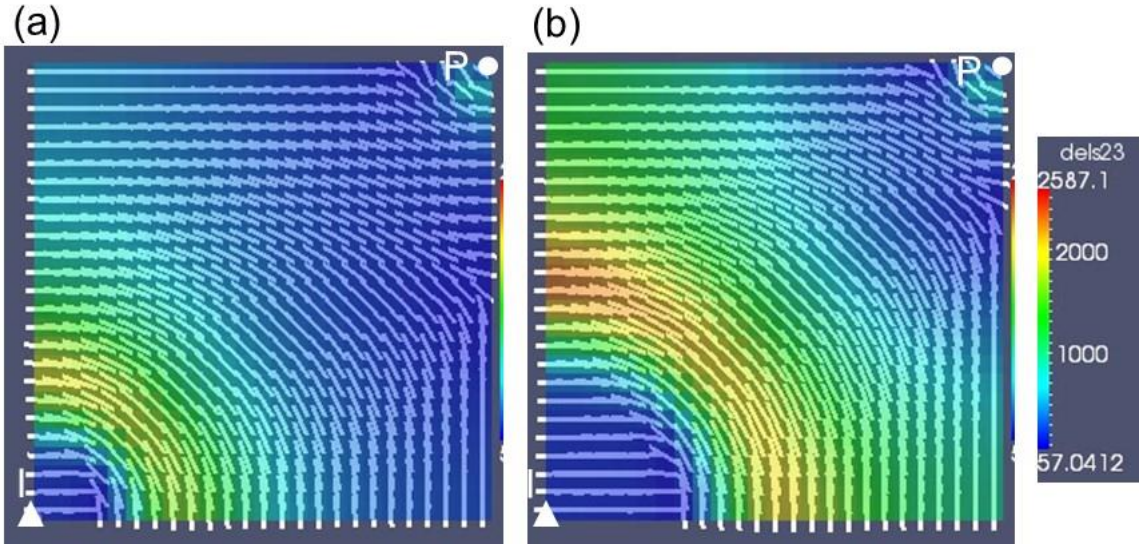

Figure 5.23: Stress reorientation (caused by thermoelasticity only) during waterflooding in a quarter five-spot well pattern. Lines indicate the directions of maximum horizontal stress. Colors indicate the differences between maximum and minimum horizontal stresses in psi. (a) t =200days, (b) t =600days.

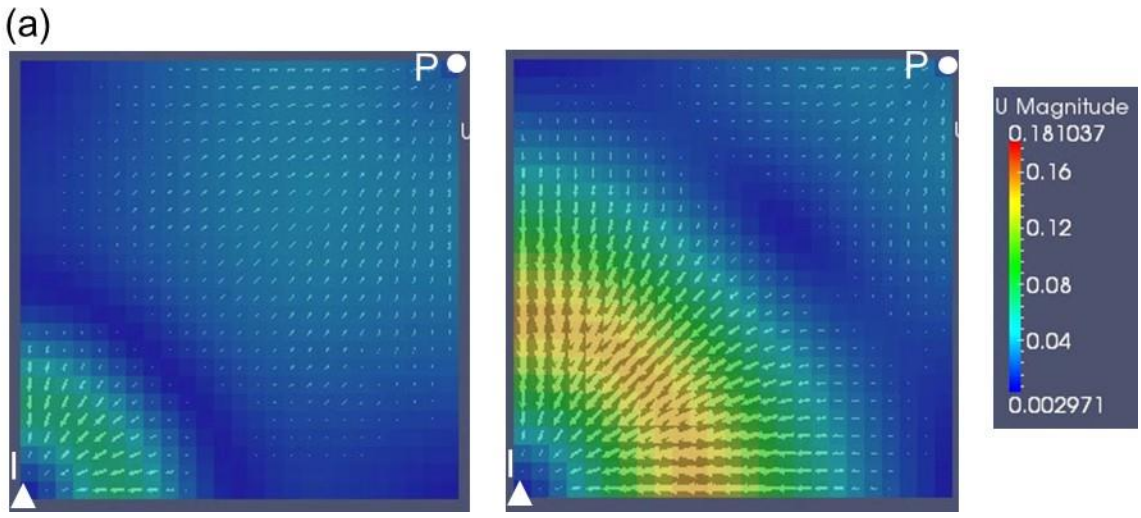

Figure 5.24: Diplacement filed for waterflooded reservoirs by both poro- and thermo-elasticity in a quarter five-spot well pattern. Arrows indicate the displacement vector. Colors indicate the magnitude of the displacement in meter. (a) t =200days, (b) t =600days.

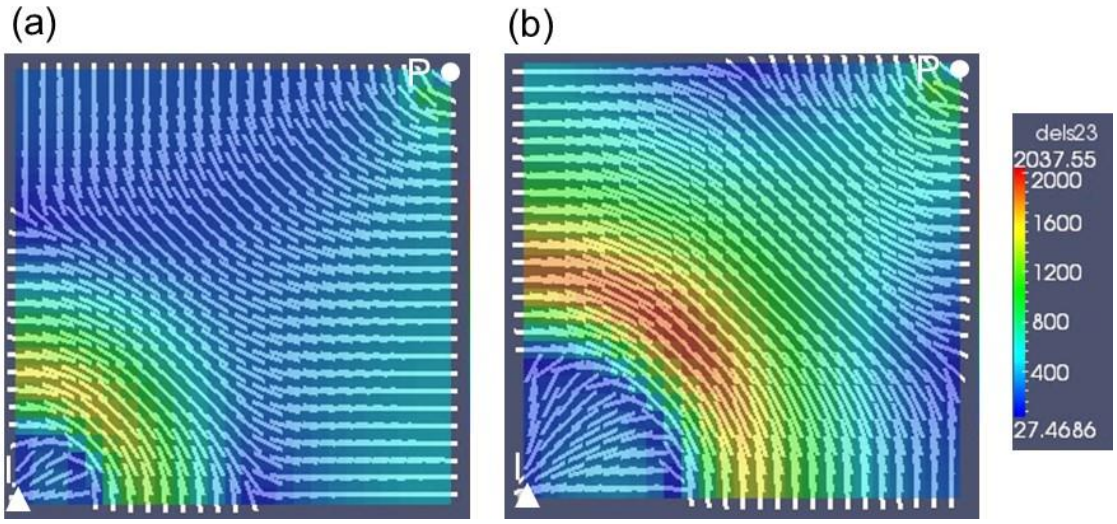

Figure 5.25: Stress reorientation (caused by both poro- and thermo-elasticity) during waterflooding in a quarter five-spot well pattern. Lines indicate the directions of maximum horizontal stress. Colors indicate the differences between maximum and minimum horizontal stresses in psi. (a) t =200days, (b) t =600days.

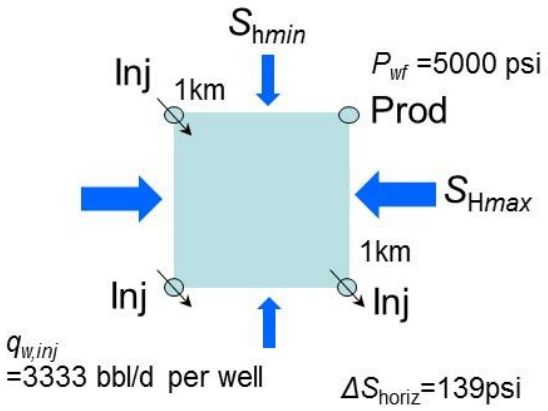

Figure 5.26: Quarter of 9-spot well pattern in size of 1km by 1km. Initial horizontal stress directions are shown.

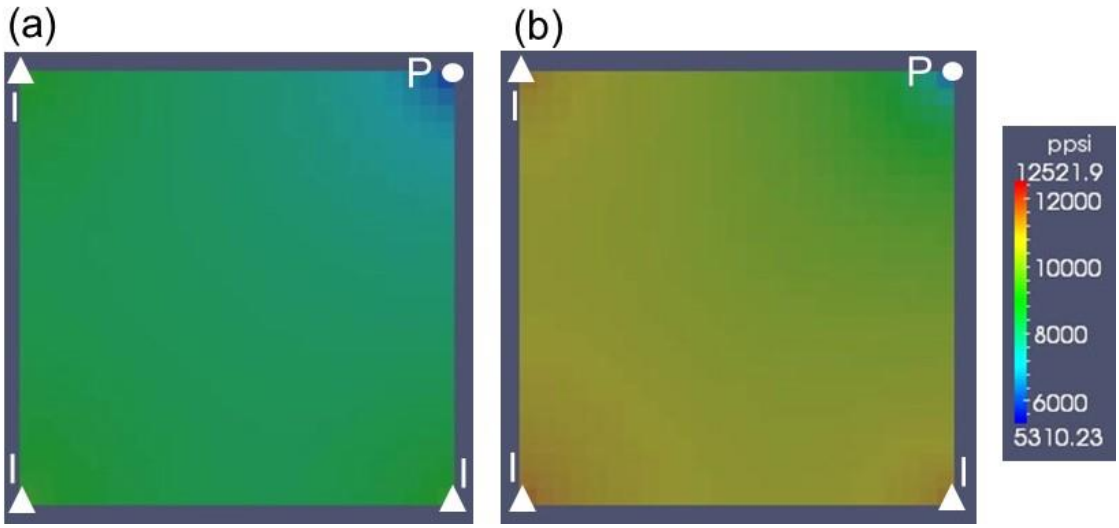

Figure 5.27: Pressure changes in a quarter nine-spot well pattern. Pressure is in psi. (a) t =200days, (b) t =600days.

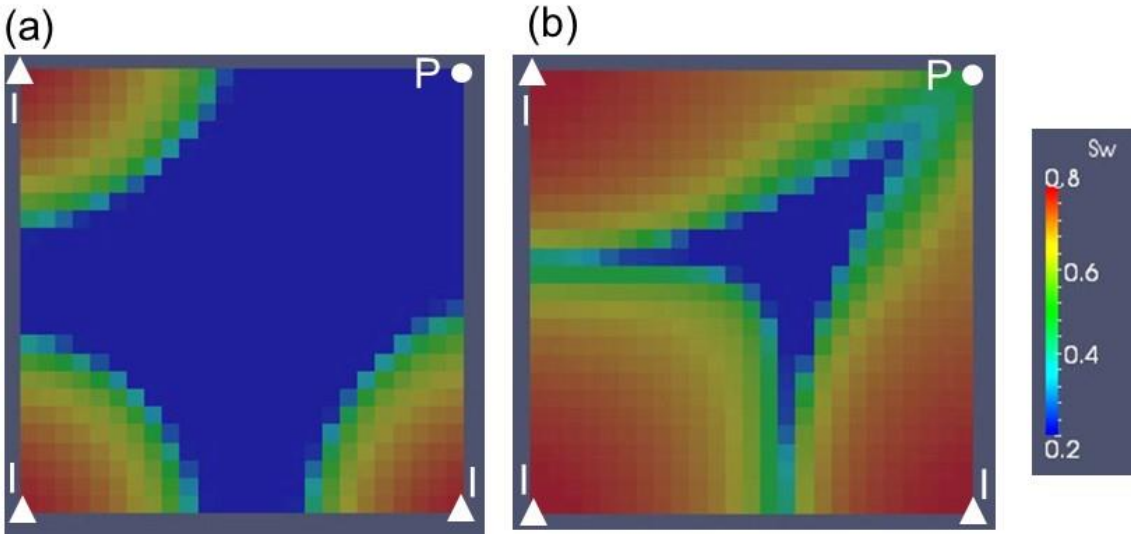

Figure 5.28: Water saturation changes in a quarter nine-spot well pattern. (a) *t* =200days, (b) *t* =600days.

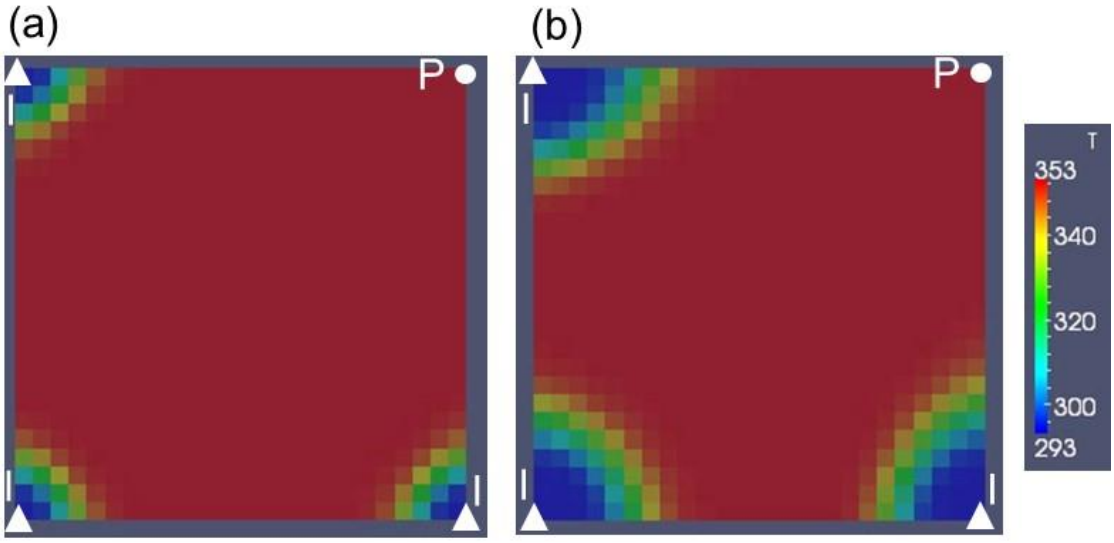

Figure 5.29: Temperature changes in a quarter nine-spot well pattern. Temperature is in Kelvin. (a) *t* =200days, (b) *t* =600days.

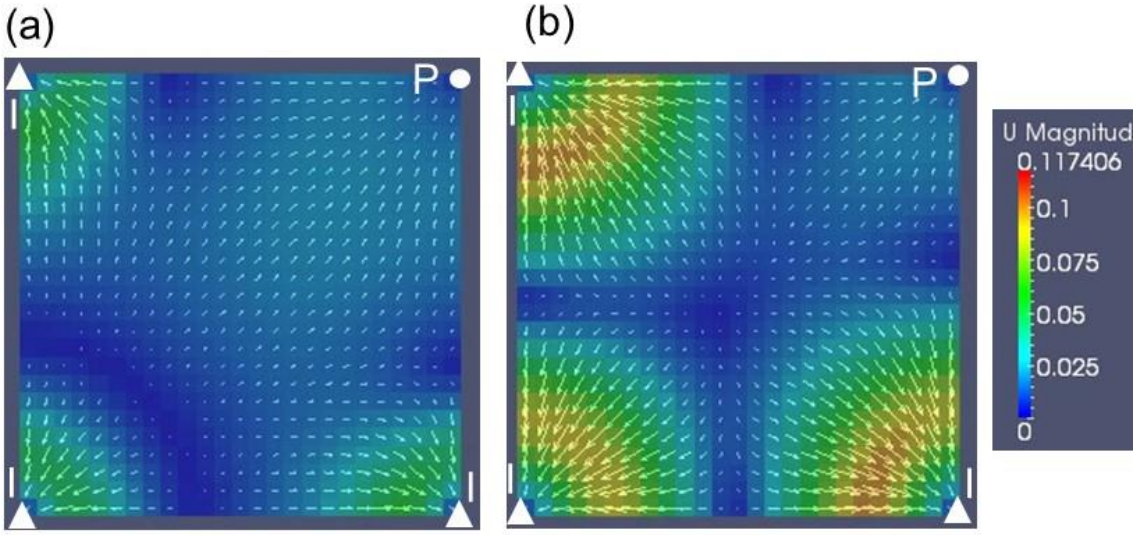

Figure 5.30: Diplacement in a quarter nine-spot well pattern. Arrows indicate the displacement vector. Colors indicate the magnitude of the displacement (in meters). (a) *t* =200days, (b) *t* =600days.

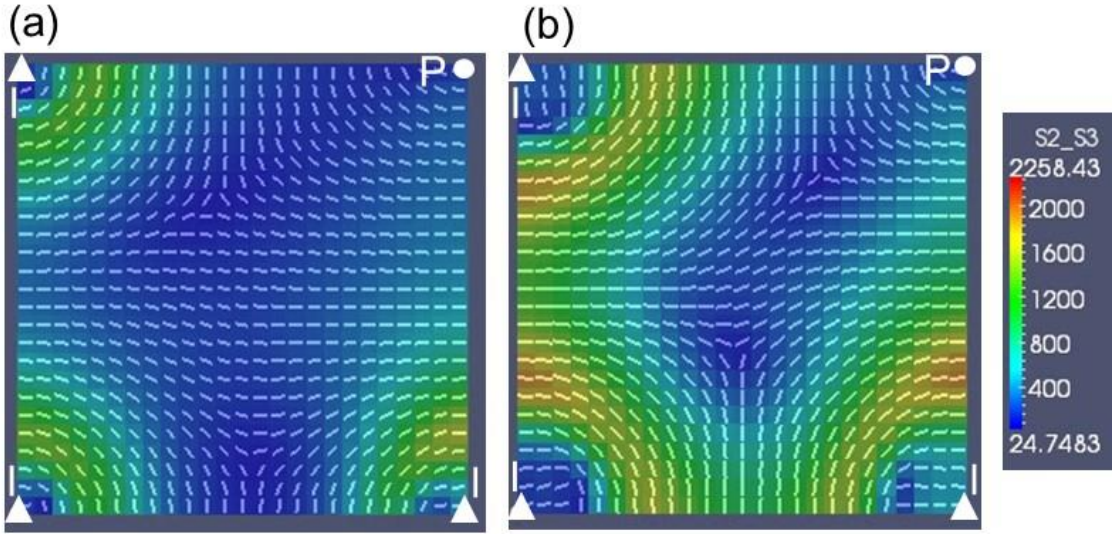

Figure 5.31: Stress reorientation (caused by both poro- and thermo-elasticity) during waterflooding in a quarter nine-spot well pattern. Lines indicate directions of maximum horizontal stress. Colors indicate the differences between maximum and minimum horizontal stresses in psi. (a) *t* =200days, (b) *t* =600days.

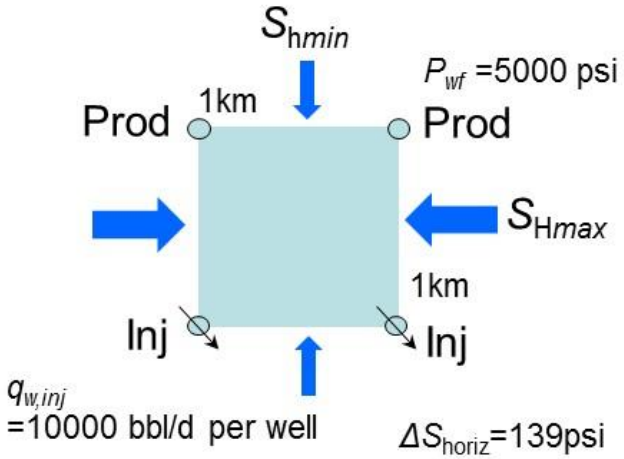

Figure 5.32: Unit section of line-drive well pattern in size of 1km by 1km. Initial horizontal stress directions are shown.

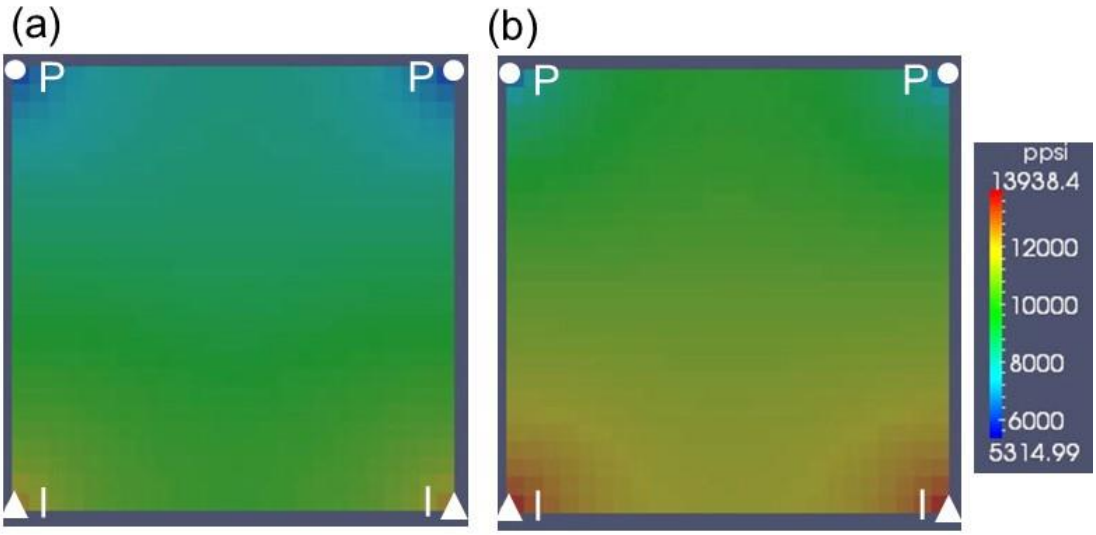

Figure 5.33: Pressure changes in a unit line-drive well pattern. Pressure is in psi. (a) t =200days, (b) t =600days.

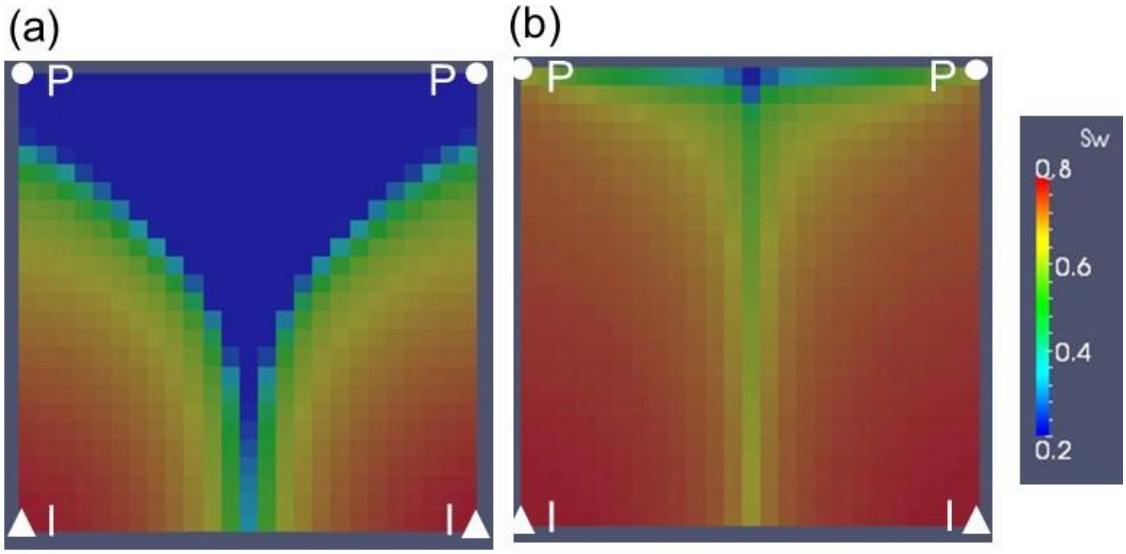

Figure 5.34: Water saturation changes in a unit line-drive well pattern. (a) *t* =200days, (b) *t* =600days.

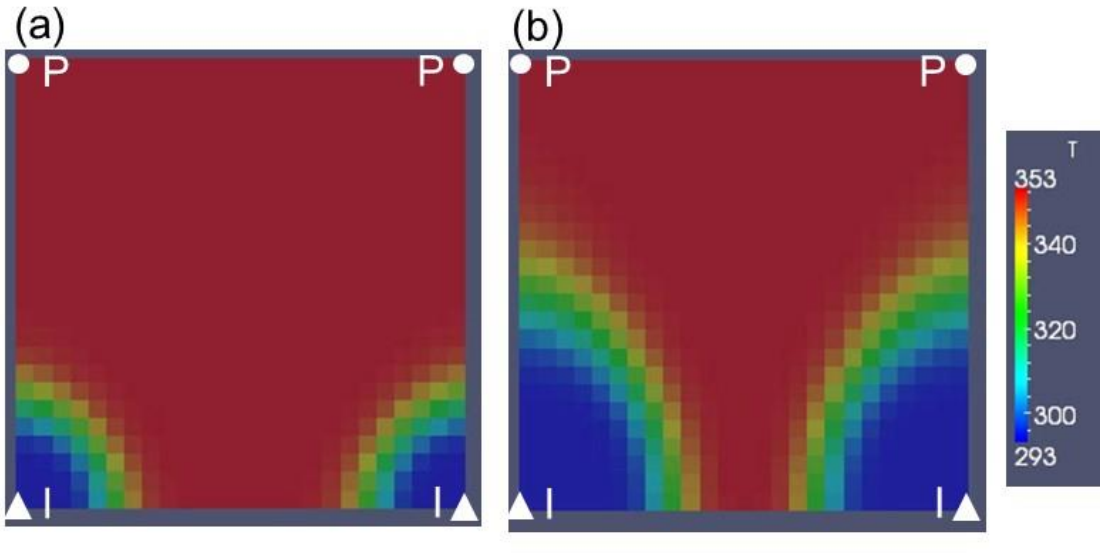

Figure 5.35: Temperature changes in a unit line-drive well pattern. Temperature is in Kelvin. (a) *t* =200days, (b) *t* =600days.

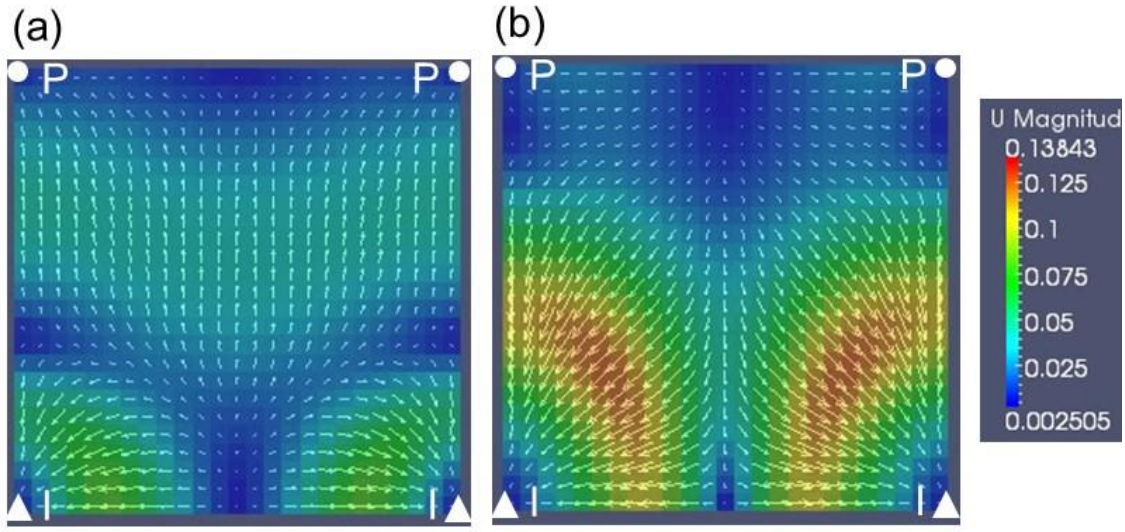

Figure 5.36: Diplacement in a unit line-drive well pattern. Arrows indicate the displacement vector. Colors indicate the magnitude of the displacement in meter. (a) *t* =200days, (b) *t* =600days.

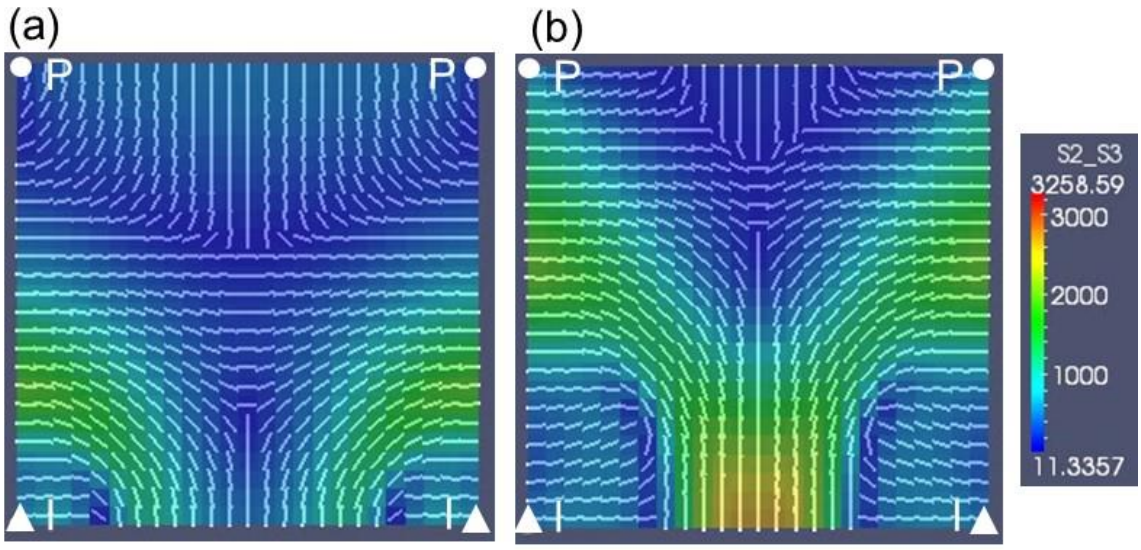

Figure 5.37: Stress reorientation (caused by both poro- and thermo-elasticity) during waterflooding in a unit line-drive well pattern. Lines indicate directions of maximum horizontal stress. Colors indicate the differences between maximum and minimum horizontal stresses in psi. (a) *t* =200days, (b) *t* =600days.

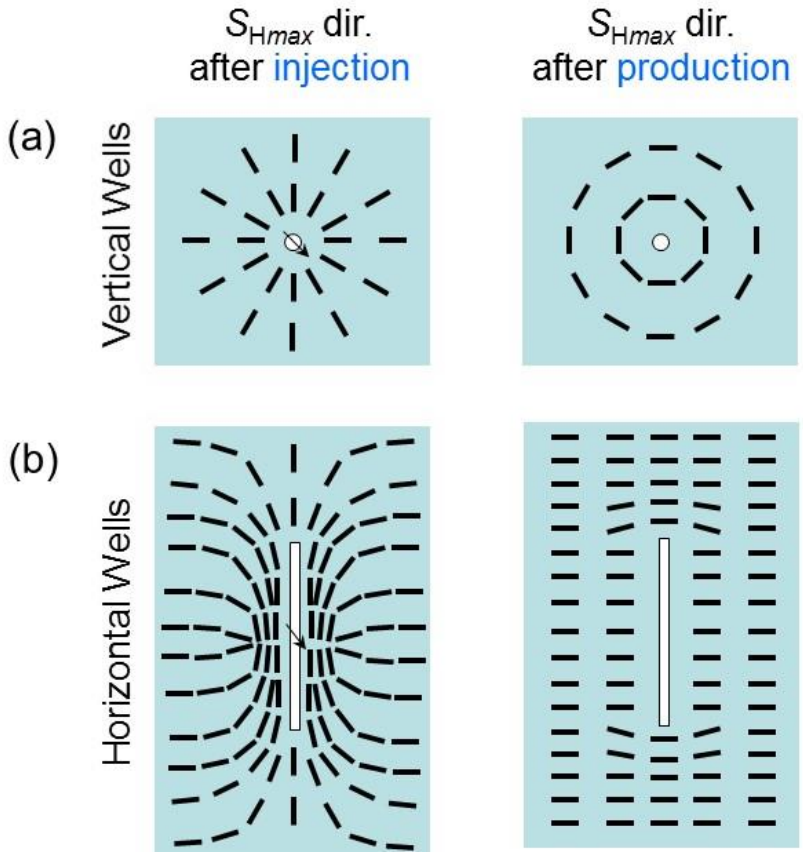

Figure 5.38: Conceptual diagrams showing S_{Hmax} reorientation in (a) vertical and (b) horizontal wells. Effects of injection and production were shown. The initial S_{Hmax} direction is the east-west direction.

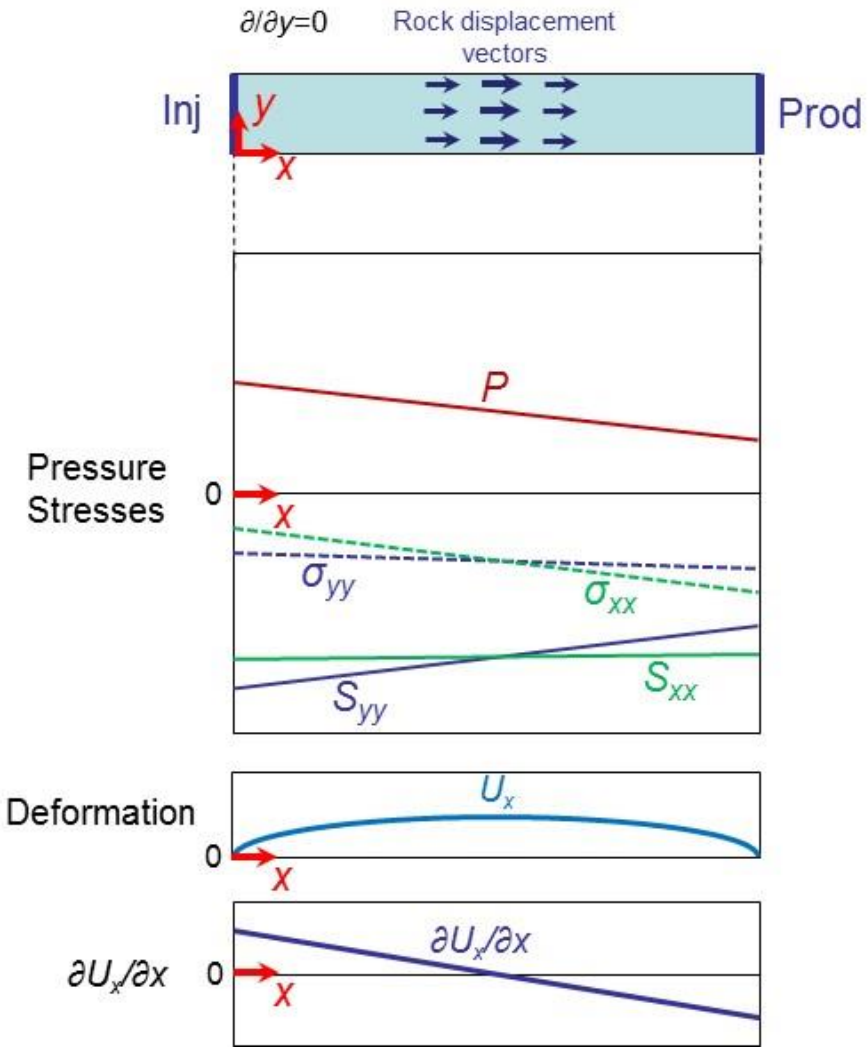

Figure 5.39: A portion of infinitely long injection and production wells parallel to each other. Pressure, stress, deformation in *x*-direction and its gradient to *x*-directions are shown along *x*-direction.

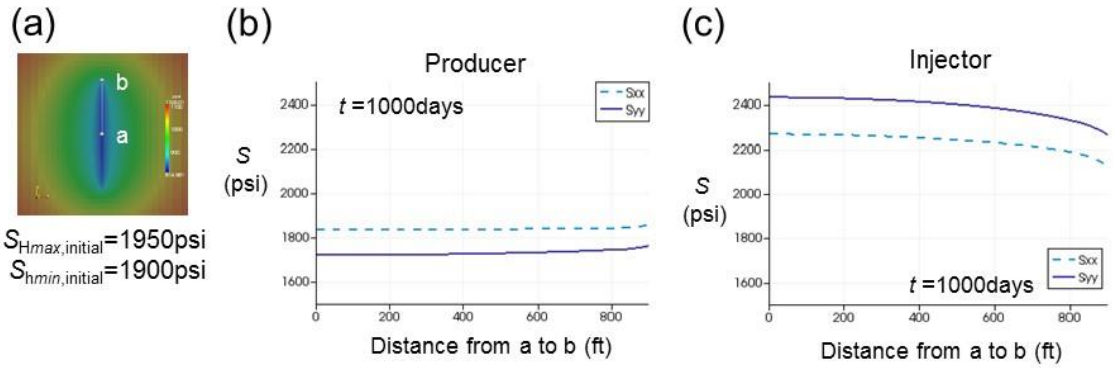

Figure 5.40: Stress magnitudes along a horizontal well section from point a to b in the section of the reservoir shown in (a). Stress magnitudes of *x*- and *y*-directions, S_{xx} and S_{yy}, are shown after 1000 days of (b) production and (c) injection.

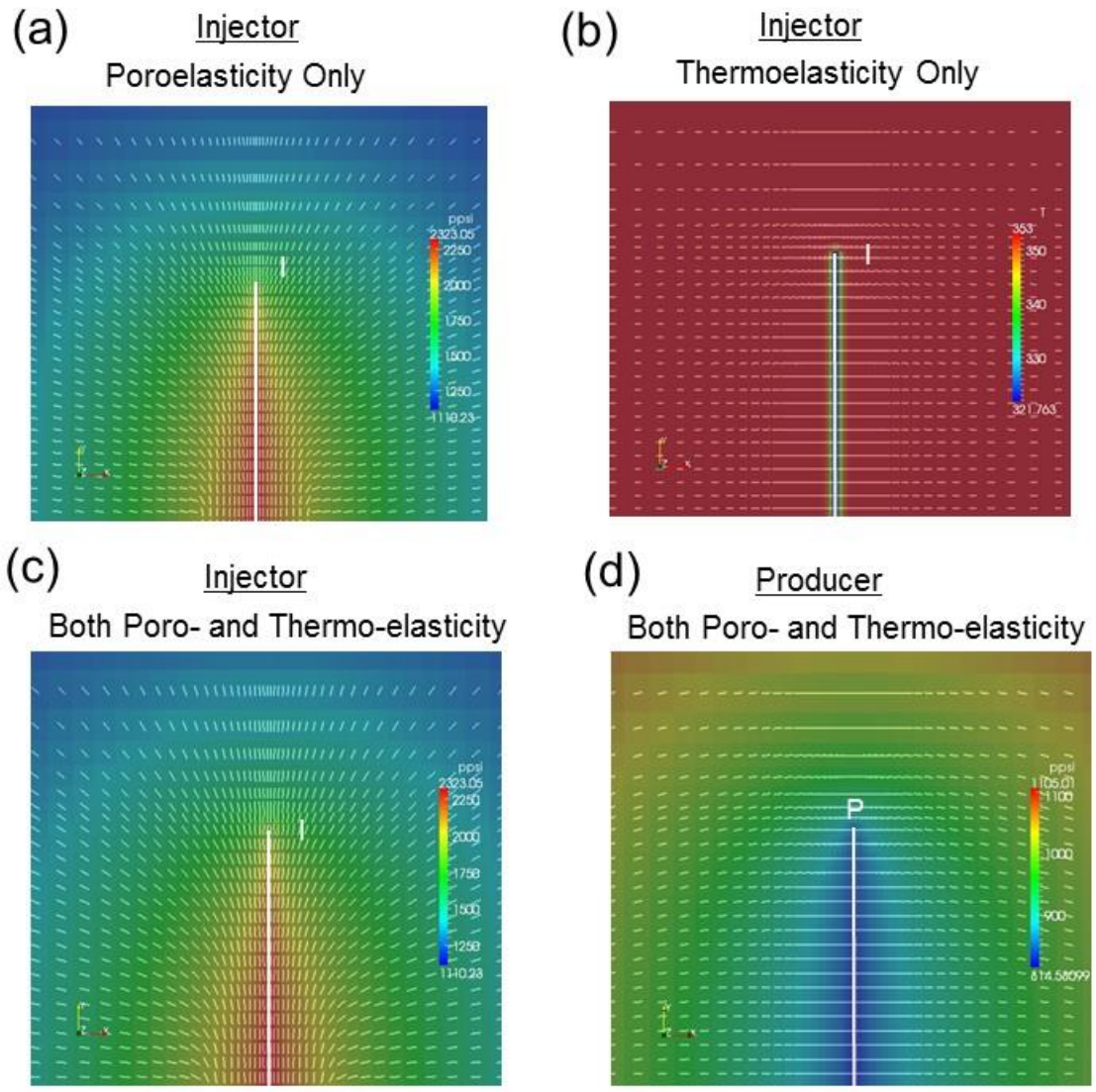

Figure 5.41: Direction of S_{Hmax} (shown as lines) after 1000 days in a single horizontal well. Colors represent pressure or temperature. For the injectors, individual effect of (a) poroelasticity, (b) thermoelasticity, and (c) combined effect of poro-thermo-elasticity were shown. For the producer, (d) combined effect was shown.

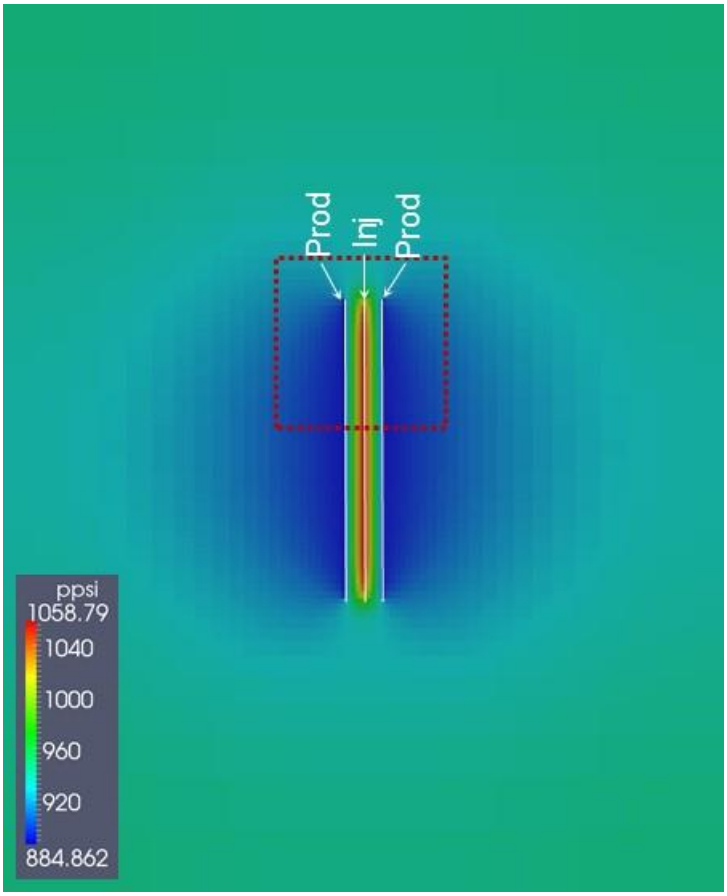

Figure 5.42: Configuration of a horizontal well pair with one injector and two producers. The area in the box with the dashed line will be shown in following figures.

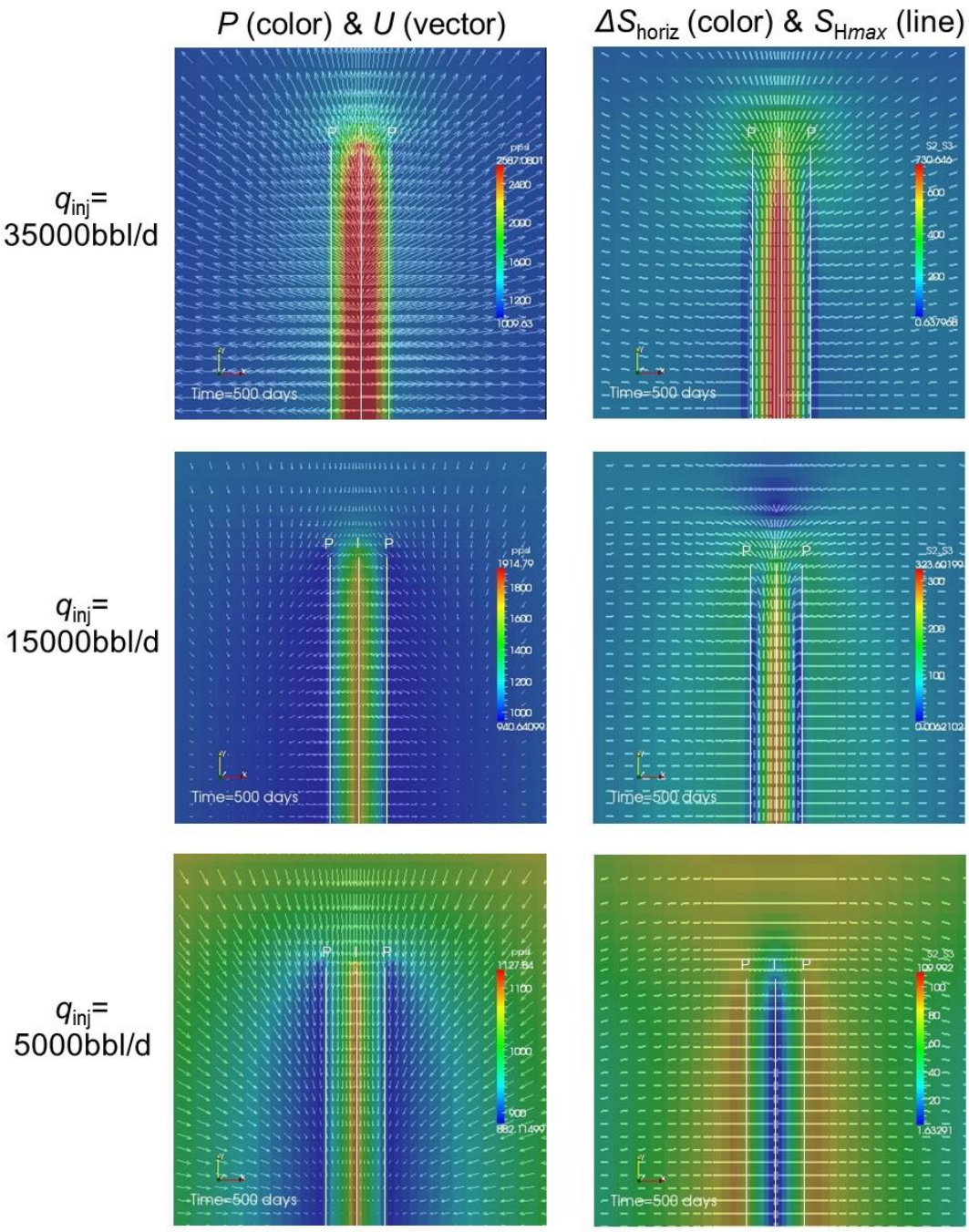

Figure 5.43: Effect of injection rate on reservoir displacement and S_{Hmax} reorientation. Pressure, displacement, horizontal stress contrast, and S_{Hmax} direction at t =500days were shown.

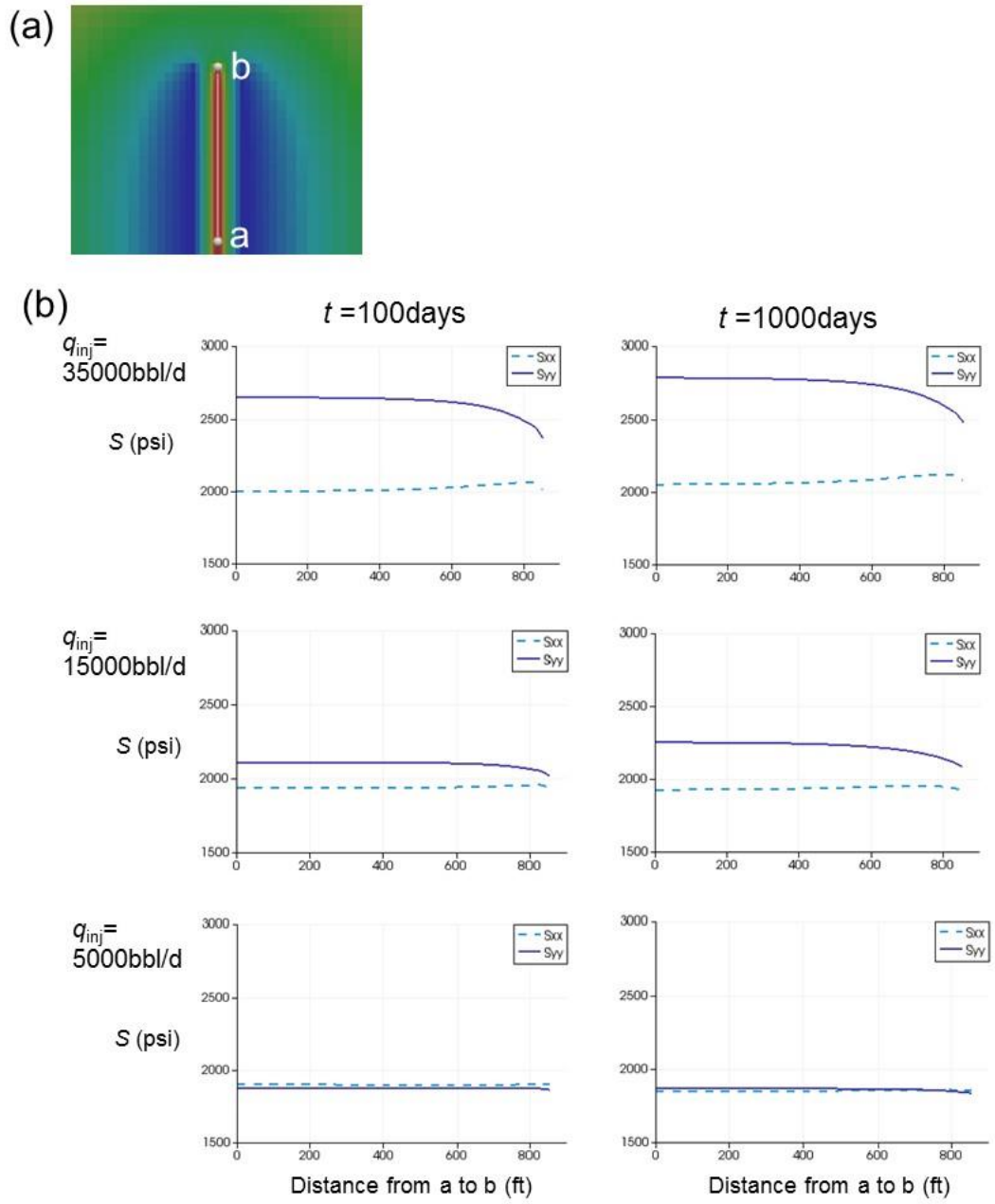

Figure 5.44: Effect of injection rate on stress magnitudes of S_{xx} and S_{yy}. (a) Values are shown along the line from the center (point a) to the tip (point b) of horizontal injector. (b) S_{xx} and S_{yy} are shown for t=100days and t=1000days.

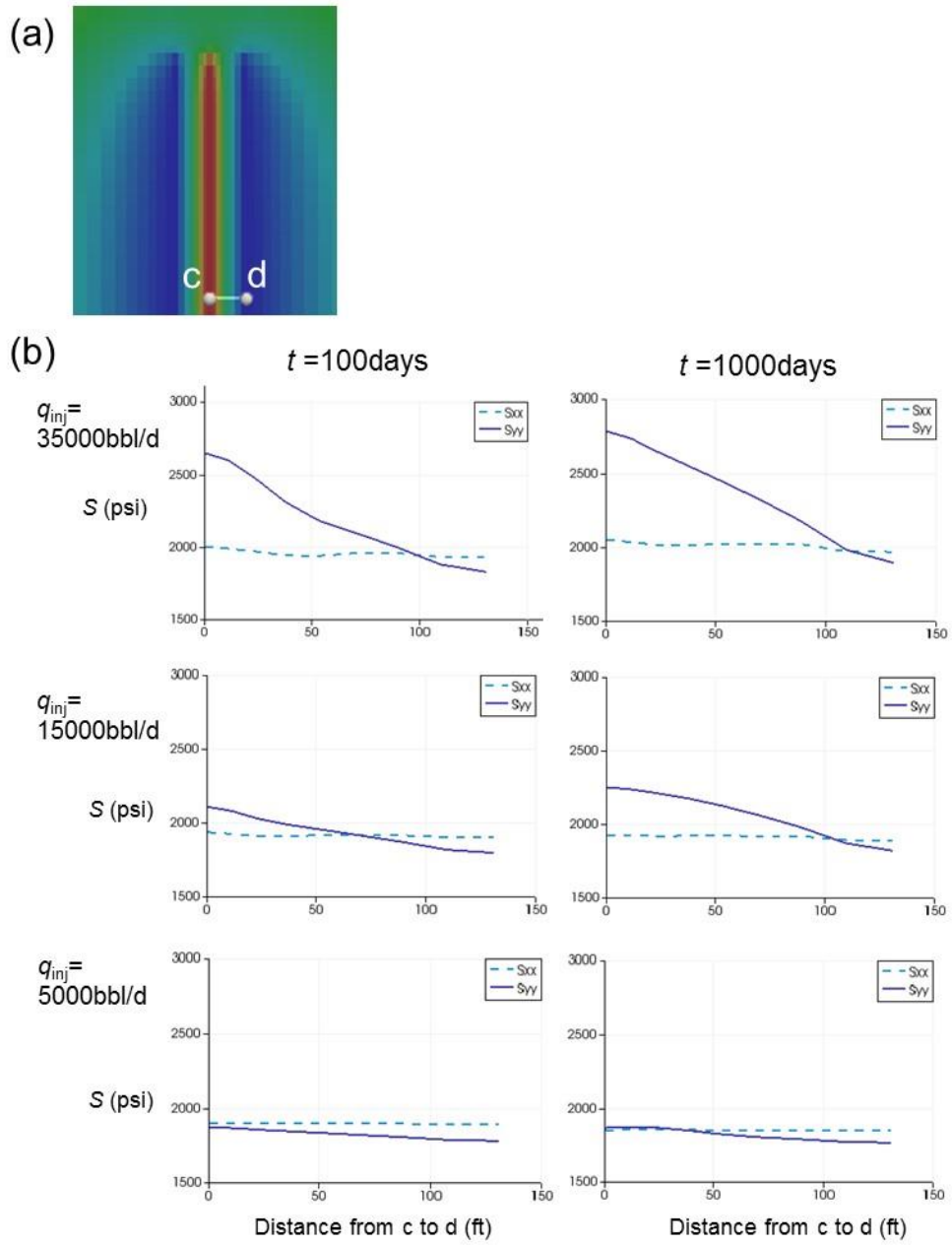

Figure 5.45: Effect of injection rate on stress magnitudes of S_{xx} and S_{yy}. (a) Values are shown along the line from the center of injector (point c) to the center of producer (point d). (b) S_{xx} and S_{yy} are shown for t=100days and t=1000days.

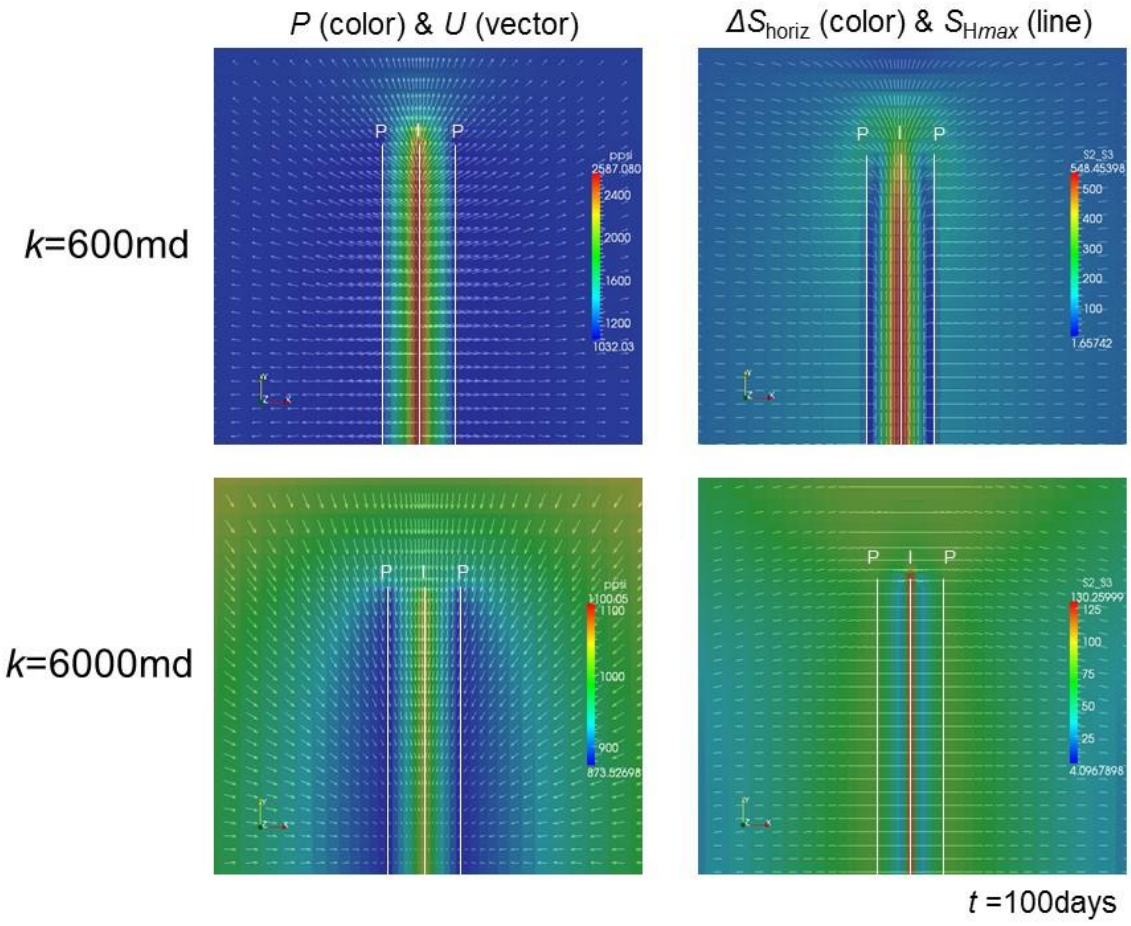

Figure 5.46: Effect of reservoir permeability on stress reorientation in horizontal well pairs. Pressure, displacement, horizontal stress contrast, and S_{Hmax} direction at t =100days were shown.

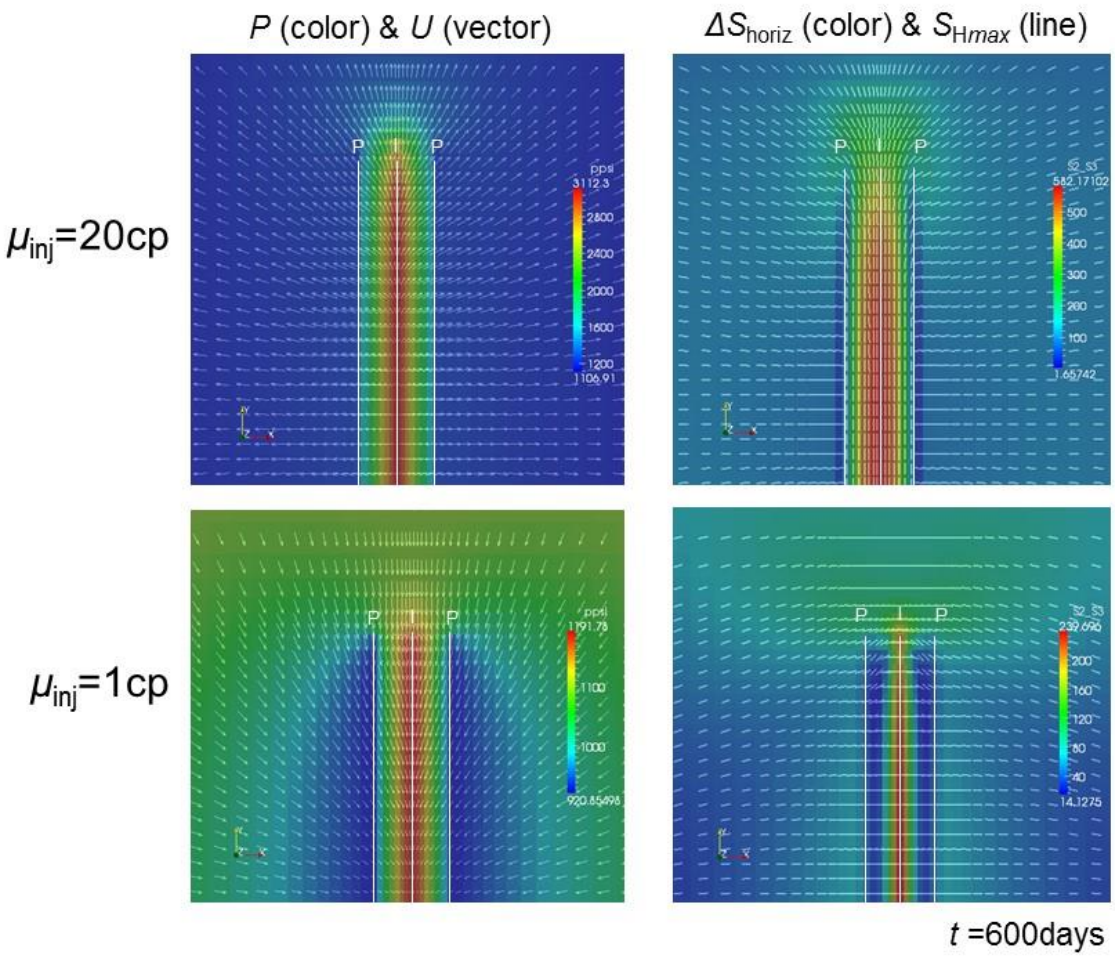

Figure 5.47: Effect of viscosity of injection fluid on stress reorientation in horizontal well pairs. Pressure, displacement, horizontal stress contrast, and S_{Hmax} direction at t =600days were shown.

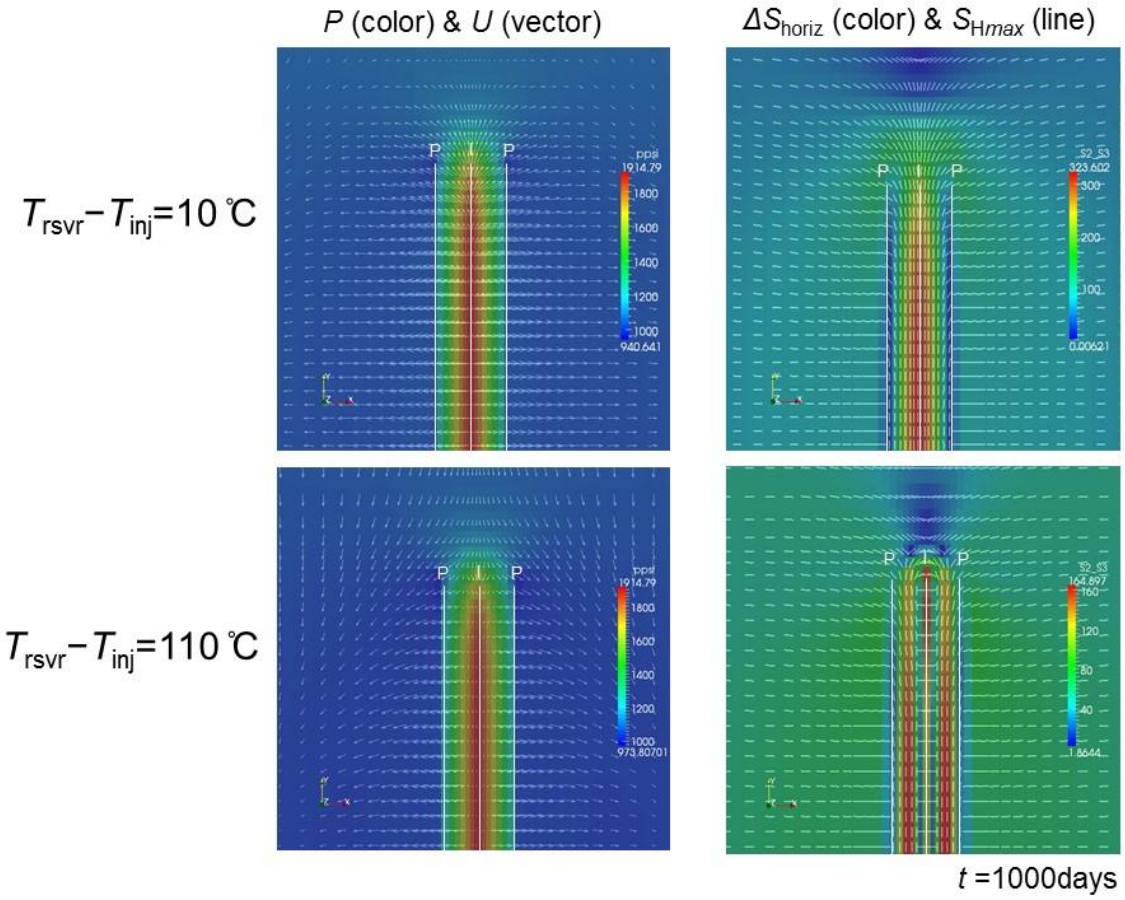

Figure 5.48: Effect of temperature difference between injection fluid and initial reservoir on stress reorientation in horizontal well pairs. Pressure, displacement, horizontal stress contrast, and S_{Hmax} direction at t =1000days were shown.

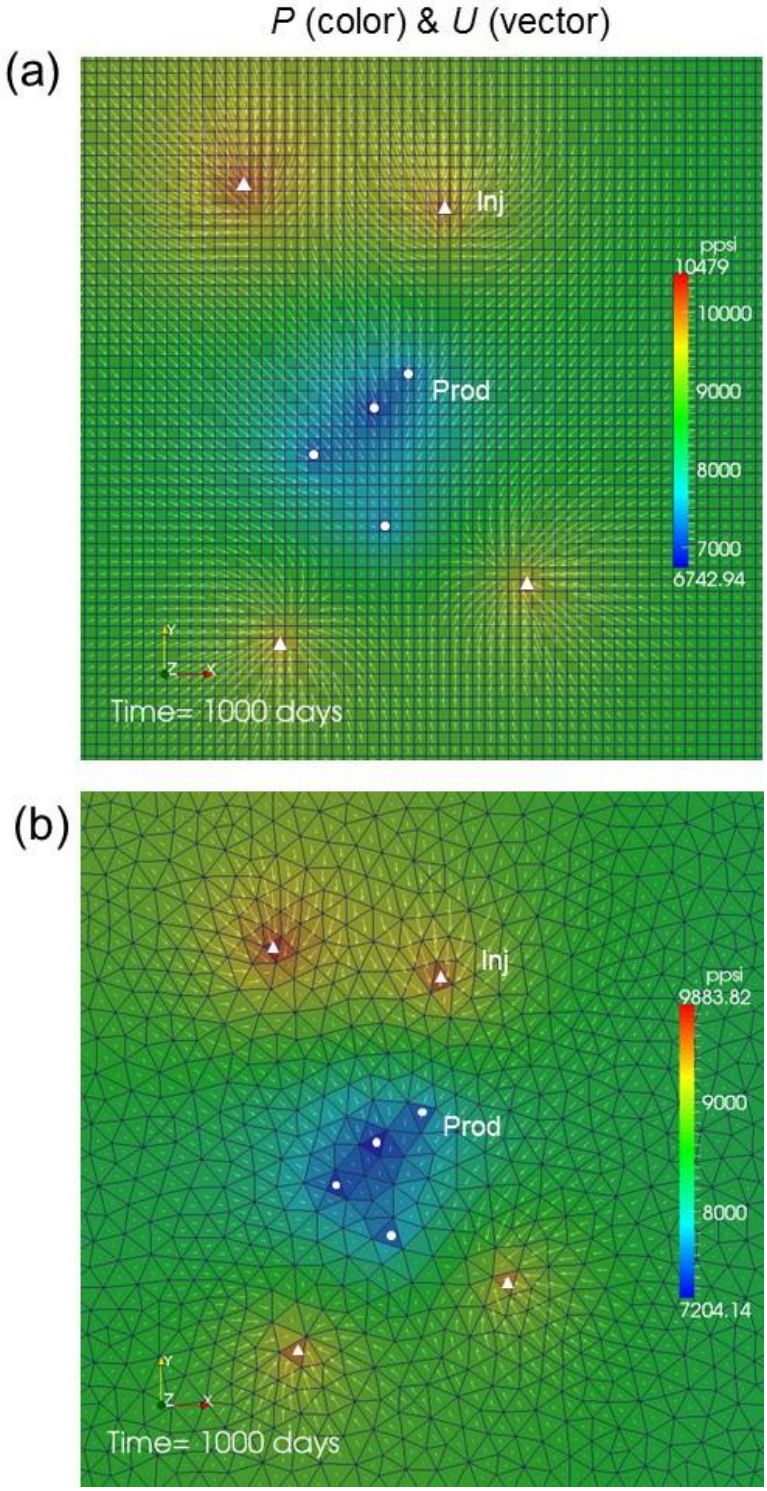

Figure 5.49: Comparison of pressure and reservoir displacement fields using (a) structured, and (b) unstructured grid blocks.

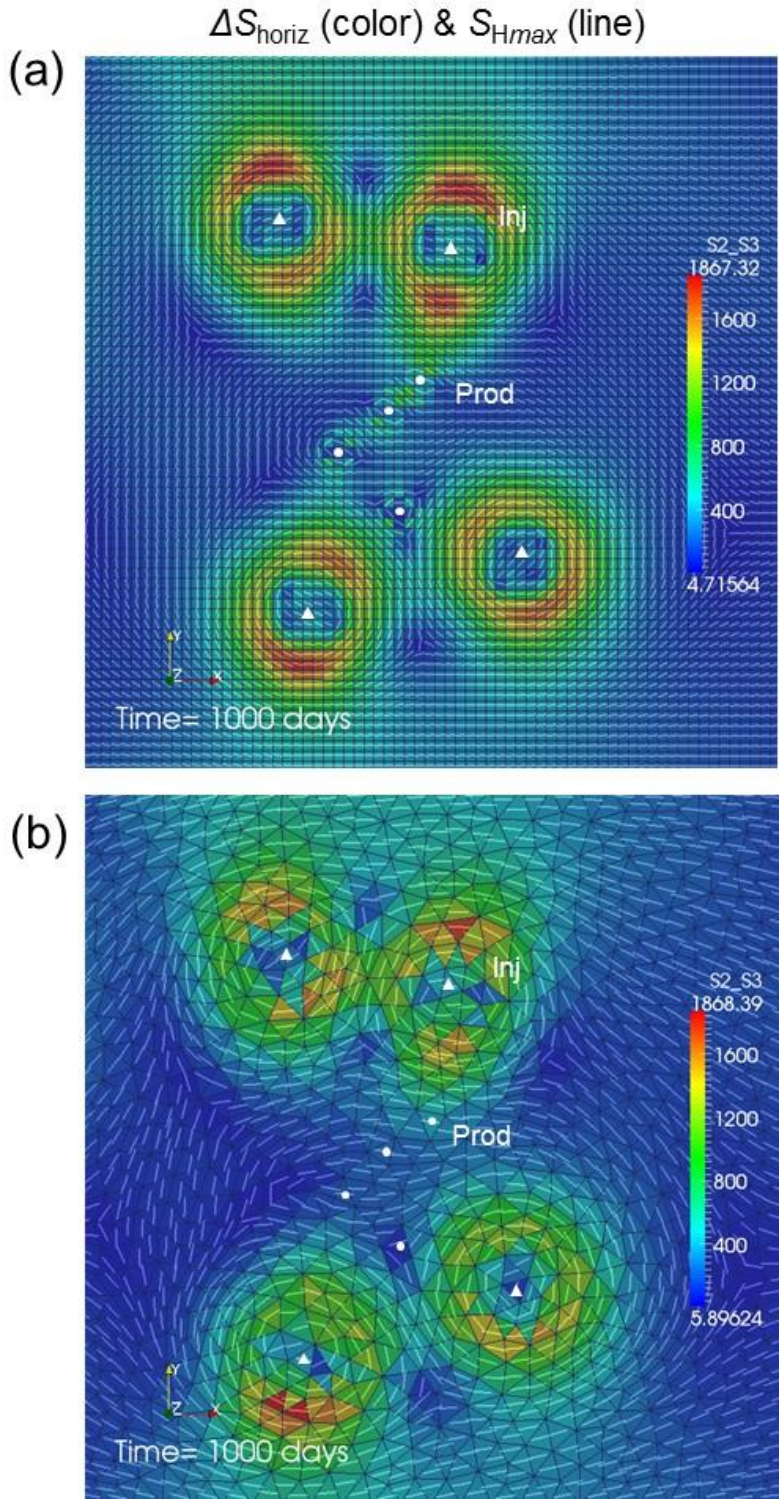

Figure 5.50: Comparison of horizontal stress contrast and maximum horizontal stress directions using (a) structured, and (b) unstructured grid blocks.

Nomenclature

A_l = Area of well block plane perpendicular to the wellbore direction, L^2, m^2

B_o = Formation volume factor, oil, L^3L^{-3}, (reservoir m^3)/(standard m^3)

B_w = Formation volume factor, water, L^3L^{-3}, (reservoir m^3)/(standard m^3)

c_g = Compressibility, grain, $m^{-1}L^1t^2$, Pa^{-1}

C_{pb} = Heat capacity, bulk, $m^1L^2t^{-2}T^{-1}$, J/K

C_{po} = Heat capacity, oil, $m^1L^2t^{-2}T^{-1}$, J/K

C_{pw} = Heat capacity, water, $m^1L^2t^{-2}T^{-1}$, J/K

c_t = Compressibility, total (bulk), $m^{-1}L^1t^2$, Pa^{-1}

c_w = Compressibility, water, $m^{-1}L^1t^2$, Pa^{-1}

E = Young's modulus, $m^1L^{-1}t^{-2}$, Pa

f_w = fractional flow for water, −

G = Shear modulus, $m^1L^{-1}t^{-2}$, Pa

h = Length of the rectangular cell in the wellbore direction, L^1, m

I = Unit tensor, −

i_l = Cell index, well location

J_l = Well index

j_l = Cell index, well location

k = Permeability, L^2, Darcy

k_b = Heat conductivity, bulk, $m^1L^1t^{-3}T^{-1}$, w/(m·K)

k_{ro} = Relative permeability to oil, −

k_{rw} = Relative permeability to water, −

P = Pressure, $m^1L^{-1}t^{-2}$, Pa

$\overline{q_o}$ = Water injection (+) or production (−) rate per unit bulk volume, L^3t^{-1}, m^3/s

$\overline{q_w}$ = Water injection (+) or production (−) rate per unit bulk volume, L^3t^{-1}, m^3/s

r_{ol} = Equivalent radius of the well block, L^1, m

r_{wl} = Well radius, L^1, m

$\overline{\overline{S}}$ = Stress tensor, total, $m^1L^{-1}t^{-2}$, Pa

S_w = Saturation, water, −

S_{wf} = Waterflood shock front saturation, −

$\Delta S_{w,tol}$ = User-specified tolerance in water saturation change, −

t = Time, t^1, s

Δt = Time step, t^1, s

T = Temperature, T^1, K

T_{ref} = Temperature, reference, T^1, K

$\vec{U}$ = Displacement vector, L^1, m

$\overrightarrow{u_o}$ = Superficial (Darcy) velocity, L^1t^{-1}, m/s

$\overrightarrow{u_w}$ = Superficial (Darcy) velocity, L^1t^{-1}, m/s

α = Biot's coefficient, −

α_T = Thermal expansion coefficient, T^{-1}, K^{-1}

$\overline{\overline{\varepsilon}}$ = Strain tensor, −

λ = Lamě's first parameter, −

$\overline{\overline{\lambda_o}}$ = Relative mobility tensor, oil ($\overline{\overline{k}}k_{ro} / B_o\mu_o$)

$\overline{\overline{\lambda_w}}$ = Relative mobility tensor, water ($\overline{\overline{k}}k_{rw} / B_w\mu_w$)

μ = Lamě's second parameter, $m^1L^{-1}t^{-2}$, Pa

μ_o = Viscosity, oil, $m^1L^{-1}t^{-1}$, Pa·s

μ_w = Viscosity, water, $m^1L^{-1}t^{-1}$, Pa·s

N = Poisson's ratio, −

ρ_b = Density, bulk, m^1L^{-3}, kg/m^3

$\overline{\overline{\sigma}}$ = Stress tensor, effective, $m^1L^{-1}t^{-2}$, Pa

Φ = Flow potential accounting for gravity, $m^1L^{-1}t^{-2}$, Pa

ϕ = Porosity, −

References

Aziz, K., & Settari, A. 1979. *Petroleum Reservoir Simulation*. Applied Science Publishers.

Biot, M. A. 1941. General Theory of Three-Dimensional Consolidation. *Journal of Applied Physics*, **12** (2): 155–164.

Chen, H.-Y., & Teufel, L. W. 2000. Coupling Fluid-Flow and Geomechanics in Dual-Porosity Modeling of Naturally Fractured Reservoirs - Model Description and Comparison. Paper SPE 59043 presented at the SPE International Petroleum Conference and Exhibition in Mexico, 1-3 February, Villahermosa, Mexico. http://dx.doi.org/10.2118/59043-MS

Chen, H.-Y., & Teufel, L. W. 2001. Reservoir Stress Changes Induced by Production/Injection. Paper SPE 71087 presented at the SPE Rocky Mountain Petroleum Technology Conference, 21-23 May, Keystone, Colorado. http://dx.doi.org/10.2118/71087-MS

Chen, Z., & Zhang, Y. 2009. Well Flow Models for Various Numerical Methods. *International Journal of Numerical Analysis and Modeling*, **6** (3): 375–388.

Dean, R. H., Gai, X., Stone, C. M., & Minkoff, S. E. 2006. A Comparison of Techniques for Coupling Porous Flow and Geomechanics. *SPE Journal*, **11** (01): 132–140. http://dx.doi.org/10.2118/79709-PA

Detournay, E., & Cheng, A. H.-D. 1993. Fundamentals of Poroelasticity. *Comprehensive Rock Engineering: Principles, Practice and Projects* (Vol. 2, pp. 113–171). Oxford; New York: Pergamon Press. Retrieved from http://scholar.google.com/citations?view_op=view_citation&hl=en&user=kj2__CcAAAAJ&citation_for_view=kj2__CcAAAAJ:u5HHmVD_uO8C

Dikken, B. J., & Niko, H. 1987. Waterflood-Induced Fractures: A Simulation Study Of Their Propagation And Effects On Waterflood Sweep Efficiency. Paper SPE 16551 presented at the Offshore Europe, 8-11 September, Aberdeen, United Kingdom. http://dx.doi.org/10.2118/16551-MS

Dons, T., Jorgensen, O., & Gommesen, L. 2007. Observations and Quantitative Analyses of Waterflood Patterns in a Chalk Reservoir Using Seismic Data, Halfdan Field, Danish North Sea. Paper SPE 108531 presented at the Offshore Europe, 4-7 September 2007, Aberdeen, Scotland, U.K. http://dx.doi.org/10.2118/108531-MS

Fredrich, J. T., Arguello, J. G., Thorne, B. J., Wawersik, W. R., et al. 1996. Three-Dimensional Geomechanical Simulation of Reservoir Compaction and Implications for Well Failures in the Belridge Diatomite. Paper SPE 36698 presented at the SPE Annual Technical Conference and Exhibition, 6-9 October, Denver, Colorado. http://dx.doi.org/10.2118/36698-MS

Gadde, P., & Sharma, M. 2001. Growing Injection Well Fractures and Their Impact on Waterflood Performance. Paper SPE 71614 presented at the SPE Annual Technical Conference and Exhibition, 30 September-3 October 2001, New Orleans, Louisiana. http://dx.doi.org/10.2118/71614-MS

Garon, A. M., Lin, C. Y., & Dunayevsky, V. A. 1988. Simulation of Thermally Induced Waterflood Fracturing in Prudhoe Bay. Paper SPE 17417 presented at the SPE California Regional Meeting, 23-25 March, Long Beach, California. http://dx.doi.org/10.2118/17417-MS

Geuzaine, C., & Remacle, J.-F. 2009. Gmsh: A 3-D finite element mesh generator with built-in pre- and post-processing facilities. *International Journal for Numerical Methods in Engineering*, **79** (11): 1309–1331. http://dx.doi.org/10.1002/nme.2579

Hustedt, B., Qiu, Y., Zwarts, D., & van den Hoek, P. J. 2005. Modeling Water-Injection Induced Fractures in Reservoir Simulation. Paper SPE 95726 presented at the SPE Annual Technical Conference and Exhibition, 9-12 October, Dallas, Texas. http://dx.doi.org/10.2118/95726-MS

Hustedt, B., Zwarts, D., Bjoerndal, H.-P., Al-Masfry, R. A., et al. 2008. Induced Fracturing in Reservoir Simulations: Application of a New Coupled Simulator to a Waterflooding Field Example. *SPE Reservoir Evaluation & Engineering*, **11** (03): 569–576. http://dx.doi.org/10.2118/102467-PA

Jaeger, J., Cook, N. G., & Zimmerman, R. 2007. *Fundamentals of Rock Mechanics* (4th edition.). Malden, MA: Wiley-Blackwell.

Jasak, H. 1996. *Error analysis and estimation for the Finite Volume method with applications to fluid flows*. Imperial College, University of London.

Jasak, H., & Weller, H. G. 2000. Application of the finite volume method and unstructured meshes to linear elasticity. *International Journal for Numerical Methods in Engineering*, **48** (2): 267–287. http://dx.doi.org/10.1002/(SICI)1097-0207(20000520)48:2<267::AID-NME884>3.0.CO;2-Q

Ji, L., Settari, A. T., Sullivan, R. B., & Orr, D. 2004. Methods For Modeling Dynamic Fractures In Coupled Reservoir And Geomechanics Simulation. Paper SPE 90874 presented at the SPE Annual Technical Conference and Exhibition, 26-29 September, Houston, Texas. http://dx.doi.org/10.2118/90874-MS

Jin, M., Somerville, J., & Smart, B. G. D. 2000. Coupled Reservoir Simulation Applied to the Management of Production Induced Stress-Sensitivity. Paper SPE 64790 presented at the International Oil and Gas Conference and Exhibition in China, 7-10 November, Beijing, China. http://dx.doi.org/10.2118/64790-MS

Kim, J., Moridis, G. J., & Rutqvist, J. 2012. Coupled Flow and Geomechanical Analysis for Gas Production in the Prudhoe Bay Unit L-106 Well Unit C Gas Hydrate Deposit in Alaska. *Journal of Petroleum Science and Engineering*, **92–93** (0): 143–157. http://dx.doi.org/10.1016/j.petrol.2012.04.012

Kim, J., Moridis, G., Yang, D., & Rutqvist, J. 2012. Numerical Studies on Two-Way Coupled Fluid Flow and Geomechanics in Hydrate Deposits. *SPE Journal*, **17** (2). http://dx.doi.org/10.2118/141304-PA

Koutsabeloulis, N. C., & Hope, S. A. 1998. "Coupled" Stress/Fluid/Thermal Multi-Phase Reservoir Simulation Studies Incorporating Rock Mechanics. Paper SPE 47393 presented at the SPE/ISRM Rock Mechanics in Petroleum Engineering, 8-10 July, Trondheim, Norway. http://dx.doi.org/10.2118/47393-MS

Lake, L. W. 1989. *Enhanced Oil Recovery*. Prentice Hall Incorporated.

Marx, J. W., & Langenheim, R. H. 1959. Reservoir Heating by Hot Fluid Injection. *Transactions of the American Institute of Mining, Metallurgical, and Petroleum Engineers*, **216**: 312–315.

Minner, W. A., Wright, C. A., Stanley, G. R., Pater, C. J., et al. 2002. Waterflood and Production-Induced Stress Changes Dramatically Affect Hydraulic Fracture Behavior in Lost Hills Infill Wells. Paper SPE 77536 presented at the SPE Annual Technical Conference and Exhibition, 29 September-2 October 2002, San Antonio, Texas. http://dx.doi.org/10.2118/77536-MS

Monteagudo, J. E. P., Rodriguez, A. A., & Florez, H. 2011. Simulation Of Flow In Discrete Deformable Fractured Porous Media. Paper SPE 141267 presented at the SPE Reservoir Simulation Symposium, 21-23 February, The Woodlands, Texas, USA. http://dx.doi.org/10.2118/141267-MS

Norris, A. 1992. On the Correspondence Between Poroelasticity and Thermoelasticity. *Journal of Applied Physics*, **71** (3): 1138–1141. http://dx.doi.org/10.1063/1.351278

Ovens, J. E. V., Larsen, F. P., & Cowie, D. R. 1998. Making Sense of Water Injection Fractures in the Dan Field. *SPE Reservoir Evaluation & Engineering*, **1** (6): 556–566. http://dx.doi.org/10.2118/52669-PA

Peaceman, D. W. 1983. Interpretation of Well-Block Pressures in Numerical Reservoir Simulation With Nonsquare Grid Blocks and Anisotropic Permeability. *Society of Petroleum Engineers Journal*, **23** (3). http://dx.doi.org/10.2118/10528-PA

Rice, J. R., & Cleary, M. P. 1976. Some basic stress diffusion solutions for fluid-saturated elastic porous media with compressible constituents. *Reviews of Geophysics*, **14** (2): 227–241. http://dx.doi.org/10.1029/RG014i002p00227

Rod, M., & Jorgensen, O. 2005. Injection Fracturing in a Densely Spaced Line Drive Waterflood - The Halfdan Example. Paper SPE 94049 presented at the SPE Europec/EAGE Annual Conference, 13-16 June, Madrid, Spain. http://dx.doi.org/10.2118/94049-MS

Roussel, N., Florez, H., & Rodriguez, A. A. 2013. Hydraulic Fracture Propagation from Infill Horizontal Wells. Paper SPE 166503 presented at the SPE Annual Technical Conference and Exhibition, 30 September-2 October, New Orleans, Louisiana, USA. http://dx.doi.org/10.2118/166503-MS

Roussel, N., & Sharma, M. 2010. Quantifying Transient Effects in Altered-Stress Refracturing of Vertical Wells. *SPE Journal*, **15** (3). http://dx.doi.org/10.2118/119522-PA

Roussel, N., & Sharma, M. 2011. Optimizing Fracture Spacing and Sequencing in Horizontal-Well Fracturing. *SPE Production & Operations*, **26** (2). http://dx.doi.org/10.2118/127986-PA

Roussel, N., & Sharma, M. 2012. Role of Stress Reorientation in the Success of Refracture Treatments in Tight Gas Sands. *SPE Production & Operations*, **27** (4). http://dx.doi.org/10.2118/134491-PA

Samier, P., Onaisi, A., & de Gennaro, S. 2008. A Practical Iterative Scheme for Coupling Geomechanics With Reservoir Simulation. *SPE Reservoir Evaluation & Engineering*, **11** (05): 892–901. http://dx.doi.org/10.2118/107077-PA

Samier, P., Onaisi, A., & Fontaine, G. 2006. Comparisons of Uncoupled and Various Coupling Techniques for Practical Field Examples. *SPE Journal*, **11** (01): 89–102. http://dx.doi.org/10.2118/79698-PA

Settari, A., & Warren, G. M. 1994. Simulation and field analysis of waterflood induced fracturing. Paper SPE 28081 presented at the Rock Mechanics in Petroleum Engineering, 29-31 August, Delft, Netherlands. http://dx.doi.org/10.2118/28081-MS

Stevens, D. G., Murray, L. R., & Shah, P. C. 2000. Predicting Multiple Thermal Fractures in Horizontal Injection Wells; Coupling of a Wellbore and a Reservoir Simulator. Paper SPE 59354 presented at the SPE/DOE Improved Oil Recovery Symposium, 3-5 April, Tulsa, Oklahoma. http://dx.doi.org/10.2118/59354-MS

Thomas, G. W. 1981. *Principles of Hydrocarbon Reservoir Simulation*. Englewood Cliffs, N.J.: Prentice-Hall.

Thomas, L. K., Chin, L. Y., Pierson, R. G., & Sylte, J. E. 2003. Coupled Geomechanics and Reservoir Simulation. *SPE Journal*, **8** (04): 350–358. http://dx.doi.org/10.2118/87339-PA

Tran, D., Settari, A., & Nghiem, L. 2002. New Iterative Coupling Between a Reservoir Simulator and a Geomechanics Module. Paper SPE 78192 presented at the SPE/ISRM Rock Mechanics Conference, 20-23 October, Irving, Texas. http://dx.doi.org/10.2118/78192-MS

Van den Hoek, P. J., Al-Masfry, R. A., Zwarts, D., Jansen, J.-D., et al. 2008. Waterflooding Under Dynamic Induced Fractures: Reservoir Management and Optimisation of Fractured Waterfloods. Paper SPE 110379 presented at the SPE Symposium on Improved Oil Recovery, 20-23 April, Tulsa, Oklahoma, USA. http://dx.doi.org/10.2118/110379-MS

Weller, H. G., Tabor, G., Jasak, H., & Fureby, C. 1998. A tensorial approach to computational continuum mechanics using object-oriented techniques. *Computers in Physics*, **12** (6): 620–631. http://dx.doi.org/10.1063/1.168744

Wright, C. A., Conant, R. A., Golich, G. M., Bondor, P. L., et al. 1995. Hydraulic Fracture Orientation and Production/Injection Induced Reservoir Stress Changes in Diatomite Waterfloods. Paper SPE 29625 presented at the SPE Western Regional Meeting, 8-10 March, Bakersfield, California. http://dx.doi.org/10.2118/29625-MS

Wright, C. A., Stewart, D. W., Emanuele, M. A., & Wright, W. W. 1994. Reorientation of Propped Refracture Treatments in the Lost Hills Field. Paper SPE 27896 presented at the SPE Western Regional Meeting, 23-25 March 1994, Long Beach, California. http://dx.doi.org/10.2118/27896-MS

Zheng, H., & Buchanan, W. L. 2013. Robust Semi-Implicit Three-Dimensional Upwind Techniques for Reducing Grid Orientation Effect in Thermal Simulations. Paper SPE 163617 presented at the SPE Reservoir Simulation Symposium, 18-20 February, The Woodlands, Texas, USA. http://dx.doi.org/10.2118/163617-MS

Zimmerman, R. W. 2000. Coupling in Poroelasticity and Thermoelasticity. *International Journal of Rock Mechanics and Mining Sciences*, **37** (1–2): 79–87. http://dx.doi.org/10.1016/S1365-1609(99)00094-5

Chapter 6 : Conclusions and Future Work

6.1 SUMMARY AND CONCLUSIONS

The objective of this dissertation was to investigate various physical phenomena involved in waterflooding operations. Four major topics were investigated:

- The flow and filtration of suspended particles and emulsions
- Simulation of the growth of injection induced fractures
- Fracture growth in previously fractured wells (frac-packed wells)
- Stress reorientation caused by water injection and hydrocarbon production using geomechanics coupled with poro- and thermo-elasticity.

These phenomena are controlled by physics at both the pore-scale and at a reservoir-scale. Experiments were conducted and the observations were incorporated into the development of numerical models to achieve the research objectives. The main conclusions and findings can be summarized as follows below.

In Chapter 1, the important role of waterflooding operations in the petroleum industry was reviewed based on global and U.S. water production trends. The importance of injector performance was reviewed and factors controlling the injectivity declines were identified. Particulate plugging, fracture growth and thermal stress changes were explained and the relevant unanswered questions for each subject were identified.

In Chapter 2, the filtration of solid particles at high fluid velocities encountered in frac-packs was experimentally observed. Filtration coefficients were found to be mainly a function of fluid velocity and particle-to-grain size ratio. The filtration coefficient was observed to decrease with time and an empirical model for this dependency was suggested. A model accounting for the effect of deposited particles on non-Darcy inertial coefficient

in the frac-pack was presented. The impact of changes in the filtration coefficient on the injectivity and fracture dimensions were shown by applying findings in this work to a comprehensive injector model.

In Chapter 3, the filtration and generation of O/W emulsion droplets were experimentally measured. For the process of emulsion generation by high velocity flows, the trapping number using the diameter of generated droplets characterized the capillary desaturation process well. Size and concentration of generated oil droplets were primarily a function of trapping number and the size of generated droplet, and an empirical correlation was suggested based on experimental observations. For the filtration of oil droplets, straining was identified as the primary filtration mechanism in a porous medium with a permeability lower than about 1 Darcy. For larger sand-grains, interception is the primary mechanism for the typical size of oil-droplets in produced water. With small sand-grain porous media, a high degree of droplet generation occurred simultaneously with filtration. The permeability decline occurred more rapidly in flow conditions when straining becomes the more important filtration mechanism.

In Chapter 4, the development of 3-dimensional fracture model for water injection well was presented, and impacts of flow and mechanical conditions on fracture growth were shown based on the model. The leak-off coefficient for water injection wells can change with time depending on the particle filtration behavior, and an adaptive leak-off model based on filtration was suggested and utilized in the simulation. The time exponent in Carter's correlation was approximately 0.4 (lower than the conventional value of 0.5) when the new leak-off model was used for water injection. This leak-off calculation can be used independently for the estimation of the leak-off coefficient from the injection and reservoir properties without specifying a leak-off coefficient a priori. It was also shown that the 3-dimensional fracture model can properly address containment issues and fracture

growth into bounding layers.

Finally in Chapter 5, an explicitly coupled two-phase flow, energy balance, geomechanics model focusing on stress reorientation was developed. In waterflooding using cold water, there were three stress reorientation regions: the low-temperature contraction region, the outer initial-temperature contraction region, and the production-dominated region. Induced fractures can turn in the outer initial-temperature contraction region due to the reoriented stress direction and high horizontal stress contrast. Near a horizontal-well-lateral region, S_{Hmax} direction reoriented parallel to injectors (or hot-water injectors), and perpendicular to producers (or cold-water injectors). Stress reorientation near injector-producer horizontal well pairs was controlled by either the injector or the producer depending on which exhibited a stronger effect. The simulation of stress reorientation during waterflooding clearly shows that this is a field-scale phenomenon.

6.2 RECOMMENDATIONS FOR FUTURE RESEARCH

Based on observations in this study, the following recommendations are suggested for future research.

6.2.1 Characterization of Near-Well Formation Damage

For the characterization of near-well formation damage by solid particles and O/W emulsion flow, the following approaches are suggested:

Application of CT scan. The deposition inside the core can be analyzed by injecting high-density particles, e.g., hematite particles, in sand-packs used in this work. The amount of deposition along the filter depth changing with time can be captured by this application of CT scan imaging. Results from imaging can be compared with the calculated specific deposition and this can be used to access the accuracy of the filtration model.

Filter cake characterization. The onset of external filter cake formation increases

the flow resistance significantly depending on the filter cake properties. The permeability of the cake and the impact of compression on cake properties can be experimentally measured. For different sources of injection water, filter cakes formed by solid particles, O/W emulsions, and microorganisms can be used. Characterization methods of filter cake properties from drilling muds with bentonite can be referred to. As the filter cake is compressible, permeability and porosity are dependent on the shear rate applied by the fluid. To address the effect of the fluid velocity and injection pressure encountered during the formation of the actual filter cake, a cross-flow filtration apparatus using the dynamic filtration cell should be used.

Effect of crude oil and emulsifier. Complexity of physical and chemical properties of crude oil can change the behavior of filtration significantly. One of examples is that crude oil contains trace amount of surfactants, and their properties can lead to unique consequences which is field-specific. Impact of crude oil types on the filtration of oil droplets can be further investigated. Using commercially available emulsifiers, methods to prevent formation damage can be suggested.

Online particle size analysis. Coulter counter provided excellent resolution of information on the particle size distributions for the analysis of fluid samples. Concentrations measured with the Coulter counter matched well with expected values when samples were synthesized. However, the practical process of sampling many times led to imperfect sampling of the flowing fluids. The way to overcome this problem is to use an online particle size analyzer. Using this, changes in concentration and size distribution with time can be more conveniently and precisely measured and processed.

Effect of particle-collector interactions on filtration. The zeta potential is a critical parameter that influences the magnitude of the interaction between colloidal particles and collectors. The impact of particle types on filtration and/or the oil-droplet generation needs

to be investigated along with measurement of the zeta potential. In addition, theoretical studies on the particle-collector interaction, such as a DLVO calculation, can be conducted. When the impact of particle types are experimentally observed, the effect of mixed solid-oil droplets can also be tested. Wettability of sands can affect the filtration behavior as well. Wettability can be altered and the differences in the filtration coefficient for water-wet, oil-wet and mixed-wet sands needs to be investigated.

6.2.2 3-Dimensional Fracture Growth Model for Water Injectors

For the 3-dimensional fracture growth model, the following ideas are suggested for future researchers:

Fracture initiation from multiple layers. Currently, only one fracture is allowed to grow in the 3-dimensional fracture model. When fractures are growing into multiple layers, competing fracture growth can be simulated by applying 3-dimensional models with multiple fractures. Existing models accounting for fluid distribution into multiple layers can be utilized, and the memory allocation issue for multiple 3-dimensional fractures needs to be addressed. Merging of two of 3-dimensional fracture meshes is another potential problem to be solved to make this improvement.

Non-uniform (local) filtration model. Currently, the leak-off rate from the fracture face is calculated by a leak-off coefficient which is changing with time, but the leak-off coefficient is not varying with location at a certain time. This is because the leak-off coefficient is calculated assuming a uniform filter-cake thickness. In the fluid flow equation formulated based on a 3-dimensional fracture, flow resistances at each grid element on the fracture face can be calculated differently, and this can be a basis of flow distributions on the facture face. This will allow us to predict the non-uniform filter cake accumulation on the face of the fracture, which perhaps is more realistic.

6.2.3 Multi-Phase Fluid-Geomechanics Simulation

For the multi-phase geomechanics simulation, the following improvements can be implemented:

Implementation of fracture growth model. A fracture growth model can be built to utilize the predicted stress reorientation states of the current simulation. The effect of production history on fracture growth directions can be simulated. This will provide more accurate sweep patterns based on the precise geometry of induce fractures. For the fracture propagation criteria, either a linear elastic fracture mechanics (LEFM) or a cohesive zone model (CZM) can be used. The pressure and width of fractures can be calculated as a secondary domain coupled with the reservoir domain by providing boundary conditions at the fracture faces.

Implementation of filtration model. In the coupled model for fracture growth and geomechanics, the calculation of internal and external filtration can be added. The damage zone can be explicitly specified for near-well and near-fracture regions, where additional flow resistances of internal and external filtration are to be added. This filtration calculation can provide more precise bottom-hole pressure predictions.

Multiple-layer simulation with simplified fracture model. Most of simulations shown in this work are 2-dimensional reservoir models with a plane strain assumption. The effect of bounding layers (over- and under-burden) can be more precisely simulated with 3-dimensional models with extended geometry. The current formulation is already applicable to this type of simulation. A simplified fracture growth model with pre-defined fracture growth directions can be built. Pressure boundary conditions can be applied to the growing fracture nodes assuming an infinite-conductivity in fractures. A simple fracture growth model can be extended to a reservoir with multiple layers. Impacts of the stress reorientation in multi-layer simulations with various stress regimes on fracture growth in

multiple layers can be investigated.

Implementation of gas-phase. The current formulations assume two-phase flow of an immiscible and slightly compressible fluid. This can be extended to a three-phase fluid simulation by using the solution gas-oil ratio, R_s and the oil vaporization ratio, R_v defined as a function of pressure. Based on this model, the effect of bubble-point pressure can be simulated for the volatile-oil fluid systems. This allows various applications of simulations for reservoirs with oil-gas-water phases.

Application to flow-back simulation. Based on the above extensions, an application to complicated issues encountered in the field which have multiple time-scale and operation stages can be simulated. The simulation of the fracturing-fluid flow-back is one example. The invasion of fracturing fluid with a precise fracture geometry can be simulated as a first stage of this simulation. Based on results of fluid-injection simulations, subsequent production can be concurrently simulated with a precise tracking of motion of fracturing and reservoir fluids.

Addition of various failure modes. The basic fracture model can have a crack propagation criteria based on tensile failure. The shear failure of rocks can be implemented and relevant permeability changes can be simulated.

Nomenclature

R_S	=	Solution gas-oil ratio, −, scf/bbl
R_v	=	Oil vaporization ratio, −, stb/MMscf
S_{Hmax}	=	Maximum horizontal stress, $m^1L^{-1}t^{-2}$, Pa

Appendix A: Experimental Equipment and Materials

Experimental equipment and materials used in Chapters 2 and 3 are explained in this Appendix. The objective of this Appendix is to provide information which can be used to reproduce experiments conducted in this work and to conduct future research. Specifications available from the manufacturer's website and information gathered through the purchasing process were organized in this Appendix.

A.1 COULTER COUNTER – MULTISIZER 3 BY BECKMAN COULTER

A Coulter Counter, Multisizer 3 from Beckman Coulter was used to measure the particle size distribution and concentration. The Coulter Counter employs the following principle. A suspended particle flowing through an orifice changes the impedance proportionally to the volume of the particle when electric current is applied to the orifice. The series of pulses in the impedance change is converted to the particle size distribution and the concentration. The specification of the equipment is explained as below:

> *Excerpted from Multisizer 3 Operator's Manual*:
> "The Beckman Coulter Multisizer 3 is a flexible, multi-channel analyzer employing the Coulter Principle (or Coulter electrical impedance method) together with state-of-the art Digital Pulse Processing (DPP) technology to provide both particle sizing and counting within an overall size range of 0.4 μm to 1200 μm."

The Coulter Counter provided a high resolution particle size distribution and highly reliable concentration information. However, when sampling is not properly conducted the results can be affected by any contamination or fluctuation of fluid flow or the sample may not be a representative of the in-line fluid. Care must be taken when sampling for the Coulter Counter.

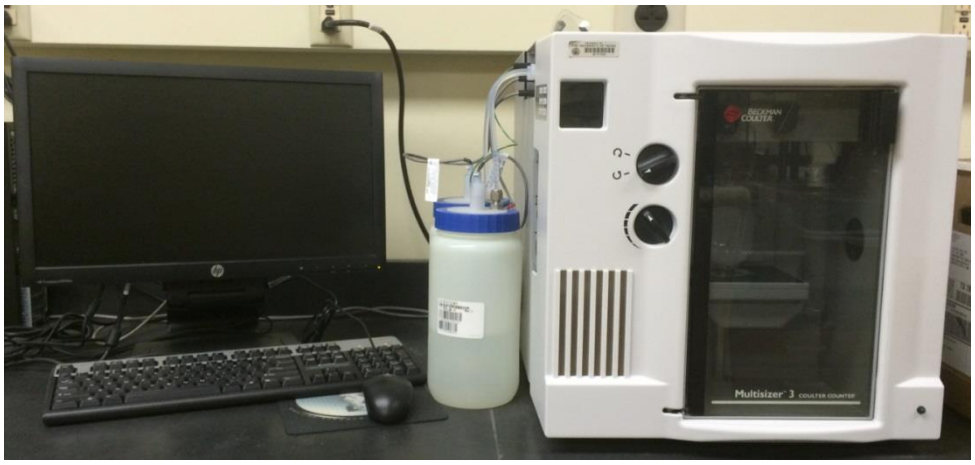

Figure A.1: Coulter Counter (Multisizer 3).

A.2 PUMP – PROGRESSING CAVITY PUMP BY MOYNO

A progressing cavity pump by Moyno (Model no. A4015A-CDQ-3AAA) was used to pump solid or oil-droplet solutions. Flow rates between 150 and 700 ml/min were obtained by the pump. Maximum discharge pressure was 200 psi. Initial torque was required to initiate the pump to overcome the initial friction between the rotor and the stator. Fluid with micron-size solid particles can be handled by this pump. The principle of the Moyno pump is explained below:

> *Excerpted from http://www.moyno.com/about-us.html*:
> "The principle of operation upon which the progressing cavity pump is based is deceptively simple. Available in either a 1:2 or 2:3 ratio configuration, Moyno progressing cavity pumps' key components are the rotor and stator. The rotor is an external helix precision machined from high-strength steel. The stator is an internal helix molded of tough, abrasion-resistant elastomer, permanently bonded within an alloy steel tube. The stator always has one more helix than the rotor to facilitate the progressing cavity pumping action. As the rotor turns within the stator, cavities are formed which progress from the suction to the discharge end of the pump, conveying the process fluid. The continuous seal line between the rotor and the stator helices keeps the fluid moving steadily at a fixed flow rate proportional to the pump's rotational speed."

Pulses in fluid flow on the discharge side of the pump were negligible and a pulsation dampening apparatus was not necessary for this pump.

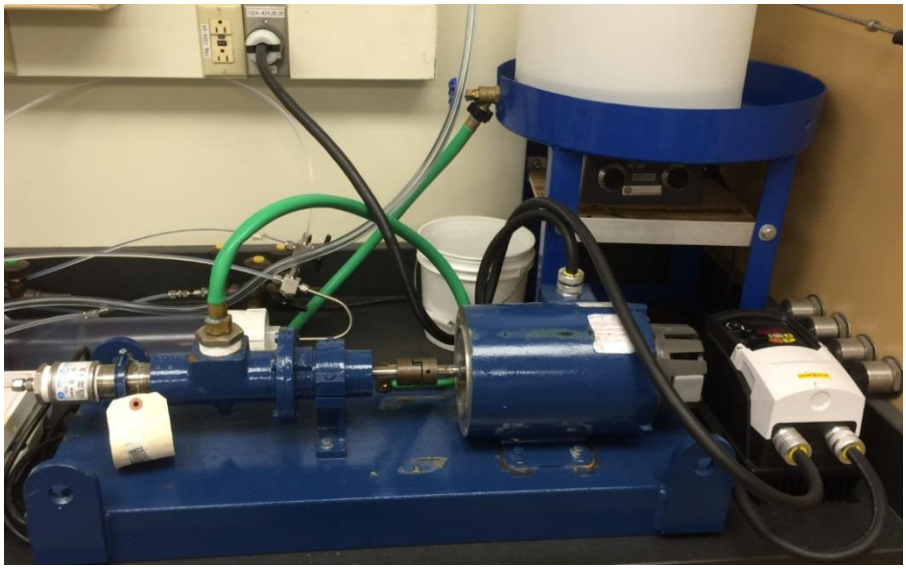

Figure A.2: Progressing cavity pump (Moyno pump).

A.3 PUMP – VOLUME PRESSURE ACTUATOR (VPA) SYRINGE PUMP BY DCI CORPORATION.

A syringe pump from DCI corporation (Model Number: Series 16, 16D-20-20-100) was used to pump fluid with low velocity. Pump can be used to flow at a constant flow rate condition or a constant discharge pressure. Some specifications of this pump are:

- Max Pressure: 10,000 psi, Max flow rate: 100mL/min,
- Cylinder volume: 20 mL
- Volume resolution: 1.2 nL
- Utilities air is required at 80 – 100 psi.
- Precisely controlled, pulseless flow
- Exact pressure control in either dynamic flow or static pressure conditions
- Clean single phase flow, hence require accumulators to displace dilute solid particle suspensions

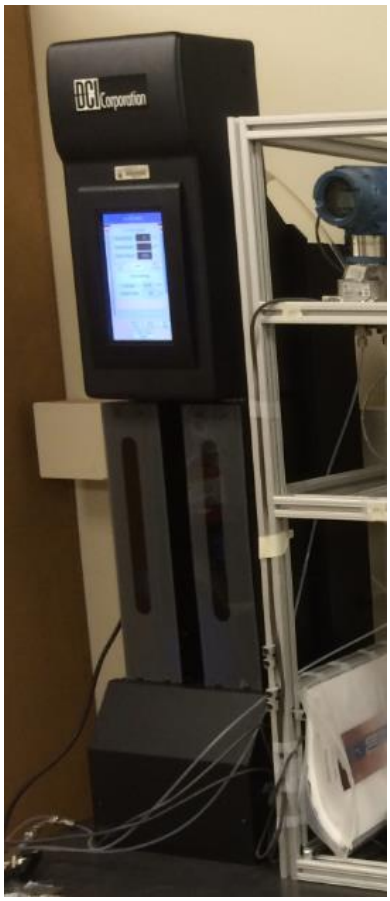

Figure A.3: Volume pressure actuator syringe pump.

A.4 ACCUMULATORS

Two accumulators were used in the experiments. The first one was used to displace oil by water from DCI pump. The main purpose was to inject oil into sand-packs saturated with water to achieve a residual water saturation. This accumulator was kept horizontal.

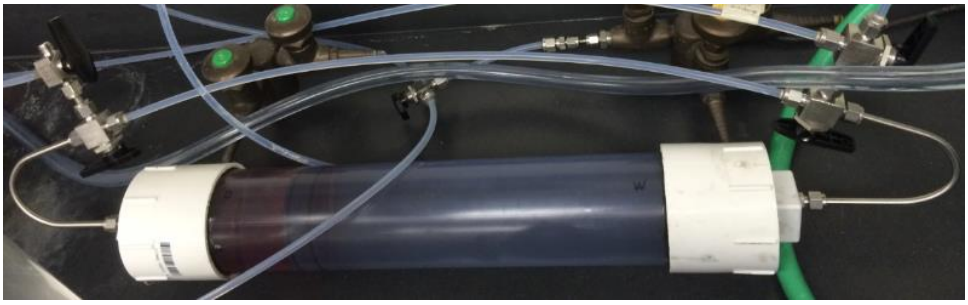

Figure A.4: Accumulator for oil displacement in low-speed and low-pressure conditions.

The other accumulator was used to displace water with solid particles or synthetic O/W emulsion droplets by either water or mineral oil. The displacing direction was vertical.

Figure A.5: Accumulator for vertical fluid displacement.

A.5 SOLID PARTICLES – CERAMIC MICROSPHERES BY 3M

Solid particles used in Chapter 2 were ceramic microspheres manufactured by 3M (Model: White Grades W-610). They are alumino-silicate ceramic particles processed to spherical shapes. Specifications are summarized as below:

Material Description

(Not for specification purposes)

Properties	3M™ Ceramic Microspheres White Grades
Shape	Solid Spheres
Composition	Alkali Alumino Silicate Ceramic
Color, Unaided Eye	White

Typical Physical Properties

(Not for specification purposes)

Properties	3M™ Ceramic Microspheres White Grades	Test Method
True Density	2.4 g/cc (20.0 lbs/gal)	
Bulk Density	1.5 g/cc (12.6 lbs/gal)	
Whiteness ("L" Value)	95+ (Hunter L,a,b scale)	ASTM D 2244
Crush Strength	> 4,200 kg/cm² (> 60,000 psi)	
pH	9.0 – 12.0	ASTM E 70
Hardness	6	Mohs Scale
Softening Point	1,020°C (1,870°F)	
Refractive Index: Predominant	1.53	Becke Line
Dielectric Constant	3.19	
UV Light Transmission	UV Transparent down to 250 nm	
Thermal Conductivity	2.3 W/mK	

Properties		3M™ Ceramic Microspheres White Grades		
		W-210	W-410	W-610
Particle Size (microns)	95th Percentile	12	24	40
	90th Percentile	9	15	28
	50th Percentile	3	4	10
	10th Percentile	1	1	1
Surface Area (m²/cc)		5	3	3
Oil Absorption*		46	44	28

*gm oil/100cc microspheres

Figure A.6: Material properties of solid particles, W-610. from www.3m.com.

3M™ Ceramic Microspheres Product Descriptions

Product	Target Crush Strength[1]	True Density[2]	Hagman Grind[3]	Particle Size[4] Distribution 10th%	50th%	90th%	Effective Top Size 95th%	Color[5]	Comments	Application Ideas
G-200	>60,000	2.5	7	1	4	10	12	gray	Finest standard product, least gloss reduction	Industrial paints and powder coatings
G-400	>60,000	2.4	6	1	5	14	24	gray	Medium gloss reduction	
G-200 PC	>60,000	2.5	7	1	4	10	12	gray	Refined version of G-200, least gloss reduction	Powder coatings. Refined top particle size offers fewer "seeds," resulting in a smoother surface
G-400 PC	>60,000	2.4	6	1	5	14	24	gray	Refined version of G-400, medium gloss reduction	
G-600	>60,000	2.3	3+	1	6	24	40	gray	325 mesh	Maintenance paints and adhesives
G-800	>60,000	2.2	–	2	18	75	200	gray	lowest cost/pound, broad distribution	Polymer concrete, textured coatings, epoxy grouts, and flooring
G-850	>60,000	2.1	–	12	40	100	200	gray	Fewer fines than G-800	
W-210	>60,000	2.4	7	1	3	11	12	white	Finest white product, least gloss reduction of any white grade	Light-colored, thin film coatings and powder coating
W-410	>60,000	2.5	6	1	4	15	24	white	Medium gloss reduction	Burnish-resistant wall and house paints, most light-colored industrial and maintenence products
W-610	>60,000	2.5	3+	1	10	28	40	white	325 mesh, most gloss reduction of any white grade	Maintenance paints thicker then 2 mils, low gloss paints, adhesives and decorative flooring

[1] 90% survival,psi
[2] g/cc
[3] ASTM D12-10
[4] Microns by volume
[5] Unaided eye

Figure A.7: Particle size distributions and material properties of solid particles, W-610 from www.3m.com

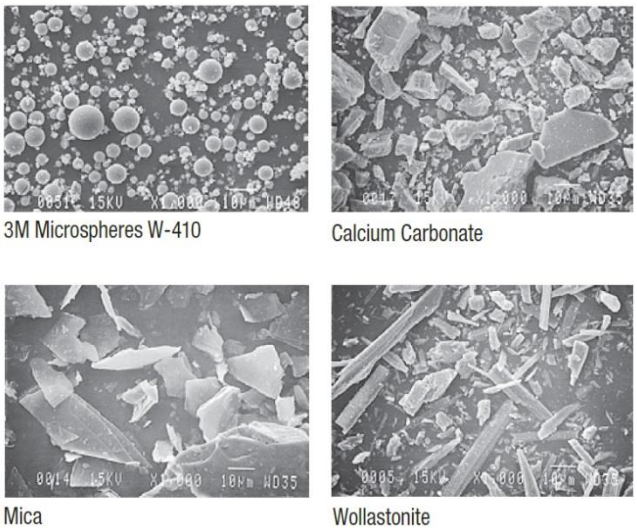

Figure A.8: Microscopic images of solid particles used in experiments conducted in Chapter 2 compared with other types of solid particles. From www.3m.com

A.6 OTTAWA SAND

Ottawa sand is widely used as a proppant during hydraulic fracturing processes. Ottawa sands with various size distributions were filled into sand-packs during our experiments. Size distribution information is described in the following tables.

Sieve Analysis - Particle Size Distribution

US Standard Sieve No.	Weight Retained (g)	Weight Retained (%)	Specifications Weight Retained (%)	
			Minimum	Maximum
16	0.00	0.0	0.0	0.1
20	0.10	0.1		
25	2.30	2.3		
30	19.30	19.7		
35	52.90	54.0		
40	19.10	19.5		
50	3.60	3.7		
Pan	0.70	0.7	0.0	1.0
Total	98.00	100.0		

Critical Analysis

	Result	Minimum	Maximum
Initial Weight (g)	98.20	80.00	120.00
Weight Difference (%)	-0.2	-0.5	0.5
In-Size, -20+40 (%)	95.5	90.0	100.0
Average or Mean Diameter (mm)	0.5498		
Median Diameter, d50 (mm)	0.5387		

Figure A.9: Grain size distribution of Ottawa sands US mesh size 20/40. From http://www.ussilica.com/

Sieve Analysis - Particle Size Distribution

US Standard Sieve No.	Weight Retained (g)	Weight Retained (%)	Specifications Weight Retained (%)	
			Minimum	Maximum
30	0.00	0.0	0.0	0.1
40	0.80	0.8		
45	16.70	16.6		
50	31.20	31.1		
60	32.20	32.1		
70	14.10	14.0		
100	4.80	4.8		
Pan	0.60	0.6	0.0	1.0
Total	100.40	100.0		

Critical Analysis

	Result	Minimum	Maximum
Initial Weight (g)	100.40	80.00	120.00
Weight Difference (%)	0.0	-0.5	0.5
In-Size, -40+70 (%)	93.8	90.0	100.0
Average or Mean Diameter (mm)	0.3006		
Median Diameter, d50 (mm)	0.2925		

Figure A.10: Grain size distribution of Ottawa sands US mesh size 40/70. From http://www.ussilica.com/

	GRADE						
% RETAINED ON	F-65	F-70	F-75	F-80	F-85	F-95	F-110
30	<1						
40	3	1	<1	<1	<1	<1	
50	15	9	6	5	2	1	<1
70	29	30	24	19	12	9	4
100	31	35	38	36	38	30	18
140	18	20	25	31	38	42	44
200	3	4	6	8	9	15	25
270	<1	<1	<1	1	1	3	8
Pan						<1	<1
AFS GFN	67	70	76	80	85	95	110

Figure A.11: Grain size distribution of Ottawa sands, model F-95.

A.7 Mineral Oil – Exxsol D110 Dearomatized fluid from ExxonMobil Chemical

Mineral oil was used to create synthetic emulsions and oil phases in sand-packs. The oil was Exxsol D110 dearomatized fluid from ExxonMobil Chemical. Specifications are as below:

Properties	Typical Value (English)		Typical Value (SI)		Test Based On
Distillation Range					ASTM D86
Initial Boiling Point (IBP)	478	°F	248	°C	
Dry Point (DP)	509	°F	265	°C	
Flash Point (Method A)	237	°F	114	°C	ASTM D93
Aromatic Content	0.4	wt%	0.4	wt%	ExxonMobil Method
Density (60.0°F (15.6°C))	6.74	lb/gal	0.808	g/ml	ASTM D4052
Vapor Pressure (68.0°F (20.0°C))	< 0.1	mm Hg	< 0.01	kPa	ExxonMobil Method
Aniline Point (Method E)	181	°F	83	°C	ASTM D611
Kinematic Viscosity (77.0°F (25.0°C))	3.43	cSt	3.43	mm²/s	ASTM D445

Figure A.12: Specification of Exxsol D110 dearomatized fluid. From https://www.exxonmobilchemical.com

A.8 Surfactant – Xiameter OFX-0193 Fluid

The surfactant added to create synthetic O/W emulsion solution is the OFX-0193 fluid from Xiameter. This is dimethyl, methyl(polyethylene oxide) siloxane (silicone polyether copolymer; INCI Name: PEG-12 Dimethicone; CAS Number: 68937-54-2). Detailed structural information is shown below:

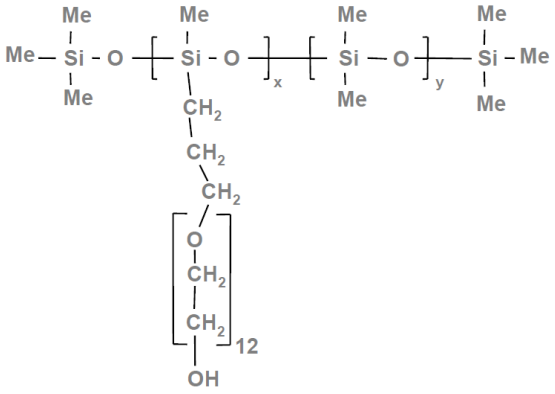

Figure A.13: Molecular structure of the surfactant, XIAMETER OFX-0193. From http://www.xiameter.com

Specifications

Test	Unit	Value
Appearance		Clear to hazy liquid, light amber color, no significant particulate
Color	Gardner	0-4
Viscosity at 25°C	cSt	260
Specific Gravity at 25°C (77°F)		1.07
Cloud Point	°C	95-100

Surface Tension Comparison

Distilled Water, mN m^{-1}	72.8
Dow Corning 193C Fluid, 1% Solution, mN m^{-1}	26-28

Foam Building Ability

Surfactant System, 3% Dow Corning 193C Fluid	
Initial height of Foam, mm	0
Final Height, After 8 minutes, mm	50.8

Figure A.14: Specification of OFX-0193 fluid. From http://www.xiameter.com

Appendix B: Models for Initial Filtration Coefficient

In Section 2.3.2, models to predict the initial filtration coefficient were explained. In these models, the initial filtration coefficient is derived from the single collector efficiency, η. The single collector efficiency is explained by three mechanisms of particle deposition: diffusion, sedimentation and interception.

The initial filtration coefficient calculated by Rajagopalan & Tien (1976) (RT model) and Tufenkji & Elimelech (2004) (TE model) are shown in Figure B.. They were compared with experimental measurements obtained in Chapter 2. The TE model generally predicted slightly higher coefficients that the RT model, especially at higher fluid velocities (1 to 10 cm/s). However, significant differences between the two models were not observed. In Chapters 2 and 3, the RT model was chosen as a representative model to predict the single collection efficiency and the initial filtration coefficient.

The single collection efficiency, η is a linear combination of collection efficiencies corresponding to each mechanism, which are interception, sedimentation and diffusion. Contributions of each filtration mechanisms were compared in Figure for various d_g/d_p used in the experiments in Chapter 2. At the higher fluid velocities, with u_s between 1 and 10 cm/s, interception is the dominant mechanism. On a logarithmic scale of η vs. u_s, it can be seen that the other two mechanisms were negligible compared to interception.

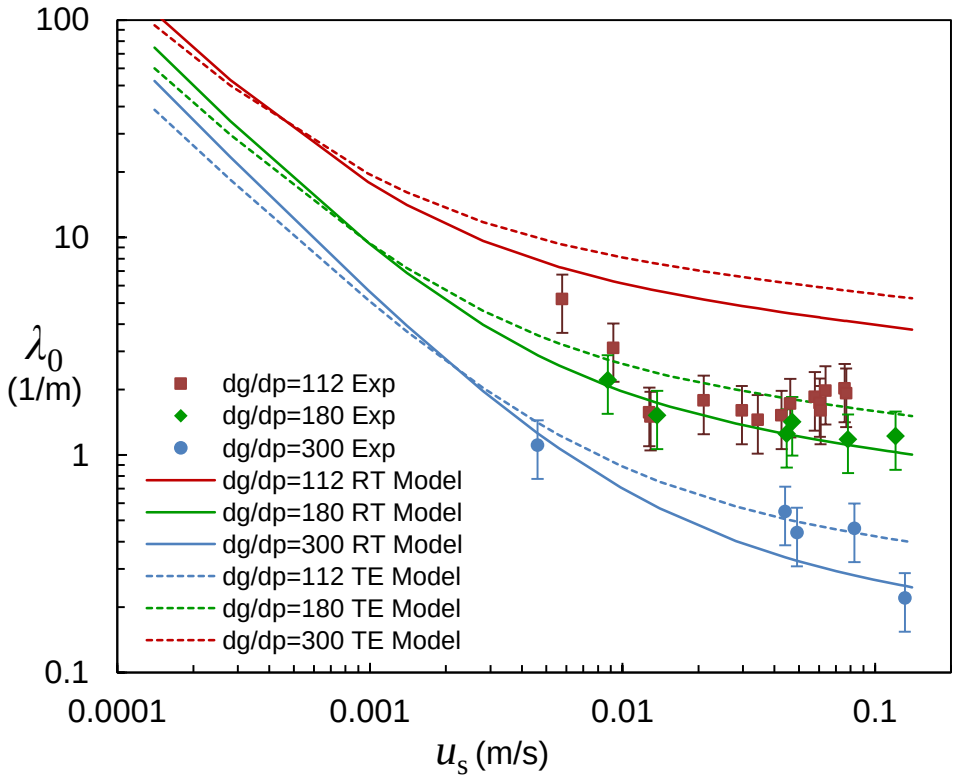

Figure B.1: Initial filtration coefficient predicted by Rajagopalan & Tien (1976) (solid lines) and Tufenkji & Elimelech (2004) (dashed lines). They were compared with experimental measurements in this work.

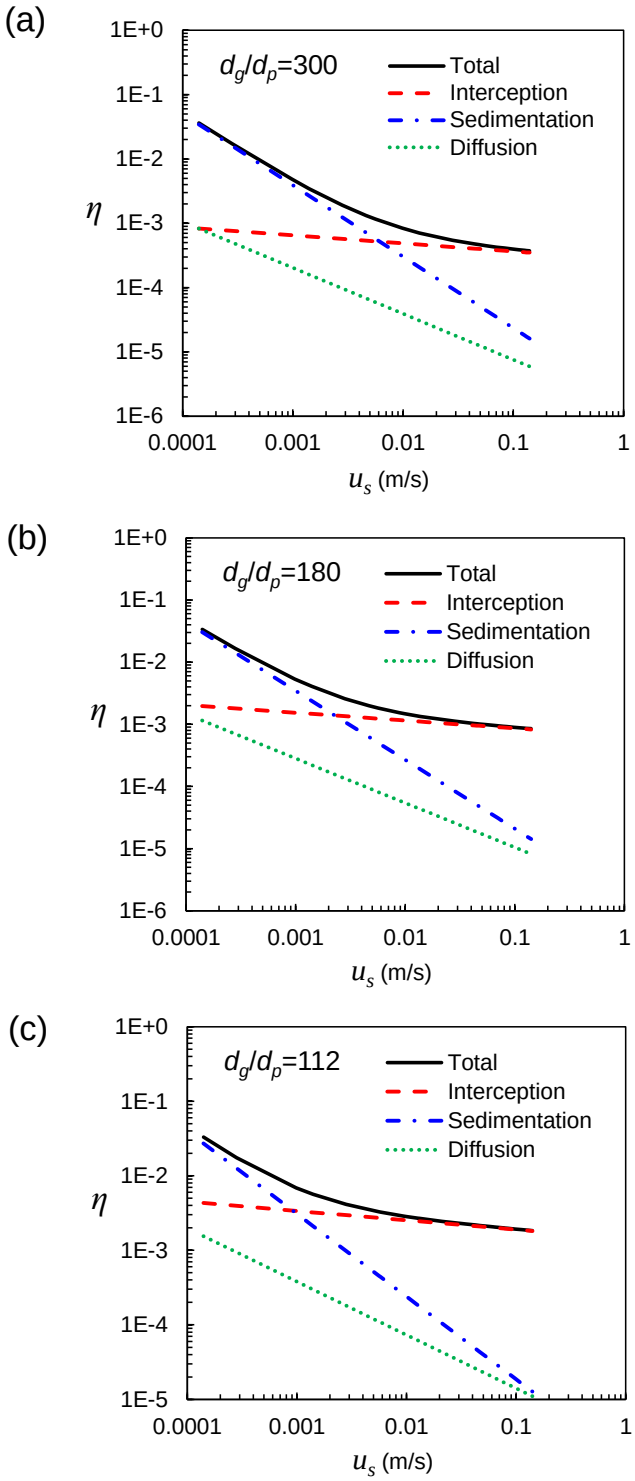

Figure B.2: Collection efficiency predicted by Tufenkji & Elimelech (2004) model. Contributions by interception, sedimentation and diffusion were compared for various d_g/d_p ratios.

Appendix C: Deposition-Dependent Model for Filtration Coefficient

In Section 2.5.2, the deposition-dependent model for filtration coefficient was derived. Here, information used in the derivation is explained. The experimental λ/λ_0 was fitted vs. PV by defining N (Eq. 2.4 and Figure C.1a and c). Then, the average specific deposition for various grain sizes was numerically calculated and an empirical correlation for these trends was developed by defining K and B (Eq. 2.5 and Figure C.1b). Further derivation described in Section 2.5.2 led to a very simple empirical correlation of deposition-dependent λ, which is a function of σ and d_g/d_p only. The characteristic of λ which exponentially declines with PV led to finite deposition in sand-packs under high-velocity conditions. This indicates the degree of deposition may be low at late filtration times when the fluid velocity is maintained continuously high. However, it should be noted that, in actual water injection conditions, the deposition can increase a lot, because fluid velocity varies. This can cause an external filter cake to build on fracture faces or at the fracture entrance depending on injection conditions.

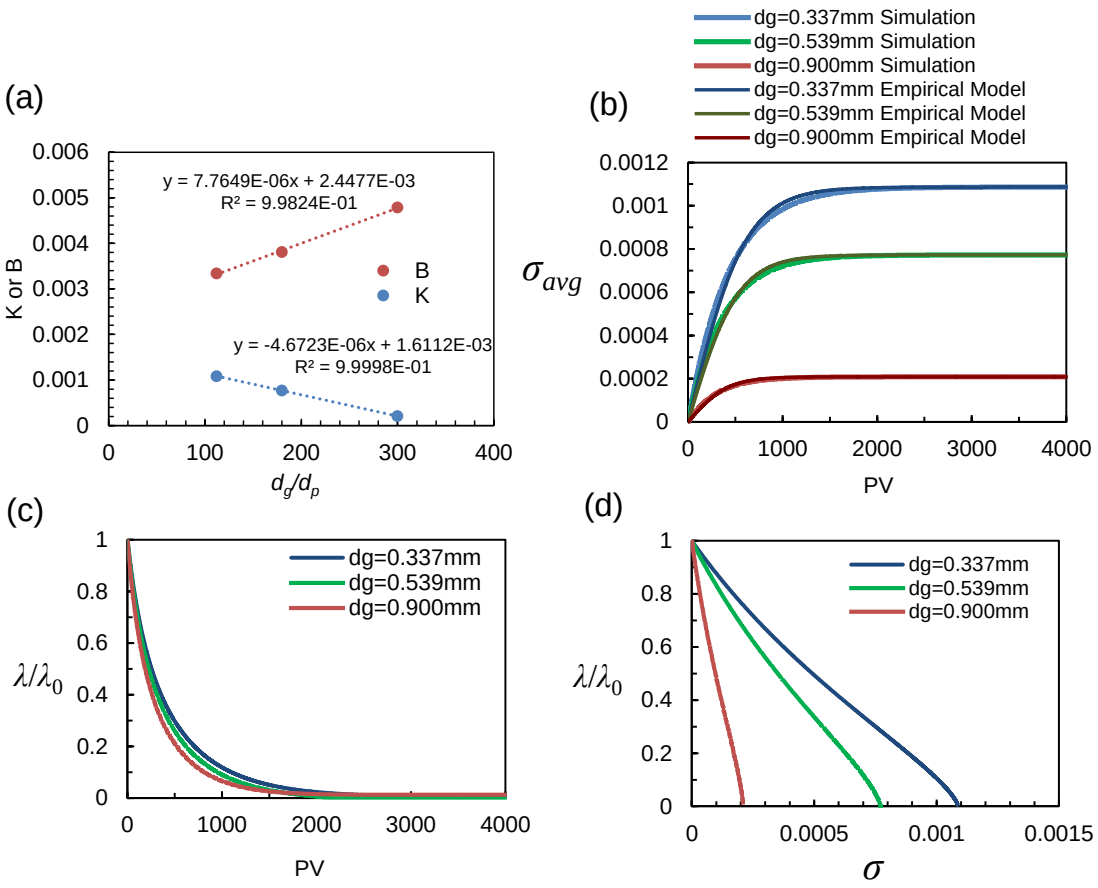

Figure C.1: (a) Empirical fitting parameters for K and B defined in Eq. (2.8), (b) Average specific deposition in sand-pack. Numerical simulation results and empirical model defined in Eq. (2.5), (c) Deposition-dependent λ model by Eq. (2.4). Corresponding experimental results are in Figure 2.5, and (d) deposition-dependent λ model defined in Eq. (2.7).

Appendix D: Magnitudes of Capillary Number and Bond Number

In Section 3.4.1, the trapping number defined by using the generated emulsion size was selected to represent the capillary desaturation process. The magnitudes of buoyancy forces were not negligible when compared with viscous forces to displace the oil phase trapped by capillary forces. The capillary force is represented by the capillary number and the buoyancy force is represented by the Bond number. The relative importance of these two displacing forces can be shown by comparing the magnitudes of the Bond number and the capillary number. In Figure D.1, their relative magnitudes are shown for the experimental conditions used in Chapter 3. When the grain size is small, the Bond number was at most approximately 15% of the sum of the Bond number and the capillary number. The relative magnitude of the buoyancy force decreased with increasing fluid velocity or trapping number. However, for larger grain sizes, the contribution of the buoyancy force was larger than the viscous force, especially at low fluid velocities.

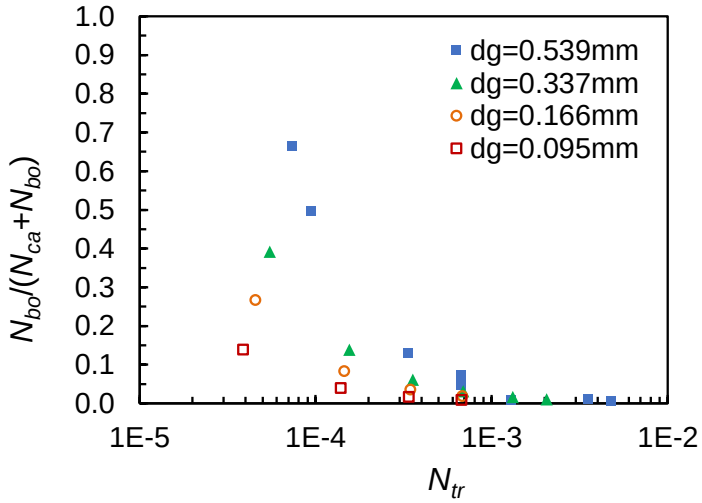

Figure D.1: Relative magnitude of Bond number to the sum of Bond number and capillary number.

Bibliography

Abou-Sayed, A., & Zaki, K. 2005. A Mechanistic Model for Formation Damage and Fracture Propagation During Water Injection. Paper SPE 94606 presented at the SPE European Formation Damage Conference, 25-27 May 2005, Sheveningen, The Netherlands. http://dx.doi.org/10.2118/94606-MS

Abou-Sayed, A. S., Sinha, K. P., & Clifton, R. J. 1984. Evaluation of the Influence of In-Situ Reservoir Conditions on the Geometry of Hydraulic Fractures Using a 3-D Simulator: Part 1-Technical Approach. Paper SPE 12877 presented at the SPE Unconventional Gas Recovery Symposium, 13-15 May 1984, Pittsburgh, Pennsylvania. http://dx.doi.org/10.2118/12877-MS

Abou-Sayed, A., Zaki, K., Wang, G., Sarfare, M., et al. 2007. Produced Water Management Strategy and Water Injection Best Practices: Design, Performance, and Monitoring. SPE Production & Operations, 22 (1). http://dx.doi.org/10.2118/108238-PA

Al-Abduwani, F. A. H., W.M.G.T. van, den, & Currie, P. K. 2001. Visual Observation of Produced Water Re-Injection Under Laboratory Conditions. Paper SPE 68977 presented at the SPE European Formation Damage Conference, 21-22 May 2001, The Hague, Netherlands. http://dx.doi.org/10.2118/68977-MS

Ali, M., Currie, P. K., & Salman, M. 2007. Permeability Damage Due to Water Injection Containing Oil Droplets and Solid Particles at Residual Oil Saturation. Paper SPE 104608 presented at the SPE Middle East Oil and Gas Show and Conference, 11-14 March 2007, Kingdom of Bahrain. http://dx.doi.org/10.2118/104608-MS

Ali, M., Currie, P., & Salman, M. 2009. The Effect of Residual Oil on Deep-Bed Filtration of Particles in Injection Water. SPE Production & Operations, 24 (1): 117–123. http://dx.doi.org/10.2118/107619-PA

Ali, S. A. 2013. Water Management. Journal of Petroleum Technology, 65 (12): 124–134.

Al-Riyamy, K., & Sharma, M. 2004. Filtration Properties of Oil-in-Water Emulsions Containing Solids. SPE Drilling & Completion, 19 (3): 164–172. http://dx.doi.org/10.2118/89015-PA

Alvarado, D. A., & Marsden Jr., S. S. 1979. Flow of Oil-in-Water Emulsions Through Tubes and Porous Media. Society of Petroleum Engineers Journal, 19 (6): 369–377. http://dx.doi.org/10.2118/5859-PA

Aziz, K., & Settari, A. 1979. Petroleum Reservoir Simulation. Applied Science Publishers.

Bachman, R. C., Harding, T. G., Settari, A. T., & Walters, D. A. 2003. Coupled Simulation of Reservoir Flow, Geomechanics, and Formation Plugging With Application to High-Rate Produced Water Reinjection. Paper SPE 79695 presented at the SPE Reservoir Simulation Symposium, 3-5 February, Houston, Texas. http://dx.doi.org/10.2118/79695-MS

Bailey, B., Elphick, J., Kuchuk, F., Romano, C., et al. 2000. Water Control. Oilfield Review, 12 (1): 30–51.

Barkman, J. H., & Davidson, D. H. 1972. Measuring Water Quality and Predicting Well Impairment. Journal of Petroleum Technology, 24 (7): 865–873. http://dx.doi.org/10.2118/3543-PA

Bedrikovetsky, P., Da Silva, M. J., Rocha Fonseca, D., Da Silva, M. F., et al. 2005. Well-History-Based Prediction of Injectivity Decline during Seawater Flooding. Paper SPE 93886 presented at the SPE European Formation Damage Conference, 25-27 May, Sheveningen, The Netherlands. http://dx.doi.org/10.2118/93886-MS

Bedrikovetsky, P., Tran, T. K., Van den Broek, W. M. G. T., Marchesin, D., et al. 2003. Damage Characterization of Deep Bed Filtration From Pressure Measurements. SPE Production & Facilities, 18 (2): 119–128. http://dx.doi.org/10.2118/83673-PA

Bentley, W. E., Kent, R. T., & Myers, G. R. 1986. Site availability for waste injection, Vickery, OH pp. 330–354. Presented at the International Symposium on the Subsurface Injection of Liquid Wastes, New Orleans.

Biot, M. A. 1941. General Theory of Three-Dimensional Consolidation. Journal of Applied Physics, 12 (2): 155–164.

BP. 2014. BP Statistical Review of World Energy. BP. Retrieved from http://www.bp.com/statisticalreview

Bui, H. D. 1977. An Integral Equations Method for Solving the Problem of a Plane Crack of Arbitrary Shape. Journal of the Mechanics and Physics of Solids, 25 (1): 29–39. http://dx.doi.org/10.1016/0022-5096(77)90018-7

Buret, S., Nabzar, L., & Jada, A. 2008. Emulsion Deposition in Porous Media : Impact on Well Injectivity. Paper SPE 113821 presented at the Europec/EAGE Conference and Exhibition, 9-12 June 2008, Rome, Italy. http://dx.doi.org/10.2118/113821-MS

Buret, S., Nabzar, L., & Jada, A. 2010. Water Quality and Well Injectivity: Do Residual Oil-in-Water Emulsions Matter? SPE Journal, 15 (2): 557–568. http://dx.doi.org /10.2118/122060-PA

Carter, R. D. 1957. Appendix I - Derivation of the General Equation for Estimating the Extent of the Fractured Area. Optimum Fluid Characteristics for Fracture Extension by G.C. Howard and C.R. Fast, Drilling and Production Practice (pp. 261–269). American Petroleum Institute.

Chang, C. K. 1985. Water Quality Considerations in Malaysia's First Waterflood. Journal of Petroleum Technology, 37 (09): 1689–1698. http://dx.doi.org/10.2118/12387-PA

Chen, H.-Y., & Teufel, L. W. 2000. Coupling Fluid-Flow and Geomechanics in Dual-Porosity Modeling of Naturally Fractured Reservoirs - Model Description and Comparison. Paper SPE 59043 presented at the SPE International Petroleum Conference and Exhibition in Mexico, 1-3 February, Villahermosa, Mexico. http://dx.doi.org/10.2118/59043-MS

Chen, H.-Y., & Teufel, L. W. 2001. Reservoir Stress Changes Induced by Production/Injection. Paper SPE 71087 presented at the SPE Rocky Mountain Petroleum Technology Conference, 21-23 May, Keystone, Colorado. http://dx.doi.org/10.2118/71087-MS

Chen, Z., & Zhang, Y. 2009. Well Flow Models for Various Numerical Methods. International Journal of Numerical Analysis and Modeling, 6 (3): 375–388.

Clark, C. E., & Veil, J. A. 2009. Produced Water Volumes and Management Practices in the United States (No. ANL/EVS/R-09/1). Argonne National Laboratory. Retrieved from http://www.netl.doe.gov/File%20Library/Research/Coal/ewr/water/anl-produced-water-volumes-sep09.pdf

Clifford, P. J., Berry, P. J., & Gu, H. 1991. Modeling the Vertical Confinement of Injection-well Thermal Fractures. SPE Production Engineering, 6 (04): 377–383. http://dx.doi.org/10.2118/20741-PA

Coleman, J. R., & McLelland, W. G. 1994. Produced Water Re-Injection; How Clean is Clean? Paper SPE 27394 presented at the SPE Formation Damage Control Symposium, 7-10 February, Lafayette, Louisiana. http://dx.doi.org/10.2118/27394-MS

Cortis, A., & Ghezzehei, T. A. 2007. On the transport of emulsions in porous media. Journal of Colloid and Interface Science, 313 (1): 1–4. http://dx.doi.org/10.1016/j.jcis.2007.04.021

Cushing, R. S., & Lawler, D. F. 1998. Depth Filtration: Fundamental Investigation through Three-Dimensional Trajectory Analysis. Environmental Science & Technology, 32 (23): 3793–3801. http://dx.doi.org/10.1021/es9707567

Dalmazzone, C., Noïk, C., Galinat, S., Masbernat, O., et al. 2005. Flow of a Concentrated Oil-Water Dispersion Through a Restriction. Paper BHR-2005-D2 presented at the 12th International Conference on Multiphase Production Technology, 25-27 May, Barcelona, Spain. Retrieved from https://www.onepetro.org/conference-paper/BHR-2005-D2

Darwish, M. I. M., van Boven, P., Hensens, H. C., & Zitha, P. L. J. 1999. Porous Media Flow of Oil Dispersions in Polymers. Paper SPE 56741 presented at the SPE Annual Technical Conference and Exhibition, 3-6 October, Houston, Texas. http://dx.doi.org/10.2118/56741-MS

De Souza, A. L. S., Fernandes, P. D., Mendes, R., Rosa, A. J., et al. 2005. The Impact of Fracture Propagation on Sweep Efficiency During a Waterflooding Process. Paper SPE 94704 presented at the SPE Latin American and Caribbean Petroleum Engineering Conference, 20-23 June, Rio de Janeiro, Brazil. http://dx.doi.org/10.2118/94704-MS

Dean, R. H., Gai, X., Stone, C. M., & Minkoff, S. E. 2006. A Comparison of Techniques for Coupling Porous Flow and Geomechanics. SPE Journal, 11 (01): 132–140. http://dx.doi.org/10.2118/79709-PA

Detienne, J. L., Creusot, M., Kessler, N., Sahuquet, B., et al. 1998. Thermally Induced Fractures: A Field-Proven Analytical Model. SPE Reservoir Evaluation & Engineering, 1 (01): 30–35. http://dx.doi.org/10.2118/30777-PA

Detienne, J. L., Ochi, J., & Rivet, P. 2005. A Simulator For Produced Water Re-injection in Thermally Fractured Wells. Paper SPE 95021 presented at the SPE European Formation Damage Conference, 25-27 May, Sheveningen, The Netherlands. http://dx.doi.org/10.2118/95021-MS

Detournay, E., & Cheng, A. H.-D. 1993. Fundamentals of Poroelasticity. Comprehensive Rock Engineering: Principles, Practice and Projects (Vol. 2, pp. 113–171). Oxford; New York: Pergamon Press. Retrieved from http://scholar.google.com/citations?view_op=view_citation&hl=en&user=kj2__CcAAAAJ&citation_for_view=kj2__CcAAAAJ:u5HHmVD_uO8C

Devereux, O. F. 1974a. Emulsion flow in porous solids: I. A flow model. The Chemical Engineering Journal, 7 (2): 121–128. http://dx.doi.org/10.1016/0300-9467(74)85005-7

Devereux, O. F. 1974b. Emulsion flow in porous solids: II. experiments with a crude oil-in-water emulsion in porous sandstone. The Chemical Engineering Journal, 7 (2): 129–136. http://dx.doi.org/10.1016/0300-9467(74)85006-9

Dikken, B. J., & Niko, H. 1987. Waterflood-Induced Fractures: A Simulation Study Of Their Propagation And Effects On Waterflood Sweep Efficiency. Paper SPE 16551 presented at the Offshore Europe, 8-11 September, Aberdeen, United Kingdom. http://dx.doi.org/10.2118/16551-MS

Dons, T., Jorgensen, O., & Gommesen, L. 2007. Observations and Quantitative Analyses of Waterflood Patterns in a Chalk Reservoir Using Seismic Data, Halfdan Field, Danish North Sea. Paper SPE 108531 presented at the Offshore Europe, 4-7 September 2007, Aberdeen, Scotland, U.K. http://dx.doi.org/10.2118/108531-MS

Economides, M. J., & Nolte, K. G. (Eds.). 2000. Reservoir Stimulation (3rd ed.). John Wiley & Sons.

Ergun, S. 1952. Fluid Flow Through Packed Columns. Chemical Engineering Progress, 48 (2): 89–94.

Eylander, J. G. R. 1988. Suspended Solids Specifications for Water Injection From Coreflood Tests. SPE Reservoir Engineering, 3 (4): 1287–1294. http://dx.doi.org/10.2118/16256-PA

Fitzpatrick, J. A., & Spielman, L. A. 1973. Filtration of Aqueous Latex Suspensions Through Beds of Glass Spheres. Journal of Colloid and Interface Science, 43 (2): 350–369. http://dx.doi.org/10.1016/0021-9797(73)90382-2

Fjelde, I. 2009. Formation Damage Caused by Emulsions During Drilling With Emulsified Drilling Fluids. SPE Drilling & Completion, 24 (02): 222–228. http://dx.doi.org/10.2118/105858-PA

Fletcher, A. J. P., Lamb, S. P., & Clifford, P. J. 1992. Formation Damage From Polymer Solutions: Factors Governing Injectivity. SPE Reservoir Engineering, 7 (02): 237–246. http://dx.doi.org/10.2118/20243-PA

Fredrich, J. T., Arguello, J. G., Thorne, B. J., Wawersik, W. R., et al. 1996. Three-Dimensional Geomechanical Simulation of Reservoir Compaction and Implications for Well Failures in the Belridge Diatomite. Paper SPE 36698 presented at the SPE Annual Technical Conference and Exhibition, 6-9 October, Denver, Colorado. http://dx.doi.org/10.2118/36698-MS

Fung, R. L., Vilayakumar, S., & Cormack, D. E. 1987. Calculation of Vertical Fracture Containment in Layered Formations. SPE Formation Evaluation, 2 (04): 518–522. http://dx.doi.org/10.2118/14707-PA

Gadde, P., & Sharma, M. 2001. Growing Injection Well Fractures and Their Impact on Waterflood Performance. Paper SPE 71614 presented at the SPE Annual Technical Conference and Exhibition, 30 September-3 October 2001, New Orleans, Louisiana. http://dx.doi.org/10.2118/71614-MS

Gadiyar, B., Meese, C., Stimatz, G., Morales, H., et al. 2004. Optimizing Frac Packs. Oilfield Review, 16 (3): 18–29.

Garcia, X., Nagel, N., Zhang, F., Sanchez-Nagel, M., et al. 2013. Revisiting Vertical Hydraulic Fracture Propagation Through Layered Formations – A Numerical Evaluation. 47th U.S. Rock Mechanics/Geomechanics Symposium. Paper ARMA 13-203 presented at the 47th U.S. Rock Mechanics/Geomechanics Symposium, 23-26 June, San Francisco, California. Retrieved from https://www.onepetro.org/conference-paper/ARMA-2013-203

Garon, A. M., Lin, C. Y., & Dunayevsky, V. A. 1988. Simulation of Thermally Induced Waterflood Fracturing in Prudhoe Bay. Paper SPE 17417 presented at the SPE California Regional Meeting, 23-25 March, Long Beach, California. http://dx.doi.org/10.2118/17417-MS

Geuzaine, C., & Remacle, J.-F. 2009. Gmsh: A 3-D finite element mesh generator with built-in pre- and post-processing facilities. International Journal for Numerical Methods in Engineering, 79 (11): 1309–1331. http://dx.doi.org/10.1002/nme.2579

Goodman, H. E. 2008. Wellbore Integrity, Sand Management, and Frac Pack. Journal of Petroleum Technology, 60 (9): 100–114.

Griffith, A. A. 1921. The Phenomena of Rupture and Flow in Solids. Philosophical Transactions of the Royal Society of London. Series A, Containing Papers of a Mathematical or Physical Character, 221 (582-593): 163–198. http://dx.doi.org/10.1098/rsta.1921.0006

Gringarten, A., Henry J., R., & Raghavan, R. 1974. Unsteady-State Pressure Distributions Created by a Well With a Single Infinite-Conductivity Vertical Fracture. Society of Petroleum Engineers Journal, 14 (4): 347–360. http://dx.doi.org/10.2118/4051-PA

Gruesbeck, C., & Collins, R. E. 1982. Entrainment and Deposition of Fine Particles in Porous Media. Society of Petroleum Engineers Journal, 22 (6). http://dx.doi.org/10.2118/8430-PA

Gu, H. 1987. Study of Propagation of Hydraulically Induced Fractures. The University of Texas at Austin, USA.

Hagoort, J., Weatherill, B. D., & Settari, A. 1980. Modeling the Propagation of Waterflood-Induced Hydraulic Fractures. Society of Petroleum Engineers Journal, 20 (04): 293–303. http://dx.doi.org/10.2118/7412-PA

Happel, J. 1958. Viscous Flow in Multiparticle Systems: Slow Motion of Fluids Relative to Beds of Spherical Particles. AIChE Journal, 4 (2): 197–201. http://dx.doi.org/10.1002/aic.690040214

Herzig, J. P., Leclerc, D. M., & Goff, P. L. 1970. Flow of Suspensions through Porous Media—Application to Deep Filtration. Industrial & Engineering Chemistry, 62 (5): 8–35. http://dx.doi.org/10.1021/ie50725a003

Hofman, J. A. M. H. 1990. Flow of Dilute Emulsions Through Porous Media. University of Eindhoven.

Hofman, J. A. M. H., & Stein, H. N. 1991. Permeability Reduction of Porous Media on Transport of Emulsions Through Them. Colloids and Surfaces, 61 (4): 317–329. http://dx.doi.org/10.1016/0166-6622(91)80318-I

Hsi, C. D., Dudzik, D. S., Lane, R. H., Buettner, J. W., et al. 1994. Formation Injectivity Damage Due to Produced Water Reinjection. Paper SPE 27395 presented at the SPE Formation Damage Control Symposium, 7-10 February, Lafayette, Louisiana. http://dx.doi.org/10.2118/27395-MS

Hussain, A., Minier-Matar, J., Gharfeh, S., Janson, A., et al. 2014. Advanced Technologies for Produced Water Treatment. OTC-24749-MS. Paper OTC 24749 OTC presented at the Offshore Technology Conference-Asia, 25-28 March, Kuala Lumpur, Malaysia. http://dx.doi.org/10.2118/24749-MS

Hustedt, B., Qiu, Y., Zwarts, D., & van den Hoek, P. J. 2005. Modeling Water-Injection Induced Fractures in Reservoir Simulation. Paper SPE 95726 presented at the SPE Annual Technical Conference and Exhibition, 9-12 October, Dallas, Texas. http://dx.doi.org/10.2118/95726-MS

Hustedt, B., Zwarts, D., Bjoerndal, H.-P., Al-Masfry, R. A., et al. 2008. Induced Fracturing in Reservoir Simulations: Application of a New Coupled Simulator to a Waterflooding Field Example. SPE Reservoir Evaluation & Engineering, 11 (03): 569–576. http://dx.doi.org/10.2118/102467-PA

Ison, C. R. 1967. Dilute Suspensions in Filtration. University of London, London, England.

Ives, K. J. 1962. Filtration using Radioactive Algae. Transactions of the American Society of Civil Engineers, 127 (3): 372–385.

Jaeger, J., Cook, N. G., & Zimmerman, R. 2007. Fundamentals of Rock Mechanics (4th edition.). Malden, MA: Wiley-Blackwell.

Jasak, H. 1996. Error analysis and estimation for the Finite Volume method with applications to fluid flows. Imperial College, University of London.

Jasak, H., & Weller, H. G. 2000. Application of the finite volume method and unstructured meshes to linear elasticity. International Journal for Numerical Methods in Engineering, 48 (2): 267–287. http://dx.doi.org/10.1002/(SICI)1097-0207(20000520)48:2<267::AID-NME884>3.0.CO;2-Q

Ji, L., Settari, A. T., Sullivan, R. B., & Orr, D. 2004. Methods For Modeling Dynamic Fractures In Coupled Reservoir And Geomechanics Simulation. Paper SPE 90874 presented at the SPE Annual Technical Conference and Exhibition, 26-29 September, Houston, Texas. http://dx.doi.org/10.2118/90874-MS

Jin, L., & Wojtanowicz, A. K. 2014. Development of Injectivity Damage Due to Oily Waste Water in Linear Flow. Paper SPE 168130 presented at the SPE International Symposium and Exhibition on Formation Damage Control, 26-28 February, Lafayette, Louisiana, USA. http://dx.doi.org/10.2118/168130-MS

Jin, M., Somerville, J., & Smart, B. G. D. 2000. Coupled Reservoir Simulation Applied to the Management of Production Induced Stress-Sensitivity. Paper SPE 64790 presented at the International Oil and Gas Conference and Exhibition in China, 7-10 November, Beijing, China. http://dx.doi.org/10.2118/64790-MS

Khatib, Z., & Verbeek, P. 2002. Water to Value - Produced Water Management for Sustainable Field Development of Mature and Green Fields. Paper SPE 73853 presented at the SPE International Conference on Health, Safety and Environment in Oil and Gas Exploration and Production, 20-22 March, Kuala Lumpur, Malaysia. http://dx.doi.org/10.2118/73853-MS

Kim, J., Moridis, G. J., & Rutqvist, J. 2012. Coupled Flow and Geomechanical Analysis for Gas Production in the Prudhoe Bay Unit L-106 Well Unit C Gas Hydrate Deposit in Alaska. Journal of Petroleum Science and Engineering, 92–93 (0): 143–157. http://dx.doi.org/10.1016/j.petrol.2012.04.012

Kim, J., Moridis, G., Yang, D., & Rutqvist, J. 2012. Numerical Studies on Two-Way Coupled Fluid Flow and Geomechanics in Hydrate Deposits. SPE Journal, 17 (2). http://dx.doi.org/10.2118/141304-PA

Koutsabeloulis, N. C., & Hope, S. A. 1998. "Coupled" Stress/Fluid/Thermal Multi-Phase Reservoir Simulation Studies Incorporating Rock Mechanics. Paper SPE 47393 presented at the SPE/ISRM Rock Mechanics in Petroleum Engineering, 8-10 July, Trondheim, Norway. http://dx.doi.org/10.2118/47393-MS

Lake, L. W. 1989. Enhanced Oil Recovery. Prentice Hall Incorporated.

Mantell, M. E. 2011. Produced Water Reuse and Recycling Challenges and Opportunities Across Major Shale Plays. presented at the EPA Hydraulic Fracturing Study

Technical Workshop #4. Retrieved from http://www2.epa.gov/sites/production /files/documents/09_Mantell_-_Reuse_508.pdf

Maroudas, A., & Eisenklam, P. 1965. Clarification of Suspensions: A Study of Particle Deposition in Granular Media: Part I—Some Observations on Particle Deposition. Chemical Engineering Science, 20 (10): 867–873. http://dx.doi.org/10.1016/0009-2509(65)80083-5

Martins, J. P., Murray, L. R., Clifford, P. J., McLelland, W. G., et al. 1995. Produced-Water Reinjection and Fracturing in Prudhoe Bay. SPE Reservoir Engineering, 10 (03): 176–182. http://dx.doi.org/10.2118/28936-PA

Mastrojannis, E. N., Keer, L. M., & Mura, T. 1980. Growth of Planar Cracks Induced by Hydraulic Fracturing. International Journal for Numerical Methods in Engineering, 15 (1): 41–54. http://dx.doi.org/10.1002/nme.1620150105

Mendez, Z. 1999. Flow of Dilute Oil-in-Water Emulsions in Porous Media. The University of Texas at Austin.

Minner, W. A., Wright, C. A., Stanley, G. R., Pater, C. J., et al. 2002. Waterflood and Production-Induced Stress Changes Dramatically Affect Hydraulic Fracture Behavior in Lost Hills Infill Wells. Paper SPE 77536 presented at the SPE Annual Technical Conference and Exhibition, 29 September-2 October 2002, San Antonio, Texas. http://dx.doi.org/10.2118/77536-MS

Monteagudo, J. E. P., Rodriguez, A. A., & Florez, H. 2011. Simulation Of Flow In Discrete Deformable Fractured Porous Media. Paper SPE 141267 presented at the SPE Reservoir Simulation Symposium, 21-23 February, The Woodlands, Texas, USA. http://dx.doi.org/10.2118/141267-MS

Myers, J. E. 2014. Chevron San Ardo Facility Unit (SAFU) Beneficial Produced Water Reuse for Irrigation. Paper SPE 168401 presented at the SPE International Conference on Health, Safety, and Environment, 17-19 March, Long Beach, California, USA. http://dx.doi.org/10.2118/168401-MS

Norris, A. 1992. On the Correspondence Between Poroelasticity and Thermoelasticity. Journal of Applied Physics, 71 (3): 1138–1141. http://dx.doi.org/10.1063/1.351278

Ochi, J., Detienne, J.-L., & Rivet, P. 2007. Internal Formation Damage Properties and Oil-Deposition Profile Within Reservoirs During PWRI Operations. Paper SPE 108010 presented at the European Formation Damage Conference, 30 May-1 June 2007, Scheveningen, The Netherlands. http://dx.doi.org/10.2118/108010-MS

Ochi, J., Dexheimer, D., & Corpel, V. 2013. Produced Water Re-Injection Design and Uncertainties Assessment. Paper SPE 165138 presented at the SPE European Formation Damage Conference & Exhibition, 5-7 June, Noordwijk, The Netherlands. http://dx.doi.org/10.2118/165138-MS

Ouyang, S. 1994. Propagation of Hydraulically Induced Fractures with Proppant Transport. The University of Texas at Austin, USA.

Ovens, J. E. V., Larsen, F. P., & Cowie, D. R. 1998. Making Sense of Water Injection Fractures in the Dan Field. SPE Reservoir Evaluation & Engineering, 1 (6): 556–566. http://dx.doi.org/10.2118/52669-PA

Paige, R. W., Murray, L. R., Martins, J. P., & Marsh, S. M. 1995. Optimising Water Injection Performance. Paper SPE 29774 presented at the Middle East Oil Show, 11-14 March, Bahrain. http://dx.doi.org/10.2118/29774-MS

Pang, S., & Sharma, M. M. 1995. Evaluating the Performance of Open-Hole, Perforated and Fractured Water Injection Wells. Paper SPE 30127 presented at the SPE European Formation Damage Conference, 15-16 May, The Hague, Netherlands. http://dx.doi.org/10.2118/30127-MS

Pang, S., & Sharma, M. M. 1997. A Model for Predicting Injectivity Decline in Water-Injection Wells. SPE Formation Evaluation, 12 (3): 194–201. http://dx.doi.org /10.2118/28489-PA

Peaceman, D. W. 1983. Interpretation of Well-Block Pressures in Numerical Reservoir Simulation With Nonsquare Grid Blocks and Anisotropic Permeability. Society of Petroleum Engineers Journal, 23 (3). http://dx.doi.org/10.2118/10528-PA

Perkins, T. K., & Gonzalez, J. A. 1985. The Effect of Thermoelastic Stresses on Injection Well Fracturing. Society of Petroleum Engineers Journal, 25 (1): 78–88. http://dx.doi.org/10.2118/11332-PA

Peters, E. J. 2012. Advanced Petrophysics: Volume 2: Dispersion, Interfacial Phenomena/Wettability, Capillarity/Capillary Pressure, Relative Permeability. Greenleaf Book Group.

Pope, G. A., Wu, W., Narayanaswamy, G., Delshad, M., et al. 2000. Modeling Relative Permeability Effects in Gas-Condensate Reservoirs With a New Trapping Model. SPE Reservoir Evaluation & Engineering, 3 (02): 171–178. http://dx.doi.org /10.2118/62497-PA

Rajagopalan, R., & Tien, C. 1976. Trajectory Analysis of Deep-Bed Filtration with the Sphere-in-Cell Porous Media Model. AIChE Journal, 22 (3): 523–533. http://dx.doi.org/10.1002/aic.690220316

Rice, J. R., & Cleary, M. P. 1976. Some basic stress diffusion solutions for fluid-saturated elastic porous media with compressible constituents. Reviews of Geophysics, 14 (2): 227–241. http://dx.doi.org/10.1029/RG014i002p00227

Rod, M., & Jorgensen, O. 2005. Injection Fracturing in a Densely Spaced Line Drive Waterflood - The Halfdan Example. Paper SPE 94049 presented at the SPE Europec/EAGE Annual Conference, 13-16 June, Madrid, Spain. http://dx.doi.org/10.2118/94049-MS

Roussel, N., & Sharma, M. 2010. Quantifying Transient Effects in Altered-Stress Refracturing of Vertical Wells. SPE Journal, 15 (3). http://dx.doi.org/10.2118/119522-PA

Roussel, N., & Sharma, M. 2011. Optimizing Fracture Spacing and Sequencing in Horizontal-Well Fracturing. SPE Production & Operations, 26 (2). http://dx.doi.org/10.2118/127986-PA

Roussel, N., & Sharma, M. 2012. Role of Stress Reorientation in the Success of Refracture Treatments in Tight Gas Sands. SPE Production & Operations, 27 (4). http://dx.doi.org/10.2118/134491-PA

Roussel, N., Florez, H., & Rodriguez, A. A. 2013. Hydraulic Fracture Propagation from Infill Horizontal Wells. Paper SPE 166503 presented at the SPE Annual Technical Conference and Exhibition, 30 September-2 October, New Orleans, Louisiana, USA. http://dx.doi.org/10.2118/166503-MS

Samier, P., Onaisi, A., & de Gennaro, S. 2008. A Practical Iterative Scheme for Coupling Geomechanics With Reservoir Simulation. SPE Reservoir Evaluation & Engineering, 11 (05): 892–901. http://dx.doi.org/10.2118/107077-PA

Samier, P., Onaisi, A., & Fontaine, G. 2006. Comparisons of Uncoupled and Various Coupling Techniques for Practical Field Examples. SPE Journal, 11 (01): 89–102. http://dx.doi.org/10.2118/79698-PA

Saraf, A., de Zwart, A., Currie, P., & Ali, M. A. J. 2010. Analysis of the Effect of Residual Oil on Particle Trapping During Produced-Water Reinjection Using X-Ray Tomography. SPE Journal, 15 (4): 943–951. http://dx.doi.org/10.2118/122137-PA

Saripalli, K. ., Sharma, M. ., & Bryant, S. . 2000. Modeling Injection Well Performance During Deep-Well Injection of Liquid Wastes. Journal of Hydrology, 227 (1–4): 41–55. http://dx.doi.org/10.1016/S0022-1694(99)00164-X

Saripalli, K., Bryant, S., & Sharma, M. 1999. Role of Fracture Face and Formation Plugging in Injection Well Fracturing and Injectivity Decline. Paper SPE 52731 presented at the SPE/EPA Exploration and Production Environmental Conference, 1-3 March 1999, Austin, Texas. http://dx.doi.org/10.2118/52731-MS

Seright, R. S., Seheult, J. M., & Talashek, T. 2009. Injectivity Characteristics of EOR Polymers. SPE Reservoir Evaluation & Engineering, 12 (05): 783–792. http://dx.doi.org/10.2118/115142-PA

Settari, A., & Warren, G. M. 1994. Simulation and field analysis of waterflood induced fracturing. Paper SPE 28081 presented at the Rock Mechanics in Petroleum Engineering, 29-31 August, Delft, Netherlands. http://dx.doi.org/10.2118/28081-MS

Sharma, M. M., & Yortsos, Y. C. 1987. Transport of Particulate Suspensions in Porous Media: Model Formulation. AIChE Journal, 33 (10): 1636–1643. http://dx.doi.org/10.1002/aic.690331007

Sharma, M. M., Pang, S., Wennberg, K. E., & Morgenthaler, L. N. 2000. Injectivity Decline in Water-Injection Wells: An Offshore Gulf of Mexico Case Study. SPE Production & Facilities, 15 (1): 6–13. http://dx.doi.org/10.2118/60901-PA

Shumbera, D., Ritter, D., Ellis, R., Jannise, R., et al. 2003. Improved Water Injector Performance in a Gulf of Mexico Deepwater Development Using an Openhole Frac Pack Completion and Downhole Filter System: Case History. Paper SPE 84416 presented at the SPE Annual Technical Conference and Exhibition, 5-8 October 2003, Denver, Colorado. http://dx.doi.org/10.2118/84416-MS

Simonson, E. R., Abou-Sayed, A. S., & Clifton, R. J. 1978. Containment of Massive Hydraulic Fractures. Society of Petroleum Engineers Journal, 18 (01): 27–32. http://dx.doi.org/10.2118/6089-PA

Soo, H., & Radke, C. J. 1986. A Filtration Model for the Flow of Dilute, Stable Emulsions in Porous Media—I. Theory. Chemical Engineering Science, 41 (2): 263–272. http://dx.doi.org/10.1016/0009-2509(86)87007-5

Soo, H., Williams, M. C., & Radke, C. J. 1986. A Filtration Model for the Flow of Dilute, Stable Emulsions in Porous Media—II. Parameter Evaluation and Estimation. Chemical Engineering Science, 41 (2): 273–281. http://dx.doi.org/10.1016/0009-2509(86)87008-7

SPE. 2011. Challenges in Reusing Produced Water. Society of Petroleum Engineers. Retrieved from http://www.spe.org/tech/2011/10/challenges-in-reusing-produced-water/

Spielman, L. A., & Goren, S. L. 1972. Theory of Coalescence by Flow through Porous Media. Industrial & Engineering Chemistry Fundamentals, 11 (1): 66–72. http://dx.doi.org/10.1021/i160041a011

Stevens, D. G., Murray, L. R., & Shah, P. C. 2000. Predicting Multiple Thermal Fractures in Horizontal Injection Wells; Coupling of a Wellbore and a Reservoir Simulator. Paper SPE 59354 presented at the SPE/DOE Improved Oil Recovery Symposium, 3-5 April, Tulsa, Oklahoma. http://dx.doi.org/10.2118/59354-MS

Suarez-Rivera, R., Stenebråten, J., Gadde, P., & Sharma, M. 2002. An Experimental Investigation of Fracture Propagation During Water Injection. Paper SPE 73740 presented at the International Symposium and Exhibition on Formation Damage Control, 20-21 February 2002, Lafayette, Louisiana. http://dx.doi.org/10.2118/73740-MS

Suri, A., & Sharma, M. 2009. Fracture Growth in Horizontal Injectors. Paper SPE 119379 presented at the SPE Hydraulic Fracturing Technology Conference, 19-21 January 2009, The Woodlands, Texas. http://dx.doi.org/10.2118/119379-MS

Suri, A., & Sharma, M. 2010. A Model for Water Injection Into Frac-Packed Wells. SPE Reservoir Evaluation & Engineering, 13 (3): 449–464. http://dx.doi.org /10.2118/110084-PA

Suri, A., Sharma, M., & Moreno, J. M. M. 2010. Injectivity of Frac-Packed Wells: A Case Study of the Guando Field. Paper SPE 125897 presented at the SPE International Symposium and Exhibiton on Formation Damage Control, 10-12 February 2010, Lafayette, Louisiana, USA. http://dx.doi.org/10.2118/125897-MS

Suri, A., Sharma, M., & Peters, E. 2011. Estimates of Fracture Lengths in an Injection Well by History Matching Bottomhole Pressures and Injection Profile. SPE Reservoir Evaluation & Engineering, 14 (4): 385–397. http://dx.doi.org/10.2118/132524-PA

Tenizbaeva, B. M., Macary, S. M., Seitim, M., & Yessaliyeva, A. 2012. Waste Water Disposal Has Become Critical Strategic Focus Area. Paper SPE 160769 presented at the SPE Russian Oil and Gas Exploration and Production Technical Conference and Exhibition, 16-18 October, Moscow, Russia. http://dx.doi.org /10.2118/160769-MS

Teufel, L. W., & Clark, J. A. 1984. Hydraulic Fracture Propagation in Layered Rock: Experimental Studies of Fracture Containment. SPE Journal, 24 (01): 19–32. http://dx.doi.org/10.2118/9878-PA

Thomas, G. W. 1981. Principles of Hydrocarbon Reservoir Simulation. Englewood Cliffs, N.J.: Prentice-Hall.

Thomas, L. K., Chin, L. Y., Pierson, R. G., & Sylte, J. E. 2003. Coupled Geomechanics and Reservoir Simulation. SPE Journal, 8 (04): 350–358. http://dx.doi.org/10.2118/87339-PA

Thomas, M. 2013. Enhanced Production. BP Magazine, (4): 31–35.

Tibbetts, P. J. C., Buchanan, I. T., Gawel, L. J., & Large, R. 1992. A Comprehensive Determination of Produced Water Composition. In J. P. Ray & F. R. Engelhardt (Eds.), Produced Water, Environmental Science Research (pp. 97–112). Springer US. Retrieved from http://link.springer.com/chapter/10.1007/978-1-4615-2902-6_9

Todd, A. C., Kumar, T., & Mohammadi, S. 1990. The Value and Analysis of Core-Based Water-Quality Experiments as Related to Water Injection Schemes. SPE Formation Evaluation, 5 (02): 185–191. http://dx.doi.org/10.2118/17148-PA

Tran, D., Settari, A., & Nghiem, L. 2002. New Iterative Coupling Between a Reservoir Simulator and a Geomechanics Module. Paper SPE 78192 presented at the SPE/ISRM Rock Mechanics Conference, 20-23 October, Irving, Texas. http://dx.doi.org/10.2118/78192-MS

Tufenkji, N., & Elimelech, M. 2003. Correlation Equation for Predicting Single-Collector Efficiency in Physicochemical Filtration in Saturated Porous Media. Environ. Sci. Technol., 38 (2): 529–536. http://dx.doi.org/10.1021/es034049r

Van den Broek, W. M. G. T., Bruin, J. N., Tran, T. K., van der Zande, M. J., et al. 1999. Core-Flow Experiments With Oil and Solids Containing Water. Paper SPE 54769 presented at the SPE European Formation Damage Conference, 31 May-1 June, The Hague, Netherlands. http://dx.doi.org/10.2118/54769-MS

Van den Hoek, P. J. 2005. Dimensions and Degree of Containment of Waterflood-Induced Fractures from Pressure Transient Analysis. SPE Reservoir Evaluation & Engineering, 8 (05): 377–387. http://dx.doi.org/10.2118/84289-PA

Van den Hoek, P. J., Al-Masfry, R. A., Zwarts, D., Jansen, J.-D., et al. 2008. Waterflooding Under Dynamic Induced Fractures: Reservoir Management and Optimisation of Fractured Waterfloods. Paper SPE 110379 presented at the SPE Symposium on Improved Oil Recovery, 20-23 April, Tulsa, Oklahoma, USA. http://dx.doi.org/10.2118/110379-MS

Van den Hoek, P. J., Matsuura, T., de Kroon, M., & Gheissary, G. 1996. Simulation of Produced Water Re-Injection Under Fracturing Conditions. Paper SPE 36846 presented at the European Petroleum Conference , 22-24 October 1996, Milan, Italy. http://dx.doi.org/10.2118/36846-MS

Van der Zande, M. J., Janssen, P. H., & van den Broek, W. M. G. T. 2001. Size of Oil Droplets Under High-Water-Cut Conditions. Paper SPE 67250 presented at the SPE Production and Operations Symposium, 24-27 March, Oklahoma City, Oklahoma. http://dx.doi.org/10.2118/67250-MS

Van Eekelen, H. A. M. 1982. Hydraulic Fracture Geometry: Fracture Containment in Layered Formations. Society of Petroleum Engineers Journal, 22 (03): 341–349. http://dx.doi.org/10.2118/9261-PA

Van Oort, E., van Velzen, J. F. G., & Leerlooijer, K. 1993. Impairment by Suspended Solids Invasion: Testing and Prediction. SPE Production & Facilities, 8 (3): 178–184. http://dx.doi.org/10.2118/23822-PA

Vaz Jr., A., Bedrikovetsky, P., Furtado, C. J., Siqueira, A., et al. 2006a. Effects of Residual Oil on Reinjection of Produced Water. Paper SPE 100341 presented at the SPE Europec/EAGE Annual Conference and Exhibition, 12-15 June 2006, Vienna, Austria. http://dx.doi.org/10.2118/100341-MS

Vaz Jr., A., Bedrikovetsky, P., Furtado, C. J., Siqueira, A., et al. 2006b. Injectivity Impairment Due to Residual Oil Mobilisation (Treatment of Laboratory Data). Paper SPE 100391 presented at the SPE Asia Pacific Oil & Gas Conference and Exhibition, 11-13 September 2006, Adelaide, Australia. http://dx.doi.org /10.2118/100391-MS

Veil, J. A. 2009. Produced Water Management Options - One Size Does Not Fit All. presented at the SPE Distinguished Lecturer Program. Retrieved from https://www.onepetro.org/other/27233

Veil, J. A., Puder, M. G., Elcock, D., & Redweik, R. 2004. A White Paper Describing Produced Water from Production of Crude Oil, Natural Gas, and Coal Bed Methane (Submitted to U.S. Department of Energy No. W-31-109-Eng-38). Argonne National Laboratory. Retrieved from http://netl.doe.gov/research/energy-analysis/publications/details?pub=2061f020-2f50-4c65-b464-779f0e23a628

Weller, H. G., Tabor, G., Jasak, H., & Fureby, C. 1998. A tensorial approach to computational continuum mechanics using object-oriented techniques. Computers in Physics, 12 (6): 620–631. http://dx.doi.org/10.1063/1.168744

Wennberg, K. E. 1998. Particle Retention in Porous Media: Applications to Water Injectivity Decline. NTNU - Norwegian University of Science and Technology, Trondheim, Norway.

Wennberg, K. E., & Sharma, M. M. 1997. Determination of the Filtration Coefficient and the Transition Time for Water Injection Wells. Paper SPE 38181 presented at the SPE European Formation Damage Conference, 2-3 June 1997, The Hague, Netherlands. http://dx.doi.org/10.2118/38181-MS

Wright, C. A., Conant, R. A., Golich, G. M., Bondor, P. L., et al. 1995. Hydraulic Fracture Orientation and Production/Injection Induced Reservoir Stress Changes in Diatomite Waterfloods. Paper SPE 29625 presented at the SPE Western Regional Meeting, 8-10 March, Bakersfield, California. http://dx.doi.org/10.2118/29625-MS

Wright, C. A., Stewart, D. W., Emanuele, M. A., & Wright, W. W. 1994. Reorientation of Propped Refracture Treatments in the Lost Hills Field. Paper SPE 27896 presented at the SPE Western Regional Meeting, 23-25 March 1994, Long Beach, California. http://dx.doi.org/10.2118/27896-MS

Yao, K.-M., Habibian, M. T., & O'Melia, C. R. 1971. Water and Waste Water Filtration. Concepts and Applications. Environmental Science & Technology, 5 (11): 1105–1112. http://dx.doi.org/10.1021/es60058a005

Yew, C. H. 1997. Mechanics of Hydraulic Fracturing. Gulf Professional Publishing.

Zechner, M., Clemens, T., Suri, A., & Sharma, M. M. 2014. Simulation of Polymer Injection under Fracturing Conditions - A Field Pilot in the Matzen Field, Austria. Paper SPE 169043 presented at the SPE Improved Oil Recovery Symposium, 12-16 April, Tulsa, Oklahoma, USA. http://dx.doi.org/10.2118/169043-MS

Zhang, N. S., Somerville, J. M., & Todd, A. C. 1993. An Experimental Investigation of the Formation Damage Caused by Produced Oily Water Injection. Paper SPE 26702 presented at the Offshore Europe, 7-10 September, Aberdeen, United Kingdom. http://dx.doi.org/10.2118/26702-MS

Zheng, H., & Buchanan, W. L. 2013. Robust Semi-Implicit Three-Dimensional Upwind Techniques for Reducing Grid Orientation Effect in Thermal Simulations. Paper SPE 163617 presented at the SPE Reservoir Simulation Symposium, 18-20 February, The Woodlands, Texas, USA. http://dx.doi.org/10.2118/163617-MS

Zimmerman, R. W. 2000. Coupling in Poroelasticity and Thermoelasticity. International Journal of Rock Mechanics and Mining Sciences, 37 (1–2): 79–87. http://dx.doi.org/10.1016/S1365-1609(99)00094-5

The citation format in Bibliography followed the Style Guide (2014) recommended by Society of Petroleum Engineers.